universität wien

DISSERTATION

Cellular Studies on Novel Critical Targets of Anti-Tumor Metal Chelators and Complexes

Robert Trondl

angestrebter akademischer Grad

Doktor der Naturwissenschaften (Dr.rer.nat.)

Wien, Mai 2012

Studienkennzahl lt. Studienblatt:	A 091 419
Dissertationsgebiet lt. Studienblatt:	Chemie
Betreuerin / Betreuer:	O. Univ.-Prof. Dr. Dr. Bernhard K. Keppler

Für meine Mutter

Danksagung

Ich möchte mich bei Prof. DDr. Bernhard Keppler für die Möglichkeit bedanken die Doktorarbeit in seiner Arbeitsgruppe durchzuführen und für das Vertrauen neue Wege im zellbiologischen Labor zu beschreiten.

Ich möchte mich bei Michael Jakupec für die sehr gute und freundschaftliche Zusammenarbeit, Betreuung und Diskussionsbereitschaft bei wissenschaftlichen Fragen bedanken Michael Jakupec hat mir fachkundig die komplexen Abläufe der Krebsforschung nähergebracht und hatte während meiner ganzen Doktorarbeit ein offenes Ohr für anfallende Probleme.

Ein großes Dankeschön geht an alle meine Kollegen des zellbiologischen Labors Simone Göschl, Caroline Bartel, Anton Legin, Gerhard Mühlgassner, Maria Novak, Mojtaba Valiahdi, Michaela Hejl und Mahsa Razavi für die freundliche und sehr angenehme Arbeitsatmosphäre. Danke auch an meine neuen Mitarbeiterinnen Katerina Brynzak und Lea Flocke. Trotz der begrenzten Zeit für ihre Betreuung in den letzten Monaten meiner Doktorarbeit, haben sie mir viel Rücksicht und Geduld entgegengebracht.

Für die gute Zusammenarbeit möchte ich mich auch bei den Kollegen aus der übrigen Arbeitsgruppe und des Instituts für Krebsforschung ganz herzlich bedanken. Ganz besonders bei Anna Bytzek, Petra Heffeter und Christian Kowol.

Bei allen meinen Freunden möchte ich mich bedanken, da sie mir den nötigen Ausgleich und Abstand zur wissenschaftlichen Arbeit gaben. Vielen Dank an Daniel, Martin, Rafael, Nici, Romi, Michael, Georg, Annett Hambo und Lili.

Ein ganz besonderer Dank gilt Carmen, sie war soweit ich denken kann und trotz der teilweise turbulenten Zeiten immer für mich da.

Bei meiner Familie möchte ich mich ganz herzlich bedanken. Obwohl die letzten Jahre sehr schwer waren, hat es immer einen starken Zusammenhalt gegeben.

Zum Schluss möchte ich der Person danken, die bei jedem einzelnem Experiment mitgefiebert hat und wahrscheinlich den größten Stolz bei der Fertigstellung dieser Arbeit empfindet. Meiner Mutter. Vielen Dank für die liebevolle und grenzenlose Unterstützung.

Abstract

Non-platinum metal compounds with anticancer activity represent a promising class of investigational drugs for cancer treatment. Since biological properties of novel metal compounds can differ from those of the well established platinum drugs, investigations on their mode of actions are essential. The research work presented in this PhD thesis is focused on cell biological studies on novel molecular targets of α-N-heterocyclic thiosemicarbazones and ruthenium complexes.

Triapine (3-aminopyridine-2-carboxaldehyde thiosemicarbazone), which entered several clinical phase I and II trials is currently the most extensively studied thiosemicarbazone. Triapine forms complexes with the biological relevant metals iron, zinc and copper in a highly effective manner and is a potent inhibitor of ribonucleotide reductase. Structure-activity relationships of Triapine derivatives and corresponding iron, gallium, zinc and copper complexes were studied on human cancer cell lines. Furthermore, intrinsic fluorescence properties of several of these compounds enabled us to study their intracellular distribution by fluorescence microscopy. Enhancement of cytotoxic properties by dimethylation of the terminal amino group and cellular accumulation in the endoplasmic reticulum (ER) inspired us to study the influence of thiosemicarbazones on the unfolded protein response (UPR), an adaptive rescue pathway of the ER. Investigations of key factors of the UPR on protein and mRNA levels revealed that enhanced cytotoxic properties resulting from dimethylation correlates with elevated UPR signaling. Moreover, proapoptotic signaling via the ER stress-related transcription factor CHOP and loss of mitochondrial membrane potential suggest that ER stress induction is an additional mechanism for the biological activity of α-N-heterocyclic thiosemicarbazones.

Beside the experimental studies a synoptic article about the investigational ruthenium drug NKP-1339 summarizing and discussing the current knowledge about this compound and its mode of action is included in this thesis. NKP-1339 was evaluated recently in a clinical phase I trial with the result of very limited side effects and several responding cases with various refractory forms of cancer.

Zusammenfassung

Neben Platinverbindungen sind auch Nicht-Platin-Metallverbindungen mit antitumoraler Wirkung eine vielversprechende Klasse potentieller Wirkstoffe für die Krebstherapie. Da sich die biologischen Eigenschaften neuartiger Metallverbindungen wesentlich von den etablierten Platinverbindungen unterscheiden, sind Wirkmechanismusstudien von großer Bedeutung. Die in dieser Doktorarbeit vorgelegten Forschungsartikel beschäftigen sich mit zellbiologischen Untersuchungen zu neuartigen molekularen Wirkmechanismen von α-N-heterozyklischen Thiosemicarbazonen und Ruthenium-Komplexen.

Triapin (3-Aminopyridin-2-carboxaldehyd-thiosemicarbazon) is derzeit der am intensivsten untersuchten Vertreter der Thiosemicarbazone und durchlief bereits zahlreiche klinische Phase I- und Phase II-Studien. Triapin geht stabile Komplexe mit den biologisch relevanten Metallen Eisen, Zink und Kupfer ein und ist ein Inhibitor der Ribonukleotid-Reduktase. Struktur-Aktivitäts-Beziehungen wurden von mehreren Triapinderivaten und dessen Eisen-, Gallium-, Zink- und Kupfer-Komplexen in humanen Tumorzellinien untersucht. Weiters wurde durch die intrinsischen Fluoreszenzeigenschaften von Triapin und Derivaten die intrazelluläre Verteilung mittels Fluoreszenzmikroskopie studiert. Die Aktivitätssteigerung durch Dimethylierung der terminalen Aminogruppe sowie die zelluläre Akkumulation im Endoplasmatischen Retikulum veranlasste uns, den Einfluss von Thiosemicarbazonen auf die Unfolded Protein Response (UPR) zu studieren. Die mit der Dimethylierung einhergehende erhöhte Zytotoxizität korreliert mit der Hochregulation von Schlüsselfaktoren der UPR auf Protein- als auch mRNA-Ebene. Zudem weisen die Aktivierung des proapoptotischen Transkriptionsfaktors CHOP im Zuge der UPR und die Depolarisierung der mitochondrialen Membranen auf einen zusätzlichen molekularen Wirkmechanismus für Thiosemicarbazone hin.

Neben experimentellen Studien beinhaltet diese Doktorarbeit auch einen synoptischen Artikel über die Ruthenium-Verbindung NKP-1339, der den aktuellen Wissensstand zu dieser Verbindung und deren Wirkmechanismus zusammenfasst und diskutiert. Diese wurde kürzlich in einer klinische Phase I Studie evaluiert und zeigte in dieser sehr geringe Nebenwirkungen sowie Wirksamkeit in mehreren Fällen verschiedener fortgeschrittenen Krebserkrankungen.

Table of Contents

1 Introduction

1.1 Definition of Cancer

The human body consists of a vast variety of different cells, each cell type equipped with its own specific functionality. Most of the cells carry the full genetic information, far more to fulfill the cell-type-specific tasks. The autonomy of the individual cells facilitates proliferation, morphogenesis and apoptosis. Such autonomy and versatility is needed for adaption of adult tissues throughout the life span, for instance repairing wounds and replacement of cells. However, at same time the autonomy and versatility of each cell implies an enormous danger for the organism, when cells activate genomic sequences that are normally not supposed for this cell type. Furthermore, alterations in gene functionality caused by mutations are bearing an additional risk for disruption of cell homeostasis. As a consequence, highly abnormal phenotypes may be incompatible with surrounding normal cells, regarding growth rates and programmed cell death. If these abnormal phenotypes are associated with aggressive cell proliferation and invasion of nearby tissue, then they are termed malignant neoplasms or cancer [1].

Cancers can arise from many specialized cell types and are normally categorized and termed after their origin organ site. Around 80% of human cancers in the Western world arise from tissues which line and cover the surfaces of cavities, channels and many organs. Epithelial-derived tumors are termed carcinomas. Most carcinomas are classified in two categories, referring to biological functions of epithelial cell types. Tumors from epithelial cells forming protective cell layers are called squamous cell carcinomas. The second class of carcinomas arises from epithelial cells which are specialized to secrete substances into cavities and are termed adenocarcinomas. Most common tissue sites forming adenocarcinomas are initiated in organs such as lung, colon, breast, pancreas and prostate [1].

Sarcomas are malignancies from non-epithelial cells and referring to neoplasms of the connective tissue. These tumors derive from a variety of mesenchymal cell types and include tumors of muscles and bones. Only 1% of cancers in the clinic are accounting to sarcomas. The second group of non-epithelial malignancies are formed by hematopoietic tissues referring to progenitor cells of the myeloid or lymphoid lineages. Hematopoietic malignancies are termed lymphomas,

solid tumors of lymphoid lineages, or leukemias, characterized by freely circulating malignant cells of either lineage. The third group of non-epithelial tumors orginate from cells of the central and peripheral nervous system and are termed neuroectodermal tumor, which include gliomas, glioblastomas and neuroblastomas.[1–3]

1.2 Epidemiology of Cancer

Cancer is the second most common cause of death after cardiovascular diseases in most Western countries and responsible for about 25% of deaths. The prevalence of cancer is strongly correlating with the age. In Austria, about three quarters of cancer patients are older than 55 years. The most affected age groups are persons between 65 and 74 years. Thus, cancer became a more serious problem for Western and newly industrializing countries with increasing life expectancy in the last decades. [1, 4]

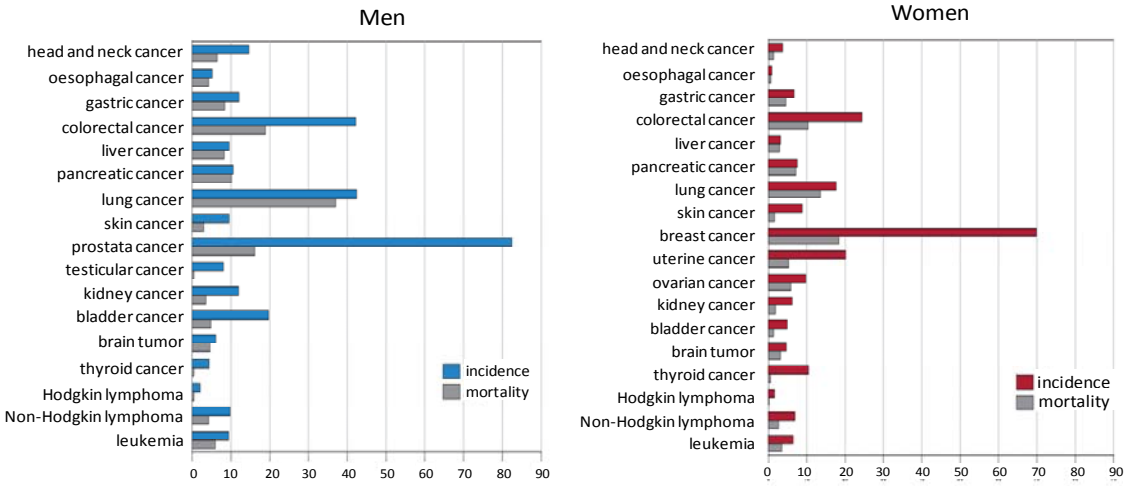

Figure 1. Incidence and mortility rates in Austria by gender in 2009 [4]

Incidences and mortalities of the various cancer types differ between genders (Fig. 1). For women, breast cancer is the most common type and has the highest mortality rate. For men, prostate cancer has the highest incidence, but lung cancer the highest mortality rate. The overall mortality rate is decreasing over the last decades, due to preventive check-up programs and progress in surgery and cancer treatment. However, the progress in cancer diagnostic and treatment is still very cancer type dependent. The mortality of testicular cancer decreased

enormously in the last decades, whereas pancreatic cancer is still fatal for about 80% of the patients. [1, 4]

1.3 Carcinogenesis

The development of human cancer is a stepwise progress usually taking decades. Pre-malignant stages of tumors appear in organs prior to the diagnosis of fully invasive malignant tumors. The process of cancer development is called carcinogenesis. The development starts with a single mutated cell and results after several years in metastasizing tumors (Fig. 2). It is a complex process of a sequence of DNA mutations and epigenetic alterations which are affecting genes controlling cell proliferation, survival, apoptosis induction and other characteristics typical for malignant cells. The pre-malignant stages are mostly caused by monoclonal expansion of a mutated single cell and the further progression reflects a biological selection process. [1, 3]

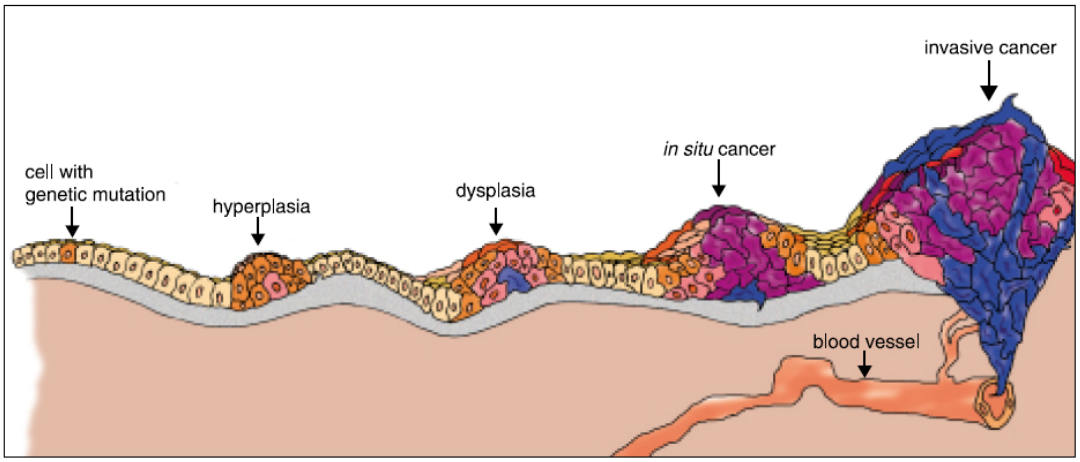

Figure 2. Multistep scheme of carcinogenesis [5]

In the last decades several approaches have been taken to indentify genes which are responsible for tumorigenicity. Already in the early 1980s several oncogenes have been identified [6]. One of the first tumor suppressor genes was the retinoblastoma (RB) gene that controls the cell cycle and prevents excessive cell growth [7]. Depending on the tumor entity, several tumor suppressor and oncogenic genes have been isolated and identified. For instance, mutations in APC, K-Ras and p53 genes are common in colorectal cancer [8]. During the course of carcinogenesis the tumors show a continuing increase of genetic alterations. These changes involve activation of proto-

oncogenes and inactivation of tumor suppressor genes. Interestingly, the number of inactivated tumor suppressor genes is considerably higher than that of activated oncogenes. [1]

In the last years the picture of multistep tumorigenesis changed with the discovery of cancer stem cells. Cancer stem cells are a minority subpopulation, while the transit amplifying cells represent the majority in the tumor mass. Cancer stem cells have characteristics like normal stem cells, such as self-renewing and the potential to differentiate to transit-amplifying cells, also called progenitor cells. This concept implies that only mutations in cancer stem cells are transmitted to the descendent tumor cells and differentiated tumor cells have only limited proliferative potential (Fig. 3). The existence of cancer stem cells was first demonstrated in acute myeloid leukemia and now there is increasing evidence for cancer stem cells in solid tumors. Nevertheless, it seems that in some tumors cancer stem cells are very rare. Furthermore it has been suggested that not all solid tumors follow the concept of clonal succession via stem cells. As long as the concept of cancer stem cells is not fully understood, it is not clear if targeting cancer stem cells will be a promising strategy for future clinical applications. [9–11]

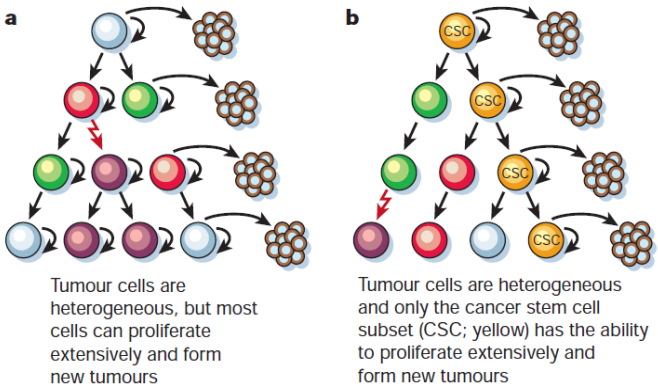

Figure 3. Conventional multistep tumorgenesis (a) and cancer stem cell model (b) [9]

1.4 Hallmarks of Cancer

In the year 2000 Hanahan and Weinberg proposed six hallmarks of cancer to describe underlying principles for all cancer types regardless of which pheno- or genotype. This rational principle provided a logical framework for understanding the complexity and diversity of malignant tissues. Progress in cancer research over the last decade inspired Hanahan and Weinberg to propose an update of the article, which included four more hallmarks (Fig. 4). In the course of the multistep

carcinogenesis, cells acquire these capabilities that enable them to become malignant. The understanding of mechanisms in biology of cancer cells as well as the interactions of cancer cells with the tumor microenvironment is of great interest for the development of new strategies for fighting cancer. Thus the following sections will give a brief summary of the hallmarks of cancer.

One of the most obvious characteristics of cancer cells is their high proliferating rate. In healthy cells production and release of growth-promoting signals is strictly regulated by the cell cycle control machinery and consistent with proliferation rates of surrounding cells. Cancer cells lack of these regulations and enable constitutive growth signals. A large part of growth signaling is processed by transmembrane receptors via an intracellular tyrosine kinase domain that activates the signaling cascades. Overexpression of growth receptors (e.g. EGFR, FGFR) and mutations of signaling kinases (e.g. Raf, Ras, PI3K) or production of own growth factors such as TGFα can be found in a large number of cancers. Along with the capability of sustained growth signaling, cancer cells also circumvent stringent mechanisms of growth suppression. Typically, proteins that operate in various ways to suppress cell proliferation were found mutated in tumors. For instance, cancer cells with mutations in the RB gene are missing an important control step in cell cycle progression, and persistent cell proliferation is the result [12, 13].

A natural barrier to cancer development is the induction of programmed cell death by apoptosis. In normal cells, persisting cellular stresses associated with growth signaling imbalance or DNA mutations induce apoptosis. During carcinogenesis premalignant cells adapt to circumvent death induction. In general, apoptosis signals can be categorized in such of extracellular and intracellular origin. The extrinsic apoptosis pathways involve Fas receptor activation and signal transmission via caspase 8. The intrinsic pathway, which is more important for cancer pathogenesis, implies mitochondrial cytochrome c release and activation of caspase 9. The well-balanced system of anti- and pro-apoptotic effectors of the bcl-2 protein family regulates the activation of the caspase cascade. Cancer cells use various strategies to create apoptosis resistance. These strategies include elimination of damage sensors (mutations in p53 gene), overexpression of anti-apoptotic factors (Bcl-2, Bcl-x_L) or downregulation of pro-apoptotic factors (Bad, Bax, Bim, Puma) [13, 14].

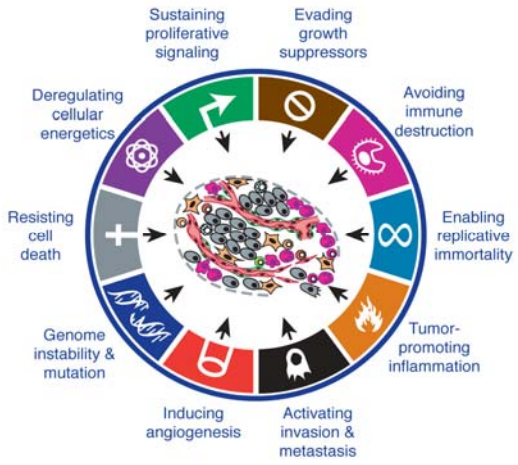

Figure 4. Hallmarks of cancer [13]

Despite to programmed cell death cancer cells have to encounter other limitations. Healthy cells pass through a limited number of cell growth and division cycles and after a phase of proliferation they enter the phase of senescence, which is a non-proliferating but viable state. Cancer cells are termed immortal, because senescence is disabled and cells stay in the phase of proliferation. This characteristic is most obvious in established cancer cell lines used for *in vitro* studies. One key factor for immortalization is the expression of telomerases. Telomerases are DNA polymerases that extend the repeated segments of telomeric DNA. In most healthy cells telomerases are absent and telomeric DNA is gradually eroded with every cell cycle, which finally leads to cell death. Cancer cells enable replicative immortality by activating genes for telomerase expression [13].

Due to the high metabolic activity in tumor cells the demand for nutrients is remarkably high. To address this need, tumors promote angiogenesis by sprouting new blood vessels of existing ones. Angiogenesis is regulated by interaction of signaling proteins that bind to cell surface receptors. A well-known angiogenesis inducer is the vascular endothelial growth factor-A (VEGF-A) that binds to the intermembrane VEGF receptor family to induce neoangiogenesis. Recent studies demonstrated that angiogenesis is not only an important factor for rapidly growing malignancies, it also contributes as an early event in the multistep evolution of tumors [12, 13, 15].

The sixth hallmark of cancer is the capacity of local invasion and distant metastasis. Carcinogenesis involves alterations in cell-to-cell adhesion, which enables cancer cells to invade

surrounding tissues and colonize distant tissues. This is a multistep process beginning with invasion of local tissues followed by intravasation of nearby blood vessels and extravasation into distant tissue where formation of a secondary tumor occurs. Tumors with high invasiveness and high metastatic properties are characterized by the loss of adhesion surface proteins such as E-cadherin and expression of proteins associated with cell migration such as N-cadherin [16].

1.4.1 Update of Hallmarks of Cancer

In the update of hallmarks of cancer in 2011 four additional traits are described, which are divided in two enabling characteristics and two emerging characteristics. Enabling characteristics are requirements for acquisition of cancer traits during multistep carcinogenesis. The most obvious enabling characteristic is the genome instability of cancer cells, which is necessary for the multistep carcinogenesis as mentioned above. The second enabling characteristic describes the effect of inflammation in premalignant states. Inflammation can facilitate delivery of bioactive molecules including growth factors, pro-angiogenic factors or survival factors.

The emerging characteristics involve changes in the energy metabolism of cancer cells and evading of destruction of cancer cells by the immune system. Already in 1927 Otto Warburg made investigations to describe cancer metabolism. He proposed the now termed “Warburg effect” that even under aerobic conditions cancer cells limit their energy metabolism largely to glycolysis [17]. Due to the ~18-fold lower efficiency of ATP production by glycolysis compared to mitochondrial respiration, cancer cells have to compensate the lower efficiency by overexpression of glucose transporters and glycolysis associated enzymes. In clinical diagnostics the higher uptake of glucose in cancer cells is utilized for visualization of many tumors by positron emission tomography with ^{18}F-fluorodesoxyglucose. The second emerging hallmark is the aspect that cancer cells find ways to evade the immune system. Several studies demonstrated that immunodeficient mice tend to form carcinogen-induced tumors more frequently relative to immunocompetent mice. It has been proposed that cancer cells may secrete immunosuppressive factors or recruit immunosuppressive cells. Due to the complexity of the immune system the understanding of interactions with cancer cells is still rudimentary [13].

1.5 Anticancer Therapy

Cancer treatment changed a lot in the last 30 years, however it is still based on the same three therapeutic approaches, namely surgery, radiotherapy, and chemotherapy. The aim of surgical treatment is to excise the complete tumor mass if possible. Surgical intervention for early stage malignancies are the most promising treatment. In 90% of patients with cured solid malignancies, surgery alone or in combinations with other therapies was applied [18]. Unfortunately, this treatment option is not applicable for difficult accessible body sites, metastasized and late stage tumors, and hematological malignancies. Adjuvant therapies, mostly chemotherapeutic approaches, are used to treat malignant cells that are left in the body after surgery. Neo-adjuvant therapies are applied to reduce the tumor size prior to surgical intervention.

In radiotherapy the tumor mass is destroyed by ionizing radiation such as gamma rays, X-rays, neutron and proton beams. DNA is thought to be the critical target of radiation. Direct damage of DNA involves single-strand and double strand breaks, loss of bases, cross-link formation, dimerization and destruction on the chromosomal level. Indirect damages of DNA are caused by hydroxyl radicals, which are formed by the reaction of ionizing radiation with water molecules in the cell. Radiotherapy can be applied in different ways. The most common form is the external beam radiotherapy (EBRT), this technique uses an external radiation source pointed to the tumor. Internal radiotherapy is applied by administration of radioactive substances such as ^{131}I for thyroid cancer [19].

Chemotherapy is defined in medical oncology as treatment of cancer by a systemic therapy. First, in the 1940s nitrogen mustard, a chemical weapon in the First World War, was used to treat lymphoma in patients and resulted in a brief remission. This experimental therapy demonstrated for the first time the potential of cytotoxic agents for cancer treatment. The first chemotherapeutics used in broader clinical application were antifolate drugs. First successful therapies of advanced human malignancies were achieved with the folic acid analogue methotrexate. Methotrexate belongs to the group of antimetabolites and inhibits the enzyme dihydrofolate reductase, which consequently leads to a blockage of nucleotide biosynthesis [18, 20].

In the following decades a wide variety of chemotherapeutics were developed. The majority of anticancer drugs used today in clinical oncology are still cytotoxic agents. In the following paragraphs a brief overview is given about chemotherapeutic agents categorized by their mode of action.

1.5.1 Alkylating Agents

Alkylating agents are characterized by electron-deficient functional groups reacting with nucleophilic groups of DNA, proteins and other biomolecules. However, most important for their antitumoral effect are the covalent bonds to nucleobases of DNA. Alkylation of DNA leads to inter- and intrastrand cross-links and bulky adducts, which are processed to single- and double-strand breaks, and apurinic and pyrimidinic sites. In highly proliferating cancer cells cellular death is executed when DNA damages cannot be repaired sufficiently. The versatile alkylating agent cyclophosphamide (Fig. 5) requires hepatic metabolization and belongs to the group of nitrogen mustards. Even though it is one of the oldest chemotherapeutics it is still used for treatment of lymphomas, breast cancer and acute lymphoblastic leukemia [18].

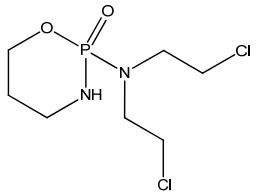

Figure 5. Structure of cyclophosphamide

1.5.2 Antimetabolites

As mentioned above antimetabolites were the first effective chemotherapeutics in clinical use. To interfere with biosynthesis pathways antimetabolite structures mimic cellular metabolites. These analogues interact either with the catalytic or regulatory site of enzymes involved in these pathways or substitute a metabolite that is incorporated into important biomolecules, resulting in non-functional products. 5-fluorouracil (5-FU), one of the most commonly applied antimetabolites does both (Fig. 6). Due to the close structural similarity it acts as an analogue of thymine and uracil. Phosphorylation of 5-FU to 5-fluorouridine triphosphate allows incorporation into RNA and DNA. Additionally, inhibition of thymidine synthase is achieved by 5-

fluorouridine monophosphate. 5-FU is used in combination therapy against several malignancies including colorectal, mammary and bladder carcinoma [21].

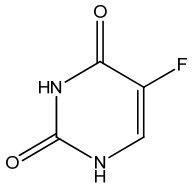

Figure 6. Structure of 5-fluorouracil

1.5.3 Topoisomerase inhibitors

Topoisomerase I and II are constitutively expressed enzymes in all mammalian cells and involved in the DNA replication and transcription process. During replication or transcription topoisomerases catalyze the unwinding of DNA regions by transient cleavage of the phosphodieester bonds of the DNA backbone. Once unwinding and the relevant DNA process is completed, topoisomerases catalyze the religation of the DNA nick. Topoisomerase I cuts one strand of the DNA double helix, whereas topoisomerase II cleaves both strands. Irinotecan, a topoisomerase I inhibitor, belongs to the group of camptothecins derived from the Chinese tree *Camptotheca acuminate* (Fig. 7). Irinotecan inhibits the process of religation and is used together with 5-FU in therapy of metastatic colorectal carcinoma [18].

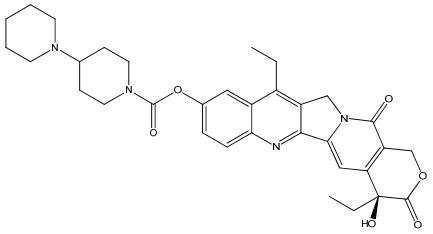

Figure 7. Structure of irinotecan

1.5.4 Intercalating agents

DNA intercalation is a reversible inclusion of chemical structures between the DNA bases. Following DNA intercalation, secondary structures of the DNA are modified, which results in inhibition of replication and transcription processes. Anthracyclines, the most relevant intercalating agents in cancer treatment, derive from the *Streptomyces* bacterium and can also be

classified as antitumor antibiotics. The anthracycline doxorubicin (Fig. 8) is one of the most effective chemotherapeutics in use. The anthraquinone moiety facilitates intercalation into DNA. Additionally, doxorubicin mediates single- and double-strand breaks by stabilizing the topoisomerase II complex. However, cardiotoxic side effects limit the use in clinical therapies. Nevertheless, doxorubicin is an important drug in anticancer therapy for several malignancies, including breast, hepatic and lymphatic cancer [18].

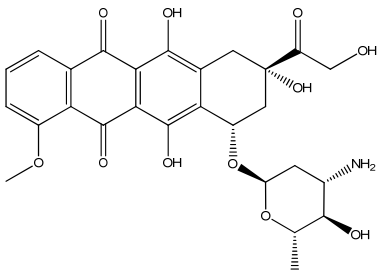

Figure 8. Structure of doxorubicin

1.5.5 Mitotic inhibitors

Vinca alkaloids and taxanes are the two major groups of mitotic inhibitors for anticancer treatment. Four vinca alkaloids are currently in clinical use, namely vincristine, vinblastine, vindesine, and vinorelbine. Vinca alkaloids are extracts of the periwinkle plant and share a common mechanism of action. Binding to tubulin prevents polymerization and consequently formation of the spindle apparatus. During mitosis microtubules are essential for chromosome migration, thus cytotoxicity of vinca alkaloids is manifested by cell cycle arrest in metaphase. Vincristine (Fig. 9) and vinblastine are used for therapy of several lymphomas.

Taxans are like the vinca alkaloids plant extracts. Currently paclitaxel and docetaxel are in clinical use are semi-synthetically produced from *Taxus* species, such as the European yew. The mechanism of action of taxanes is precisely opposite of the vinca alkaloids. Inhibition of the depolymerization process of microtubules during mitosis leads to cell cycle arrest and consequently to apoptosis induction. Docetaxel and paclitaxel are used in for treatment of ovarian, lung and mamma carcinoma [18].

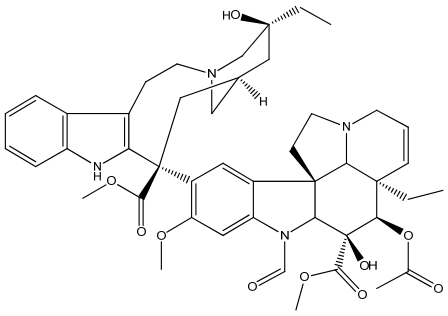

Figure 9. Structure of vincristine

1.5.6 Platinum compounds

In studies about effects of electrical current on bacterial proliferation, Barnett Rosenberg made the fortuitous discovery of the cytotoxic properties of cisplatin (*cis*-diamminedichloroplatinum(II)). In the experimental setting cisplatin was formed from the platinum electrodes in the bacterial growth medium [22, 23]. In the following years antiproliferative properties were studied in detail and cisplatin was approved for anticancer therapy in 1978. The introduction of cisplatin into clinical use had a great impact on cure rates for several cancer entities. The survival rate for patients with testicular cancer increased to >80% and other cancers such as cervical, ovarian and bladder cancer became well treatable. However, several other cancers are not responding to cisplatin treatment. The mode of action of cisplatin is based on the interaction of platinum with DNA. After aquation and hydrolysis cisplatin forms crosslinks with DNA, causing inhibition of transcription and replication processes. Cisplatin forms mainly intrastrand crosslinks with the N7 position of guanins. Monofunctional adducts and interstrand crosslinks are only formed in a small number. In the following decades two more platinum compounds, carboplatin and oxaliplatin (Fig. 10), were approved for clinical therapy. Carboplatin (*cis*-diammine(1,1-cyclobutanedicarboxylato)platinum(II)) is closely related to cisplatin but the toxicity profile differs from that of cisplatin. The more tolerable toxicity profile is characterized by less neurotoxicity, ototoxicity and gastrointestinal side effects. As with the alkylating agents, the dose limiting toxicity is myelosuppression. The most recent worldwide approved platinum compound is oxaliplatin ([(1R,2R)-cyclohexane-1,2-diamine](ethanedioato-O,O')platinum(II)). It is active against cisplatin and carboplatin resistant tumors and used as first line therapy against colorectal carcinoma in combination with 5-FU and folinic acid (FOLFOX

scheme). Even if the proposed mechanism of action is the same for all platinum compounds, they possess different toxicity profiles as well as antitumor activities [18, 24, 25].

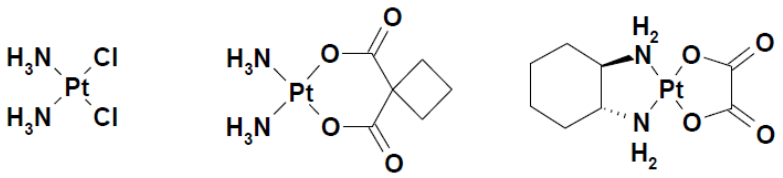

Figure 10. Structure of cisplatin, carboplatin and oxaliplatin (left to right)

1.5.7 Targeted Therapies

Targeted therapeutics are the newest approach in cancer therapy. In contrast to the conventional cytotoxic approach of chemotherapeutics, targeted therapeutics are designed to interfere with a specific molecular target, mostly proteins, that is important for tumor growth or progression [26]. In the last decade several targeted therapeutics were approved for clinical use. Targeted therapies can be roughly categorized in protein kinase inhibition by small molecules and targeting of surface proteins or growth factors by monoclonal antibodies. Imatinib (Fig. 11) was the first drug inhibiting certain tyrosine kinases involved in chronic myelogenous leukemia (CML) and gastrointestinal stroma tumors (GIST). CML is characterized by the mutant kinase fusion protein Bcr-Abl, which leads to a constitutively activated kinase function. GIST is driven by point mutations of c-Kit or platelet derived growth factor receptor (PDGFR)-α kinases. Imatinib inhibits all three kinases selectively by competitive binding to the ATP binding site of the enzymes [27, 28]. Clinical use of monoclonal antibodies, the second category of targeted therapies, began with the approval of rituximab in 1999. The chimeric monoclonal antibody rituximab targets the surface protein CD20, which is expressed in >90% of B-cell lymphomas [29]. In the last years several other targeted therapeutics were approved including sorafinib (multiple kinase inhibitor), sunitinib (multiple receptor tyrosine kinase inhibitor), bevacizumab (antibody against vascular endothelial growth factor), and cetuximab (antibody against epidermal growth factor receptor) [26, 30].

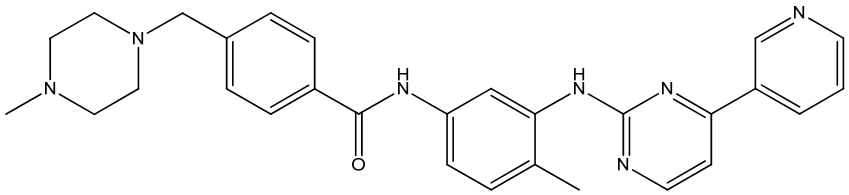

Figure 11. Structure of imatinib

1.6 Novel Anticancer Metal Compounds

As mentioned above, platinum compounds are currently the most important metal compounds in chemotherapy. It is supposed that in more than 50% of all chemotherapies cisplatin or its two analogues carboplatin and oxaliplatin are used as mono- or combination therapy. Beside platinum compounds, arsenic trioxide is the only approved metal compound for anticancer therapy [31].

Nevertheless several other metal compounds showed promising biological activity in preclinical and clinical studies. The titanium compound budotitane showed activities *in vivo* and entered a clinical phase I study, the gallium compounds $GaNO_3$ and KP46 were clinically tested and for KP46 clinical studies are still ongoing. Also gold complexes displayed anticancer activities in several preclinical settings. Currently, ruthenium complexes draw the most attention along all metal complexes for a possible clinical application in chemotherapy.

1.6.1 Ruthenium Compounds

Among non-platinum metal drugs, ruthenium complexes are the most promising compounds on the edge to clinical application. As with cisplatin, cytotoxic properties were discovered on growth inhibition studies on *Escherichia coli* bacteria [32]. Subsequent studies with a panel of ruthenium complexes showed that *fac*-$[Ru^{III}Cl_3(NH_3)_3]$ is most active in EMT-6 sarcoma in mice [33].

Due to solubility reasons further clinical evaluation was not possible, and with the discovery of the better water-soluble and more active imidazole-containing complexes a new lead structure was found in KP418 (Fig. 12). Further studies on analogues of KP418 led to the indazole derivative KP1019 (indazolium *trans*-[tetrachloridobis(1H-indazole)ruthenate(III)]. *In vivo* studies with KP1019 in autochthonous chemically induced colorectal tumors in rats demonstrated a reduction of the tumor volume up to 90% and a reduction up to two thirds of the tumor number.

Furthermore, KP1019 showed activity superior to 5-FU, a standard agent against colorectal tumors, and no severe side effects [34].

Beside KP1019, the development of the DMSO-containing ruthenium complex NAMI-A was inspired by the antitumor activity of KP418. In contrast to KP1019, NAMI-A displayed antimetastatic properties rather than activity against already established tumors [35–37].

The most recent milestone on the way to clinical application of ruthenium compounds was made with the completion of the clinical phase 1 study of NKP-1339 (sodium *trans*-[tetrachloridobis(1*H*-indazole)ruthenate(III)]). NKP-1339, originally a precursor in the formulation of KP1019, was chosen for further clinical development due to improved water solubility, which allowed clinical application of higher drug doses to the patients.

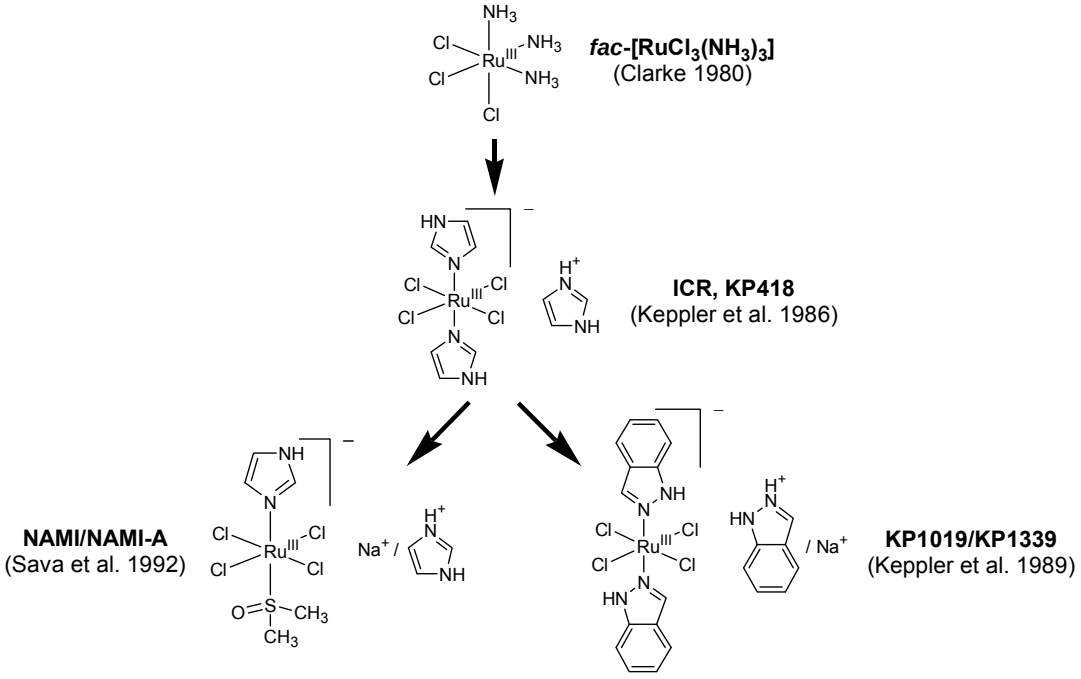

Figure 12. Genealogy of anticancer ruthenium complexes [34, 38–40]

It has been proposed that the drug delivery to the tumor is mediated by the high affinity of NKP-1339 to the serum proteins albumin and transferrin. Overexpression of transferrin receptors was frequently observed in tumor cells, and accumulation of albumin in the solid tumor microenvironment was described as the "enhanced permeability and retention (EPR) effect" [41].

Since NKP-1339 is redox active under biological conditions, it has been suggested that the compound is reduced to ruthenium(II) species after protein release in the cell. The fact that ruthenium(II) is more reactive than ruthenium(III) and the enhanced reduction process in hypoxic tumor microenvironment accelerate the interactions with target molecules in malignant tissues. This proposed effect is termed thesis "activation-by-reduction" hypothesis.

Preliminary results of the clinical phase I trial of NKP-1339 showed very limited side effects in 24 patients. Moreover, at least 6 patients with different refractory cancer types experienced stable disease for at least 12 weeks [42, 43].

1.6.2 Thiosemicarbazones

Thiosemicarbazones were not primarily developed to be used in form of metal complexes for cancer therapy, but they form complexes with the biologically relevant metals zinc, iron and copper in an efficient manner. The first biologically active compound, 2-formylpyridine thiosemicarbazone, was discovered in 1956 (Fig. 13), which showed antileukemic activity in a mouse model [44]. Further studies on structure-activity relationships revealed that only compounds with *N,N,S* donor sites are active. In addition, the heterocyclic nitrogen has to be in α-position for biological activity.

Based on these results a series α-N-heterocyclic thiosemicarbazones were screened and the most promising compound was 5-hydroxy-2-formylpyridine thiosemicarbazone (5-HP) [45, 46]. However, 5-HP showed in clinical evaluation severe side effects and turned out to be inactivated rapidly by glucuronidation [47, 48]. Sartorelli et al. synthesized in the early 1990s several derivates of 5-HP, and the amino substituted compound 3-aminopyridine-2-carboxaldehyde thiosemicarbazone (Triapine, 3-AP) displayed a higher activity in the L1210 leukemia mouse model than 5-HP [49].

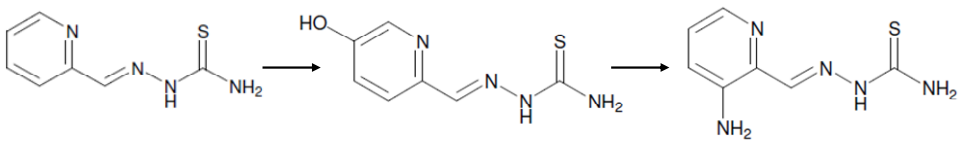

Figure 13. Genealogy of biologically active thiosemicarbazones [44–46, 49]

It has been assumed that the anticancer activity of Triapine is based on the inhibition of ribonucleotide reductase. The enzyme ribonucleotide reductase is involved in the de novo DNA synthesis by reducing ribonucleotides to deoxyribonucleotides. The human ribonucleotide reductase is formed of two large (hRRM1) and two small (hRRM2 or p53R2) subunits. The small subunit contains a tyrosyl radical and an iron center. Both, the iron center as well as the tyrosyl radical are essential for the catalytic activity of the enzyme. Ribonucleotide reductase is a promising molecular target for cancer therapy due to the higher DNA replication rate of cancer cells.

As with other iron chelating compounds, the mechanism of ribonucleotide reductase inhibition by Triapine was thought to be based on complexation of essential iron of the active enzyme site. However, cell culture experiments demonstrated that addition of iron prior to Triapine treatment had no influence on its cytotoxicity. This stands in contrast to findings with other iron chelators such as deferoxamine or 311, where iron addition led to a remarkable decrease in cytotoxicity [50].

The hypothesis that the iron complex of thiosemicarbazones is the active form was first confirmed by Thelander and Gräslund; EPR experiments demonstrated that by reduction to an iron(II) complex a hydroxyl radical is formed, which consequently leads to destruction of the tyrosyl radical of the ribonucleotide reductase [51]. Further EPR studies with recombinant ribonucleotide reductase showed that neither Triapine alone nor the corresponding iron(III) complex were capable of inhibiting the enzyme [52]. The different properties of Triapine compared to other iron chelators raise the question if additional targets contribute to its antitumoral activity.

A search of registered clinical cancer trials on www.clincaltrials.gov using Triapine as a single agent or in combination therapy displays 27 clinical phase I and phase II studies. The majority of the studies are completed, and Triapine was evaluated for treatment of solid tumors, hematological malignancies and as a radiosensitizer. Results of phase II studies in advanced solid malignancies did not report any increase in survival. Also only low or no objective response rates were observed. Triapine displayed a significant toxicity profile; the most common dose limiting toxicities were myelosuppression, methemoglobinemia, hypoxia and fatigue. However, activity

of Triapine as an adjunct has been observed in clinical phase I studies with a nucleotide analogue. In a combination therapy with the purine analogue fludarabine response rates of 17% were observed, whereas no response was reported with Triapine or fludarabine alone [53].

1.7 Endoplasmic Reticulum Stress

The endoplasmic reticulum (ER) comprises more than a half of the total membranes of an average animal cell. Its functions are various and essential for every cell. They include several activities of the protein machinery such as posttranslational modifications, proper protein folding, and protein trafficking. Moreover, the ER acts as intracellular calcium storage by high concentrations of calcium binding proteins [3, 54].

Dysfunctions of the ER or a high burden of unfolded or misfolded proteins result in ER stress which in turn triggers an adaptive pathway (Fig. 15) known as the unfolded protein response (UPR). Perturbations ofER functions can caused by various cellular stress stimuli such as high expression of mutant or misfolded proteins, disruption of redox environment (eg. hypoxia), viral infections and calcium depletion [55]. In response to such disruptions, UPR is activated and primary acts to increase the ER folding capacities by transcriptional induction of luminal ER chaperones such as GRP78. However, sustained severe ER stress leads to a switch in UPR to proapoptotic signaling and cell death is mediated via proteins such as CHOP or JNK [56, 57].

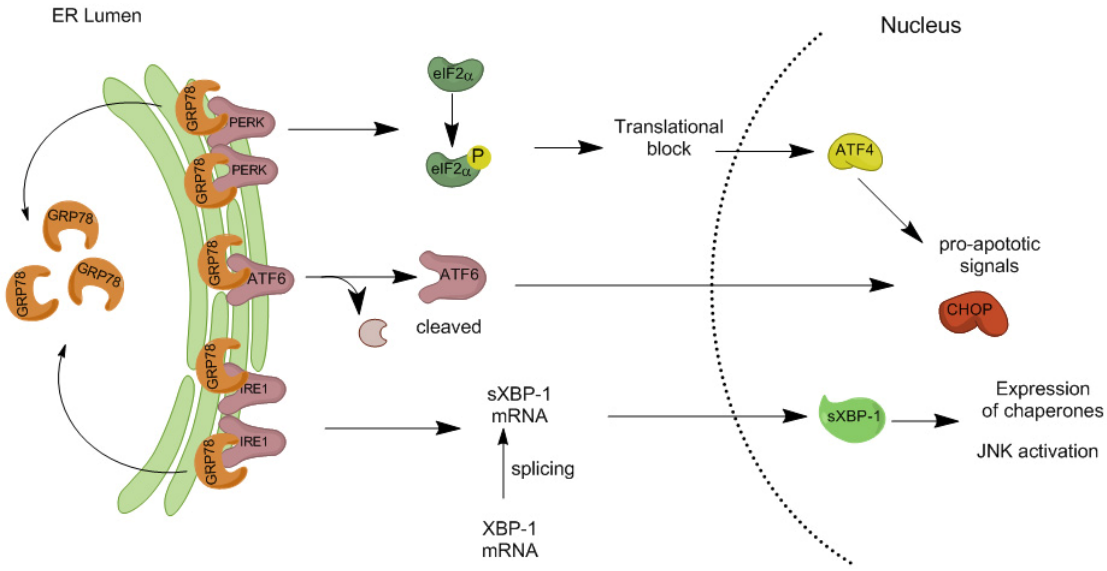

Figure 14. Pathway of unfolded protein response

Due to the high metabolism rate and increased amount of misfolded proteins in cancer cells, targeting ER functions is a promising target for cancer therapy. To compensate the overload of proteins, which have to be processed in the ER, cancer cells tend to upregulate key factors of the UPR. GRP78 was found to be overexpressed in tumor cells and associated with reestablishment of ER homeostasis and pro-survival signaling. In several studies on melanoma and prostate cancer, upregulation of GRP78 is related to poor patient outcome, greater risk of cancer recurrence and overall decrease in patient survival [58–60]. Moreover, a retrospective study of tumor specimens demonstrated 67% of breast cancer patients with upregulated GRP78 had shorter times of recurrence [61].

Two approaches for targeting ER stress have been proposed. The first strategy involves overloading the capacity of the ER protein folding machinery. The severe disruptions of ER homeostasis change UPR signaling from prosurvival to proapoptotic. Proteasome inhibitors (eg. bortezomib) block protein degradation and are thought to cause protein accumulation in the ER. Studies reported that bortezomib sensitizes pancreatic cancer cells to ER stress-related apoptosis and enhances the anticancer activity of cisplatin [62]. The second approach is to inhibit key factors of the unfolded protein response, such that cancer cells cannot adapt to high proliferations rates. The above mentioned ruthenium complex NKP-1339 inhibtits GRP78, which may contribute to its antitumor activity [43].

References

1. Weinberg, R.A.: The Biology of Cancer. Garland Science. 850 (2007).

2. Pecorino, L.: Molecular Biology of Cancer: Mechanisms, Targets, and Therapeutics. Oxford University Press. (2008).

3. Alberts, B., Johnson, A., Lewis, J., Raff, M.: Molecular Biology of the Cell, 5th edition. Garland Science. (2008).

4. Zielonke, N., Hackl, M., Baldaszti, E.: Krebsinzidenz und Krebsmortalität in Österreich. Statistik Austria. (2010).

5. Resch, B.C., Anderson, D., Andrews, K.: Cell Biology and Cancer (NIH Curriculum Supplement Series). National Institue of Health Publications. (1999).

6. Bishop, J.M.: Cellular oncogenes and retroviruses. Annual review of biochemistry. 52, 301-354 (1983).

7. Friend, S.H., Bernards, R., Rogelj, S., Weinberg, R.A., Rapaport, J.M., Albert, D.M., Dryja, T.P.: A human DNA segment with properties of the gene that predisposes to retinoblastoma and osteosarcoma. Nature. 323, 643-646 (1986).

8. Smith, G., Carey, F.A., Beattie, J., Wilkie, M.J.V., Lightfoot, T.J., Coxhead, J., Garner, R.C., Steele, R.J.C., Wolf, C.R.: Mutations in APC, Kirsten-ras, and p53--alternative genetic pathways to colorectal cancer. Proceedings of the National Academy of Sciences of the United States of America. 99, 9433-8 (2002).

9. Reya, T., Morrison, S.J., Clarke, M.F., Weissman, I.L.: Stem cells, cancer, and cancer stem cells. Nature. 414, 105-11 (2001).

10. Visvader, J.E., Lindeman, G.J.: Cancer stem cells in solid tumours: accumulating evidence and unresolved questions. Nature reviews. Cancer. 8, 755-68 (2008).

11. Rosen, J.M., Jordan, C.T.: The increasing complexity of the cancer stem cell paradigm. Science (New York, N.Y.). 324, 1670-3 (2009).

12. Hanahan, D., Weinberg, R.A.: The hallmarks of cancer. Cell. 100, 57-70 (2000).

13. Hanahan, D., Weinberg, R.A.: Hallmarks of Cancer: The Next Generation. Cell. 144, 646-674 (2011).

14. Adams, J.M., Cory, S.: The Bcl-2 apoptotic switch in cancer development and therapy. Oncogene. 26, 1324-37 (2007).

15. Raica, M., Cimpean, A.M., Ribatti, D.: Angiogenesis in pre-malignant conditions. European journal of cancer (Oxford, England : 1990). 45, 1924-34 (2009).

16. Cavallaro, U., Christofori, G.: Cell adhesion and signalling by cadherins and Ig-CAMs in cancer. Nature Reviews. Cancer. 4, 118–132 (2004).

17. Warburg, O., Wind, F., Negelein, E.: The metabolism of tumors in the body. Journal of General Physiology. 8, 519-530 (1927).

18. Lenhard, Raymond E Osteen, R.T., Gansler, T.: Clinical Oncology: American Cancer Society. Blackwell Publishing. (2001).

19. Kutcher, G.J., Coia, L., Gillin, M., Hanson, W.F., Leibel, S., Morton, R.J., Palta, J.R., Purdy, J.A., Reinstein, L.E., Svensson, G.K.: Comprehensive QA for radiation oncology: report of AAPM Radiation Therapy Committee Task Group 40. Medical Physics. 21, 581-618 (1994).

20. Goodman, L.S., Wintrobe, M.M.: Nitrogen mustard therapy; use of methyl-bis (beta-chloroethyl) amine hydrochloride and tris (beta-chloroethyl) amine hydrochloride for Hodgkin's disease, lymphosarcoma, leukemia and certain allied and miscellaneous disorders. Journal of the American Medical Association. 132, 126-32 (1946).

21. Grem, J.L.: 5-Fluorouracil: forty-plus and still ticking. A review of its preclinical and clinical development. Investigational new drugs. 18, 299-313 (2000).

22. Rosenberg, B., Van Camp, L., Krigas, T.: Inhibition of Cell Division in Escherichia coli by Electrolysis Products from a Platinum Electrode. Nature. 205, 698-699 (1965).

23. Rosenberg, B., VanCamp, L., Trosko, J.E., Mansour, V.H.: Platinum compounds: a new class of potent antitumour agents. Nature. 222, 385-6 (1969).

24. Wang, D., Lippard, S.J.: Cellular processing of platinum anticancer drugs. Nature reviews. Drug discovery. 4, 307-20 (2005).

25. Jakupec, M.A., Galanski, M., Keppler, B.K.: Tumour-inhibiting platinum complexes--state of the art and future perspectives. Reviews of physiology, biochemistry and pharmacology. 146, 1-54 (2003).

26. Sawyers, C.: Targeted cancer therapy. Nature. 432, 294-7 (2004).

27. Demetri, G.D., von Margaret, M., Blanke, C.D., Van Annick D., den A., Eisenberg, B., Roberts, P.J., Heinrich, M.C., Tuveson, D.A., Singer, S., Janicek, M., Fletcher, J.A., Silverman, S.G., Silberman, S.L., Capdeville, R., Kiese, B., Peng, B., Dimitrijevic, S., Druker, B.J., Corless, C., Fletcher, C.D.M., Joensuu, H.: Efficacy and safety of imatinib

mesylate in advanced gastrointestinal stromal tumors. New England Journal of Medicine. 347, 472-480 (2002).

28. Kantarjian, H., Sawyers, C., Hochhaus, A., Guilhot, F., Schiffer, C., Cambacorti-Passerini, C., Niederwieser, D., Resta, D., Capdeville, R., Zoellner, U., Talpaz, M., Druker, B.: Hematologic and cytogenetic responses to imatinib mesylate in chronic myelogenous leukemia. New England Journal of Medicine. 346, 645-652 (2002).

29. McLaughlin, P., Grillo-López, A.J., Link, B.K., Levy, R., Czuczman, M.S., Williams, M.E., Heyman, M.R., Bence-Bruckler, I., White, C.A., Cabanillas, F., Jain, V., Ho, A.D., Lister, J., Wey, K., Shen, D., Dallaire, B.K.: Rituximab chimeric anti-CD20 monoclonal antibody therapy for relapsed indolent lymphoma: half of patients respond to a four-dose treatment program. Journal of clinical oncology : official journal of the American Society of Clinical Oncology. 16, 2825-33 (1998).

30. Li, J., Chen, F., Cona, M.M., Feng, Y., Himmelreich, U., Oyen, R., Verbruggen, A., Ni, Y.: A review on various targeted anticancer therapies. Targeted oncology. (2012).

31. Shen, Z.-X., Chen, G.-Q., Ni, J.-H., Li, X.-S., Xiong, S.-M., Qiu, Q.-Y., Zhu, J., Tang, W., Sun, G.-L., Yang, K.-Q., Chen, Y., Zhou, L., Fang, Z.-W., Wang, Y.-T., Ma, J., Zhang, P., Zhang, T.-D., Chen, S.-J., Chen, Z., Wang, Z.-Y.: Use of Arsenic Trioxide (As2O3) in the Treatment of Acute Promyelocytic Leukemia (APL): II. Clinical Efficacy and Pharmacokinetics in Relapsed Patients . Blood . 89 , 3354-3360 (1997).

32. Durig, J.R., Danneman, J., Behnke, W.D., Mercer, E.E.: The induction of filamentous growth in Escherichia coli by ruthenium and palladium complexes. Chemico-Biological Interactions. 13, 287-294 (1976).

33. Srivastava, S.C., Mausner, L.F., Clarke, M.J.: Radioruthenium-labeled compounds for diagnostic tumor imaging. Progress in Clinical Biochemistry and Medicine. 10, 111-149 (1989).

34. Keppler, B.K., Henn, M., Juhl, U.M., Berger, M.R., Niebl, R., Wagner, F.E.: New ruthenium complexes for the treatment of cancer. Progress in Clinical Biochemistry and Medicine. 10, 41-69 (1989).

35. Sava, G., Frausin, F., Cocchietto, M., Vita, F., Podda, E., Spessotto, P., Furlani, A., Scarcia, V., Zabucchi, G.: Actin-dependent tumour cell adhesion after short-term exposure to the antimetastasis ruthenium complex NAMI-A. European Journal of Cancer. 40, 1383-96 (2004).

36. Frausin, F., Scarcia, V., Cocchietto, M., Furlani, A., Serli, B., Alessio, E., Sava, G.: Free exchange across cells, and echistatin-sensitive membrane target for the metastasis inhibitor NAMI-A (imidazolium trans-imidazole dimethyl sulfoxide tetrachlororuthenate) on KB tumor cells. Journal of Pharmacology and Experimental Therapeutics. 313, 227-233 (2005).

37. Vacca, A., Bruno, M., Boccarelli, A., Coluccia, M., Ribatti, D., Bergamo, A., Garbisa, S., Sartor, L., Sava, G.: Inhibition of endothelial cell functions and of angiogenesis by the metastasis inhibitor NAMI-A. British Journal of Cancer. 86, 993-998 (2002).

38. Clarke, M.J.: Oncological implication of the chemistry of ruthenium. Metal Ions in Biological Systems. 11, 231-283 (1980).

39. Keppler, B.K., Rupp, W.: Antitumor activity of imidazolium-bisimidazole-tetrachlororuthenate(III). A representative of a new class of inorganic antitumor agents. Journal of Cancer Research and Clinical Oncology. 111, 166-168 (1986).

40. Sava, G., Pacor, S., Mestroni, G., Alessio, E.: Na[trans-RuCl4(DMSO)Im], a metal complex of ruthenium with antimetastatic properties. Clinical & Experimental Metastasis. 10, 273-280 (1992).

41. Kratz, F.: Albumin as a drug carrier: design of prodrugs, drug conjugates and nanoparticles. Journal of controlled release. 132, 171-83 (2008).

42. NP: Niiki Pharma Announces Positive Interim Data from Ongoing Clinical Trial of Novel Anti-Cancer Agent NKP-1339. Press Release. (2011).

43. Dickson, N.R., Jones, S.F., Burris, H.A., Ramanathan, R.K., Weiss, G.J., Infante, J.R., Bendell, J.C., McCulloch, W., Von Hoff, D.D.: A phase I dose-escalation study of NKP-1339 in patients with advanced solid tumors refractory to treatment. J Clin Oncol (ASCO Abstracts 2011). 2607 (2011).

44. Brockman, R.W., Thomson, J.R., Bell, M.J., Skipper, H.E.: Observations on the antileukemic activity of pyridine-2-carboxaldehyde thiosemicarbazone and thiocarbohydrazone. Cancer Research. 16, 167-70 (1956).

45. French, F.A., Blanz Jr., E.J., DoAmaral, J.R., French, D.A.: Carcinostatic activity of thiosemicarbazones of formyl heteroaromatic compounds. VII. 2-Formylpyridine derivatives bearing additional ring substituents. Journal of Medicinal Chemistry. 13, 1124-1130 (1970).

46. French, F.A., Blanz Jr., E.J., DoAmaral, J.R., French, D.A.: Carcinostatic activity of thiosemicarbazones of formyl heteroaromatic compounds. VI. 1-Formylisoquinoline derivatives bearing additional ring substituents, with notes on mechanism of action. Journal of Medicinal Chemistry. 13, 1117-1124 (1970).

47. DeConti, R.C., Toftness, B.R., Agrawal, K.C., Tomchick, R., Mead, J.A., Bertino, J.R., Sartorelli, A.C., Creasey, W.A.: Clinical and pharmacological studies with 5-hydroxy-2-formylpyridine thiosemicarbazone. Cancer research. 32, 1455-1462 (1972).

48. Krakoff, I.H., Etcubanas, E., Tan, C., Mayer, K., Bethune, V., Burchenal, J.H.: Clinical trial of 5-hydroxypicolinaldehyde thiosemicarbazone (5-HP; NSC-107392), with special reference to its iron-chelating properties. Cancer chemotherapy reports. Part 1. 58, 207-212 (1974).

49. Liu, M.C., Lin, T.C., Sartorelli, A.C.: Synthesis and antitumor activity of amino derivatives of pyridine-2-carboxaldehyde thiose micarbazone. Journal of Medicinal Chemistry. 35, 3672-3677 (1992).

50. Chaston, T.B., Lovejoy, D.B., Watts, R.N., Richardson, D.R.: Examination of the Antiproliferative Activity of Iron Chelators. Clinical Cancer Research. 9, 402-414 (2003).

51. Thelander, L., Gräslund, A.: Mechanism of inhibition of mammalian ribonucleotide reductase by the iron chelate of 1-formylisoquinoline thiosemicarbazone. The Journal of Biological Chemistry. 258, 4063-6 (1983).

52. Shao, J., Zhou, B., Di Bilio, A.J., Zhu, L., Wang, T., Qi, C., Shih, J., Yen, Y.: A Ferrous-Triapine complex mediates formation of reactive oxygen species that inactivate human ribonucleotide reductase. Molecular Cancer Therapeutics. 5, 586-92 (2006).

53. Miah, A.B., Harrington, K.J., Nutting, C.M.: Triapine in Clinical Practice. European Journal of Clinical & Medical Oncology. 2, (2009).

54. Boyce, M., Yuan, J.: Cellular response to endoplasmic reticulum stress: a matter of life or death. Cell Death and Differentiation. 13, 363-73 (2006).

55. Healy, S.J.M., Gorman, A.M., Mousavi-Shafaei, P., Gupta, S., Samali, A.: Targeting the endoplasmic reticulum-stress response as an anticancer strategy. European Journal of Pharmacology. 625, 234-46 (2009).

56. Merksamer, P.I., Papa, F.R.: The UPR and cell fate at a glance. Journal of Cell Science. 123, 1003-6 (2010).

57. Shore, G.C., Papa, F.R., Oakes, S. a: Signaling cell death from the endoplasmic reticulum stress response. Current Opinion in Cell Biology. 1-7 (2010).

58. Zhuang, L., Scolyer, R. a, Lee, C.S., McCarthy, S.W., Cooper, W. a, Zhang, X.D., Thompson, J.F., Hersey, P.: Expression of glucose-regulated stress protein GRP78 is related to progression of melanoma. Histopathology. 54, 462-70 (2009).

59. Daneshmand, S., Quek, M.L., Lin, E., Lee, C., Cote, R.J., Hawes, D., Cai, J., Groshen, S., Lieskovsky, G., Skinner, D.G., Lee, A.S., Pinski, J.: Glucose-regulated protein GRP78 is up-regulated in prostate cancer and correlates with recurrence and survival. Human pathology. 38, 1547-52 (2007).

60. Pootrakul, L., Datar, R.H., Shi, S.-R., Cai, J., Hawes, D., Groshen, S.G., Lee, A.S., Cote, R.J.: Expression of stress response protein Grp78 is associated with the development of castration-resistant prostate cancer. Clinical cancer research□: an official journal of the American Association for Cancer Research. 12, 5987-93 (2006).

61. Lee, E., Nichols, P., Spicer, D., Groshen, S., Yu, M.C., Lee, A.S.: GRP78 as a novel predictor of responsiveness to chemotherapy in breast cancer. Cancer research. 66, 7849-53 (2006).

62. Nawrocki, S.T., Carew, J.S., Pino, M.S., Highshaw, R. a, Dunner, K., Huang, P., Abbruzzese, J.L., McConkey, D.J.: Bortezomib sensitizes pancreatic cancer cells to endoplasmic reticulum stress-mediated apoptosis. Cancer Research. 65, 11658-66 (2005).

2 Results

This cumulative PhD thesis is based on the following research articles and manuscripts.

Di-methylation of Triapine induces enhanced ER stress

Robert Trondl, Petra Heffeter, Christian R. Kowol, Ute Jungwirth, Georg E. Mair, Ralf Steinborn, Éva A. Enyedy, Michael A. Jakupec, Walter Berger and Bernhard K. Keppler

Molecular Cancer Therapeutics **2012**, manuscript in preparation

The α-heterocyclic thiosemicarbazone Triapine and its terminal dimethylated derivate 3-AP-Me were investigated on cancer cell lines regarding intracellular distribution, induction of the unfolded protein response and activation of the mitochondrial apoptosis pathway.
I performed intracellular distribution studies of the compounds by fluorescence microscopy and co-localisation studies with organelle-specific trackers. I analyzed changes of protein expression and phosphorylation associated with the unfolded protein response and quantified changes in splicing variants of the transcription factor XBP-1. I measured depolarization of mitochondrial membranes by means of the JC-1 assay. Moreover, I prepared the manuscript and wrote most of the introduction, results and discussion of the data.

NKP-1339, the first ruthenium-based anticancer drug on the edge to clinical application

Robert Trondl, Petra Heffeter, Christian R. Kowol, Michael A. Jakupec, Walter Berger and Bernhard B. Keppler

Chemical Science **2012,** manuscript in preparation

This synoptic article about the investigational ruthenium drug NKP-1339 summarizes the current knowledge and recent developments in preclinical and clinical studies. The review article discusses the binding properties of NKP-1339 to serum proteins, which is important for the drug delivery to tumor tissue. Following chapters report about the activation-by-reduction hypothesis and novel insights in the mechanism of action of the drug candidate. Furthermore, preliminary results of the recently completed clinical phase I study are summarized.
As first author I contributed to all chapters of the review and coordinated the participation of the co-authors.

Impact of metal coordination on cytotoxicity of 3-aminopyridine-2-carboxaldehyde thiosemicarbazone (triapine) and novel insights into terminal dimethylation

Christian R Kowol, Robert Trondl, Petra Heffeter, Vladimir B Arion, Michael A Jakupec, Alexander Roller, Markus Galanski, Walter Berger, Bernhard K Keppler

Journal of Medicinal Chemistry **2009** 52:16.5032-5043

In series of newly synthesized α-N heterocyclic thiosemicarbazones the coordination on gallium and iron as well as the terminal dimethylation of the ligand was studied. Beside the chemical characterization of the compounds, various cell biological experiments were conducted.
I contributed to this paper with investigations of structure-activity relationship in 41M (ovarian cancer), SK-BR3 (breast cancer) and HL-60 (leukemia) cells. I conducted cytotoxicity experiments and participated in writing of the experimental, results and discussion sections.

Fluorescence properties and cellular distribution of the investigational anticancer drug triapine (3-aminopyridine-2-carboxaldehyde thiosemicarbazone) and its zinc(II) complex.

Christian R Kowol, Robert Trondl, Vladimir B Arion, Michael A Jakupec, Irene Lichtscheidl, Bernhard K Keppler

Dalton Transactions **2010** 39:3.704-706

Intrinsic fluorescent properties of Triapine and its zinc complex were investigated in this short communication article. Cellular distribution in SW480 colon cancer cells of both compounds were studied by fluorescence microscopy.
I performed live cell imaging of subcellular distribution of both compounds by fluorescence microscopy. Furthermore, I conducted immunofluorescence experiments to study co-localization of the zinc complex with the nucleoli. Moreover, I did the cytotoxicity assay in two cancer cell lines and contributed in writing of the experimental, results and discussion.

Mechanisms underlying reductant-induced reactive oxygen species formation by anticancer copper(II) compounds

Christian R Kowol, Petra Heffeter, Walter Miklos, Lars Gille, Robert Trondl, Loredana Cappellacci, Walter Berger, Bernhard K Keppler.

Journal of Biological Inorganic Chemistry **2012** 17:3.409-423

The aim of this study was to compare the electrochemical properties as well as anticancer activity of the first copper(II) complexes of Triapine and its terminally dimethylated derivative. Additionally, interactions with biologically relevant antioxidants were studied as well as the role of ROS formation in their anticancer activity against tumor cells.
I contributed to this article by cytotoxicity experiments and by the evaluation of the manuscript.

L- and D-proline thiosemicarbazone conjugates: coordination behavior in solution, and the effect of copper(II) coordination on their antiproliferative activity

Miljan NM Milunovic, Éva A Enyedy, Nóra V Nagy, Tamás Kiss, Robert Trondl, Michael A. Jakupec, Bernhard K. Keppler, Regina Krachler, Ghenadie Novitchi, Vladimir B. Arion

Inorganic Chemistry **2012,** submitted May 2012

Two enantiomerically pure thiosemicarbazone-proline conjugates with enhanced aqueous solubility were studied on their coordination behavior to copper(II) and antiproliferative characteristics on cancer cells.
I conducted cytotoxicity experiments by means of the MTT colorimetric assay of the proline conjugated ligand as well as their copper(II) complexes and participated in the writing of the results and discussion section .

Targeting the DNA-topoisomerase complex in a double-strike approach with a topoisomerase inhibiting moiety and covalent DNA binder

Andrea Kurzwernhart, Wolfgang Kandioller, Caroline Bartel, Simone Bachler, Robert Trondl, Gerhard Muhlgassner, Michael A Jakupec, Vladimir Arion, Doris Marko, Bernhard K Keppler, Christian Hartinger

Chemical Communications **2012**, Epub ahead of print

Ruthenium (II) arene–flavonoid were synthesized and characterized by x-ray crystallography and ^{1}H-NMR spectroscopy. Additionally, antiproliferative activity, topoisomerase II inhibition and subcellular distribution were studied.

I performed subcellular distribution and co-localization experiments by using confocal laser scanning microscopy.

2.1 Di-methylation of Triapine induces enhanced ER stress

Robert Trondl, Petra Heffeter, Christian R. Kowol, Ute Jungwirth, Georg E. Mair, Ralf Steinborn, Éva A. Enyedy, Michael A. Jakupec, Walter Berger and Bernhard K. Keppler

Molecular Cancer Therapeutics **2012**, manuscript in preparation

Working title:

Di-methylation of Triapine induces enhanced ER stress

Robert Trondl[a], Petra Heffeter[b,c,f], Christian R. Kowol[a,c], Ute Jungwirth[b,c,f], Georg E. Mair[d], Ralf Steinborn[d], Éva A. Enyedy[e], Michael A. Jakupec[a,c]*, Walter Berger[b,c,f] and Bernhard K. Keppler[a,c]

a) Institute of Inorganic Chemistry, University of Vienna, Waehringer Str. 42, A-1090 Vienna, Austria; Tel: +43 1 4277 52600; E-mail: berhard.keppler@univie.ac.at

b) Institute of Cancer Research, Medical University of Vienna, Borschkegasse 8a, A-1090 Vienna

c) University of Vienna, Research Platform Translational Cancer Therapy Research, Waehringer Str. 42, A-1090 Vienna, Austria

d) VetCore Facility for Research, VetOmics, University of Veterinary Medicine, Veterinärplatz 1, A-1210 Vienna, Austria

e) Department of Inorganic and Analytical Chemistry, University of Szeged, Dóm tér 7, 6720 Szeged, Hungary

f) Comprehensive Cancer Centre of the Medical University Vienna, Austria

*corresponding author

Abstract

Triapine (3-AP), a known ribonucleotide reductase inhibitor, entered several clinical phase I and phase II studies in the last years. Intrinsic fluorescence properties of 3-AP enabled us to study subcellular distribution by fluorescence microscopy. 3-AP accumulates in the cytosol and co-localizes with endoplasmic reticulum and mitochondria. Further investigations in SW480 colon cancer cells revealed that 3-AP induces endoplasmic reticulum stress (ER stress). Moreover, we were able to show that the derivative 3-AP-Me, characterized by dimethylation of the terminal nitrogen of 3-AP, led to enhanced induction of ER stress compared to 3-AP. Following treatment with 3-AP or 3-AP-Me, SW480 cells displayed induction of the transcription factor CHOP which is associated with pro-apoptotic signaling of the unfolded protein response (UPR). Furthermore, 3-AP-Me treatment stronger induced phosphorylation of eukaryotic translation initiation factor 2 alpha (p-eIF2α) than 3-AP and led to a 16-fold upregulation of the alternatively spliced *XBP1* mRNA variant 2 as determined by reverse transcription quantitative real-time PCR (RT-qPCR). In contrast, no induction of alternative *XBP1* splicing was observed in 3-AP treated cells. In correlation with enhanced ER stress, 3-AP-Me is more potent in inducing depolarization of mitochondrial membranes, which suggests that ER stress-dependent apoptosis induction is a crucial factor in the mechanism of action. These studies demonstrate for the first time that induction of ER stress contributes to the mode of action of Triapine and the possibility to enhance this by terminal dimethylation of the molecule.

Introduction

Triapine (3-AP) belongs to the class of α-N-heterocyclic thiosemicarbazones and its antitumor activity is known for more than a decade and was studied in several clinical phase I and phase II trials (1–4). The anticancer activity of 3-AP has been ascribed to the inhibition of ribonucleotide reductase (5). The human ribonucleotide reductase enzyme is a tetramer and consists of two large (hRRM1) and two small (hRRM2 or p53R2) subunits. It catalyzes the reduction of ribonucleotides to deoxyribonucleotides, which are needed for DNA replication and repair. Due to a higher demand of DNA replication and repair machinery in tumors, ribonucleotide reductase is a suitable molecular target for cancer therapy. It can be inhibited by radical scavengers, which interfere with the tyrosyl radical of the small subunit (e.g. hydroxyurea), nucleoside and nucleotide analogues (e.g. gemcitabine, cytarabine) and iron chelators (e.g. desferrioxamine or KP772) which are interacting with the iron center of the enzyme (6; 7). 3-AP belongs to the group of α-heterocyclic thiosemicarbazones, which are known to form iron complexes in a highly effective manner. Thus, chelation of iron and subsequent inhibition of ribonucleotide reductase is thought to be a critical mechanism of its anticancer activity. Chaston and co-workers demonstrated in EPR measurements with 3-AP treated neuroepitheloma cells a decrease of the tyrosyl radical to 61% of the control, which is comparable to the effect of the pyridoxal isonicotinoyl class iron chelator 311 (8). Interestingly, the addition of iron to 3-AP prior to cell treatment had no significant effects on its cytotoxicity, which stands in contrast to the markedly decreased cytotoxicity of the iron chelators desferrioxamine and 311. Furthermore, cytotoxicity tests on hydroxyurea-resistant cell lines which are characterized by overexpression of hRRM2 subunit of ribonucleotide reductase showed no resistance to 3-AP (9; 10). Analysis of recombinant ribonucleotide reductase by EPR spectroscopy revealed Triapine does not remove iron significantly from the active site of hRRM2. However, iron(II)-bound Triapine inhibited ribonucleotide reductase by formation of reactive oxygen species in cell free settings (11). The complexity of the results obtained in these numerous studies indicates that additional to ribonucleotide reductase inhibition further unknown mechanisms contribute to the activity of AP-3. In previous studies we demonstrated that chemical modification of various thiosemicarbazones by dimethylation of the terminal amino group has an important impact on their biological activity (12). In the present study, subcellular distribution and co-localization of 3-AP and its

dimethylated derivative 3-AP-Me with mitochondria and endoplasmic reticulum as well as induction of the endoplasmic reticulum stress (ER stress) pathway was examined. One of the functions of the endoplasmic reticulum (ER) is folding of secreted and resident proteins into their native structures and the corresponding quality control of newly synthesized proteins (13). ER stress is induced by an accumulation of misfolded and/or unfolded proteins in the ER lumen, which leads to loss of ER homeostasis. Subsequently, the unfolded protein response (UPR) is initiated by dissociation of the ER-resident chaperon glucose-regulated protein 78 kDa (GRP78) from the three ER transmembrane proteins PERK, IRE1α, and ATF6 (14; 15). This cellular response is followed by the upregulation of ER-related chaperones and inhibition of the translation machinery to restore correct folding of proteins and ER homeostasis. However, severe ER stress (e.g. initiated by cytotoxic agents) leads to a change in the UPR pathway from pro-survival to pro-apoptotic signaling (16). Thereby the transcription factor CHOP (CCAAT/enhancer binding protein homologous transcriptions factor, also called GADD153) is crucial for switching to pro-apoptotic signaling (17). CHOP is involved in the suppression of Bcl-2 expression, stimulation of death receptor 5 (DR5), activation of caspases and consequently induction of the mitochondrial apoptosis pathway. Due to high metabolic activity and elevated levels of chronic stress in cancer cells, targeting ER stress response is a novel promising strategy for fighting cancer (18).

In this study we demonstrate that dimethylation of the terminal amino group of 3-AP (3-AP-Me, Fig. 1) leads to a markedly higher expression of proteins associated with ER stress and more efficient depolarization of the mitochondrial membrane potential. Our studies demonstrate induction of ER stress as a novel molecular mechanism of thiosemicarbazones and offer a new insight in apoptosis induction by 3-AP. Furthermore, dimethylation of Triapine enhanced the induction of the ER stress and apoptosis, which will be relevant for further development of thiosemicarbazones as anti-cancer treatment.

Materials and Methods

Reagents and antibodies. 3-AP and 3-AP-Me were synthesized as reported previously (12). Both compounds were dissolved in DMSO and diluted in cell culture medium to obtain the indicated concentrations. P-eIF2α, total eIF2-α, p-p38 MAPK, total p38 MAPK, GRP78, p-JNK,

total JNK and β-actin antibodies were purchased from Cell Signaling Technology. CHOP antibody was purchased from Abcam. Horseradish peroxidase-labeled anti-mouse IgG and anti-rabbit IgG secondary antibodies were purchased from Cell Signaling Technology. Thapsigargin was obtained from Sigma Aldrich.

Cell culture conditions SW480 cells (colon carcinoma, human) and HL-60 cells (promyeleocytic leukemia, human) were purchased from the American Type Culture Collection (ATCC). Cells were grown in Eagle's Minimal Essential Medium (MEM) supplemented with heat-inactivated 10% fetal bovine serum, 1 mM sodium pyruvate, 4 mM L-glutamine, and 1% nonessential amino acids (100x) in a humidified incubator at 37 °C and 5% CO_2. For cell culture experiments, exponentially grown cells were washed with phosphate buffered saline (PBS) buffer before used in the methods described below.

Fluorescence microscopy SW480 cells were cultured on cover slips in 6-well plates. A flow cell slide was used for stepwise staining of the cell population. Fluorescence microscope BX40 (Olympus) with F-View CCD Camera (Olympus), Cell^F fluorescence imaging software (Olympus) and 60x magnification oil immersion objective lens were used. Cells were incubated with 100 μM 3-AP and 3-AP-Me in MEM for 5 minutes and washed with PBS thrice before image acquisition. ER-Tracker Green and Mito-Tracker Red (Invitrogen) were used according instructions of the manufacturer. Use of a flow cell microscope slide allowed a stepwise staining procedure and prevented bleed-through of fluorochromes.

Measurement of intracellular oxidants 2′,7′-Dichlorofluorescein diacetate (DCF-DA) was used to detect the production of reactive oxygen species (ROS) (19). DCF-DA stock solutions (33.4 mM, DMSO) were stored at –20 °C. HL60 cells (2.5×105 cells per sample in phenol-free Hanks balanced salt solution) were incubated with DCF-DA (1 μM) for 30 min. Subsequently, the compounds were added in the indicated concentrations. After incubation for another 30 min, mean fluorescence intensity was measured by flow cytometry using a fluorescence-activated cell sorting (FACS) Calibur instrument (Becton Dickinson, Palo Alto, CA). A concentration of 200 μM H2O2 was used as positive control. The resulting histograms were quantified using the ModeFit software (BD).

Western blot analysis 2.5×105 SW480 cells were seeded 24 hours prior to treatment in 6-well plates. Cells were exposed to 1, 5 and 25 μM 3-AP or 3-AP-Me for different incubation times. Thapsigargin (0.5 μM) was used as a positive control. Total cell lysates were prepared by lysis with radioimmunoprecipitation assay (RIPA) buffer including protease and phosphatase inhibitor cocktails (Sigma-Aldrich). Identical amounts of total proteins were resolved by SDS-PAGE and electrophoretically transferred onto nitrocellulose membrane by using a semi-dry blotter (Peqlab). The membrane was blocked with 5% BSA in TBST buffer for 1 hour at room temperature. Primary antibodies were diluted according to the instructions of the manufacturer and incubated overnight at 4 °C. Anti-β-actin was used as a loading control. Secondary antibodies were appropriately diluted and incubated for 1 hour at room temperature. Horseradish peroxidase-coupled secondary antibodies were detected by chemiluminescence using Super Signal chemiluminescence substrate from Pierce and chemiluminescence detection system Fusion SL (Vilber Lourmat). Densitometrical analysis of blots was performed with ImageJ software (20).

RT-qPCR. Sequences of primers and hydrolysis probes (Table S1) were designed with Primer Express version 2.0 software (Applied Biosystems). Primers were analyzed for all primer secondary structures including hairpins, self-dimers, and cross-dimers in primer pairs using NetPrimer software (Premier Biosoft) and for specificity using Primer-BLAST of NCBI. Amplicon secondary structure was assessed with mfold web server (21).

Treated and mock-treated SW480 cells were lyzed with QIAzol (Qiagen). For automated isolation of total RNA the miRNeasy Kit (Qiagen) was used on the QIAcube robot (Qiagen). RNA amount was measured spectrophotometrically with the BioPhotometer 6131 combined with the TrayCell cuvette (Eppendorf; Hellma Worldwide). RNA integrity number (RIN) determined with the RNA 6000 Nano Chip Kit (Agilent Technologies) on the 2100 Bioanalyzer (Agilent Technologies) was ≥ 7 for experimental samples. The High-Capacity Reverse Transcription Kit (Applied Biosystems) was used for random hexamer primed cDNA synthesis incubated at 37 °C for 120 min. The 20 μl multiplexed qPCR consisted of Rotor Gene Multiplex PCR Kit (Qiagen), 150 nM of each primer, 150 nM target probe, 150 nM reference gene probe and performed with 1 ng cDNA triplicates. For qPCR conducted on the ViiA7 Real-Time PCR System (Applied Biosystems) a temperature protocol of an initial hot start at 95 °C for 5 min followed by 50 amplification cycles (95 °C for 15 s, 58 °C for 25 s, 60 °C for 25 s) was used. Target expression

was normalized by the reference gene ornithine decarboxylase antizyme (*OAZ1*, (22; 23) which displayed minimal variation across experimental groups (ΔCq < 0,84). A series of five eight-fold dilutions of a control cDNA from mock treated SW480 cells amplified in triplicate was used to generate a standard curve. Reaction efficiencies (E) calculated from the slope of the standard curve using the formula $E = 10^{-1/slope} - 1$ ranged from 0.86 to 0.98.

Calculation of expression changes and evaluation of their statistical significance were performed using the Relative Expression Software Tool (REST) 2007 software including the Pair Wise Fixed Reallocation Randomisation Test (24). Finally, the *n*-fold expression change of the two splicing variants was given relative to the untreated control group.

Analysis of mitochondrial membrane potential. Depolarization of mitochondrial membrane potential was determined by FACS analysis using JC-1 (5,5,6,6-tetrachloro-1,1,3,3-tetraethylbenzimidazol-carbocyanine iodide, Biovision) which forms multimer J-aggregates in intact mitochondria, emitting fluorescence at 590 nm. Loss of mitochondrial membrane potential leads to dissociation of J-aggregates to monomers, which implicates a change in emission light to 527 nm (25). For this purpose, HL-60 cells were treated with 0.25, 0.5 and 1 µM 3-AP or 3-AP-Me for 24 hours. After treatment cells were pelleted, washed with PBS and stained with 2 µg/ml JC-1 for 20 min at 37 °C. After staining cells were washed twice with PBS and analyzed with a Guava 8HT Flow Cytometer (Millipore). Results were repeated in three independent experiments, and statistical analysis was done with FlowJo software.

Results

Co-localization of 3-AP and 3-AP-Me with endoplasmic reticulum and mitochondria. The intrinsic fluorescence properties of 3-AP were reported in a previous publication (26). 3-AP and AP-3-Me have similar fluorescence properties in terms of maximum excitation and emission wavelengths (Fig.1). In the present study, intracellular distribution of both compounds in SW480 colon carcinoma cells was examined by fluorescence microscopy of in a live cell setting. The cellular uptake of both compounds was remarkable quick (within 5 min), and longer incubation times did not improve the image quality. Sequential co-staining in a flow cell with ER-Tracker Green and Mito-Tracker Red were used to study the co-localization with organelles of both compounds and prevented crosstalk of the fluorochromes. Microscopic images (Fig. 2) showed a

preferred localization of both compounds in structures of the cytoplasm. 3-AP accumulated in more granular structures, which match with the mitochondria (see zoomed details Fig. 2A). On the contrary, images of 3-AP-Me showed a mesh-like structure, which was comparable with the structures observed with ER Tracker green. Intracellular distribution on the light microscopy scale suggests a direct interaction of both compounds with endoplasmic reticulum and/or mitochondria.

3-AP and 3-AP-Me induce pro-apoptotic signaling of UPR in a ROS independent way. The comparable cytotoxicity of 3-AP and 3-AP-Me (Fig. 3C) are ideal requirements to study differences in molecular mechanisms. First, the influence of 3-AP and 3-AP-Me on endoplasmic reticulum homeostasis was investigated by Western blot analysis of proteins involved in UPR signaling (Fig. 3A). As activation of UPR proteins is a strongly time-dependent mechanism, different time points for Western blot analysis were chosen. The ER-stress inducer thapsigargin was used as a positive control. As shown in Figure 3, already 1 μM 3-AP-Me treatment of SW480 cells led to the phosphorylation of eIF-2α, a downstream target of PERK and suppressor of the protein translation machinery after 12 hours incubation time. In contrast, 3-AP slightly increased eIF-2α phosphorylation only at the highest tested concentration (25 μM). The enhanced and concentration-independent phosphorylation of eIF-2α was followed by a strong upregulation of CHOP expression after 24 hours 3-AP-Me treatment, while CHOP upregulation in 3-AP-treated cells was only observed at the highest concentration (25 μM). Surprisingly, after 24 hours, no GRP78 upregulation was observed for both compounds, whereas thapsigargin treatment showed a clear induction of this upstream initiator of UPR signaling (data not shown). However, after 48 hour treatment higher expression of GRP78, was found also after 3-AP or 3-AP-Me treatment, with again 3-AP-Me being more active than 3-AP. All together, this indicates that both drugs induce severe ER stress and activation of pro-apoptotic signaling but 3-AP to a lesser extent than 3-AP-Me.ROS is a critical factor for ER stress induction and generation of ROS by induction of Fenton-like reactions was demonstrated for the iron-3-AP complex (11). To investigate the role of ROS in the anticancer activity of 3-AP and 3-AP-Me against SW480 cells, the known radical scavenger N-acetyl cysteine (NAC) was used. Figure 3B shows the H_2O_2 and hydroxyl radical generation after 30 min drug treatment visualized by the ROS-sensitive dye DCF-DA (19). Neither 3-AP nor 3-AP-Me led to significant increase of intracellular ROS levels

and, thus, NAC cotreatment had no effect in these experiments. Also in 72 hour viability assays, co-treatment with NAC did not protect cells from 3-AP or 3-AP-Me (Fig. 3C) indicating that ROS generation does not play a major role in the anticancer activity of these drugs, at least in our hand.

3-AP-Me treatment leads to alternative splicing of *XBP1* mRNA. To address the effects of 3-AP and 3-AP-Me on the transcriptional level of UPR, the two splicing variants of *XBP1* mRNA were quantified by RT-qPCR. Substantial ER stress promotes alternative splicing to the 26 bp shorter *XBP1* mRNA variant 2 (141 bp), which results in a frameshift and encodes the bZip transcription factor X-box binding protein 1 (XBP1s) (27). Fluorescence-labeled probes were designed to quantify the mRNA splicing of *XBP1* variant 1 and the alternatively spliced *XBP1* variant 2 via qRT-PCR in a duplex reaction. After 24 hours treatment thapsigargin induced splicing of *XBP1* mRNA variant 2 and led to an 18-fold higher expression, while variant 1 showed a 3.5-fold lower expression compared to the control. As shown in Figure 4a, 3-AP-Me treated cells displayed a 16- and 15-fold upregulation of *XBP1* mRNA variant 2 at concentrations of 0.5 and 1 μM, respectively. At the same time, a significant downregulation (11-fold) of variant 1 was observed for 3-AP-Me treatment at 1 μM. On the contrary, 3-AP treated cells did not upregulate the alternatively spliced mRNA variant 2 at any used concentration. Surprisingly, a slight downregulation (4-fold) of variant 2 was detected after treatment with 1 μM 3-AP. As already 8 hours incubation with thapsigargin led to a 30-fold upregulation of *XBP1* mRNA variant 2, 3-AP and 3-AP-Me induced *XBP1* splicing was analyzed at this time point. In contrast, after 8 hours incubation both thiosemicarbazones did not change the expression of both splicing variants (Fig. 4b). . Taken together, our findings show a significant induction of alternative *XBP1* splicing for 3-AP-Me. These results are in good agreement with the Western blot analysis of UPR-related proteins. On the other hand, it was quite surprising that no upregulation of alternative splicing was observed for 3-AP. However, the slower induction of UPR signaling compared to thapsigargin indicates a different way of interference with the protein folding machinery for thiosemicarbazones.

3-AP and 3-AP-Me activate the p38 MAPK and JNK pathway. Next, the effects of 3-AP and 3-AP-Me treatment on p38 MAPK and JNK activation were studied. Previously it has been

reported that the activation of JNK and p38 MAPK is associated with ER stress and ER stress initiated cell death (28–30). Western blot experiments with SW480 cells showed phosphorylation of JNK and p38 MAPK after 12 hour incubation with 3-AP or 3-AP-Me (Fig. 5). In these experiments, 3-AP treatment led to a concentration-dependent increase of JNK and p38 MAPK activation. Again, 3-AP-Me treatment led to a stronger effect than 3-AP. (Fig. 5). Unexpectedly, a sharp decrease in phosphorylated levels of JNK and p38 MAPK were observed at the highest tested concentration of 3-AP-Me (25 μM). Nevertheless, both compounds show induction of p38 MAPK and JNK pathway and dimethylation of 3-AP leads to a more pronounced effect at lower concentrations.

Dimethylation of 3-AP leads to enhanced depolarization of mitochondrial membranes. Changes in mitochondrial membrane potential ($\Delta\Psi_m$) are key events in apoptosis induction, and recent studies showed that non-resolved ER stress leads to increased mitochondrial membrane transition by downregulation of bcl-2 through CHOP (31). To monitor $\Delta\Psi_m$, flow cytometer analysis with the fluorescence dye JC-1 was used. Human HL-60 leukemia cells were treated with 3-AP or 3-AP-Me with different concentrations for 24 hours., which is in good agreement with its enhanced capacity of inducing ER stress found in Western blots and qRT-PCR experiments before. As shown in the contour plots in Figure 6, HL-60 cells treated with 0.25 and 0.5 μM of 3-AP showed only a slight or no decrease in $\Delta\Psi_m$. However, 3-AP treatment led to a distinct decrease in the number of cells with functional mitochondria at a concentration of 1 μM. In contrast, the amount of cells with depolarized mitochondria membrane distinctly increased after 3-AP-Me treatment. Even the lowest concentration of 0.25 μM resulted in decreased $\Delta\Psi_m$ in ~30 % of the cell population, whereas concentrations of 0.5 and 1 μM result in up to 50 % of cells with depolarized mitochondrial membranes.

Discussion

In previous studies, we reported about the visualization of 3-AP with fluorescence microscopy in live cells as a useful tool for better understanding of intracellular distribution. In the present work, co-localization studies of 3-AP with fluorescent specific organelle trackers were the basis for studying new aspects of the anticancer activity. In this study, it is shown for the first time that 3-AP treatment leads to induction of ER stress indicated by activation of UPR-associated factors.

Moreover, it was discovered that dimethylation of the terminal amino group of 3-AP yields a compound which activates more potently the UPR. The differences between 3-AP and 3-AP-Me in upregulation of UPR are consistent with the enhanced depolarization of mitochondrial membranes. This suggests that ER stress induction is an additional mechanism of the biological activity of 3-AP and other promising thiosemicarbazones.

Previously, a study reported about four-dentate copper and zinc thiosemicarbazone complexes with intrinsic fluorescence properties used as probes in cancer cells. However, no conclusion could be made about organelle specific accumulation (32). Our results suggest that intracellular accumulation of 3-AP and 3-AP-Me in the ER and mitochondria coincide with the activation of the UPR. The UPR can be triggered by a wide variety of disruptions, including accumulation of misfolded/unfolded proteins, imbalances in ER lipids and glycolipids, changes in the redox environment of ER caused by ROS, and disruption of Ca^{2+} homeostasis. Recent studies showed that the Cu^{2+} complex of the thiosemicarbazone NSC 689534 induces oxidative and ER stress, whereas NSC 689534 lacking metal coordination does not induce oxidative nor ER stress (33). On the contrary, 3-AP and 3-AP-Me activate of ER stress without metal coordination. Furthermore, no generation of ROS was observed, nor was their cytotoxicity associated with oxidative stress. However, in good agreement with the study of Hancock et al (33) our results also suggests that induction of apoptosis is correlated with upregulation or ER stress genes.

The activation of the UPR was proven by upregulation several proteins including p-eIF2α, GRP78 and CHOP. The translation initiation factor eIF2α gets phosphorylated on Ser51 by PERK, a type I transmembrane protein and initiator of UPR (34). By phosphorylation of the α-subunit of eIF2 the translation of most mRNAs is downregulated to reduce the burden on the stressed ER by decreasing the traffic of newly synthesized polypeptides (35). On the other hand, p-eIF2α upregulates activating transcription factor (ATF4), which in turn stimulates the expression of ER chaperons such as GRP78 to restore ER homeostasis (36). However, if the protein machinery is disturbed severely the pro-survival signaling can switch to a pro-apoptotic pathway by upregulation of CHOP, whose induction strongly depends on ATF4 (15). CHOP plays an essential role in ER stress-mediated apoptosis by regulating genes involved in cell life and death decisions (37). Overexpression of CHOP leads to downregulation of anti-apoptotic

Bcl-2 and to translocation of the pro-apoptotic Bax protein to mitochondria, where death signaling is executed (38; 39). Western blot analysis displayed a strong upregulation of eIF2α phosphorylation after 3-AP-Me treatment, whereas for 3-AP only a slight upregulation was observed. Interestingly, upregulated CHOP levels were found after 24 hours treatment with 3-AP or 3-AP-Me, whereas no higher expression of GRP78 was observed at this time point. In order to overcome acute ER stress, chaperons such as GRP78 are upregulated by UPR to increase the ER folding capacity, and thus high levels of GRP78 confer with pro-survival signaling of ER stress responses (40; 41). We found upregulated expression of GRP78 only after 48 hour treatment with 3-AP and 3-AP-Me. In contrast, treatment with the ER stress inducer thapsigargin led to upregulation of GRP78 already after 8 hours (data not shown). Increased levels of CHOP prior to upregulation of GRP78 suggest a severely disturbed ER homoeostasis and indicate an imbalance of anti- and pro-apoptotic signals in favor of the latter (42). Furthermore, the more pronounced induction of CHOP by 3-AP-Me compared to 3-AP supports the assumption that the dimethylated moiety is responsible for the induction of pro-apoptotic signaling of the UPR.

In good accordance with our results, mRNA expression studies with the thiosemicarbazone Dp44mT suggested that iron depletion is responsible for elevated levels of *DITT3* (a synonym for the gene encoding CHOP)(43). Indeed, investigations regarding the stability of 3-AP and 3-AP-Me complexes with iron, zinc and copper revealed that dimethylated 3-AP forms complexes in a more stable manner (44; 45). This suggests that metal complexation properties of thiosemicarbazones may interfere with proper folding of metalloproteins which consequently leads to the induction of ER stress.

During ER stress XBP1s regulates several UPR-related proteins, such as GRP78, $p58^{IPK}$, CHOP and XBP1 itself (46). Analysis of both *XBP1* mRNA splicing variants by qRT-PCR showed a strong induction of the alternatively spliced variant 2 for 3-AP-Me treatment, while in the case of 3-AP no upregulation of spliced *XBP1* mRNA was observed. This underlines that the dimethylamine moiety is a crucial factor for induction of the IRE1α-XBP1 branch of the UPR. Furthermore, the IRE1α-TRAF2-ASK1 pathway is thought to be coupled with cellular stress-activated protein kinases such as JNK and p38 MAPK, which are assumed to play an important role in ER stress-mediated apoptosis (28; 30; 47). Thus, the phosphorylation of p38 MAPK and

JNK was investigated. In accordance with the enhanced induction of UPR protein expressions of 3-AP-Me also JNK and p38 MAPK activation was enhanced by dimethylation. For yet unknown reasons, higher concentrations of 3-AP-Me led to a reversal of activated JNK and p38 MAPK, while this effect was not observed with 3-AP. Nevertheless, activated levels of JNK and p38 MAPK indicate an influence of JNK and MAPK pathways in the biological mechanism for both 3-AP and 3-AP-Me.

The close contact of endoplasmic reticulum and mitochondria supports signaling between those two organelles of various cellular events including regulation of ER chaperones, ATP synthesis and apoptosis (48). Thus, mitochondria seem to play a crucial role in ER stress-induced apoptosis. Recent studies showed ER stress triggers loss of mitochondrial membrane potential via multiple signals such as caspase activation and induction of BH3-only proteins (31). In this study it was shown that the enhanced ER stress induction potency of 3-AP-Me are associated with more pronounced depolarization of mitochondrial membranes. Furthermore, these results let us assume that enhanced ER stress induction by dimethylation of 3-AP-Me is associated with a stronger induction of the apoptosis cascade.

In earlier studies, we synthesized and screened various chemical derivatives of 3-AP regarding their biological activity. Dimethylation of the terminal amino group was one factor to improve cytotoxicity against cancer cells (12). Here, we were able to show that chemical modification of 3-AP by dimethylation results in increased ER stress induction, which led to enhanced apoptosis induction. Furthermore, we could show in the present study ER stress induction seems to be relevant for the biological activity of 3-AP, which may be important for further development of the drug.

References

1. Ocean AJ, Christos P, Sparano J a, et al. Phase II trial of the ribonucleotide reductase inhibitor 3-aminopyridine-2-carboxaldehydethiosemicarbazone plus gemcitabine in patients with advanced biliary tract cancer. Cancer Chemotherapy and Pharmacology. 2011;68(2):379-88.

2. Traynor AM, Lee J-W, Bayer GK, et al. A phase II trial of triapine (NSC# 663249) and gemcitabine as second line treatment of advanced non-small cell lung cancer: Eastern Cooperative Oncology Group Study 1503. Investigational New Drugs. 2010;28(1):91-7.

3. Kunos CA, Waggoner S, Gruenigen VV, et al. Phase I Trial of Pelvic Radiation , Weekly Cisplatin , and 3-Aminopyridine-2-Carboxaldehyde Thiosemicarbazone (3-AP , NSC # 663249) for Locally Advanced Cervical Cancer. Clinical Cancer Research. 2010;16(4):1298-1306.

4. Nutting CM, van Herpen CML, Miah AB, et al. Phase II study of 3-AP Triapine in patients with recurrent or metastatic head and neck squamous cell carcinoma. Annals of Oncology. 2009;20(7):1275-9.

5. Finch RA, Liu M, Grill SP, et al. Triapine (3-aminopyridine-2-carboxaldehyde-thiosemicarbazone): A potent inhibitor of ribonucleotide reductase activity with broad spectrum antitumor activity. Biochemical Pharmacology. 2000;59(8):983-91.

6. Wijerathna SR, Ahmad MF, Xu H, et al. Targeting the Large Subunit of Human Ribonucleotide Reductase for Cancer Chemotherapy. Pharmaceuticals. 2011;4(10):1328-1354.

7. Heffeter P, Popovic-Bijelic A, Saiko P, et al. Ribonucleotide reductase as one important target of [Tris(1,10-phenanthroline)lanthanum(III)] trithiocyanate (KP772). Current Cancer Drug Targets. 2009;9(5):595-607.

8. Chaston TB, Lovejoy DB, Watts RN, Richardson DR. Examination of the Antiproliferative Activity of Iron Chelators. Clinical Cancer Research. 2003;9(1):402-414.

9. Finch R, Liu M, Cory AH, Cory JG, Sartorelli AC. Triapine (3-aminopyridine-2-carboxaldehyde thiosemicarbazone; 3-AP): an inhibitor of ribonucleotide reductase with antineoplastic activity. Advances in Enzyme Regulation. 1999;39(98):3.

10. Yen Y, Grill SP, Dutschman GE, Chang CN, Zhou BS, Cheng YC. Characterization of a hydroxyurea-resistant human KB cell line with supersensitivity to 6-thioguanine. Cancer Research. 1994;54(14):3686-91.

11. Shao J, Zhou B, Di Bilio AJ, et al. A Ferrous-Triapine complex mediates formation of reactive oxygen species that inactivate human ribonucleotide reductase. Molecular Cancer Therapeutics. 2006;5(3):586-92.

12. Kowol CR, Trondl R, Heffeter P, et al. Impact of metal coordination on cytotoxicity of 3-aminopyridine-2-carboxaldehyde thiosemicarbazone (triapine) and novel insights into terminal dimethylation. Journal of Medicinal Chemistry. 2009;52(16):5032-43.

13. Ellgaard L, Helenius A. Quality control in the endoplasmic reticulum. Nature Reviews. Molecular Cell Biology. 2003;4(3):181-91.

14. Ron D, Walter P. Signal integration in the endoplasmic reticulum unfolded protein response. Nature Reviews. Molecular Cell Biology. 2007;8(7):519-29.

15. Szegezdi E, Logue SE, Gorman AM, Samali A. Mediators of endoplasmic reticulum stress-induced apoptosis. EMBO Reports. 2006;7(9):880-5.

16. Xu C, Bailly-Maitre B, Reed JC. Endoplasmic reticulum stress: cell life and death decisions. Journal of Clinical Investigation. 2005;115(10):2656–2664.

17. Oyadomari S, Mori M. Roles of CHOP/GADD153 in endoplasmic reticulum stress. Cell Death and Differentiation. 2004;11(4):381-9.

18. Healy SJM, Gorman AM, Mousavi-Shafaei P, Gupta S, Samali A. Targeting the endoplasmic reticulum-stress response as an anticancer strategy. European Journal of Pharmacology. 2009;625(1-3):234-46.

19. Gomes A, Fernandes E, Lima JLFC. Fluorescence probes used for detection of reactive oxygen species. Journal of biochemical and biophysical methods. 2005;65(2-3):45-80.

20. Abràmoff MD, Magalhães PJ, Ram SJ. Image Processing with ImageJ. Biophotonics International. 2004;11(7):36-42.

21. Zuker M. Mfold web server for nucleic acid folding and hybridization prediction. Nucleic Acids Research. 2003;31(13):3406-3415.

22. Kwon MJ, Oh E, Lee S, et al. Identification of novel reference genes using multiplatform expression data and their validation for quantitative gene expression analysis. PloS one. 2009;4(7):e6162.

23. de Jonge HJM, Fehrmann RSN, de Bont ESJM, et al. Evidence based selection of housekeeping genes. PloS one. 2007;2(9):e898.

24. Pfaffl MW, Horgan GW, Dempfle L. Relative expression software tool (REST) for group-wise comparison and statistical analysis of relative expression results in real-time PCR. Nucleic acids research. 2002;30(9):e36.

25. Salvioli S, Ardizzoni A, Franceschi C, Cossarizza A. JC-1, but not DiOC6(3) or rhodamine 123, is a reliable fluorescent probe to assess ΔΨ changes in intact cells: implications for studies on mitochondrial functionality during apoptosis. FEBS Letters. 1997;411(1):77-82.

26. Kowol CR, Trondl R, Arion VB, Jakupec MA, Lichtscheidl I, Keppler BK. Fluorescence properties and cellular distribution of the investigational anticancer drug triapine (3-aminopyridine-2-carboxaldehyde thiosemicarbazone) and its zinc(II) complex. Dalton Transactions. 2010;39(3):704-6.

27. Yoshida H, Matsui T, Yamamoto a, Okada T, Mori K. XBP1 mRNA is induced by ATF6 and spliced by IRE1 in response to ER stress to produce a highly active transcription factor. Cell. 2001;107(7):881-91.

28. Luo S, Lee AS. Requirement of the p38 mitogen-activated protein kinase signalling pathway for the induction of the 78 kDa glucose-regulated protein/immunoglobulin heavy-chain binding protein by azetidine stress: activating transcription factor 6 as a target for stress-i. The Biochemical journal. 2002;366(Pt 3):787-95.

29. Maytin EV, Ubeda M, Lin JC, Habener JF. Stress-inducible transcription factor CHOP/gadd153 induces apoptosis in mammalian cells via p38 kinase-dependent and -independent mechanisms. Experimental Cell Research. 2001;267(2):193-204.

30. Urano F, Wang X, Bertolotti A, et al. Coupling of stress in the ER to activation of JNK protein kinases by transmembrane protein kinase IRE1. Science. 2000;287(5453):664-6.

31. Gupta S, Cuffe L, Szegezdi E, et al. Mechanisms of ER Stress-Mediated Mitochondrial Membrane Permeabilization. International Journal of Cell Biology. 2010;20101-10.

32. Pascu SI, Waghorn PA, Conry TD, et al. Designing Zn(II) and Cu(II) derivatives as probes for in vitro fluorescence imaging. Dalton Transactions. 2007;2007(43):4988-97.

33. Hancock CN, Stockwin LH, Han B, et al. A Copper Chelate of Thiosemicarbazone NSC 689534 induces Oxidative/ER Stress and Inhibits Tumor Growth In Vitro and In Vivo. Free Radical Biology and Medicine. 2010;

34. Schmitt E, Naveau M, Mechulam Y. Eukaryotic and archaeal translation initiation factor 2: a heterotrimeric tRNA carrier. FEBS Letters. 2010;584(2):405-12.

35. Boyce M, Yuan J. Cellular response to endoplasmic reticulum stress: a matter of life or death. Cell Death and Differentiation. 2006;13(3):363-73.

36. Harding HP, Zhang Y, Zeng H, et al. An Integrated Stress Response Regulates Amino Acid Metabolism and Resistance to Oxidative Stress. Molecular Cell. 2003;11(3):619-633.

37. Matsumoto M, Minami M, Takeda K, Sakao Y, Akira S. Ectopic expression of CHOP (GADD153) induces apoptosis in M1 myeloblastic leukemia cells. FEBS Letters. 1996;395(2-3):143-7.

38. Gotoh T, Terada K, Oyadomari S, Mori M. hsp70-DnaJ chaperone pair prevents nitric oxide- and CHOP-induced apoptosis by inhibiting translocation of Bax to mitochondria. Cell Death and Differentiation. 2004;11(4):390-402.

39. McCullough KD, Martindale JL, Klotz LO, Aw TY, Holbrook NJ. Gadd153 sensitizes cells to endoplasmic reticulum stress by down-regulating Bcl2 and perturbing the cellular redox state. Molecular and Cellular Biology. 2001;21(4):1249-59.

40. Pyrko P, Schönthal AH, Hofman FM, Chen TC, Lee AS. The unfolded protein response regulator GRP78/BiP as a novel target for increasing chemosensitivity in malignant gliomas. Cancer Research. 2007;67(20):9809-16.

41. Lee AS. GRP78 induction in cancer: therapeutic and prognostic implications. Cancer Research. 2007;67(8):3496-9.

42. Suzuki T, Lu J, Zahed M, Kita K, Suzuki N. Reduction of GRP78 expression with siRNA activates unfolded protein response leading to apoptosis in HeLa cells. Archives of Biochemistry and Biophysics. 2007;468(1):1-14.

43. Yu Y, Richardson DR. Cellular iron-depletion stimulates the JNK and p38 MAP signaling transduction pathways, dissociation of ASK1-thioredoxin and activation of ASK1. The Journal of Biological Chemistry. 2011;286(17):15413-15427.

44. Enyedy ÉA, Primik MF, Kowol CR, Arion VB, Kiss T, Keppler BK. Interaction of Triapine and related thiosemicarbazones with iron(III)/(II) and gallium(III): a comparative solution equilibrium study. Dalton transactions. 2011;40(22):5895-905.

45. Enyedy ÉA, Nagy NV, Zsigó É, et al. Comparative Solution Equilibrium Study of the Interactions of Copper(II), Iron(II) and Zinc(II) with Triapine (3-Aminopyridine-2-carbaldehyde Thiosemicarbazone) and Related Ligands. European Journal of Inorganic Chemistry. 2010;(Ii):NA-NA.

46. Lee A-H, Iwakoshi NN, Glimcher LH. XBP-1 regulates a subset of endoplasmic reticulum resident chaperone genes in the unfolded protein response. Molecular and Cellular Biology. 2003;23(21):7448-59.

47. Gupta S, Deepti A, Deegan S, Lisbona F, Hetz C, Samali A. HSP72 Protects Cells from ER Stress-induced Apoptosis via Enhancement of IRE1α-XBP1 Signaling through a Physical Interaction. PLoS Biology. 2010;8(7):e1000410.

48. Gupta S, Cuffe L, Szegezdi E, et al. Mechanisms of ER Stress-Mediated Mitochondrial Membrane Permeabilization. International Journal of Cell Biology. 2010;20101-10.

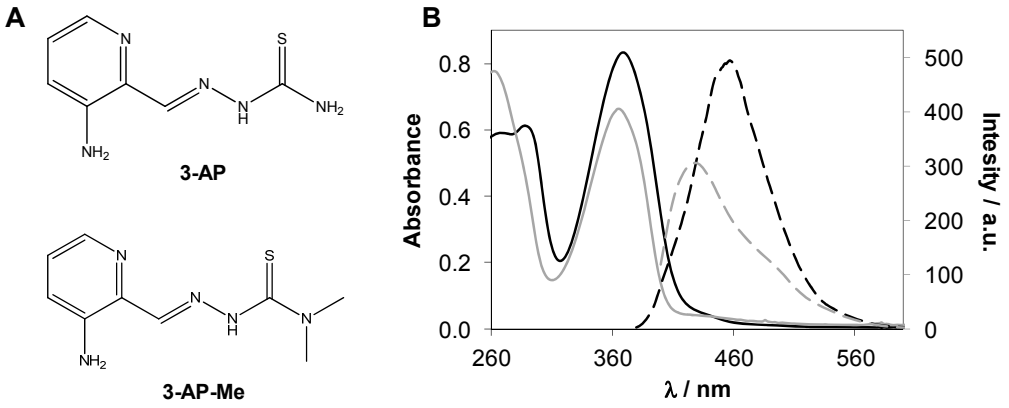

Fig 1. Chemical structures and absorption/emission spectra of 3-AP and 3-AP-Me. A) structural formula of 3-AP and 3-AP-Me. B) UV/vis absorption spectrum of 3-AP (black solid line) and 3-AP-Me (grey solid line) (c_L = 0.05 mM) and fluorescence emission spectrum of 3-AP (black dashed line) and 3-AP-Me (gray dashed line) (c_L = 0.01 mM; λ_{EX} = 360 nm), pH 7.4 in 30% (w/w) DMSO/H_2O, t = 25.0 °C, I = 0.10 M (KCl).

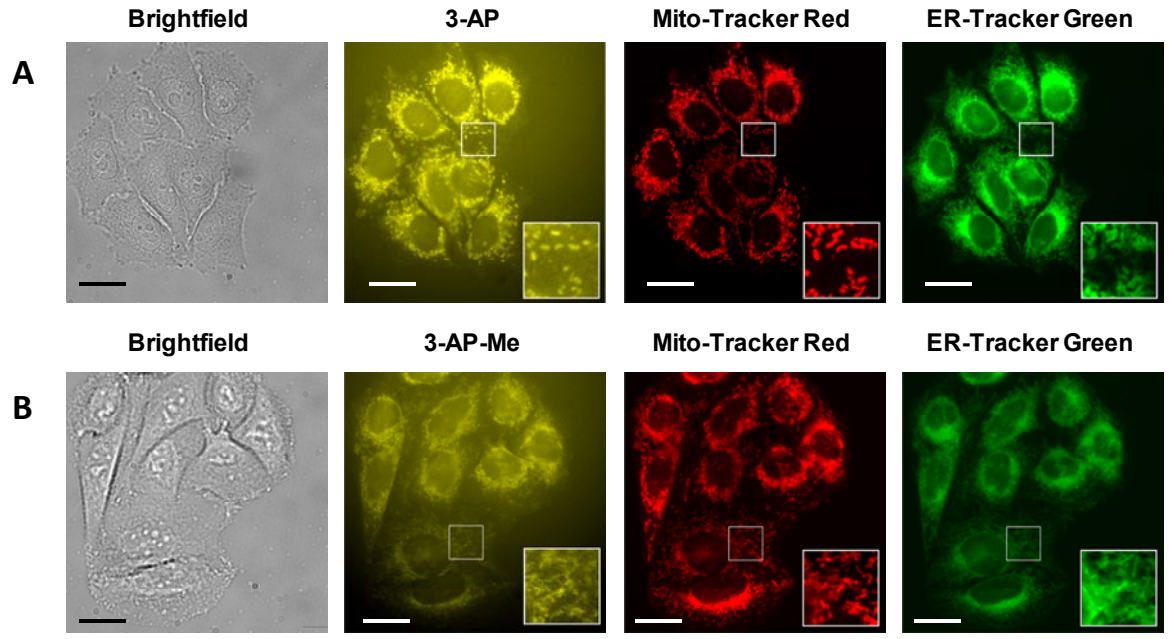

Fig. 2. Live cell fluorescence microscopy images of SW480 colon carcinoma cells. Cells were co-stained in a stepwise procedure in a flow cell with 100 µM 3-AP or 3-AP-Me and ER-Tracker Green (1 µM) or Mito-Tracker Red (200 nM) for 5 minutes each. After each staining step, cells

were washed three times with PBS. Staining series A) with 3-AP, and B) with 3-AP-me. Zoomed details are showed in right corner. Scale bar is 20 µm.

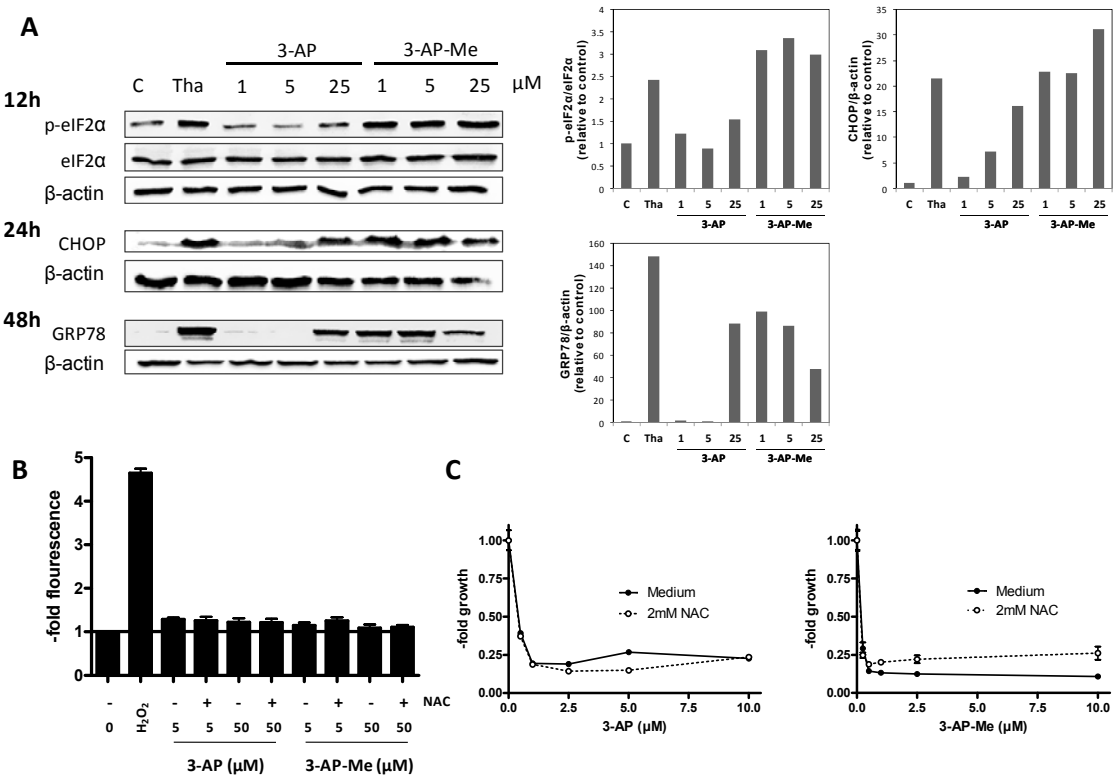

Fig 3. 3-AP and 3-AP-Me induces ER Stress in a ROS independent manner. (A) Western blot analysis of eIF2α phosphorylation and expression of CHOP and GRP78 were analyzed in SW480 colon carcinoma cells after 3-AP or 3-AP-Me treatment. Thapsigargin (0.5 µM) was used a positive control. Blots were analyzed with ImageJ software and relative ratios of GRP78 or CHOP expression to β-actin or eIF2α phosphorylation to unphosphorylated form were calculated and are demonstrated in bar graphs. Shown results are representatives out of three independent experiments. (B) Influence of pre-treatment with 2 mM NAC on the intracellular ROS levels in HL60 cells after 30 min drug incubation was determined using the ROS indicator DCF-DA. One representative experiment out of three delivering comparable results is shown. (C) After 30 min pre-incubation with NAC (2 mM) SW480 cells were treated for 72 h with the indicated

concentrations of 3-AP and 3-AP-Me. Viability was determined using MTT assay. Values given are means ± S.D. of three determinations out of three experiments.

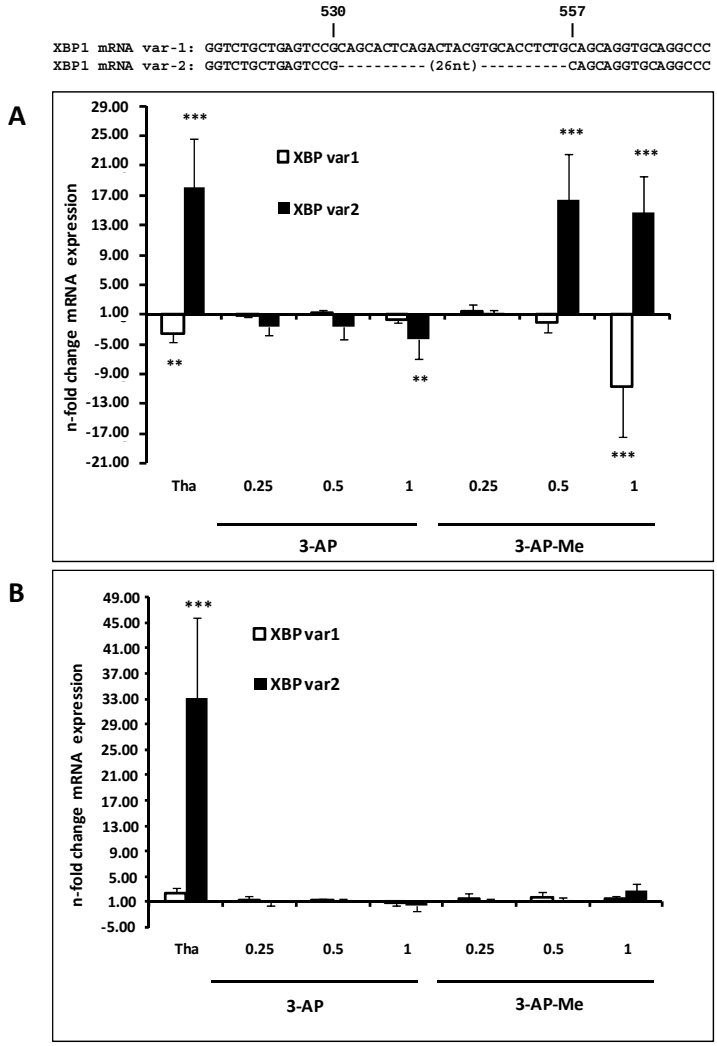

Fig.4 Change in gene expression of splicing variants of *XBP1* mRNA measured by RT-qPCR. SW480 cells were treated with 0.25, 0.5 and 1 μM 3-AP or 3-AP-Me for (A) 24 hours and (B) 8 hours. Bars display means ± S.D. of three independent experiments; $^{**}p < 0.05$; $^{***}p < 0.01$.

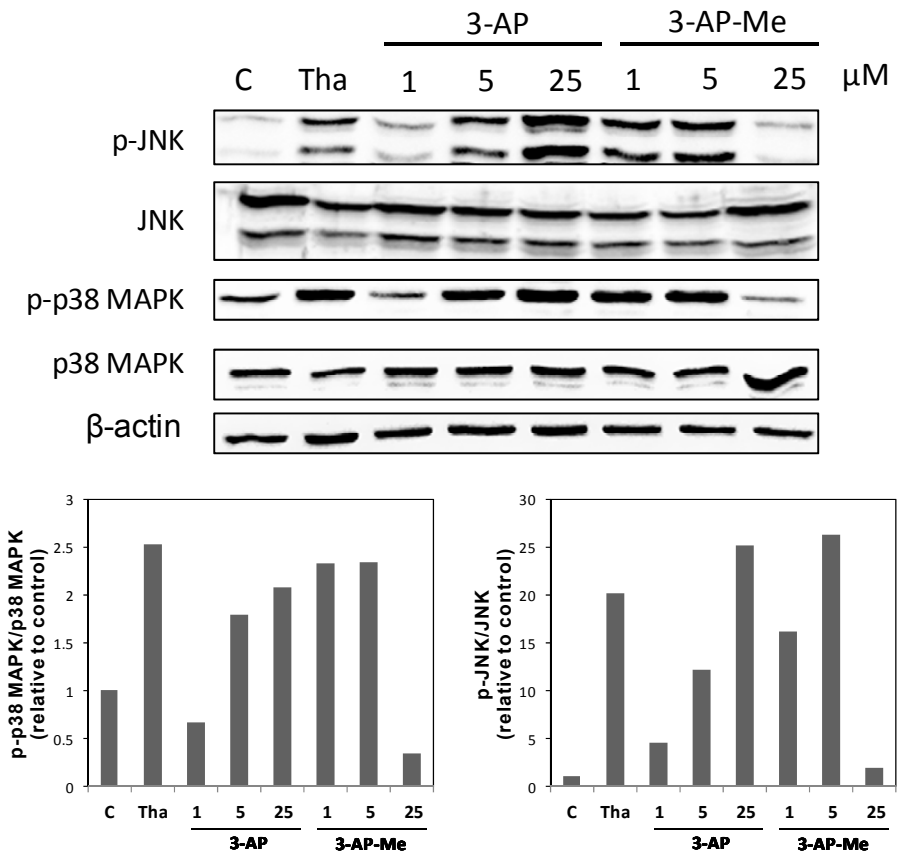

Fig 5: Activation of JNK and p38-MAPK pathway by 3-AP and 3-AP-Me. Western blot analysis of JNK and p38 MAPK phosphorylation in SW480 cells after 12 hour treatment. Cells were treated with 1, 5, 25 μM of 3-AP or 3-AP-Me. Thapsigargin (0.5 μM) was used a positive control. Blots were analyzed with ImageJ software and relative ratios of phosphorylation to unphosphorylated form were calculated. Results shown are representatives out of three independent experiments.

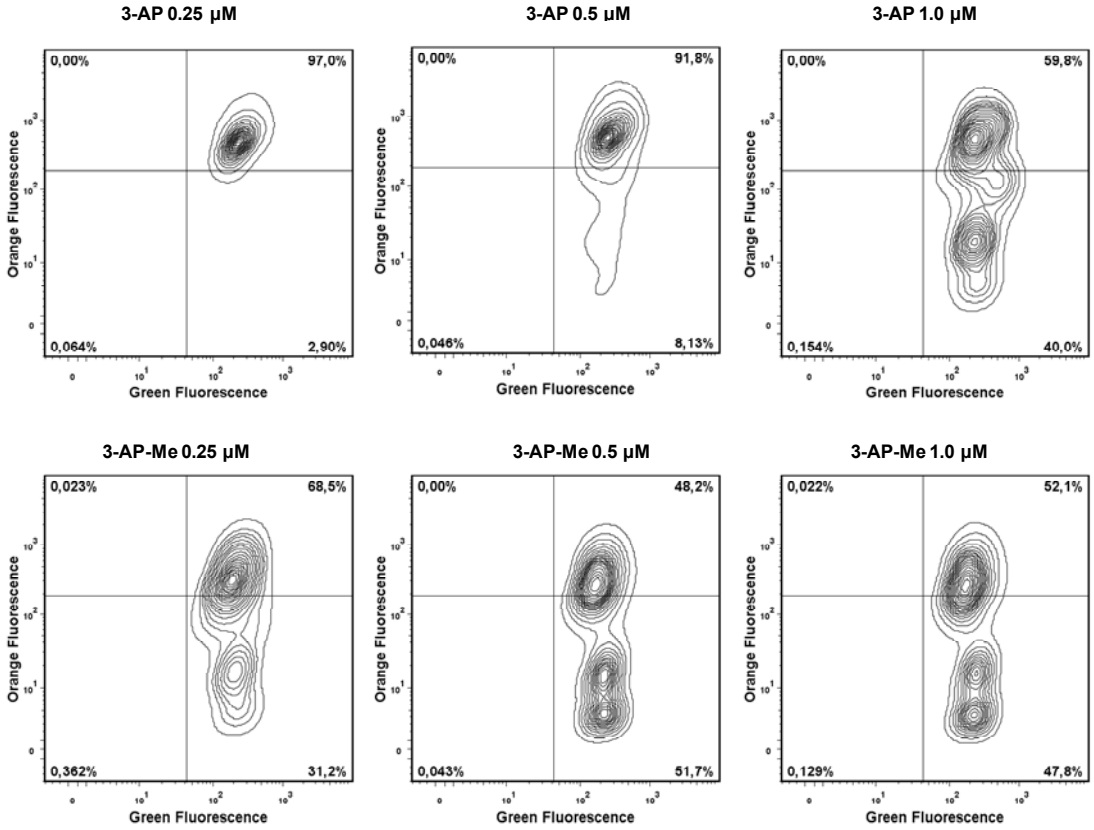

Fig.6: Depolarization of mitochondria membranes by 3-AP and 3-AP-Me was detected by flow cytometry analysis upon JC-1 staining. JC-1 forms aggregates (orange fluorescence) under normal membrane potential, while in depolarized mitochondrial membranes JC-1 dissociates to monomers (green fluorescence). HL-60 leukemia cells were treated with 0.25, 0.5 or 1 µM 3-AP or 3-AP-Me for 24 hours. For contour plot of untreated control see supplementary information. Results shown are representatives out of three independent experiments.

2.2 NKP-1339, the first ruthenium-based anticancer drug on the edge to clinical application

Robert Trondl, Petra Heffeter, Christian R. Kowol, Michael A. Jakupec, Walter Berger and Bernhard B. Keppler

Chemical Science **2012,** manuscript in preparation

NKP-1339, the first ruthenium-based anticancer drug on the edge to clinical application

Robert Trondl,[a,d] Petra Heffeter,[b,c,d] Christian R. Kowol,[a,c] Michael A. Jakupec,[a,c] Walter Berger[b,c] and Berhard B. Keppler*[a,c]

[a]Institute of Inorganic Chemistry, University of Vienna, Waehringer Str. 42, A-1090 Vienna, Austria; Tel: +43 1 4277 52600; E-mail: berhard.keppler@univie.ac.at

[b]Institute of Cancer Research, Medical University of Vienna, Borschkegasse 8a, A-1090 Vienna

[c]University of Vienna, Research Platform Translational Cancer Therapy Research, Waehringer Str. 42, A-1090 Vienna, Austria

[d] These authors contributed equally to this work

Ruthenium compounds are the most promising non-platinum metal drugs which are in clinical development against solid cancer. Such, NKP-1339 (the sodium salt of indazolium *trans*-[tetrachloridobis(1H-indazole)ruthenate(III); KP1019) is currently tested successfully in phase I clinical trials. Ruthenium compounds such as KP1019 and NKP-1339 have a high tumour targeting potential based 1) on their strong binding to serum proteins like albumin and transferrin as well as 2) on the activation in the reductive tumour milieu. The redox activity of ruthenium compounds is also dominant in their mode of action underlying their anticancer activity leading to disturbance of the cellular redox balance and consequently induction of G_2/M arrest, blockage of DNA synthesis and induction of apoptosis via the mitochondrial pathway. Moreover, a potent synergistic activity of NKP-1339 together with clinically approved tyrosine kinase inhibitor sorafenib against human hepatoma cell lines was recently discovered. Taken together, KP1019 and NKP-1339 are very promising drug candidates and especially the very limited side effects observed so far in clinical phase I trials, seems to be on major advantage of these ruthenium drugs.

A genealogy of antitumour ruthenium compounds

The idea of studying ruthenium compounds as antitumour agents was originally inspired by the observations that certain ruthenium compounds preferentially localize in tumour tissue (reviewed by ref. 4). Additionally, *fac*-[$Ru^{III}Cl_3(NH_3)_3$] and [$Ru^{II}Cl_2(DMSO)_4$]) were found to force the filamentous growth of *Escherichia coli* by inhibition of cell division – an unusual test model, but repeatedly applied at that time[1,2]. Subsequent investigations on a panel of ruthenium complexes with different numbers of ammine ligands, revealed *fac*-[$Ru^{III}Cl_3(NH_3)_3$] as most efficacious against EMT-6 sarcoma in mice[3, 4]. However, *fac*-[$Ru^{III}Cl_3(NH_3)_3$] was considered unsuitable for further clinical evaluation due to its poor aqueous solubility[5]. Consequently, subsequent efforts focused on ionic complexes (in particular anionic species with a higher number of halide ligands) with better solubility (Fig. 1).

A lead structure was found in the imidazole-containing complex ICR (KP418), imidazolium *trans*-[tetrachloridobis(1*H*-imidazole)ruthenate(III)] which proved therapeutic activity against murine P388 leukaemia and B16 melanoma[6]. Moreover, KP418 showed significant reduction of tumour burden in rats with autochthonous, chemically induced colorectal cancer[7], a model, which closely resembles colorectal cancer in patients regarding histopathology, malignant progression, and chemosensitivity pattern.

Subsequent studies on a large number of analogues lead to the discovery of the indazole derivative KP1019 (indazolium *trans*-[tetrachloridobis(1H-indazole)ruthenate(III)], which was found to be superior in its activity against this cancer model. In these studies, KP1019 treatment yielded efficacy with up to 90% reduction of tumour volume as well as up to two thirds reduction in tumour number without severe side effects and, such, was found to be superior to 5-fluorouracil, the standard agent against colorectal cancer[8]. Based on this promising activity, KP1019 was selected for further (pre)clinical evaluations.

Besides inspiring the development of KP1019, KP418 had also a decisive impact on the field of DMSO-containing ruthenium complexes (pursued by Sava and co-workers) resulting in the synthesis of the imidazolium *trans*-[tetrachlorido(1*H*-imidazole)(*S*-dimethyl sulfoxide)ruthenate(III)] (NAMI-A)[9]. Notably, this ruthenium drug turned out, in contrast to

KP1019, to effect cancer metastasis rather than acting against the primary tumour side or already established metastases. The antimetastatic activity of NAMI-A is probably based on enhanced cell adhesion, integrin-dependent inhibition of cancer cell motility and invasiveness[10, 11] as well as on inhibition of neoangiogenesis in the tumour tissue[12]. Thus, despite their chemical relatedness, NAMI-A and KP1019 behave quite differently *in vitro* and *in vivo*[13] and, accordingly, they have been developed with completely different scopes and aims.

The most recent representative ruthenium compound is NKP-1339 (sodium *trans*-[tetrachloridobis(1*H*-indazole)ruthenate(III)], KP1339). It had originally been prepared as an precursor in the formulation of KP1019 for clinical testing[14]. Based on its higher water solubility, the sodium salt of KP1019, NKP-1339, has been selected as lead candidate for further clinical development. This decision not only facilitated manufacturing and handling for the clinical trials, but also allowed clinical application of larger drug doses to the patients. As many of the early findings relevant for the development of NKP-1339 were made with KP1019, the following sections will deal with both compounds.

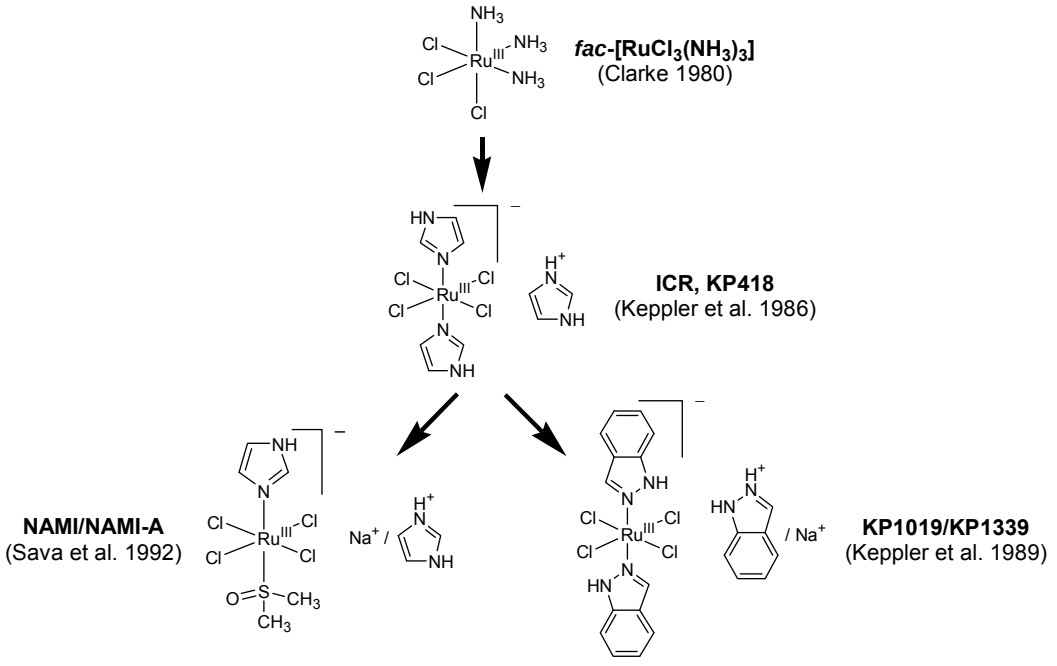

Fig. 1 Genealogy of tumour-inhibiting ruthenium complexes. References refer to the first published evidence for therapeutic activity of the compounds in an *in vivo* tumour model [5, 6, 8, 15, 16]. Both NAMI-A and NKP-1339 are currently subject of clinical evaluation.

Drug delivery through plasma proteins

KP1019 and NKP-1339 are administered intravenously, thus, the interaction of the complexes with serum proteins is of great relevance. Several studies show a strong affinity of KP1019 and NKP-1339 to proteins in the blood stream, in particular to albumin and transferrin[17, 18]. Accordingly, it has been suggested that these two proteins act as transport and delivery systems of the two ruthenium complexes and, thus, are essential for their tumour targeting. In general, both, transferrin as well as albumin, are considered as highly interesting carriers for drug delivery, however, the underlying mechanisms are different. The interest in the iron transport protein transferrin is based on the higher demand of tumours for iron and on the overexpression of the transferrin receptor (CD71), which is frequently observed in cancer cells. Consequently, it has been shown that tumour cells can be specifically targeted by drug binding to transferrin[18,19]. On the other hand, albumin has been shown to accumulate in malignant and inflamed tissues due to the combination of leaky blood capillaries with the absence/defect of lymphatic drainage, which is also called "enhanced permeability and retention **(**EPR) effect"[21]. Subsequently, degradation of albumin leads to release of the drug[22]. Recently, a detailed SEC-ICP/MS analysis on the protein-binding pattern of KP1019 in cell culture medium containing 10% fetal calf serum showed that the Ru complex is mainly bound to the albumin- and transferrin-containing protein fraction of 60-80 kDa[23] (Fig. 2a). This is in accordance to earlier studies on plasma of KP1019-treated patients, where ruthenium was also exclusively found in this fraction[18]. The detailed investigation of the binding of the ruthenium(III) drugs to transferrin was the aim of several *in vitro* studies. Such, the binding of KP1019 and apolactotransferrin was proven by X-ray crystal structure analysis, revealing that after binding via histidine-253 the two indazole ligands still remain bound to the ruthenium center[24]. Moreover, it was shown that the reaction of transferrin with KP1019 or NKP-1339 is quick and completed within several minutes[25]. In contrast, the formation of the transferrin adduct of the imidazole analogue KP418 (ICR) takes several hours[26].

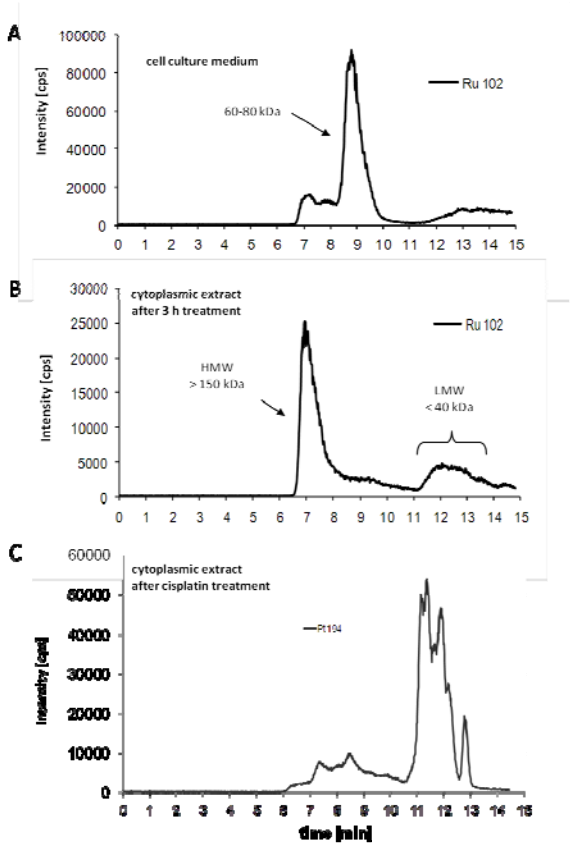

Fig. 2 Drug–protein binding patterns of KP1019. A) Size-exclusion chromatography SEC-ICP-MS determination of cell culture medium supplemented with fetal calf serum after 3 h of incubation with KP1019. B) Cytosolic fractions of KP1019-treated KB-3-1 cells were isolated after 3h treatment and protein-bound ruthenium was determined by SEC-ICP-MS. C) Cytosolic fractions of cisplatin-treated KB-3-1 cells were isolated after 3h treatment with 50 µM cisplatin and protein-bound platinum was determined by SEC-ICP-MS[23].

Uptake studies on human cancer cell lines are in good agreement with these data, showing a 10-fold lower uptake of KP418 than of KP1019[27]. Additionally, it was shown that the cellular uptake of KP1019 and NKP-1339 is very rapid and finished within the first hour of drug exposure[23]. Furthermore, co-incubation experiments with equimolar amounts of KP1019 and transferrin in the presence of a physiological iron concentration showed a >2,5-fold higher uptake of the ruthenium complex in the colon cancer cell line SW480. These experiments suggested that a certain amount of iron binding is needed for optimal ruthenium binding to transferrin.

As a consequence of the experimental focus on the transferrin-mediated transport and uptake of KP1019, the "Trojan Horse" hypothesis was developed. It describes a selective delivery of KP1019 into the malignant tissue via transferrin followed by cellular uptake via transferrin receptors. The receptor-mediated incorporation of transferrin is accomplished by endosomes, in which pH is lower (~5.5) than the pH value in the extracellular space (~7.4), and the drop of pH is, consequently, thought to trigger for the release of the ruthenium complex inside the cell.

Although it is widely accepted that the binding of KP1019/NKP-1339 to serum proteins is essential for their tumour targeting, recent analytical studies started a new discussion about the importance of transferrin in the drug delivery[28]. These studies showed that although adduct formation with transferrin is kinetically preferred, thermodynamically more stable adducts are formed with albumin[9]. Moreover, cell-free competition studies with equimolar concentrations of albumin and transferrin showed that less than 20% of KP1019 is bound to transferrin over 10 h incubation time. Taking into account that the albumin concentration in the bloodstream is ~15-fold higher than that of transferrin, the total amount of transferrin-bound KP1019 has to be expected to be less than 2%. In agreement with these results found in cell-free settings, SEC-ICP/MS analysis of blood samples taken from a patient of the clinical phase I trial of KP1019 showed that the ruthenium complex was preferably bound to albumin, while the amount of KP1019 bound to transferrin was not detectable[18].

All these observations raise the question, which role transferrin mediated uptake actually plays in the anti-tumour activity of KP1019/ NKP-1339 *in vivo*? Based on the above mentioned EPR effect, albumin itself might be sufficient as a KP1019/NKP-1339 carrier. Consequently, further studies are needed to clarify the function of albumin-bound ruthenium species and their role in drug delivery to the tumour tissue.

The activation-by-reduction hypothesis

Under physiological conditions, ruthenium mainly exists in two oxidation states, Ru(III) and Ru(II). In general, ruthenium complexes of the oxidation state +III are more inert toward ligand exchange reactions compared to ruthenium(II). Thus, the aquation process (replacement of

chlorido ligands by aqua ligands) is considerably accelerated upon reduction, resulting in "activated" species with higher reactivity toward biomolecules. In general, it has been shown that the ruthenium complexes are not reduced effectively while bound to serum proteins[25,26]. However, it is suggested that the compounds are activated by reduction after release from the protein. This activation process depends on the redox potential of the Ru(III)/Ru(II) oxidation states, which in turn strongly depends on the ligands coordinated to the ruthenium centre. Thus, the choice of ligands with suitable electron donor properties enables the tuning of the redox potential to obtain complexes which are redox active in the biological environment, such as KP1019 and NKP-1339[31, 32]. This redox activity in combination with the fact that Ru(II) complexes are more reactive than the corresponding Ru(III) compounds are considered suitable for exploiting the pathophysiological conditions of solid tumours. Insufficient vascularization and poor blood flow in tumour blood vessels frequently result in a lower oxygen partial pressure (hypoxia) in solid tumours as compared to normal tissues, which is paradoxically associated with poor prognosis in several malignancies. The latter can be explained by the constitutive upregulation of glycolysis in tumour cells, which allows them to tolerate hypoxic conditions and concomitant development of acid resistance[33]. Moreover, reducing conditions have to be expected also in malignancies of tissues with high endogenous amounts of the reducing agent and radical scavenger ascorbic acid (e.g. of the pancreas)[34]. Several observations with pentaammineruthenium(III) complexes prompted Clarke to propose what became known as the "activation-by-reduction" hypothesis[35]. Such, the reduction of Ru(III) to Ru(II) and the subsequent binding to heterocyclic nitrogen bases can be catalyzed by mitochondrial, microsomal, and soluble subcellular fractions of rat liver cells in the presence of succinate or NADH. Exposure to air markedly decreases the rate of this reaction, probably due to rapid re-oxidation to Ru(III). Based on the higher reactivity, reduction to Ru(II) accelerates coordination to potential target molecules. Thus, Ru(III) complexes may serve as prodrugs that are activated preferentially in the less oxygenated environment of solid tumours, while sparing normal tissues from toxic effects[36].

By analogy, this mechanism has been assumed to apply also to azole-containing Ru(III) complexes such as KP1019. The physiologically accessible redox potential window ranges from around –0.4 V (NADPH, the strongest physiological reductant[37]) to +0.8 V vs. NHE (dioxygen, the strongest physiological oxidant; NHE = normal hydrogen electrode) [38]. Electrochemical

investigations of NKP-1339 in phosphate buffer at pH 7 revealed a quasi-reversible reduction wave at +0.03 V vs. NHE (KP418 = –0.16 V vs. NHE)[39, 40]. These potentials suggest a possible activation by reduction in the biological environment. Nevertheless, it has to be kept in mind that any change in the coordination sphere of the complex prior to the reduction process can strongly alter the redox potential of the ruthenium(III) metal centre. Further support for the validity of the "activation-by-reduction" hypothesis has been provided by studies showing an increased cytotoxicity and DNA binding of KP418 under reduced oxygen pressure[41]. Also in case of KP1019, NMR experiments regarding the reduction of Ru(III) to Ru(II) in the presence of glutathione (GSH) and ascorbic acid showed a complete reduction under buffered conditions within 3.5 h and within minutes, respectively. Additionally, in accordance to the experiments on KP418, an increased binding to guanosine monophosphate (GMP) was found upon addition of two equivalents of GSH[40]. Also in studies of Bartel et al. a distinctly higher activity of KP1019 in cell culture experiments was observed in the presence of ascorbic acid at concentrations from 50 to 700 μM, which went again hand in hand with improved binding to biomolecules in cell culture as well as in cell-free systems[42].

However, it has to be mentioned that incubation of KP1019 with a 10-fold excess of GSH was shown to result in a decrease in GMP binding[40]. The decreased binding can possibly be explained by an inactivation of the complex via direct binding of GSH to the ruthenium centre[43]. This indicates also that GSH might play a role in resistance of cancer cells against KP1019 (Compare Section "Drug resistance). Thus, proper concentrations of the reductive agents seem to be important for the activation of KP1019 and NKP-1339.

Mechanisms underlying the anticancer activity

Based on the "activation by reduction" theory, it is not surprising that the mode of action underlying the anticancer activity of KP1019 and NKP-1339 seems to be tightly linked to their redox activity (Fig. 3). "Activation by reduction" results in the generation of reactive ruthenium(II) species of NKP-1339, which can be expected to react with diverse biomolecules such as proteins and nucleotides. Thus, the interaction of the ruthenium compounds with DNA has been repeatedly and extensively studied especially in cell-free settings[44-46].

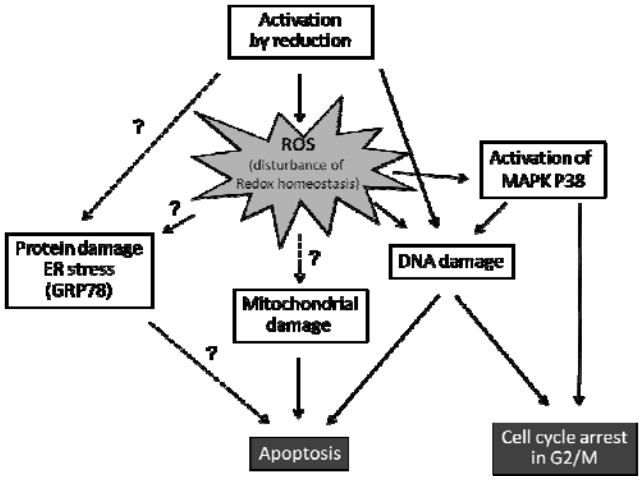

Fig. 3 Mechanisms underlying the anticancer activity of KP1019 and NKP-1339.

Although Ru has been detected in nuclei and bound to extracted DNA of cells after drug treatment, there is increasing evidence that the anticancer activity of KP1019 is not primarily based on direct DNA damage[23, 47, 35]. However, in contrast to DNA binding, the reaction of ruthenium compounds with intracellular proteins has been far less investigated. A recent study on the intracellular cytosolic protein-binding patterns of KP1019 and NKP-1339[23] showed that Ru-binding can be detected mainly in protein factions of two size classes: protein aggregates/complexes > 700 kDa and protein (complexes) < 40 kDa. Notably, this intracellular drug binding patterns strongly differed from those of cells exposed to cisplatin, which is found mainly in the fraction of low-molecular-weight proteins (Fig.2 b-c). Additionally, the glucose-regulated protein of 78 kDa (GRP78) was recently suggested as cytosolic target for NKP-1339[48]. GRP78 is a key factor of the unfolded protein response (UPR)[49], suggesting an interaction of NKP-1339 with the protein maintenance machinery of the cell.

Besides direct biomolecule damage/interactions, the redox activity of ruthenium(III) compounds can be expected to interfere with the cellular redox balance via direct as well as indirect mechanisms[50]. Such, ruthenium(III) compounds might participate in Fenton-like reactions leading to generation of reactive oxygen species (ROS). On the other hand, the reaction of ruthenium(III) drugs with GSH can be expected to induce depletion of the intracellular GSH

pools, which renders cells more susceptible to endogenous and exogenous oxidative stress. Indeed, formation of intracellular ROS as well as induction of ROS-mediated DNA damage was shown in human colon cancer cells after short-time KP1019 treatment[51]. Moreover, depletion of the intracellular GSH pools by pre-treatment with buthioninesulfoximine (BSO) led to increased sensitivity of cancer cells to KP1019[52], again arguing for the participation of ROS in the mechanism underlying anticancer activity of this drug.

Interestingly, NKP-1339 (as well as NAMI-A) has recently been identified as direct nitric oxide ($NO^{\bullet}$) scavenger[53]. Reaction with $NO^{\bullet}$ was shown to result in reduction of Ru(III) and formation of a [Ru(II)-NO^{+}] moiety. As $NO^{\bullet}$ is a known messenger for diverse physiological signalling processes, especially in vascular homeostasis and neurotransmission as well as inflammatory/immune response and tumour progression[54], this might suggest some effects of KP1019 and NKP-1339 on endothelial cell migration and angiogenesis.

As a consequence of this (redox) stress, treatment with KP1019 and NKP-1339 was shown to induce apoptosis of cancer cells via the mitochondrial pathway[52,26]. Recent studies indicated that NKP-1339 treatment (comparable to NAMI-A[55] but in contrast to KP418[56]) leads to cell cycle arrest in G2/M phase. Moreover, unpublished studies reveal a potent synergistic activity of NKP-1339 when combined with the multi-targeted tyrosine kinase inhibitor sorafenib (BAY 43-9006, Nexavar) against human hepatoma cell lines. Notably, synergistic activity with NKP-1339 was found in sorafenib-resistant as well as sorafenib-responsive cell lines (manuscript in preparation).

Drug resistance

The occurrence of drug resistance (either intrinsically or acquired during drug treatment) is one of the major obstacles for the treatment of cancer at the disseminated stage. The mechanisms which can lead to resistance are multiple and can involve basically all steps from reduced tumour delivery and cellular drug uptake to defects in apoptosis execution. Besides platinum drugs, the characterisation of relevant resistance mechanisms against metal compounds is still at a very early stage. In general, it has to be expected that the resistance mechanisms often reflect the mode of action of the respective anticancer drug. As already discussed above, GSH is one of the most important intracellular reductants, which is believed to be involved in the activation of ruthenium

compounds. Additionally, enhanced GSH levels are frequently associated with resistance against sulphur-affine compounds such as the platinum(II) drugs cis- or oxaliplatin. The impact of enhanced GSH levels on the anticancer activity of ruthenium compounds is still not fully understood. As already discussed above, presence of GSH leads to reduction of the ruthenium centre and, thus, drug activation. However, high concentrations of GSH were show to interfere with the DNA binding activities of KP1019[40], and depletion of intracellular GSH pools led to increased sensitivity against KP1019[52]. Correspondingly, pre-treatment with the radical scavenger and precursor of GSH, N-acetylcysteine, protected human colon carcinoma cells for the anticancer activity of KP1019[51] also indicating that activation by reduction is only observed at ideal reductant concentrations and that at higher GSH levels the complex is inactivated via GSH-conjugation.

On the other hand, it has to be kept in mind that studies on the cisplatin-resistant cell models (O-342/DPP and A2780cis) revealed that these cells, which are displaying enhanced GSH levels are not cross-resistant *in vitro* and *in vivo* against several Ru(III) drugs[57, 58]. Additionally and in contrast to observations with cisplatin, no reduction of GSH levels was observed in rat kidney cells after treatment of animals with KP1019[59]. Taken together, this suggests that, in contrast to platinum drugs, the anticancer activity of ruthenium compounds might be at least less susceptible to enhanced cellular GSH levels, which is probably due to the consumption of GSH during the "activation by reduction" process.

Another well described mechanism which is frequently involved in drug resistance is the overexpression of ATP-driven efflux proteins, especially ABC transporters. The family of ABC transporter proteins is large but only a few of its family members (such as several ABCCs, ABCB1 and ABCG2) have been associated with drug resistance. We have recently studied the impact of these transport proteins on the anticancer activity of KP1019[60]. In this study, it was discovered that ABCC1 (multidrug-resistance protein 1, MRP1) expression had no impact on the anticancer activity of KP1019[60]. This is especially of interest as most ABCC family members have a strong substrate affinity for GSH conjugates. In contrast to ABCC1, several ABCB1 (P-glycoprotein, P-gp)-overexpressing cell lines showed weak resistance (about 2-fold) to KP1019 based on reduced drug accumulation, compared to > 100 fold resistance of common P-gp

substrates (e.g. doxorubicin). Notably, the interaction of KP1019 with ABCB1 strongly dependents on the serum protein levels, indicating that the strong binding to serum proteins might protect KP1019 from export by ABCB1. This is in accordance to studies with the high affinity ABCB1 substrate doxorubicin, where conjugation to the iron transport protein transferrin was able to circumvent efflux by ABCB1 and, consequently, to enhance cytotoxic activity against ABCB1-overexpressing cells[19, 20].

To investigate a possible acquired resistance to KP1019, KB-3-1 cells were selected by exposure to stepwise increasing concentrations of KP1019. Notably, this resulted only in a 2-fold resistance to KP1019[60], which was not based on reduced drug accumulation and ABC transporter overexpression. The mechanism underlying KP1019 resistance is still under investigation. Recent studies using comparative genomic hybridization revealed that KP1019-resistant KB-3-1 cells are characterized by several chromosome losses including chromosome 5, 7q, 12, 13q and 16q in comparison to their parental cell line (unpublished results). Moreover, no gene amplification was observed indicating that the acquired resistance of this cell line is probably supported by gene loss and/or regulated by epigenetic mechanisms.

Evaluation in clinical studies

Both, KP1019 and NKP-1339, belong to the few ruthenium compounds, which have been already evaluated in clinical studies[61, 62, 48]. In fact, the antimetastatic drug NAMI-A is the only other ruthenium compound studied in a phase I trial[63]. In the case of KP1019 an open-label flat-dose escalation trial was performed in patients with advanced solid tumours without further therapeutic options[62]. Eight patients were accrued receiving intravenous KP1019 doses from 25 to 600 mg twice weekly over three weeks. The pharmacokinetic analysis suggested that in accordance to previous observations in vitro the drug is rapidly bound to plasma proteins and has a long half-life (about 69-284 h). Clearance and the volume of distribution were low, and the AUC (area under the curve) and C_{max} increased dose-proportionally. Notably, KP1019 and NKP-1339 were extremely well tolerated with only very limited side effects and accordingly the maximum tolerated dose was not reached (dose escalation had to be stopped because of the high infusion volume required for solubility reasons). This is in contrast to the study regarding NAMI-

A, where painful blister formation at hands, fingers, and toes was considered as the dose-limiting toxicity[63].

Despite this dose limitation, five of six evaluable patients showed disease stabilization for eight to ten weeks. Interestingly, this clinical effect was not strictly depending on the applied dose. Consequently, the study suggested a 400–600 mg flat dose regimen for a phase II study with a longer application time (10 weeks), based on data derived from preclinical animal models and the observation of long-lasting stable diseases.

In order to avoid dose limitation by the high infusion volume, the clinical development was recently changed to the better soluble NKP-1339, which allows the application of higher doses. The respective phase I study is almost completed, and the interims data were presented at the ASCO meeting 2011[48]. Very minor side effects have been observed so far, and dose escalation is ongoing. NKP-1339 was administered as 30-90 minute infusion (based on volume to be infused) on days 1, 8, and 15 of a 28 day cycle. A total of 32 patients with various solid tumours have been treated so far at 9 different dose levels (20, 40, 80, 160, 320, 420, 500, 625 and 780 mg/m^2 body weight). At higher doses a transient green discoloration of the plasma without other clinical symptoms like jaundice was observed. Unrelated to this phenomenon, only grade 1-2 pyrexia and/or rigors were observed so far in some patients, which were prevented in subsequent patients by steroid-based premedication. Also for NKP-1339, preliminary pharmacokinetic analyses indicated dose proportionality of C_{max} and AUC, suggesting linear pharmacokinetics. Interestingly, two patients with stage IV neuroendocrine tumours, one patient with gastrinoma and two patients with non-small cell lung cancer (NSCLC) have experienced stable disease for up to 20 cycles so far. As also in case of NAMI-A the one patient (out of 24), which suffered from NSCLC[63], experienced stable disease, these data might indicate enhanced sensitivity of NSCLC against ruthenium compounds.

Conclusions

Until now platinum is the only metal, which plays an important role in clinical treatment of various cancer types. However, research work in the field of ruthenium-based anticancer drugs, in fact progressing over the last 20 years, is now entering the crucial phase towards clinical

application. The tremendous efforts on the characterization of the chemical and biological properties of ruthenium-based drugs made clear that ruthenium compounds are not just platinum analogues. Several key studies elucidated that ruthenium-based complexes exhibit different mechanisms of accumulation, uptake, activation and mode of action within the cell, compared to platinum drugs. Besides the promising anticancer activities in heavily pre-treated patients, especially the very limited adverse effects observed so far in clinical phase I trials of KP1019 and NKP-1339 are a major advantage in comparison to other anticancer metal drugs. Beside low general toxicity, tumour selectivity and the development of predictive biomarkers are the most important criteria for successful clinical approval. Therefore gain of a deeper insight into the interactions on NKP-1339 with target molecules within the cancer cell will be one of the main challenges for further investigations.

References

1 C. Monti-Bragadin, L. Ramani, L. Samer, G. Mestroni, and G. Zassinovich, *Antimicrobial agents and chemotherapy*, 1975, 7, 825-7.

2 J. R. Durig, J. Danneman, W. D. Behnke, and E. E. Mercer, *Chemico-Biological Interactions*, 1976, 13, 287-294.

3 M. J. Clarke, S. Bitler, D. Rennert, M. Buchbinder, and A. D. Kelman, *Journal of inorganic biochemistry*, 1980, 12, 79-87.

4 S. C. Srivastava, L. F. Mausner, and M. J. Clarke, *Progress in Clinical Biochemistry and Medicine*, 1989, 10, 111-149.

5 M. J. Clarke, *Metal Ions in Biological Systems*, 1980, 11, 231-283.

6 B. K. Keppler and W. Rupp, *Journal of Cancer Research and Clinical Oncology*, 1986, 111, 166-168.

7 F. T. Garzon, M. R. Berger, B. K. Keppler, and D. Schmaehl, *Cancer Chemotherapy and Pharmacology*, 1987, 19, 347-349.

8 B. K. Keppler, M. Henn, U. M. Juhl, M. R. Berger, R. Niebl, and F. E. Wagner, *Progress in Clinical Biochemistry and Medicine*, 1989, 10, 41-69.

9 I. Bratsos, T. Gianferrara, E. Alessio, C. G. Hartinger, M. A. Jakupec, and B. K. Keppler, in *Bioinorganic Medicinal Chemistry*, Wiley Online Library, 2011, p. 151.

10 G. Sava, F. Frausin, M. Cocchietto, F. Vita, E. Podda, P. Spessotto, A. Furlani, V. Scarcia, and G. Zabucchi, *European journal of cancer*, 2004, 40, 1383-96.

11 F. Frausin, V. Scarcia, M. Cocchietto, A. Furlani, B. Serli, E. Alessio, and G. Sava, *Journal of Pharmacology and Experimental Therapeutics*, 2005, 313, 227-233.

12 A. Vacca, M. Bruno, A. Boccarelli, M. Coluccia, D. Ribatti, A. Bergamo, S. Garbisa, L. Sartor, and G. Sava, *British Journal of Cancer*, 2002, 86, 993-998.

13 A. Bergamo, A. Masi, M. A. Jakupec, B. K. Keppler, and G. Sava, *Metal-based drugs*, 2009, 2009, 681270.

14 W. Peti, T. Pieper, M. Sommer, B. K. Keppler, and G. Giester, *European Journal of Inorganic Chemistry*, 1999, 1999, 1551-1555.

15 A. Bergamo, C. Gaiddon, J. H. M. Schellens, J. H. Beijnen, and G. Sava, *Journal of Inorganic Biochemistry*, 2011.

16 G. Sava, S. Pacor, G. Mestroni, and E. Alessio, *Clinical & Experimental Metastasis*, 1992, 10, 273-280.

17 F. Kratz, B. K. Keppler, M. Hartmann, L. Messori, and M. R. Berger, *Metal-based drugs*, 1996, 3, 15-23.

18 M. Sulyok, S. Hann, C. G. Hartinger, B. K. Keppler, G. Stingeder, and G. Koellensperger, *Journal of Analytical Atomic Spectrometry*, 2005, 20, 856.

19 M. Fritzer, K. Barabas, V. Szuts, A. Berczi, T. Szekeres, W. P. Faulk, and H. Goldenberg, *International journal of cancer. Journal international du cancer*, 1992, 52, 619-623.

20 M. Fritzer, T. Szekeres, V. Szuets, H. N. Jarayam, and H. Goldenberg, *Biochemical Pharmacology*, 1996, 51, 489-493.

21 H. Maeda, J. Wu, T. Sawa, Y. Matsumura, and K. Hori, *Journal of Controlled Release*, 2000, 65, 271-284.

22 F. Kratz, *Journal of controlled release*, 2008, 132, 171-83.

23 P. Heffeter, K. Böck, B. Atil, M. A. Reza Hoda, W. Körner, C. Bartel, U. Jungwirth, B. K. Keppler, M. Micksche, W. Berger, and G. Koellensperger, *Journal of biological inorganic chemistry*, 2010, 15, 737-48.

24 C. A. Smith, A. J. Sutherland-Smith, F. Kratz, E. N. Baker, and B. H. Keppler, *Journal of Biological Inorganic Chemistry*, 1996, 1, 424-431.

25 A. R. Timerbaev, A. V. Rudnev, O. Semenova, C. G. Hartinger, and B. K. Keppler, *Analytical biochemistry*, 2005, 341, 326-33.

26 F. Kratz, M. Hartmann, B. Keppler, and L. Messori, *The Journal of biological chemistry*, 1994, 269, 2581-8.

27 S. Kapitza, M. Pongratz, M. A. Jakupec, P. Heffeter, W. Berger, L. Lackinger, B. K. Keppler, and B. Marian, *Journal of cancer research and clinical oncology*, 2005, 131, 101-10.

28 A. K. Bytzek, K. Boeck, G. Hermann, S. Hann, B. K. Keppler, C. G. Hartinger, and G. Koellensperger, *Metallomics*, 2011, 3, 1049-55.

29 F. Piccioli, S. Sabatini, L. Messori, P. Orioli, C. G. Hartinger, and B. K. Keppler, *Journal of inorganic biochemistry*, 2004, 98, 1135-42.

30 A. R. Timerbaev, L. S. Foteeva, A. V. Rudnev, J. K. Abramski, K. Połeć-Pawlak, C. G. Hartinger, M. Jarosz, and B. K. Keppler, *Electrophoresis*, 2007, 28, 2235-40.

31 M. A. Jakupec, E. Reisner, A. Eichinger, M. Pongratz, V. B. Arion, M. Galanski, C. G. Hartinger, and B. K. Keppler, *Journal of medicinal chemistry*, 2005, 48, 2831-7.

32 E. Reisner, V. B. Arion, B. K. Keppler, and A. J. L. Pombeiro, *Inorganica Chimica Acta*, 2008, 361, 1569-1583.

33 R. A. Gatenby and R. J. Gillies, *Nature Reviews Cancer*, 2004, 4, 891-899.

34 S. Brown, M. Georgatos, C. Reifel, J. H. Song, S. H. Shin, and M. Hong, *Endocrine*, 2002, 18, 91-6.

35 M. J. Clarke, *Coordination Chemistry Reviews*, 2003, 236, 209-233.

36 A. D. Kelman, M. J. Clarke, S. D. Edmonds, and H. J. Peresie, *Journal of Clinical Hematology and Oncology*, 1977, 7, 274-288.

37 F. Q. Schafer and G. R. Buettner, *Free Radical Biology and Medicine*, 2001, 30, 1191-1212.

38 C. S. Sevier and C. A. Kaiser, *Nature reviews. Molecular cell biology*, 2002, 3, 836-47.

39 E. Reisner, V. B. Arion, M. F. C. Guedes da Silva, R. Lichtenecker, A. Eichinger, B. K. Keppler, V. Y. Kukushkin, and A. J. L. Pombeiro, *Inorganic chemistry*, 2004, 43, 7083-93.

40 P. Schluga, C. G. Hartinger, A. Egger, E. Reisner, M. Galanski, M. a Jakupec, and B. K. Keppler, *Dalton transactions*, 2006, 1796-802.

41 D. Frasca, J. Ciampa, J. Emerson, R. S. Umans, and M. J. Clarke, *Metal-Based Drugs*, 1996, 3, 197-209.

42 C. Bartel, A. E. Egger, M. A. Jakupec, P. Heffeter, M. Galanski, W. Berger, and B. K. Keppler, *Journal of Biological Inorganic Chemistry*, 2011, 16, 1205-15.

43 D. R. Frasca and M. J. Clarke, *Journal of the American Chemical Society*, 1999, 121, 8523-8532.

44 M. Groessl, Y. O. Tsybin, C. G. Hartinger, B. K. Keppler, and P. J. Dyson, *Journal of biological inorganic chemistry*, 2010, 15, 677-88.

45 A. Küng, T. Pieper, R. Wissiack, E. Rosenberg, and B. K. Keppler, *Journal of Biological Inorganic Chemistry*, 2001, 6, 292-299.

46 A. Egger, V. B. Arion, E. Reisner, B. Cebrián-Losantos, S. Shova, G. Trettenhahn, and B. K. Keppler, *Inorganic chemistry*, 2005, 44, 122-32.

47 M. J. Clarke, F. Zhu, and D. R. Frasca, *Chemical Reviews*, 1999, 99, 2511-2533.

48 N. R. Dickson, S. F. Jones, H. A. Burris, R. K. Ramanathan, G. J. Weiss, J. R. Infante, J. C. Bendell, W. McCulloch, and D. D. Von Hoff, *J Clin Oncol (ASCO Abstracts 2011)*, 2011, 2607.

49 M. Ni, Y. Zhang, and A. S. Lee, *The Biochemical journal*, 2011, 434, 181-8.

50 U. Jungwirth, C. R. Kowol, B. K. Keppler, C. G. Hartinger, W. Berger, and P. Heffeter, *Antioxidants & redox signaling*, 2011, 15, 1085-127.

51 S. Kapitza, M. A. Jakupec, M. Uhl, B. K. Keppler, and B. Marian, *Cancer letters*, 2005, 226, 115-21.

52 P. Heffeter, U. Jungwirth, M. Jakupec, C. Hartinger, M. Galanski, L. Elbling, M. Micksche, B. Keppler, and W. Berger, *Drug resistance updates*, 2008, 11, 1-16.

53 L. Morbidelli, S. Donnini, S. Filippi, L. Messori, F. Piccioli, P. Orioli, G. Sava, and M. Ziche, *British journal of cancer*, 2003, 88, 1484-91.

54 A. Bencini, P. Failli, B. Valtancoli, and D. Bani, *Cardiovascular & hematological agents in medicinal chemistry*, 2010, 8, 128-146.

55 A. Bergamo, S. Zorzet, M. Cocchietto, M. E. Carotenuto, M. Magnarin, and G. Sava, *Anticancer Research*, 2001, 21, 1893-1898.

56 S. Zorzet, A. Bergamo, M. Cocchietto, A. Sorc, B. Gava, E. Alessio, E. Iengo, and G. Sava, *Journal of Pharmacology and Experimental Therapeutics*, 2000, 295, 927-933.

57 S. Frühauf and W. J. Zeller, *Cancer research*, 1991, 51, 2943-8.

58 S. Fruehauf and W. J. Zeller, *Cancer Chemotherapy and Pharmacology*, 1991, 27, 301-307.

59 L. Kersten, H. Bräunlich, B. K. Keppler, C. Gliesing, M. Wendelin, and J. Westphal, *Journal of applied toxicology*, 1998, 18, 93-101.

60 P. Heffeter, M. Pongratz, E. Steiner, P. Chiba, M. A. Jakupec, L. Elbling, B. Marian, W. Körner, F. Sevelda, M. Micksche, B. K. Keppler, and W. Berger, *The Journal of pharmacology and experimental therapeutics*, 2005, 312, 281-9.

61 F. Lentz, A. Drescher, A. Lindauer, M. Henke, R. a Hilger, C. G. Hartinger, M. E. Scheulen, C. Dittrich, B. K. Keppler, and U. Jaehde, *Anti-cancer drugs*, 2009, 20, 97-103.

62 C. G. Hartinger, M. A. Jakupec, S. Zorbas-Seifried, M. Groessl, A. Egger, W. Berger, H. Zorbas, P. J. Dyson, and B. K. Keppler, *Chemistry & Biodiversity*, 2008, 5, 2140-55.

63 J. M. Rademaker-Lakhai, D. B. Van Desiree, D. Pluim, J. H. Beijnen, and J. H. M. Schellens, *Clinical Cancer Research*, 2004, 10, 3717-3727.

2.3 Impact of metal coordination on cytotoxicity of 3-aminopyridine-2-carboxaldehyde thiosemicarbazone (triapine) and novel insights into terminal dimethylation

Christian R Kowol, Robert Trondl, Petra Heffeter, Vladimir B Arion, Michael A Jakupec, Alexander Roller, Markus Galanski, Walter Berger, Bernhard K Keppler

Journal of Medicinal Chemistry **2009** 52:16.5032-5043

5032 J. Med. Chem. 2009, 52, 5032–5043
DOI: 10.1021/jm900528d

Journal of Medicinal Chemistry Article

Impact of Metal Coordination on Cytotoxicity of 3-Aminopyridine-2-carboxaldehyde Thiosemicarbazone (Triapine) and Novel Insights into Terminal Dimethylation

Christian R. Kowol,[†] Robert Trondl,[†] Petra Heffeter,[‡] Vladimir B. Arion,*[,†] Michael A. Jakupec,[†] Alexander Roller,[†] Markus Galanski,[†] Walter Berger,[‡] and Bernhard K. Keppler*[,†]

[†]*University of Vienna, Institute of Inorganic Chemistry, Währinger Strasse 42, A-1090 Vienna, Austria, and* [‡]*Department of Medicine I, Institute of Cancer Research, Medical University of Vienna, Borschkegasse 8a, A-1090 Vienna, Austria*

Received April 24, 2009

The first metal complexes of 3-aminopyridine-2-carboxaldehyde thiosemicarbazone (Triapine) were synthesized. Triapine was prepared by a novel three-step procedure in 64% overall yield. In addition, a series of related ligands, namely, 2-formylpyridine thiosemicarbazone, 2-acetylpyridine thiosemicarbazone, 2-pyridineformamide thiosemicarbazone, and their N^4-dimethylated derivatives (including the N^4-dimethylated analogue of Triapine) were prepared, along with their corresponding gallium(III) and iron(III) complexes with the general formula $[M(L)_2]^+$, where HL is the respective thiosemicarbazone. The compounds were characterized by elemental analysis, ^{1}H and ^{13}C NMR, IR and UV−vis spectroscopies, mass spectrometry, and cyclic voltammetry. In addition, Triapine and its iron(III) and gallium(III) complexes were studied by X-ray crystallography. All ligands and complexes were tested for their in vitro antiproliferative activity in two human cancer cell lines (41M and SK-BR-3), and structure−activity relationships were established. In general, the coordination to gallium(III) increased the cytotoxicity while the iron(III) complexes show reduced cytotoxic activity compared to the metal-free thiosemicarbazones. Selected compounds were investigated for the capacity of inhibiting ribonucleotide reductase by incorporation of ^{3}H-cytidine into DNA.

Introduction

Thiosemicarbazones are versatile ligands, as they adopt various binding modes with transition and main group metal ions.[1] They can act as mono- or bidentate ligands,[2] and their coordination capacity can be further increased, if aldehydes or ketones which contain additional functional group(s) in position(s) suitable for chelation are used for their preparation.[3,4] Besides their exciting coordination chemistry, thiosemicarbazones are known to possess a wide range of pharmaceutical properties such as antitumor, antiviral, antifungal, antibacterial, and antimalarial activity.[5] In addition, ^{64}Cu-bis(thiosemicarbazonate) complexes are under investigation as hypoxia-selective positron emission tomography tracers.[6] The first thiosemicarbazone with antitumor properties, namely, 2-formylpyridine thiosemicarbazone, was reported about 50 years ago.[7] Further studies showed that a prerequisite for biological activity is a nitrogen heterocycle that contains a suitable functional group for condensation with thiosemicarbazide derivatives at the α-position.[8] 5-Hydroxy-2-formylpyridine thiosemicarbazone (5-HP) was the first compound of this series that entered phase I clinical trials. However, 5-HP is rapidly transformed in the body and eliminated as an inactive glucuronide conjugate.[9,10] In addition, 5-HP showed severe hematological and gastrointestinal side effects that prevented its further clinical development. The currently most promising thiosemicarbazone as antitumor agent is 3-aminopyridine-2-carboxaldehyde thiosemicarbazone (Triapine[a]), which entered several phase I and phase II clinical trials.[11−15]

As the principal molecular target of α-N-heterocyclic thiosemicarbazones, the enzyme ribonucleotide reductase (RR) has been identified.[16−18] This enzyme catalyzes the conversion of ribonucleotides into deoxyribonucleotides, providing the precursors required for DNA synthesis and repair. α-N-Heterocyclic thiosemicarbazones are the most potent inhibitors of RR known so far. They are several orders of magnitude more effective than hydroxyurea, the first clinically applied RR inhibitor.[19] Faster proliferation of tumor cells compared to normal cells and therefore higher expression of RR make this enzyme a suitable and well established target in cancer chemotherapy.[20] The human RR consists of two homodimeric subunits: R1 and R2. The first subunit harbors the nucleotide binding site and the second subunit a diiron center and a tyrosyl radical. Transfer of the radical electron from tyrosine of R2 occurs by a proton-coupled mechanism via a chain of hydrogen-bonded amino acids over a distance of 35 Å to a cysteine of the R1 subunit, where it generates a thiyl radical essential for reduction of the substrates.[21] Recently, a second R2 subunit, called p53R2, has been identified in human cells with ∼80% sequence homology with R2 but with p53-dependent expression.[22] The p53 protein actively

*To whom correspondence should be addressed. For V.B.A.: phone, +431427752615; fax, +431427752680; e-mail, vladimir.arion@univie.ac.at. For B.K.K.: phone, +431427752600; fax, +431427752680; e-mail, bernhard.keppler@univie.ac.at.

[a] Abbreviations: Triapine, 3-amino-2-carboxaldehyde thiosemicarbazone; RR, ribonucleotide reductase; DFO, desferrioxamine; ROS, reactive oxygen species.

 Published on Web 07/28/2009

Scheme 1. Library of the Synthesized Compounds[a]

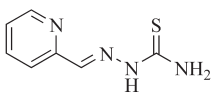

HL^{A}

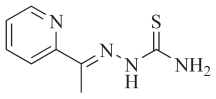

HL^{B}

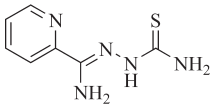

HL^{C}

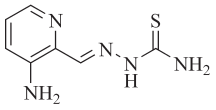

HL^{D}; Triapine

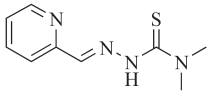

HL^{E}

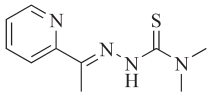

HL^{F}

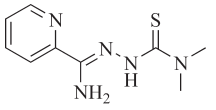

HL^{G}

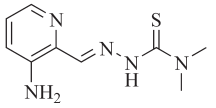

HL^{H}

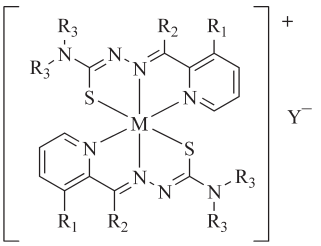

M = Ga, L = L^{A}, Y = NO_3; [Ga(L^{A})$_2$][NO_3] **(1A)**

M = Ga, L = L^{B}, Y = NO_3; [Ga(L^{B})$_2$][NO_3] **(1B)**

M = Ga, L = L^{C}, Y = NO_3; [Ga(L^{C})$_2$][NO_3] **(1C)**

M = Ga, L = L^{D}, Y = NO_3; [Ga(L^{D})$_2$][NO_3] **(1D)**

M = Ga, L = L^{E}, Y = PF_6; [Ga(L^{E})$_2$][PF_6] **(1E)**

M = Ga, L = L^{F}, Y = PF_6; [Ga(L^{F})$_2$][PF_6] **(1F)**

M = Ga, L = L^{G}, Y = NO_3; [Ga(L^{G})$_2$][NO_3] **(1G)**

M = Ga, L = L^{H}, Y = PF_6; [Ga(L^{H})$_2$][PF_6] **(1H)**

M = Fe, L = L^{A}, Y = NO_3; [Fe(L^{A})$_2$][NO_3] **(2A)**

M = Fe, L = L^{B}, Y = NO_3; [Fe(L^{B})$_2$][NO_3] **(2B)**

M = Fe, L = L^{C}, Y = NO_3; [Fe(L^{C})$_2$][NO_3] **(2C)**

M = Fe, L = L^{D}, Y = NO_3; [Fe(L^{D})$_2$][NO_3] **(2D)**

M = Fe, L = L^{E}, Y = PF_6; [Fe(L^{E})$_2$][PF_6] **(2E)**

M = Fe, L = L^{F}, Y = PF_6; [Fe(L^{F})$_2$][PF_6] **(2F)**

M = Fe, L = L^{G}, Y = NO_3; [Fe(L^{G})$_2$][NO_3] **(2G)**

M = Fe, L = L^{H}, Y = NO_3; [Fe(L^{H})$_2$][NO_3] **(2H)**

[a] Underlined species were studied by X-ray crystallography.

suppresses tumor formation, and the majority of human tumors have been found to contain mutations in p53 or defects in the pathways responsible for its activation.[23] Thus, the discovery of p53R2 revealed a link between the most important tumor suppressor and the synthesis of deoxyribonucleotides.

We reported previously that the gallium(III) complexes of N^4-disubstituted α-N-heterocyclic thiosemicarbazones (HL) with the composition $[Ga(L)_2]^+$ exhibit enhanced cytotoxicity in the low nanomolar range in human cancer cell lines. In contrast, the corresponding iron(III) complexes displayed a much lower cytotoxicity (in the micromolar range) than the metal-free ligands.[24] EPR measurements on isolated mouse R2 subunits of RR showed that the effects of the complexation to gallium(III) and iron(III) on the destruction of the R2 specific tyrosine free radical in the presence of the reductant dithiothreitol (DTT) are in the reverse order. The iron(III) complexes show the fastest destruction of the tyrosyl radical in RR, followed by the metal-free ligands and the corresponding gallium(III) complexes.[24] In the case of Triapine, iron also enhances radical quenching.[25] However, in contrast to N^4-dimethylated α-N-heterocyclic thiosemicarbazones, addition of iron(III) to Triapine results only in small changes in cytotoxicity.[26,27]

In order to evaluate the effect of complexation on the cytotoxicity of Triapine, the gallium(III) and iron(III) complexes were synthesized for the first time. For elucidation of further structure−activity relationships, a series of related ligands and their corresponding gallium(III) and iron(III) complexes were prepared (Scheme 1). In particular, the effects of the amino group and its position as well as the influence of N^4-disubstitution on cytotoxicity were investigated, including the Triapine analogue 3-aminopyridine-2-carboxaldehyde *N*^{4}-dimethylthiosemicarbazone. In addition, selected compounds were tested for their capacity of inhibiting ribonucleotide reductase by a ^{3}H-cytidine DNA incorporation assay.

Results and Discussion

Syntheses. The first reported synthesis of Triapine with an overall yield of 9% (six steps) started from 2-chloro-3-nitropyridine (Scheme S1; see Supporting Information).[28] An improved five-step synthesis[29] starting from the same material, via a Suzuki coupling in the first step, afforded 2-methyl-3-nitropyridine, which was further converted into an enamine intermediate. Oxidation of the latter led to 3-nitropyridine-2-carboxaldehyde, which was then reacted with thiosemicarbazide. In the final step the nitro derivative was reduced to Triapine in an overall yield of 55% (Scheme S2). The best overall yield of 64% was achieved in a four-step synthesis.[30] 3-Amino-2-chloropyridine was converted via a

Scheme 2. Novel Synthetic Pathway to Triapine ($\mathbf{HL^D}$)[a]

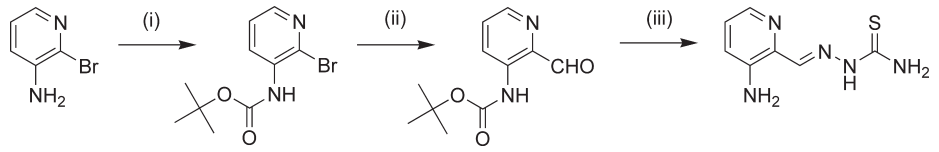

[a] Reagents and conditions: (i) sodium bis(trimethylsilyl)amide (~1 M/THF), $(Boc)_2O$, 82%; (ii) *n*-BuLi, *N*-formylpiperidine, 86%; (iii) thiosemicarbazide, conc HCl, $NaHCO_3$, 91%, overall yield 64%.

Heck reaction using styrene, followed by protection of the NH_2 group and then ozonolysis to the desired carboxaldehyde. The latter was transformed into Triapine by condensation with thiosemicarbazide and deprotection (Scheme S3). In this study, we developed a novel straightforward three-step synthesis of Triapine ($\mathbf{HL^D}$) in 64% overall yield, starting from the commercially available 3-amino-2-bromopyridine as shown in Scheme 2.

In the first step the amino group was protected with di-*tert*-butyl dicarbonate in dry THF, using sodium bis(trimethylsilyl)amide[31] as a base. Treatment of the *tert*-Boc protected 3-amino-2-bromopyridine with *n*-BuLi in dry THF resulted in the lithiated species, which was further reacted with *N*-formylpiperidine to give the carboxaldehyde.[32] Finally, the condensation reaction with thiosemicarbazide in ethanol in the presence of concentrated HCl afforded Triapine hydrochloride, which was converted into the free base ($\mathbf{HL^D}$) by treatment with sodium bicarbonate.[29] The Triapine analogue 3-aminopyridine-2-carboxaldehyde N^4-dimethylthiosemicarbazone ($\mathbf{HL^H}$) was prepared in 84% yield by using the same protocol. However, the conversion into the free base was performed by treatment of the hydrochloride with excess *N*-methylmorpholine.

The gallium(III) complexes $[Ga(L^A)_2]^+$ (**1A**) and $[Ga(L^D)_2]^+$ (**1D**) were prepared by reaction of $Ga(NO_3)_3 \cdot 9H_2O$ with the corresponding ligand ($\mathbf{HL^A}$ or $\mathbf{HL^D}$) in methanol in the presence of $NaOCH_3$ or triethylamine as a base in 27% and 72% yields, respectively (Scheme 1). The ^{1}H NMR spectra of these two complexes showed the presence of 0.5 and 0.15 equiv of methanol, correspondingly, in accord with the microanalytical data. Reaction of 2-acetylpyridine thiosemicarbazone ($\mathbf{HL^B}$) and 2-pyridineformamide thiosemicarbazone ($\mathbf{HL^C}$) with $Ga(NO_3)_3 \cdot 9H_2O$ in 2:1 molar ratio in ethanol in the absence of a base produced complexes **1B** and **1C** in 69% and 55% yields, respectively. The gallium complexes of the ligands $\mathbf{HL^E}$–$\mathbf{HL^H}$ were prepared in methanol or ethanol and isolated as nitrates or in some cases as hexafluorophosphates ($\mathbf{HL^F}$ and $\mathbf{HL^H}$) by addition of excess NH_4PF_6 to the reaction mixture (60–91% yield).[24] Starting from $Fe(NO_3)_3 \cdot 9H_2O$ and the ligands $\mathbf{HL^B}$ and $\mathbf{HL^D}$–$\mathbf{HL^H}$ in methanol or ethanol, the iron(III) complexes were obtained in 66–76% yield (**2E** and **2F** were isolated as hexafluorophosphates).[24] The synthesis of the iron(III) complexes of $\mathbf{HL^A}$ and $\mathbf{HL^C}$ was carried out in the presence of *N*-methylmorpholine because this was found to improve their purity.

Characterization. The positive ion ESI mass spectra of all complexes showed very strong peaks due to $[M(L)_2]^+$ ions. A peak with m/z 145, attributed to $[PF_6]^-$, was registered in the negative ion mode for the hexafluorophosphates. In line with the UV–vis spectra of gallium(III) complexes of 2-acetylpyridine thiosemicarbazones,[24] **1A**–**1H** display a strong absorption band centered between 389 and 411 nm associated with intraligand transitions. This band is split and shifted to lower energies for **1D** (441 and 459 nm) and **1H** (451 and 469 nm). In the case of iron(III) complexes, charge transfer bands, intraligand transitions, and a d–d band centered between 829 and 977 nm attributed to the $^2T_{2g} \rightarrow {}^2T_{1g}$ transition for the d^5 low-spin system were observed.[33] The ^{1}H NMR spectrum of the ligand $\mathbf{HL^H}$ in DMSO-d_6 indicates the presence of only one isomeric form in solution. In contrast, two and three isomers were found for $\mathbf{HL^E}$ and $\mathbf{HL^F}$ in DMSO-d_6.[34,35] Interestingly, a second isomer with chemical shifts at 9.18 (NH), 8.58 (py), 7.86 (py), 7.45 (py), 6.78 (NH_2), and 3.28 ($N(CH_3)_2$) ppm (one pyridine proton signal overlaps with a signal of the main species) and ~20% content relative to the main isomer was found for $\mathbf{HL^G}$ in DMSO-d_6, in contrast to the data reported.[36] The signal intensity of the minor species decreases with time, implying its conversion into the main isomeric form of the ligand. In contrast to the metal-free ligands, the gallium(III) complexes show only one set of signals in the ^{1}H NMR spectra, due to the stabilization of the ligand configuration upon coordination to the metal and the equivalence of both ligands bound to gallium(III) in solution. The most remarkable difference between the ^{1}H NMR spectra of the metal-free ligands and those of the gallium(III) complexes is the absence of the N–H proton signals of the thiosemicarbazide moiety in the latter, indicating deprotonation of the ligands upon coordination.

X-ray Crystallography. X-ray diffraction quality single crystals of Triapine ($\mathbf{HL^D}$) were obtained by slow evaporation of the sodium bicarbonate neutralized mother liquor. The result of the X-ray diffraction study of $\mathbf{HL^D}$ is shown in Figure 1a, along with its gallium(III) (**1D**) and iron(III) (**2D**) complexes (Figure 1b and Figure 1c). Selected bond distances and angles are quoted in the caption of Figure 1. $\mathbf{HL^D}$ crystallized in the orthorhombic space group $Pna2_1$ with two crystallographically independent molecules in the asymmetric unit. Both adopt the *E*-isomeric form in terms of the nomenclature used for the conformations of α-N-heterocyclic thiosemicarbazones,[37] unlike the X-ray crystal structure of $\mathbf{HL^E}$ with a *Z* conformation (see Supporting Information Figure S2). In the gallium(III) and iron(III) complexes of Triapine (**1D** and **2D**) the coordination polyhedron approaches an octahedron, where the two ligands coordinate to the metal via the pyridine nitrogen atom and the nitrogen and sulfur donors of the thiosemicarbazide moiety. Deprotonation of both ligands is accompanied by an elongation of the carbon–sulfur bonds [**1D**, 1.735(6) and 1.743(7) Å; **2D**, 1.754(5) and 1.750(5) Å] compared to that in the metal-free ligand $\mathbf{HL^D}$ at 1.697(2) Å.

Electrochemistry. In phase I and phase II clinical trials, patients treated with Triapine developed methemoglobinemia,[15,38] a disorder characterized by the presence of a higher than normal level of methemoglobin (metHb) in the blood. This side effect was ascribed to the redox activity of the iron complex of Triapine, although its electrochemical

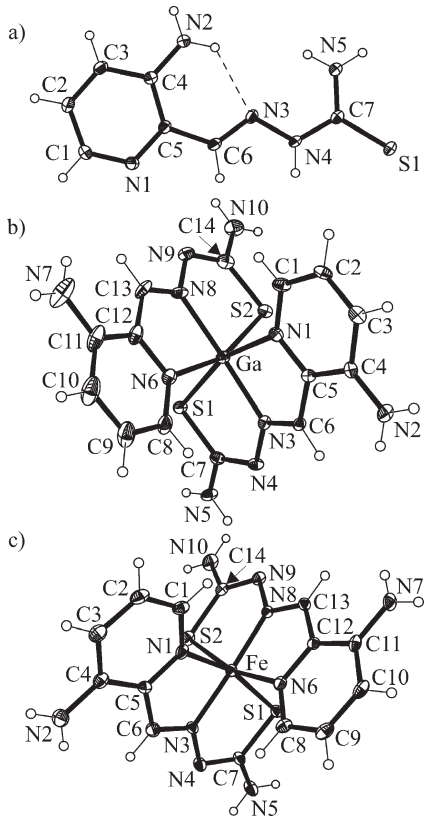

Figure 1. ORTEP plots of Triapine ($\mathbf{HL^D}$) (a), its gallium(III) complex (**1D**) (b), and iron(III) complex (**2D**) (c) with atom numbering schemes. The thermal ellipsoids are drawn at 50% ($\mathbf{HL^D}$ and **2D**) and 30% (**1D**) probability levels. Selected bond lengths (Å) and bond angles (deg) for $\mathbf{HL^D}$: C6−N3 1.283(2), N3−N4 1.384(2), N4−C7 1.344(2), C7−S1 1.697(2), C7−N5 1.325(3) Å; $\Theta_{(N2-C4-C5-C6)}$ 0.1(3)°, $\Theta_{(C5-C6-N3-N4)}$ 179.48(17)°, $\Theta_{(N3-N4-C7-S1)}$ 178.92(14)°. **1D**: Ga−N1 2.130(4), Ga−N6 2.110(5), Ga−N3 2.034(4), Ga−N8 2.040(5), Ga−S1 2.3722(14), Ga−S2 2.3563(16), C6−N3 1.301(6), C13−N8 1.279(7), N3−N4 1.362(6), N8−N9 1.379(7), N4−C7 1.339(7), N9−C14 1.332(8), C7−S1 1.735(6), C14−S2 1.743(7) Å; N1−Ga−N3 77.77(17)°, N6−Ga−N8 77.60(19)°, N3−Ga−S1 82.56(12)°, N8−Ga−S2 82.79(15)°. **2D**: Fe−N1 1.995(4), Fe−N6 2.011(4), Fe−N3 1.922(4), Fe−N8 1.925(4), Fe−S1 2.2302(13), Fe−S2 2.2171(14), C6−N3 1.299(6), C13−N8 1.299(6), N3−N4 1.379(5), N8−N9 1.379(5), N4−C7 1.318(6), N9−C14 1.323(6), C7−S1 1.754(5), C14−S2 1.750(5) Å; N1−Fe−N3 80.85(17)°, N6−Fe−N8 80.97(17)°, N3−Fe−S1 83.92(12)°, N8−Fe−S2 84.24(12)°.

Table 1. Electrochemical Data[a] for **1A**−**H** and **2A**−**H**

Gallium Complexes			
	$E_{1/2}/^{I}L^{red}$	$E_{1/2}/^{II}L^{red}$	$E_p/^{III}L^{red}$
1A	−0.82	−1.10	−1.63[b,c]
1B	−0.93	−1.21	−1.80[b,c]
1C	−1.21	−1.46	−2.02[b,c]
1D	−0.94	−1.23	−1.78[b,c]
1E	−0.80	−1.09	−1.67[b,c]
1F	−0.92	−1.21	−1.77[b,c]
1G	−1.21	−1.47	−2.02[b,c]
1H	−0.93	−1.22	−1.78[b,c]
Iron Complexes			
	$E_{1/2}/Fe^{III/II}$	$E_{1/2}/^{I}L^{red}$	$E_{1/2}/^{II}L^{red}$
2A	0.15	−1.44	−1.80[b]
2B	0.04	−1.58	−1.92[b]
2C	−0.21	−1.63	−2.02[b]
2D	0.01	−1.56	−1.92[b]
2E	0.18	−1.47	−1.78
2F	0.07	−1.60	−1.99[b,c]
2G	−0.22	−1.66	−2.04[b]
2H	0.03	−1.62	−1.92

[a] Potentials in V ± 0.01 vs NHE in 0.20 M [*n*-Bu_4N][BF_4]/DMSO. [b] For the irreversible waves, the E_p values are given. [c] Two-electron wave.

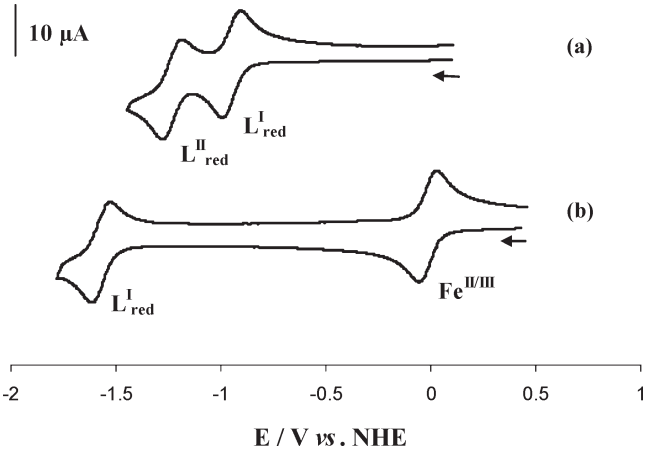

Figure 2. Cyclic voltammograms of complexes **1D** (a) and **2D** (b) in DMSO solution containing 0.20 M [*n*-Bu_4N][BF_4] at a scan rate of 0.20 V s^{-1} using a glassy carbon working electrode, displaying the ligand (L^{red}) and the Fe^{II}/Fe^{III} redox couple.

behavior was not studied. We investigated the electrochemical properties of all synthesized metal complexes by cyclic voltammetry, and the results are summarized in Table 1.

In 0.20 M [*n*-Bu_4N][BF_4]/DMSO solution all iron complexes display a reversible Fe^{III}/Fe^{II} redox couple between −0.21 and +0.18 V vs NHE (normal hydrogen electrode) depending on the ligand identity. A decrease of the redox potential in the order **2A** > **2B** > **2C** is in line with an increase of the electron donor properties of the corresponding ligands due to the presence of different substituents at the azomethine group (NH_2 > CH_3 > H). Likewise the electron donating properties of the amino group cause the redox potential shift of the iron(III) complex of Triapine (**2D**) at 0.01 V compared to the iron(III) complex of 2-formylpyridine thiosemicarbazone **2A** at +0.15 V vs NHE. Compared to **2A**−**D**, the reduction waves for the N^4-dimethyl substituted analogues **2E**−**H** are shifted by 10−30 mV to more positive potentials, in contrast to the expected negative shift because of the stronger electron donating properties of dimethylamine compared to ammonia [pK_a: dimethylamine, 10.73; ammonia, 9.25].[39] Besides the metal-centered reductions, the iron complexes display two ligand-centered reduction waves, the first ($^{I}L_{red}$) between −1.44 and −1.66 V (Figure 2) and the second ($^{II}L_{red}$) between −1.80 and −2.04 V vs NHE close to the solvent cutoff. For the corresponding gallium(III) complexes **1A**−**H** two reversible reductions ($^{I}L_{red}$ and $^{II}L_{red}$) from −0.80 to −1.21 and from −1.09 to −1.47 V, correspondingly, and an irreversible two-electron reduction ($^{III}L_{red}$) between −1.63 and −2.02 V vs NHE were observed. In comparison the ligand-centered redox couples $^{I}L_{red}$ and $^{II}L_{red}$ of the corresponding iron(III) complexes (which first are reduced to the iron(II) species) are negatively shifted by 400−700 mV. All the ligand-centered

redox processes can be attributed to the reduction of the C=N double bond(s) adjacent to the pyridine ring[40] (supplementary data on the electrochemical behavior of the complexes in DMSO and CH_3CN can be found in Supporting Information).

The influence of water on the iron redox potentials was studied by cyclic voltammetry measurements in H_2O/DMSO (7:3 v/v) mixtures with 0.2 M $NaClO_4$ as the supporting electrolyte. The low aqueous solubility of the complexes prevented the use of pure aqueous electrolyte solutions. The Fe^{III}/Fe^{II} redox couples remained reversible in H_2O/DMSO solution but were shifted by 10−50 mV to lower redox potentials, with exception of complexes **2D** (Figure S1) and **2H** which showed a positive shift by 30−40 mV.

Our data are in very good agreement with recently reported redox potentials for **2B** and **2F** in CH_3CN/H_2O (7:3) at 0.02 and 0.05 V vs NHE.[41] In cell-free assays Triapine was reported to enhance ascorbate oxidation, benzoate hydroxylation, and quenching of purified RR tyrosyl radical in the presence of iron salts.[27] In addition, EPR measurements showed that the iron(II) complex of Triapine is capable of reducing O_2 to reactive oxygen species (ROS).[25] The potential range and the reversibility of the redox couple of the iron complex **2D** in H_2O/DMSO solution provide further evidence that the complex is able to undergo redox cycling and produce ROS under physiological conditions. This conclusion is also valid for the other iron complexes studied in this work but probably to a lesser extent for complexes **2C** and **2G** with more negative potentials of the Fe^{III}/Fe^{II} redox couples at around −0.2 V vs NHE.

Cytotoxicity. The cytotoxic potency of the thiosemicarbazones and their corresponding gallium(III) and iron(III) complexes was measured in the human tumor cell lines 41M (ovarian carcinoma) and SK-BR-3 (mammary carcinoma) by means of the colorimetric MTT assay. Generally, the 41M cells were more sensitive to the compounds investigated in this study. The metal-free ligands and the corresponding metal complexes cover a broad range of activity, with IC_{50} values ranging from nanomolar to high micromolar concentrations, depending on the ligand substitutions and the metal ion (Table 2).

Structure−Activity Relationships of the Metal-Free Ligands. Specific structural modifications on the ligand were made to explore the following structure−activity relationships.

(i) Effect of Substituents at the Carbon Atom of the Azomethine Group. Substitution of the hydrogen atom in $\mathbf{HL^A}$ by a methyl group does not change the antiproliferative activity. However, the substitution of the hydrogen atom by a NH_2 group ($\mathbf{HL^C}$) results in about 2-fold decrease of cytotoxicity in both cell lines.

IC_{50} values for the ligands $\mathbf{HL^A}$ and $\mathbf{HL^B}$ were documented in the literature.[42] These are very similar, varying from 1 to 10 μM, depending on the cell line. The first 2-pyridineformamide thiosemicarbazones were synthesized 10 years ago with the aim of increasing aqueous solubility.[43] The first results on their cytotoxicity were reported only quite recently. In particular, $\mathbf{HL^C}$ tested in glioblastoma cell lines showed cytotoxicities in the micromolar concentration range (3.6−7.3 μM).[44] In the case of Triapine the reported IC_{50} values range from 0.2 to 3.0 μM.[27,45] However, because of the use of different cell lines and conditions, the impact of the structural changes in the ligands $\mathbf{HL^A}$−$\mathbf{HL^D}$ (all containing a terminal NH_2 group) remained vague. Our cytotoxicity data in both cell lines 41M and SK-BR-3 confirm that the antiproliferative activity of $\mathbf{HL^A}$ is very similar to that of $\mathbf{HL^B}$, whereas $\mathbf{HL^C}$ possesses a slightly lower cytotoxic potency (Table 2, Figure 3, Figure S5). Interestingly, $\mathbf{HL^D}$ shows IC_{50} values by a factor 10 lower than $\mathbf{HL^C}$, indicating that the effect of the second amino group is dependent on its position.

Table 2. Cytotoxicity of α-N-Heterocyclic Thiosemicarbazones ($\mathbf{HL^A}$−$\mathbf{HL^H}$) and Their Gallium(III) (**1A**−**H**) and Iron(III) Complexes (**2A**−**H**) in Two Human Cancer Cell Lines

	IC_{50} (μM)[a]	
compd	41M	SK-BR-3
	Ligands	
$\mathbf{HL^A}$	2.9 ± 0.6	3.2 ± 0.6
$\mathbf{HL^B}$	2.5 ± 0.3	3.6 ± 0.2
$\mathbf{HL^C}$	4.9 ± 0.04	5.6 ± 1.1
$\mathbf{HL^D}$, Triapine	0.45 ± 0.03	0.52 ± 0.08
$\mathbf{HL^E}$	0.0040 ± 0.0009	0.0098 ± 0.0011
$\mathbf{HL^G}$	0.32 ± 0.03	0.29 ± 0.01
$\mathbf{HL^H}$	0.21 ± 0.13	0.29 ± 0.08
	Ga(III) Complexes	
1A	1.5 ± 0.1	1.5 ± 0.5
1B	1.2 ± 0.1	1.0 ± 0.1
1C	3.4 ± 1.0	4.6 ± 1.1
1D	0.25 ± 0.05	0.35 ± 0.04
1E	0.0029 ± 0.0001	0.0050 ± 0.0009
1G	0.11 ± 0.05	0.12 ± 0.04
1H	0.074 ± 0.001	0.081 ± 0.006
	Fe(III) Complexes	
2A	2.7 ± 0.5	4.9 ± 0.5
2B	28 ± 12	>100
2C	>100	>100
2D	1.5 ± 0.5	1.7 ± 0.4
2E	0.11 ± 0.04	0.15 ± 0.05
2G	1.6 ± 0.7	1.5 ± 0.4
2H	5.2 ± 0.2	6.0 ± 0.9
$Ga(NO_3)_3$[b]	70 ± 4	>100
$Fe(NO_3)_3$[b]	>100	>100

[a] 50% inhibitory concentrations in 41M and SK-BR-3 cells after exposure for 96 h in the MTT assay. Values are the mean ± standard deviation obtained from at least three independent experiments. [b] Values taken from ref 24.

(ii) Dimethylation of the Terminal NH_2 Group. Terminal dimethylation enhances the activity of the thiosemicarbazones. However, the magnitude of this effect is strongly dependent on the other ligand substitutions. The strongest enhancement was observed when comparing $\mathbf{HL^A}$ with its dimethylated counterpart $\mathbf{HL^E}$. The N^4-dimethylation results in a 725-fold (41M) and 320-fold (SK-BR-3) increase of cytotoxicity (Table 2, Figure 3). The same trend but with distinctly smaller differences was observed for the two ligands containing a 2-pyridinecarboxamide moiety ($\mathbf{HL^C}$ vs $\mathbf{HL^G}$), with an increase of cytotoxicity by a factor of 15−20 as a result of dimethylation. The effect was found to be weakest for Triapine and its dimethylated derivative ($\mathbf{HL^D}$ vs $\mathbf{HL^H}$). In this case only a 2-fold increase of cytotoxicity was observed.

(iii) Effect of an Amino Group in Terminally Dimethylated Thiosemicarbazones. The cytotoxicity of the terminally dimethylated Triapine analogue $\mathbf{HL^H}$ is strongly diminished

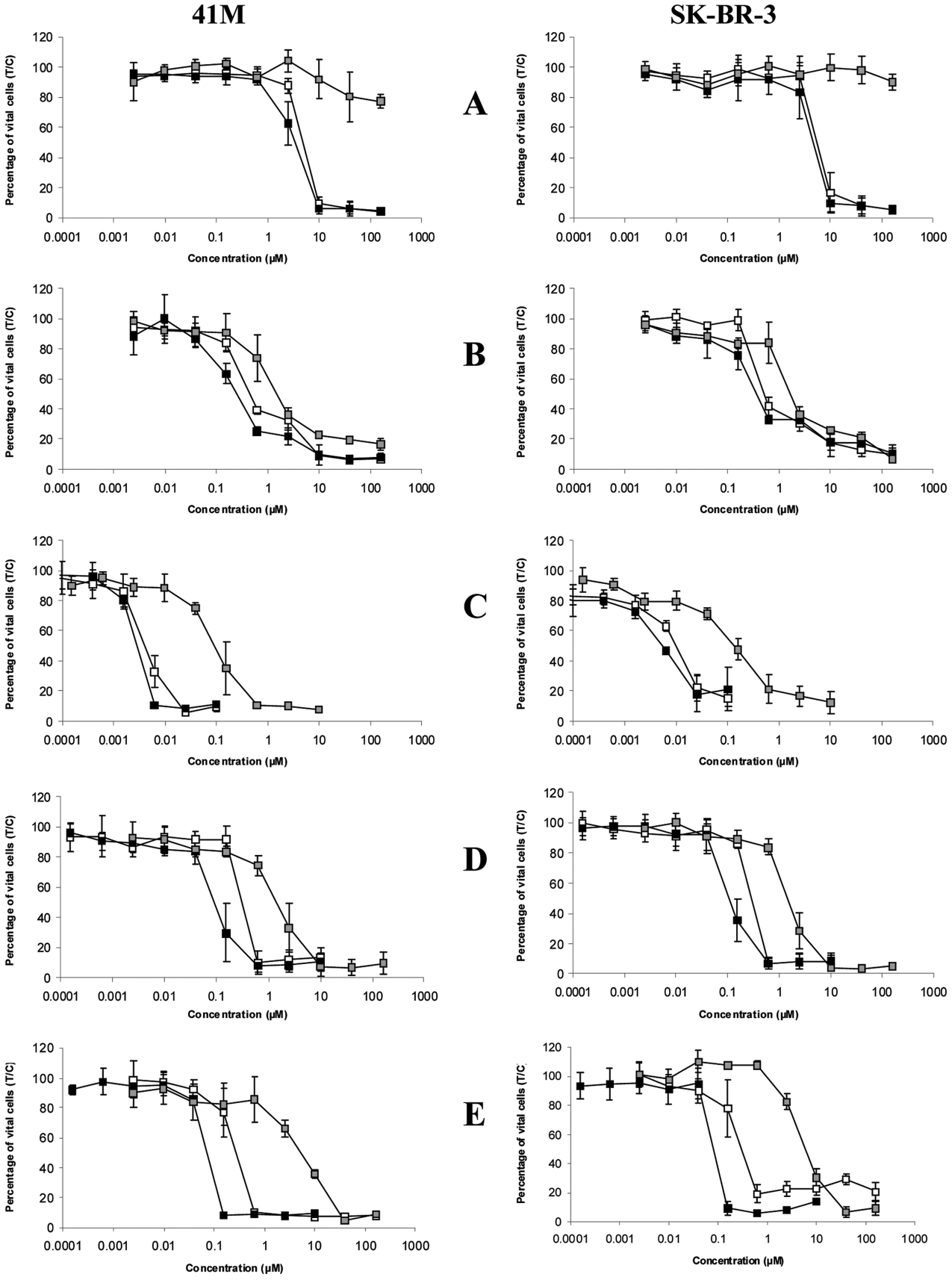

Figure 3. Concentration−effect curves of metal-free thiosemicarbazones (white symbols), their gallium(III) complexes (black symbols), and iron(III) complexes (gray symbols), obtained by the MTT assay in 41M cells (left panels) and SK-BR-3 cells (right panels): (A) **HL^{C}**, **1C**, **2C**; (B) **HL^{D}**, **1D**, **2D**; (C) **HL^{E}**, **1E**, **2E**; (D) **HL^{G}**, **1G**, **2G**; (E) **HL^{H}**, **1H**, **2H**. Values are the mean ± standard deviation from at least three independent experiments.

compared to that of $\mathbf{HL^E}$, in which the amino group in position 3 of the pyridine heterocycle is absent. Thus, the addition of a NH_2 functionality to $\mathbf{HL^E}$ results in a 50- and 30-fold decrease of IC_{50} values in 41M and SK-BR-3 cells, respectively. Likewise the presence of the NH_2 group at the carbon atom of the azomethine bond in $\mathbf{HL^G}$ results in 30- to 80-fold decrease of cytotoxicity when compared to that of $\mathbf{HL^E}$. Together, these data suggest a critical role of the NH_2 group on the biological activity of terminally dimethylated α-N-heterocyclic thiosemicarbazones.

Thus, the most striking enhancement in cytotoxic activity (by a factor of ~300 to 700) was achieved by dimethylation of the terminal amino group of $\mathbf{HL^A}$. A similar effect was observed when the terminal NH_2 group of 2-acetylpyridine thiosemicarbazone was disubstituted.[41,46] On the other hand, our results demonstrate that the enhancement of cytotoxic potency by N^4-dimethylation is nearly annihilated when another NH_2 group is present ($\mathbf{HL^H}$, $\mathbf{HL^G}$). Hence, contrary to what has been assumed in the literature,[46] addition of the terminal methyl groups, while necessary, is not sufficient for the drastic enhancement in cytotoxic activity of these derivatives. Removal of any NH_2 functionality is also necessary.

Structure−Activity Relationships of the Metal Complexes. The effects of thiosemicarbazone complexation to gallium(III) and iron(III) are divergent (Table 2, Figure 3, Figure S5) and have been established by comparison of cytotoxicities of metal complexes and metal-free ligands. Generally, the iron(III) complexes show reduced cytotoxicity in comparison to that of the corresponding ligands. The effects vary from 3-fold to >28-fold increased IC_{50} values. In contrast to the iron(III) complexes, gallium(III) thiosemicarbazonates are 1.2−3.6 times more cytotoxic than the corresponding metal-free ligands.

In all previous studies the effect of Triapine complexation to iron has been determined by simple addition of iron salt to a solution of Triapine, assuming the formation of the desired complex. However, the applied procedure does not guarantee its formation. Given the conditions for complexation reactions are provided, mixtures of complexes with different metal-to-ligand stoichiometries and various coligands can be produced. This might explain why the reported effects of Triapine complexation to iron are divergent. On the one hand, an enhancement in cytotoxic activity was observed in murine leukemia cells.[26] On the other hand, a slight decrease was found in neuroblastoma cells,[27] whereas no difference was discernible in neuroephithelioma cells.[47] No marked differences were found between the cytotoxic potencies of iron(II) and iron(III) complexes, presumably because of spontaneous oxidation of iron(II) to iron(III) in cell culture medium.[26,47] Generally, the reported influence of the complexation of Triapine to iron is moderate, in contrast to classic iron chelating agents such as DFO (desferrioxamine), which result in iron complexes that are almost devoid of antiproliferative activity.[47] As the iron complex of Triapine retains reasonable activity, it is still conceivable that this complex is the active species. The latter is based on findings in cell-free assays showing that the iron(II) complex is able to react with dioxygen and generate reactive oxygen species (ROS) and that the preformed iron complex inhibits ribonucleotide reductase (RR) much more effectively than the metal-free ligand.[25]

In this study, the isolated iron(III) complex of Triapine (**2D**) is 3 times less cytotoxic in both cell lines than the metal-free ligand. Interestingly, this decrease in activity upon complexation with iron(III) is smaller than in the case of $\mathbf{HL^B}$, $\mathbf{HL^C}$, and $\mathbf{HL^E}$−$\mathbf{HL^H}$. Iron(III) complexes of these ligands are 5−30 times less cytotoxic than the uncomplexed ligands. Only complexation of $\mathbf{HL^A}$ to iron(III) did not result in a change in cytotoxicity. Taking into account the 1:2 stoichiometry of the iron thiosemicarbazonate complexes, the decrease in activity is even more pronounced. However, there is no clear correlation between the cytotoxic potencies of the iron(III) complexes and the uncomplexed ligands, suggesting that the binding strength to iron(III) or another factor has a modulating effect on cytotoxicity. The decreased cytotoxicity of the iron(III) complexes compared to that of the metal-free ligands can presumably be explained at least partially by the positive charge that impairs their ability to cross the cell membrane (see RR inhibition capacities below).

Table 3. Comparison of the RR Inhibitory Potency and Cytotoxicity of $\mathbf{HL^D}$, $\mathbf{HL^E}$, and Their Iron(III) Complexes **2D** and **2E** in HL60 Cells

	IC_{50} (μM)[a]	
compd	RR inhibition	cytotoxicity
$\mathbf{HL^D}$, Triapine	5.4 ± 2.4	0.27 ± 0.06
2D	53 ± 8.8	0.84 ± 0.05
$\mathbf{HL^E}$	0.80 ± 0.13	0.0068 ± 0.0022
2E	1.5 ± 0.8	0.11 ± 0.05

[a] 50% inhibitory concentrations in HL60 cells. RR inhibition was determined using ^{3}H-cytidine DNA incorporation assays after 4 h of drug incubation. Cytotoxicity was determined after exposure for 96 h by the MTT assay. Values are the mean ± standard deviations from at least three independent experiments.

We have previously noted an enhancement of antiproliferative activity of gallium(III) complexes in comparison to their corresponding ligands.[24] In this study this trend is preserved, with about 2-fold increase of cytotoxic activity compared to the respective metal-free ligands. These results suggest that the higher activity of the gallium(III) complexes is mainly due to the stoichiometric effect of the 1:2 gallium-to-ligand complexes.

Inhibition of Ribonucleotide Reductase. ^{3}H-Cytidine DNA incorporation assays were performed in HL60 cells after 4 h of drug incubation for $\mathbf{HL^D}$, $\mathbf{HL^E}$, **2D**, and **2E** in order to ascertain whether the differences in cytotoxicity induced by coordination to iron(III) and/or by terminal dimethylation are related to different capacities of inhibiting RR. As shown in Table 3, the RR inhibitory potential follows the same trends as observed in the cytotoxicity tests, but in detail some differences are obvious. The cytotoxicity data show only a small increase in the IC_{50} values after coordination of $\mathbf{HL^D}$ to iron(III) (**2D**), whereas the effect of coordination to iron(III) on RR inhibition is much more pronounced. The magnitudes of these effects are in reversed order for $\mathbf{HL^E}$ and **2E**. While the ability of **2E** to inhibit RR is only slightly decreased, the cytotoxicity of **2E** is reduced by a factor of 16 compared to the metal-free ligand $\mathbf{HL^E}$. Concerning the terminal dimethylation, the strong increase in cytotoxicity from $\mathbf{HL^D}$ to $\mathbf{HL^E}$ is not paralleled to the same extent by their ability to inhibit RR. Notably, in the IC_{50} range even small increases in drug concentration of the metal-free ligands induce strong effects on RR activity (Figure 4). In contrast, the iron complexes show a gradual increase of RR inhibition over a broad drug concentration range.

It should be noted that the RR inhibitory potential of Triapine ($\mathbf{HL^D}$) is well documented in the literature. In particular, in cell-free systems short-time treatment of

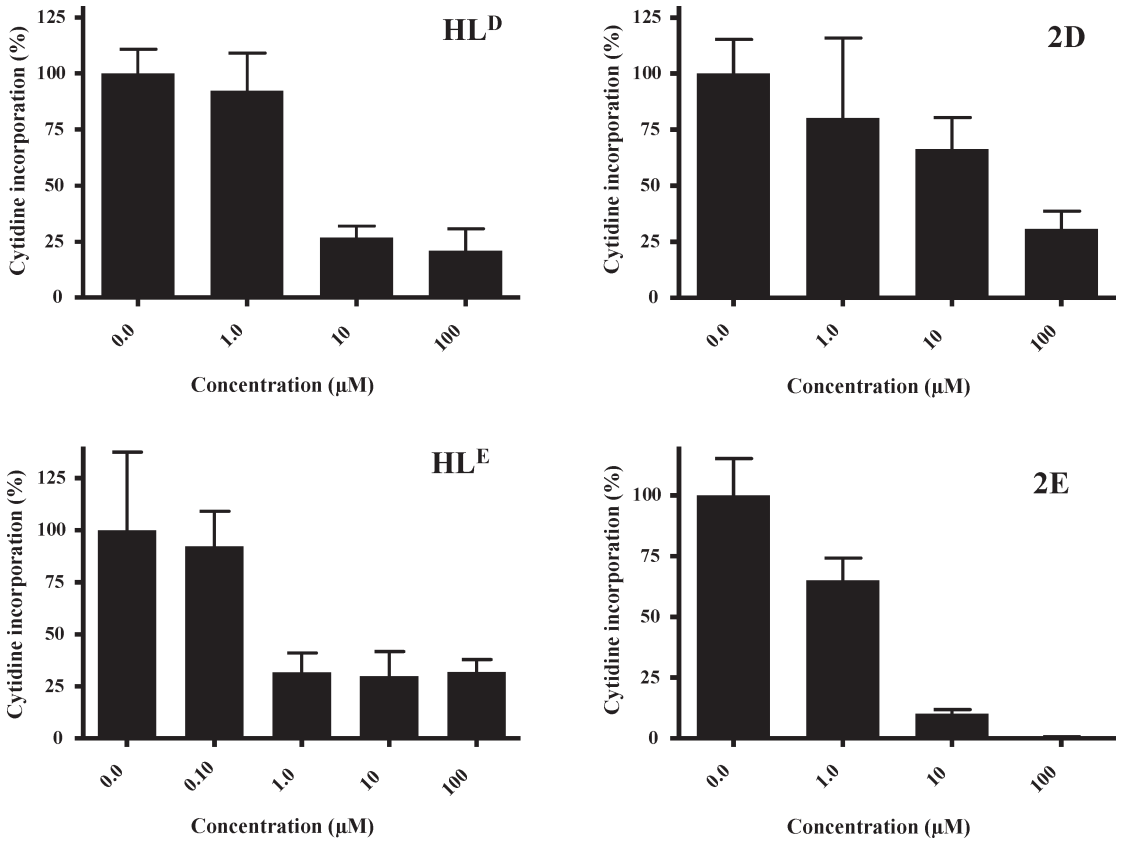

Figure 4. Inhibition of ribonucleotide reductase by $\mathbf{HL^D}$ (Triapine), $\mathbf{HL^E}$, and their iron(III) complexes **2D** and **2E** as determined by ^{3}H-cytidine DNA incorporation assays in HL60 cells.

purified prokaryotic or mouse RR with Triapine resulted in reduced ^{3}H-cytidine incorporation into DNA.[25,26] In line with these data, EPR measurements of intact SK-MC neuroepithelioma cells after their treatment with 25 μM Triapine for 24 h showed a 39% quenching of the tyrosyl radical.[27] To our knowledge the RR inhibitory activity of the iron(III) complex of Triapine (**2D**) was so far determined exclusively under reducing conditions in cell-free systems.[25,26] Precomplexation of Triapine to iron was found to strongly enhance RR inhibition. This is in line with our previous report on enhanced tyrosyl radical quenching in isolated mouse R2 subunits by iron(III) N^4-dimethylated thiosemicarbazonates.[24] In the present study, the ability of $\mathbf{HL^D}$, $\mathbf{HL^E}$ and their iron(III) complexes to inhibit RR was determined in living cells. Here, iron(III) complexes show a reduced RR inhibitory activity compared to the metal-free ligands, the difference being much more evident between $\mathbf{HL^D}$ and **2D**. The mechanisms underlying these effects are still not known. A possible explanation is the ionic nature and the reduced lipophilicity of the iron complex, which probably results in lower uptake into the cell. To clarify whether the differences observed between metal-free ligands and the respective iron complexes are based on reduced drug uptake or depend on other yet unknown mechanisms is a matter of ongoing investigations.

With regard to the impact of N^4-disubstitution on the RR inhibitory potency, only some in vitro tests with 5-hydroxy-2-formylpyridine thiosemicarbazones using purified RR have been reported so far.[48] In contrast to our data in living cells, those studies showed that dimethylation of the terminal amino group markedly decreased the RR inhibitory activity. However, taking into account that different assays for determination of RR inhibitory potencies were performed and that no cytotoxicity data were reported in the earlier study,[48] a direct comparison is not possible. Our data suggest that the enhancement in antiproliferative activity by terminal dimethylation cannot be solely dependent on RR inhibition and that other intracellular targets may be involved.

Conclusions

In this study we developed a novel straightforward three-step synthesis of Triapine, the most promising α-N-heterocyclic thiosemicarbazone for cancer therapy today. In addition, iron(III) and gallium(III) complexes of Triapine were prepared for the first time. The synthesis of 2-formylpyridine, 2-acetylpyridine, 2-pyridineformamide thiosemicarbazones, and their N^4-dimethylated analogues as well as the corresponding gallium(III) and iron(III) complexes allowed us to establish novel structure−cytotoxicity relationships. In particular, they revealed an increase of cytotoxicity by complexation of Triapine and related ligands to gallium(III), while coordination to iron(III) reduces their activity. Terminal nitrogen dimethylation was found to strongly enhance the cytotoxicity of metal-free ligands as well as their iron(III) and gallium(III) complexes. This is, however, not the case, when a NH_2 functionality is present anywhere at the thiosemicarbazone backbone. ^{3}H-Cytidine DNA incorporation assays showed that the increased cytotoxicity upon terminal dimethylation is only partly dependent on the ability of these compounds to inhibit RR, implying that other mechanisms are involved. Taken together, this study indicates the importance of detailed structure−activity relationship analyses for

the understanding of the molecular mechanisms underlying the anticancer activity of thiosemicarbazones and for the creation of more effective chemotherapeutics.

Experimental Section

All solvents and reagents were obtained from commercial suppliers and used without further purification. 2-Acetylpyridine N^4-dimethylthiosemicarbazone ($\mathbf{HL^F}$) and its gallium(III) (**1F**) and iron(III) complexes (**2F**) were prepared as previously reported.[24] 2-Formylpyridine thiosemicarbazone ($\mathbf{HL^A}$) was synthesized by refluxing 2-formylpyridine with thiosemicarbazide in EtOH/H_2O, 3:2, for 5 h, and 2-formylpyridine N^4-dimethylthiosemicarbazone ($\mathbf{HL^E}$) by refluxing 2-formylpyridine and N^4-dimethylthiosemicarbazide[49] in MeOH for 5 h (X-ray diffraction quality crystals of $\mathbf{HL^E}$ were obtained by recrystallization from methanol). 2-Acetylpyridine thiosemicarbazone ($\mathbf{HL^B}\cdot 0.5H_2O$) was obtained by refluxing 2-acetylypridine and thiosemicarbazide in EtOH for 5 h, followed by recrystallization in EtOH. The content of water was confirmed by thermogravimetric analysis. 2-Pyridineformamide thiosemicarbazone ($\mathbf{HL^C}$) was prepared following the literature protocol.[50] 2-Pyridineformamide N^4-dimethylthiosemicarbazone ($\mathbf{HL^G}$) was synthesized in a similar manner by using N^4-dimethylthiosemicarbazide instead of thiosemicarbazide, with a 76% yield, in comparison to 25% reported in the literature.[36] *tert*-Butyl (2-formylpyridin-3-yl)carbamate was obtained using *tert*-butyl (2-bromopyridin-3-yl)carbamate (see Supporting Information), *n*-butyllithium, and *N*-formylpiperidine.[32] The condensation reaction with thiosemicarbazide and deprotection were performed according to the published procedure.[29] Elemental analyses of prepared compounds were carried out on a Carlo Erba microanalyzer at the Microanalytical Laboratory of the University of Vienna and are within ±0.4% of the calculated values, confirming their ≥95% purity. Electrospray ionization mass spectrometry was carried out with a Bruker Esquire 3000 instrument (Bruker Daltonic, Bremen, Germany). Expected and experimental isotope distributions were compared. Infrared spectra were obtained from KBr pellets with a Perkin-Elmer FT-IR 2000 instrument (4000−400 cm^{-1}). UV−vis spectra were recorded on a Perkin-Elmer Lambda 650 UV−vis spectrophotometer using samples dissolved in methanol (900−210 nm). The iron(III) complexes were also measured on a Hewlett-Packard 8453 UV−vis spectrophotometer (1100−210 nm). The content of water in complexes **1C**, **2C**, and **2D** was verified by thermogravimetric analysis (TGA) with a Mettler Toledo TGA/SDTA851e apparatus, with a 3 °C/min heating rate under an air atmosphere. ^1H and ^{13}C one- and two-dimensional NMR spectra were recorded in DMSO-d_6, with a Bruker Avance III 500 MHz FT-NMR spectrometer. The residual ^1H and ^{13}C present in DMSO-d_6 were used as internal references. Abbreviations for NMR data are as follows: py = pyridine, $C_{q,py}$ = quaternary carbon of pyridine.

Electrochemistry. Cyclic voltammograms were measured in a three-electrode cell using a 2.0 mm diameter glassy carbon working electrode, a platinum auxiliary electrode, and an Ag|Ag^+ reference electrode containing 0.10 M $AgNO_3$. Measurements were performed at room temperature using an EG & G PARC 273A potentiostat/galvanostat. Deaeration of solutions was accomplished by passing a stream of argon through the solution for 5 min prior to the measurement and then maintaining a blanket atmosphere of argon over the solution during the measurement. The potentials were measured in 0.20 M [*n*-Bu_4N][BF_4]/DMSO, using [Fe(η^5-C_5H_5)$_2$] ($E_{1/2}$ = +0.68 V vs NHE)[51] as internal standard and are quoted relative to the normal hydrogen electrode (NHE). For cyclic voltammetry measurements in 0.20 M $NaClO_4$ DMSO/H_2O (3:7 v/v) solutions, a 2.0 mm diameter glassy carbon working electrode, a platinum auxiliary electrode, and an Ag|Ag^+ reference electrode containing 3.0 M NaCl were used.

Synthesis of Ligands and Metal Complexes. 3-Aminopyridine-2-carboxaldehyde-N^4-dimethylthiosemicarbazone ($\mathbf{HL^H}$). To *tert*-butyl (2-formylpyridin-3-yl)carbamate (147 mg, 0.66 mmol) and N^4-dimethylthiosemicarbazide (79 mg, 0.66 mmol) in ethanol (3 mL) and H_2O (1 mL) was added concentrated HCl (0.3 mL), and the mixture was stirred under reflux for 5 h. After the mixture was cooled to room temperature, 10% (w/w) aqueous $NaHCO_3$ (0.8 mL) was added and the mixture was stirred for further 30 min. The yellow hygroscopic $\mathbf{HL^H}\cdot$HCl was filtered off, washed with cold water, cold ethanol (−20 °C), and diethyl ether, and dried in vacuo. Yield: 130 mg (76%). ^1H NMR (500.10 MHz, DMSO-d_6): δ 12.00 (s, 1H, NH), 8.88 (s, 1H, HC=N), 8.15 (br s, 2H, NH_2), 8.03 (m, 1H, py), 7.69 (d, $^3J_{H,H}$ = 8.2 Hz, 1H, py), 7.57 (m, 1H, py), 3.35 (s, 6H, $N(CH_3)_2$). The $\mathbf{HL^H}\cdot$HCl salt (90 mg, 0.35 mmol) was dissolved in H_2O (4 mL) at 70 °C, and *N*-methylmorpholine (60 μL, 0.55 mmol) was added. The reaction mixture was cooled to room temperature and stirred for 1 h. The precipitate was filtered off, washed with H_2O, cold ethanol (−20 °C), and diethyl ether, and dried in vacuo and afterward over P_2O_5. Yield: 65 mg (84%). Anal. ($C_9H_{13}N_5S$) C, H, N, S. ^1H and ^{13}C NMR, IR, and UV−vis spectroscopy and mass spectrometry data for $\mathbf{HL^H}$ and all reported complexes can be found in Supporting Information.

[Bis(2-formylpyridinethiosemicarbazonato)-*N*,*N*,*S*-gallium(III)] Nitrate, [Ga($\mathbf{L^A}$)$_2$]$NO_3\cdot 0.5CH_3OH$ (1A). To 2-formylpyridine thiosemicarbazone ($\mathbf{HL^A}$) (140 mg, 0.78 mmol) and $NaOCH_3$ (63 mg, 1.17 mmol) in dry methanol (14 mL) at 70 °C under an argon atmosphere, gallium(III) nitrate nonahydrate (162 mg, 0.39 mmol) was added, and the mixture was stirred at 70 °C for 3 h, then cooled to room temperature and filtered from undissolved impurities. The clear solution was allowed to stand at +4 °C for 3 days, and the crystals formed were filtered off, washed with cold methanol (−20 °C), and dried in vacuo. Yield: 54 mg (27%). Anal. ($C_{14}H_{14}GaN_9O_3S_2\cdot 0.5CH_3OH$) C, H, N.

[Bis(2-acetylpyridinethiosemicarbazonato)-*N*,*N*,*S*-gallium(III)] Nitrate, [Ga($\mathbf{L^B}$)$_2$]NO_3 (1B). To 2-acetylpyridine thiosemicarbazone ($\mathbf{HL^B}$) (200 mg, 1.03 mmol) in ethanol (5 mL) at 70 °C, gallium(III) nitrate nonahydrate (217 mg, 0.52 mmol) in ethanol (2 mL) was added, and the solution was stirred at 50 °C for 2 h. The reaction mixture was cooled to room temperature and allowed to stand at +4 °C for 4 h. The yellow precipitate was filtered off, washed with cold ethanol (−20 °C) and diethyl ether, and dried in vacuo. Yield: 185 mg (69%). Anal. ($C_{16}H_{18}GaN_9O_3S_2$) C, H, N, S.

[Bis(2-pyridineformamidethiosemicarbazonato)-*N*,*N*,*S*-gallium(III)] Nitrate, [Ga($\mathbf{L^C}$)$_2$]$NO_3\cdot 0.5H_2O$ (1C). To 2-pyridineformamide thiosemicarbazone ($\mathbf{HL^C}$) (200 mg, 1.02 mmol) in ethanol (20 mL) at 70 °C, gallium(III) nitrate nonahydrate (214 mg, 0.51 mmol) in ethanol (2.5 mL) was added, and the mixture was stirred at the same temperature for 1 h. The yellow solid was separated from the hot solution by filtration, washed with ethanol, dried in vacuo at 50 °C and then over P_2O_5. Yield: 148 mg (55%). Anal. ($C_{14}H_{16}GaN_{11}O_3S_2\cdot 0.5H_2O$) C, H, N, S.

[Bis(3-aminopyridine-2-carboxaldehydethiosemicarbazonato)-*N*,*N*,*S*-gallium(III)] Nitrate, [Ga($\mathbf{L^D}$)$_2$]$NO_3\cdot 0.15CH_3OH$ (1D). To a suspension of 3-aminopyridine-2-carboxaldehyde thiosemicarbazone ($\mathbf{HL^D}$) (150 mg, 0.77 mmol) in methanol (10 mL) and triethylamine (112 μL, 0.81 mmol) at 50 °C, gallium(III) nitrate nonahydrate (166 mg, 0.40 mmol) in methanol (2.5 mL) was added, and the mixture was stirred for 20 min at 50 °C and 2.5 h at room temperature. The bright-orange precipitate formed was filtered off, washed with cold methanol (−20 °C), and dried in vacuo and afterward over P_2O_5. Yield: 144 mg (72%). Anal. ($C_{14}H_{16}GaN_{11}O_3S_2\cdot 0.15CH_3OH$) C, H, N, S. Crystals suitable for X-ray data collection were obtained by slow evaporation of an ethanolic solution of **1D**.

[Bis(2-formylpyridine-N^4-dimethylthiosemicarbazonato)-*N*,*N*,*S*-gallium(III)] Hexafluorophosphate, [Ga($\mathbf{L^E}$)$_2$]PF_6 (1E). To 2-formylpyridine N^4-dimethylthiosemicarbazone ($\mathbf{HL^E}$) (87 mg, 0.42 mmol) in methanol (6 mL) at 40 °C, gallium(III) nitrate

nonahydrate (87 mg, 0.21 mmol) in methanol (2 mL) was added, and the mixture was stirred at room temperature for 3 h. Addition of ammonium hexafluorophosphate (100 mg, 0.61 mmol) to the reaction mixture led to the formation of a yellow solid which was filtered off, washed with methanol, and dried in vacuo. Yield: 92 mg (70%). Anal. ($C_{18}H_{22}F_6GaN_8PS_2$) C, H, N, S.

[Bis(2-pyridineformamide-N^4-dimethylthiosemicarbazonato)-*N,N,S*-gallium(III)] Nitrate [Ga(L^G)$_2$]NO_3, (1G). To 2-pyridineformamide N^4-dimethylthiosemicarbazone (HL^G) (400 mg, 1.79 mmol) in ethanol (20 mL) at 70 °C, gallium(III) nitrate nonahydrate (375 mg, 0.90 mmol) in ethanol (5 mL) was added, and the mixture was stirred at the same temperature for 2 h. The yellow-orange solid was separated from the hot solution by filtration, washed with ethanol, and dried in vacuo. Yield: 380 mg (74%). Anal. ($C_{18}H_{24}GaN_{11}O_3S_2$) C, H, N, S.

[Bis(3-aminopyridine-2-carboxaldehyde-N^4-dimethylthiosemicarbazonato)-*N,N,S*-gallium(III)] Hexafluorophosphate, [Ga(L^H)$_2$]PF_6 (1H). To a suspension of 3-aminopyridine-2-carboxaldehyde N^4-dimethylthiosemicarbazone hydrochloride ($HL^H \cdot HCl$) (150 mg, 0.58 mmol) in ethanol (15 mL), gallium(III) nitrate nonahydrate (130 mg, 0.31 mmol) in ethanol (3 mL) was added and the mixture was stirred for 1.5 h at room temperature. Subsequently a solution of ammonium hexafluorophosphate (200 mg, 1.23 mmol) in ethanol (2 mL) was added. After 2 h the orange precipitate was filtered off, washed with cold ethanol (−20 °C), and dried in vacuo. Yield: 114 mg (60%). Anal. ($C_{18}H_{24}F_6GaN_{10}PS_2$) C, H, N, S.

[Bis(2-formylpyridinethiosemicarbazonato)-*N,N,S*-iron(III)] Nitrate, [Fe(L^A)$_2$]NO_3 (2A). To 2-formylpyridine thiosemicarbazone (HL^A) (200 mg, 1.11 mmol) and *N*-methylmorpholine (120 μL, 1.09 mmol) in methanol (20 mL) at 70 °C, iron(III) nitrate nonahydrate (222 mg, 0.55 mmol) in methanol (2 mL) was added dropwise, and the reaction mixture was stirred for 3 h at 70 °C. After the mixture was cooled to room temperature, about one half of the solvent was removed under reduced pressure and the reaction mixture was allowed to stand at +4 °C overnight. The black crystalline product was filtered off, washed with cold methanol, and dried in vacuo and afterward over P_2O_5. Yield: 195 mg (74%). Anal. ($C_{14}H_{14}FeN_9O_3S_2$) C, H, N, S.

[Bis(2-acetylpyridinethiosemicarbazonato)-*N,N,S*-iron(III)] Nitrate, [Fe(L^B)$_2$]NO_3 (2B). To 2-acetylpyridine thiosemicarbazone (HL^B) (200 mg, 1.03 mmol) in methanol (10 mL) at room temperature, iron(III) nitrate nonahydrate (208 mg, 0.51 mmol) in methanol (2 mL) was added dropwise, and the reaction mixture was stirred for 3 h. The black product formed was filtered off, washed with methanol, and dried in vacuo and then over P_2O_5. Yield: 198 mg (74%). Anal. ($C_{16}H_{18}FeN_9O_3S_2$) C, H, N, S.

[Bis(2-pyridineformamidethiosemicarbazonato)-*N,N,S*-iron(III)] Nitrate, [Fe(L^C)$_2$]$NO_3 \cdot 1.5H_2O$ (2C). To 2-pyridineformamide thiosemicarbazone (HL^C) (200 mg, 1.02 mmol) and *N*-methylmorpholine (111 μL, 1.01 mmol) in methanol (10 mL) at 50 °C, iron(III) nitrate nonahydrate (205 mg, 0.51 mmol) in methanol (2 mL) was added, and the mixture was stirred at 50 °C for 2 h. After the mixture was cooled to room temperature, about one half of the solvent was removed under reduced pressure and the reaction mixture was allowed to stand at +4 °C overnight. The black crystals were filtered off, washed with cold methanol, and dried in vacuo. Yield: 213 mg (78%). Anal. ($C_{14}H_{16}FeN_{11}O_3S_2 \cdot 1.5H_2O$) C, H, N, S.

[Bis(3-aminopyridine-2-carboxaldehydethiosemicarbazonato)-*N,N,S*-iron(III)] nitrate, [Fe(L^D)$_2$]$NO_3 \cdot H_2O$ (2D). To a suspension of 3-aminopyridine-2-carboxaldehyde thiosemicarbazone (HL^D) (150 mg, 0.77 mmol) in ethanol (24 mL) at 50 °C, iron(III) nitrate nonahydrate (157 mg, 0.39 mmol) in ethanol (2 mL) was added dropwise, and the mixture was stirred for 10 min at 50 °C and 3 h at room temperature. The black-green precipitate was filtered off, washed with cold ethanol (−20 °C) and diethyl ether, and dried in vacuo and afterward over P_2O_5. Yield: 132 mg (66%). Anal. ($C_{14}H_{16}FeN_{11}O_3S_2 \cdot H_2O$) C, H, N, S. Crystals suitable for X-ray data collection were obtained by slow evaporation of a methanolic solution of **2D**.

[Bis(2-formylpyridine-N^4-dimethylthiosemicarbazonato)-*N,N,S*-iron(III)] Hexafluorophosphate, [Fe(L^E)$_2$]PF_6 (2E). To 2-formylpyridine N^4-dimethylthiosemicarbazone (HL^E) (70 mg, 0.34 mmol) dissolved in ethanol (7 mL) at 40 °C, iron(III) nitrate nonahydrate (68 mg, 0.17 mmol) in ethanol (2 mL) was added, and the mixture was stirred at room temperature for 1.5 h. After addition of ammonium hexafluorophosphate (90 mg, 0.55 mmol) the reaction mixture was stirred further for 1 h. The solid was filtered off, washed three times with cold ethanol (−20 °C), and dried in vacuo and then over P_2O_5. Yield: 79 mg (76%). Anal. ($C_{18}H_{22}F_6FeN_8PS_2$) C, H, N, S.

[Bis(2-pyridineformamide-N^4-dimethylthiosemicarbazonato)-*N,N,S*-iron(III)] Nitrate, [Fe(L^G)$_2$]NO_3 (2G). To 2-pyridineformamide N^4-dimethylthiosemicarbazone (HL^G) (400 mg, 1.79 mmol) in methanol (30 mL) at 50 °C, iron(III) nitrate nonahydrate (362 mg, 0.90 mmol) in methanol (3 mL) was added, and the mixture was stirred at the same temperature for 2 h. After the mixture was cooled to room temperature about one half of the solvent was removed under reduced pressure and the reaction mixture was allowed to stand at +4 °C overnight. The precipitate was filtered off, washed with ethanol, and dried in vacuo at 50 °C. Yield: 340 mg (68%). Anal. ($C_{18}H_{24}FeN_{11}O_3S_2$) C, H, N, S.

[Bis(3-aminopyridine-2-carboxaldehyde-N^4-dimethylthiosemicarbazonato)-*N,N,S*-iron(III)] nitrate, [Fe(L^H)$_2$]NO_3 (2H). To a suspension of 3-aminopyridine-2-carboxaldehyde N^4-dimethylthiosemicarbazone hydrochloride ($HL^H \cdot HCl$) (120 mg, 0.46 mmol) in ethanol (12 mL), iron(III) nitrate nonahydrate (100 mg, 0.25 mmol) in ethanol (1 mL) was added dropwise, and the mixture was stirred for 3 h at room temperature. The brown precipitate was filtered off, washed with cold ethanol (−20 °C) and diethyl ether, and dried in vacuo at 50 °C and then over P_2O_5. Yield: 95 mg (73%). Anal. ($C_{18}H_{24}FeN_{11}O_3S_2$) C, H, N, S.

Crystallographic Structure Determination. X-ray diffraction measurements were performed on a Bruker X8 APEX II CCD diffractometer. Crystal data, data collection parameters, and structure refinement details for HL^D, HL^E, **1D**, and **2D** are given in Tables S1 and S2. The structures were solved by direct methods and refined by full-matrix least-squares techniques. Non-hydrogen atoms were refined with anisotropic displacement parameters. H atoms were placed at calculated positions and refined as riding atoms in the subsequent least-squares model refinements. The isotropic thermal parameters were estimated to be 1.2 times the values of the equivalent isotropic thermal parameters of the atoms to which hydrogens were bonded. The following computer programs were used: structure solution, SHELXS-97;[52] refinement, SHELXL-97;[53] molecular diagrams, ORTEP;[54] computer, Pentium IV; scattering factors.[55] Crystallographic data have been deposited at the Cambridge Crystallographic Data Center with numbers CCDC729370-729373. Copies of data can be obtained, free of charge, on application to CCDC, 12 Union Road, Cambridge CB2 1EZ, U.K. (deposit@ccdc.com.ac.uk).

Cell Lines and Culture Conditions. Human 41 M (ovarian carcinoma) and SK-BR-3 (mammary carcinoma) cells were kindly provided by Lloyd R. Kelland (CRC Centre for Cancer Therapeutics, Institute of Cancer Research, Sutton, U.K.) and Evelyn Dittrich (Department of Medicine I, Medical University of Vienna, Austria), respectively. Cells were grown in 75 cm^2 culture flasks (Iwaki/Asahi Technoglass, Gyouda, Japan) as adherent monolayer cultures in minimal essential medium (MEM) supplemented with 10% heat-inactivated fetal bovine serum, 1 mM sodium pyruvate, 4 mM L-glutamine, and 1% nonessential amino acids (100×) (all purchased from Sigma-Aldrich, Vienna, Austria). Cultures were maintained at 37 °C in a humidified atmosphere containing 5% CO_2.

Cytotoxicity Tests in Cancer Cell Lines. Antiproliferative effects were determined by means of a colorimetric microculture assay (MTT assay, MTT = 3-(4,5-dimethyl-2-thiazolyl)-2,5-diphenyl-2*H*-tetrazolium bromide). Cells were harvested from culture flasks by trypsinization and seeded in 100 μL aliquots into 96-well microculture plates (Iwaki/Asahi Technoglass, Gyouda, Japan) in densities of 4×10^3 cells/well, in order to ensure exponential growth of untreated controls throughout the experiment. After a 24 h preincubation, dilutions of the test compounds in 100 μL/well complete culture medium were added. Because of low aqueous solubility, the test compounds were dissolved in DMSO first and then serially diluted in complete culture medium such that the effective DMSO content did not exceed 0.5%. After exposure for 96 h, all media were replaced by 100 μL/well RPMI 1640 medium (supplemented with 10% heat-inactivated fetal bovine serum and 2 mM L-glutamine) plus 20 μL/well MTT solution in phosphate-buffered saline (5 mg/mL). After incubation for 4 h, the medium/MTT mixtures were removed, and the formazan crystals formed by vital cells were dissolved in 150 μL of DMSO per well. Optical densities at 550 nm were measured with a microplate reader (Tecan Spectra Classic), using a reference wavelength of 690 nm to correct for unspecific absorption. The quantity of vital cells was expressed in terms of T/C values by comparison to untreated control microcultures, and 50% inhibitory concentrations (IC_{50}) were calculated from concentration−effect curves by interpolation. Evaluation is based on mean values from at least three independent experiments, each comprising at least three microcultures per concentration level.

Ribonucleotide Reductase Inhibition. To compare the RR inhibitory potential of $\mathbf{HL^D}$ and $\mathbf{HL^E}$ with that of their corresponding iron complexes **2D** and **2E**, ^{3}H-cytidine incorporation assays were performed.[56] For this purpose, exponentially growing HL60 cells (5×10^6) were incubated with the test substances for 4 h. After the incubation period, the cells were pulsed with ^{3}H-cytidine (0.3125 μCi, 5 nM) for 1 h at 37 °C. Then cells were collected and washed with PBS. For cell lysis, the cell pellets were resuspended in a lysis buffer containing 10 mM EDTA, 50 mM Tris (pH 8.0), and 0.5% sodium lauryl sarcosine and frozen at −20 °C. For DNA extraction, the cell lysate was incubated with 20 units RNAse at 37 °C for 1 h followed by 24 h of treatment with 150 μg of proteinase K. Subsequently DNA was extracted using standard procedures. After precipitation with ethanol, DNA was resuspended in water, DNA content was measured, and radioactivity was determined.[57]

Acknowledgment. The authors are indebted to the FFG (Austrian Research Promotion Agency, Project No. 811591), to the Austrian Council for Research and Technology Development, and to COST (European Cooperation in the Field of Scientific and Technical Research) for financial support. We also thank Florian Biba and Anatoly Dobrov for thermogravimetric and mass spectrometry measurements, respectively.

Supporting Information Available: Literature reaction pathways to Triapine, cyclic voltammogram of the iron(III) complex **2D** in H_2O/DMSO, supplementary data on the electrochemical behavior of the complexes in DMSO and CH_3CN, spectroscopic (^{1}H and ^{13}C NMR, IR, and UV−vis) and microanalytical data for all novel compounds, crystallographic data in CIF format, details of X-ray data collection and refinement, results of X-ray diffraction studies of $\mathbf{HL^E}$, packing diagrams of $\mathbf{HL^D}$, $\mathbf{HL^E}$, **1D**, and concentration−effect curves of $\mathbf{HL^A}$, **1A**, **2A**, $\mathbf{HL^B}$, **1B**, and **2B**. This material is available free of charge via the Internet at http://pubs.acs.org.

References

(1) Casas, J. S.; Garcia-Tasende, M. S.; Sordo, J. Main group metal complexes of semicarbazones and thiosemicarbazones. A structural review. *Coord. Chem. Rev.* **2000**, *209*, 197–261.

(2) Lobana, T. S.; Rekha; Butcher, R. J.; Castineiras, A.; Bermejo, E.; Bharatam, P. V. Bonding trends of thiosemicarbazones in mononuclear and dinuclear copper(I) complexes: syntheses, structures, and theoretical aspects. *Inorg. Chem.* **2006**, *45*, 1535–1542.

(3) Barbazan, P.; Carballo, R.; Casas, J. S.; Garcia-Martinez, E.; Pereiras-Gabian, G.; Sanchez, A.; Vazquez-Lopez, E. M. Synthesis and characterization of new trimeric rhenium(I) complexes. The influence of steric factors on the size of pyrazolonaterhenium(I) metallomacrocycles. *Inorg. Chem.* **2006**, *45*, 7323–7330.

(4) Pedrido, R.; Romero, M. J.; Bermejo, M. R.; Gonzalez-Noya, A. M.; Garcia-Lema, I.; Zaragoza, G. Metal-catalyzed oxidation processes in thiosemicarbazones: new complexes with the ligand *N*-{2-([4-*N*-ethylthiosemicarbazone]-methyl)phenyl}-*p*-toluenesulfonamide. *Chem.—Eur. J.* **2008**, *14*, 500–512.

(5) West, D. X.; Padhye, S. B.; Sonawane, P. B. Structural and physical correlations in the biological properties of transition metal heterocyclic thiosemicarbazone and *S*-alkyl dithiocarbazate complexes. *Struct. Bonding* (*Berlin*) **1991**, *76*, 1–50.

(6) Bonnitcha, P. D.; Vavere, A. L.; Lewis, J. S.; Dilworth, J. R. In vitro and in vivo evaluation of bifunctional bisthiosemicarbazone ^{64}Cu-complexes for the positron emission tomography imaging of hypoxia. *J. Med. Chem.* **2008**, *51*, 2985–2991.

(7) Brockman, R. W.; Thomson, J. R.; Bell, M. J.; Skipper, H. E. Observations on the antileukemic activity of pyridine-2-carboxaldehyde thiosemicarbazone and thiocarbohydrazone. *Cancer Res.* **1956**, *16*, 167–170.

(8) French, F. A.; Blanz, E. J., Jr. The carcinostatic activity of thiosemicarbazones of formyl heteroaromatic compounds. III. Primary correlation. *J. Med. Chem.* **1966**, *9*, 585–589.

(9) DeConti, R. C.; Toftness, B. R.; Agrawal, K. C.; Tomchick, R.; Mead, J. A. R.; Bertino, J. R.; Sartorelli, A. C.; Creasey, W. A. Clinical and pharmacological studies with 5-hydroxy-2-formylpyridine thiosemicarbazone. *Cancer Res.* **1972**, *32*, 1455–1462.

(10) Krakoff, I. H.; Etcubanas, E.; Tan, C.; Mayer, K.; Bethune, V.; Burchenal, J. H. Clinical trial of 5-hydroxypicolinaldehyde thiosemicarbazone (5-HP; NSC-107392), with special reference to its iron-chelating properties. *Cancer Chemother. Rep.* **1974**, *58*, 207–212.

(11) Yu, Y.; Wong, J.; Lovejoy, D. B.; Kalinowski, D. S.; Richardson, D. R. Chelators at the cancer coalface: desferrioxamine to triapine and beyond. *Clin. Cancer Res.* **2006**, *12*, 6876–6883.

(12) Ma, B.; Goh, B. C.; Tan, E. H.; Lam, K. C.; Soo, R.; Leong, S. S.; Wang, L. Z.; Mo, F.; Chan, A. T. C.; Zee, B.; Mok, T. A multicenter phase II trial of 3-aminopyridine-2-carboxaldehyde thiosemicarbazone (3-AP, Triapine) and gemcitabine in advanced non-small-cell lung cancer with pharmacokinetic evaluation using peripheral blood mononuclear cells. *Invest. New Drugs* **2008**, *26*, 169–173.

(13) Karp, J. E.; Giles, F. J.; Gojo, I.; Morris, L.; Greer, J.; Johnson, B.; Thein, M.; Sznol, M.; Low, J. A phase I study of the novel ribonucleotide reductase inhibitor 3-aminopyridine-2-carboxaldehyde thiosemicarbazone (3-AP, Triapine) in combination with the nucleoside analog fludarabine for patients with refractory acute leukemias and aggressive myeloproliferative disorders. *Leuk. Res.* **2008**, *32*, 71–77.

(14) Mackenzie, M. J.; Saltman, D.; Hirte, H.; Low, J.; Johnson, C.; Pond, G.; Moore, M. J. A Phase II study of 3-aminopyridine-2-carboxaldehyde thiosemicarbazone (3-AP) and gemcitabine in advanced pancreatic carcinoma. A trial of the Princess Margaret Hospital Phase II consortium. *Invest. New Drugs* **2007**, *25*, 553–558.

(15) Knox, J. J.; Hotte, S. J.; Kollmannsberger, C.; Winquist, E.; Fisher, B.; Eisenhauer, E. A. Phase II study of Triapine in patients with metastatic renal cell carcinoma: a trial of the National Cancer Institute of Canada Clinical Trials Group (NCIC IND.161). *Invest. New Drugs* **2007**, *25*, 471–477.

(16) Moore, E. C.; Zedeck, M. S.; Agrawal, K. C.; Sartorelli, A. C. Inhibition of ribonucleoside diphosphate reductase by 1-formylisoquinoline thiosemicarbazone and related compounds. *Biochemistry* **1970**, *9*, 4492–4498.

(17) French, F. A.; Blanz, E. J., Jr.; Shaddix, S. C.; Brockman, R. W. α-(*N*)-Formylheteroaromatic thiosemicarbazones. Inhibition of tumor-derived ribunucleoside diphosphate reductase and correlation with in vivo antitumor activity. *J. Med. Chem.* **1974**, *17*, 172–181.

(18) Moore, E. C.; Sartorelli, A. C. Inhibition of ribonucleotide reductase by α-(N)-heterocyclic carboxaldehyde thiosemicarbazones. *Pharmacol. Ther.* **1984**, *24*, 439–447.

(19) Liu, M.-C.; Lin, T.-S.; Sartorelli, A. C. Chemical and biological properties of cytotoxic α-(N)-heterocyclic carboxaldehyde thiosemicarbazones. *Prog. Med. Chem.* **1995**, *32*, 1–35.

(20) Shao, J.; Zhou, B.; Chu, B.; Yen, Y. Ribonucleotide reductase inhibitors and future drug design. *Curr. Cancer Drug Targets* **2006**, *6*, 409–431.

(21) Kolberg, M.; Strand, K. R.; Graff, P.; Andersson, K. K. Structure, function, and mechanism of ribonucleotide reductases. *Biochim. Biophys. Acta* **2004**, *1699*, 1–34.
(22) Tanaka, H.; Arakawa, H.; Yamaguchi, T.; Shlralsh, K.; Fukuda, S.; Matsui, K.; Take, Y.; Nakamura, Y. A ribonucleotide reductase gene involved in a p53-dependent cell-cycle checkpoint for DNA damage. *Nature* **2000**, *404*, 42–49.
(23) Nakano, K.; Balint, E.; Ashcroft, M.; Vousden, K. H. A ribonucleotide reductase gene is a transcriptional target of p53 and p73. *Oncogene* **2000**, *19*, 4283–4289.
(24) Kowol, C. R.; Berger, R.; Eichinger, R.; Roller, A.; Jakupec, M. A.; Schmidt, P. P.; Arion, V. B.; Keppler, B. K. Gallium(III) and iron(III) complexes of α-N-heterocyclic thiosemicarbazones: synthesis, characterization, cytotoxicity, and interaction with ribonucleotide reductase. *J. Med. Chem.* **2007**, *50*, 1254–1265.
(25) Shao, J.; Zhou, B.; Di Bilio, A. J.; Zhu, L.; Wang, T.; Qi, C.; Shih, J.; Yen, Y. A ferrous-triapine complex mediates formation of reactive oxygen species that inactivate human ribonucleotide reductase. *Mol. Cancer Ther.* **2006**, *5*, 586–592.
(26) Finch, R. A.; Liu, M.-C.; Cory, A. H.; Cory, J. G.; Sartorelli, A. C. Triapine (3-aminopyridine-2-carboxaldehyde thiosemicarbazone; 3-AP). An inhibitor of ribonucleotide reductase with antineoplastic activity. *Adv. Enzyme Regul.* **1999**, *39*, 3–12.
(27) Chaston, T. B.; Lovejoy, D. B.; Watts, R. N.; Richardson, D. R. Examination of the antiproliferative activity of iron chelators: multiple cellular targets and the different mechanism of action of triapine compared with desferrioxamine and the potent pyridoxal isonicotinoyl hydrazone analogue 311. *Clin. Cancer Res.* **2003**, *9*, 402–414.
(28) Wang, Y.; Liu, M.-C.; Lin, T.-S.; Sartorelli, A. C. Synthesis and antitumor activity of 3- and 5-hydroxy-4-methylpyridine-2-carboxaldehyde thiosemicarbazones. *J. Med. Chem.* **1992**, *35*, 3667–3671.
(29) Niu, C.; Li, J.; Doyle, T. W.; Chen, S.-H. Synthesis of 3-amino-2-pyridinecarboxaldehyde thiosemicarbazone (3-AP). *Tetrahedron* **1998**, *54*, 6311–6318.
(30) Li, J.; Zheng, L.-M.; King, I.; Doyle, T. W.; Chen, S.-H. Syntheses and antitumor activities of potent inhibitors of ribonucleotide reductase: 3-amino-4-methylpyridine-2-carboxaldehyde-thiosemicarbazone (3-AMP), 3-amino-pyridine-2-carboxaldehyde-thiosemicarbazone (3-AP) and its water-soluble prodrugs. *Curr. Med. Chem.* **2001**, *8*, 121–133.
(31) Kelly, T. A.; McNeil, D. W. A simple method for the protection of aryl amines as their *t*-butylcarbamoyl (Boc) derivatives. *Tetrahedron Lett.* **1994**, *35*, 9003–9006.
(32) Venuti, M. C.; Stephenson, R. A.; Alvarez, R.; Bruno, J. J.; Strosberg, A. M. Inhibitors of cyclic AMP phosphodiesterase. 3. Synthesis and biological evaluation of pyrido and imidazolyl analogs of 1,2,3,5-tetrahydro-2-oxoimidazo[2,1-*b*]quinazoline. *J. Med. Chem.* **1988**, *31*, 2136–2145.
(33) Sreekanth, A.; Fun, H.-K.; Kurup, M. R. P. Structural and spectral studies of an iron(III) complex $[Fe(Pranthas)_2][FeCl_4]$ derived from 2-acetylpyridine-*N*(4),*N*(4)-(butane-1,4-diyl) thiosemicarbazone (HPranthas). *J. Mol. Struct.* **2005**, *737*, 61–67.
(34) Kowol, C. R.; Eichinger, R.; Jakupec, M. A.; Galanski, M.; Arion, V. B.; Keppler, B. K. Effect of metal ion complexation and chalcogen donor identity on the antiproliferative activity of 2-acetylpyridine *N*,*N*-dimethyl(chalcogen)semicarbazones. *J. Inorg. Biochem.* **2007**, *101*, 1946–1957.
(35) Pessoa, M. M. B.; Andrade, G. F. S.; Paoli Monteiro, V. R.; Temperini, M. L. A. 2-Formylpyridinethiosemicarbazone and methyl derivatives: spectroscopic studies. *Polyhedron* **2001**, *20*, 3133–3141.
(36) Bermejo, E.; Castifieiras, A.; Fostiak, L. M.; Garcia, I.; Llamas-Saiz, A. L.; Swearingen, J. K.; West, D. X. Synthesis; characterization and molecular structure of 2-pyridylformamide *N*(4)-dimethylthiosemicarbazone and some five-coordinated zinc(II) and cadmium(II) complexes. *Z. Naturforsch., B: Chem. Sci.* **2001**, *56*, 1297–1305.
(37) West, D. X.; Bain, G. A.; Butcher, R. J.; Jasinski, J. P.; Li, Y.; Pozdniakiv, R. Y. Structural studies of three isomeric forms of heterocyclic N(4)-substituted thiosemicarbazones and two nickel(II) complexes. *Polyhedron* **1996**, *15*, 665–674.
(38) Odenike, O. M.; Larson, R. A.; Gajria, D.; Dolan, M. E.; Delaney, S. M.; Karrison, T. G.; Ratain, M. J.; Stock, W. Phase I study of the ribonucleotide reductase inhibitor 3-aminopyridine-2-carboxaldehyde-thiosemicarbazone (3-AP) in combination with high dose cytarabine in patients with advanced myeloid leukemia. *Invest. New Drugs* **2008**, *26*, 233–239.
(39) *CRC Handbook of Chemistry and Physics*; Lide, D. R., Ed.; CRC Press: Boca Raton, FL, 2004.
(40) Kowol, C. R.; Reisner, E.; Chiorescu, I.; Arion, V. B.; Galanski, M.; Deubel, D. V.; Keppler, B. K. An electrochemical study of antineoplastic gallium, iron and ruthenium complexes with redox non-innocent α-N-heterocyclic chalcogensemicarbazones. *Inorg. Chem.* **2008**, *47*, 11032–11047.
(41) Richardson, D. R.; Kalinowski, D. S.; Richardson, V.; Sharpe, P. C.; Lovejoy, D. B.; Islam, M.; Bernhardt, P. V. 2-Acetylpyridine thiosemicarbazones are potent iron chelators and antiproliferative agents: redox activity, iron complexation and characterization of their antitumor activity. *J. Med. Chem.* **2009**, *52*, 1459–1470.
(42) Easmon, J.; Heinisch, G.; Hofmann, J.; Langer, T.; Grunicke, H. H.; Fink, J.; Purstinger, G. Thiazolyl and benzothiazolyl hydrazones derived from α-(*N*)-acetylpyridines and diazines: synthesis, antiproliferative activity and CoMFA studies. *Eur. J. Med. Chem.* **1997**, *32*, 397–408.
(43) West, D. X.; Swearingen, J. K.; Valdes-Martinez, J.; Hernandez-Ortega, S.; El-Sawaf, A. K.; Van Meurs, F.; Castineiras, A.; Garcia, I.; Bermejo, E. Spectral and structural studies of iron(III), cobalt(II,III) and nickel(II) complexes of 2-pyridineformamide *N*(4)-methylthiosemicarbazone. *Polyhedron* **1999**, *18*, 2919–2929.
(44) Mendes, I. C.; Soares, M. A.; dos Santos, R. G.; Pinheiro, C.; Beraldo, H. Gallium(III) complexes of 2-pyridineformamide thiosemicarbazones: cytotoxic activity against malignant glioblastoma. *Eur. J. Med. Chem.* **2009**, *44*, 1870–1877.
(45) Yuan, J.; Lovejoy, D. B.; Richardson, D. R. Novel di-2-pyridyl-derived iron chelators with marked and selective antitumor activity: in vitro and in vivo assessment. *Blood* **2004**, *104*, 1450–1458.
(46) Easmon, J.; Heinisch, G.; Holzer, W.; Rosenwirth, B. Novel thiosemicarbazones derived from formyl- and acyldiazines: synthesis, effects on cell proliferation, and synergism with antiviral agents. *J. Med. Chem.* **1992**, *35*, 3288–3296.
(47) Richardson, D. R.; Sharpe, P. C.; Lovejoy, D. B.; Senaratne, D.; Kalinowski, D. S.; Islam, M.; Bernhardt, P. V. Dipyridyl thiosemicarbazone chelators with potent and selective antitumor activity form iron complexes with redox activity. *J. Med. Chem.* **2006**, *49*, 6510–6521.
(48) Agrawal, K. C.; Lee, M. H.; Booth, B. A.; Moore, E. C.; Sartorelli, A. C. Potential antitumor agents. 11. Inhibitors of alkaline phosphatase, an enzyme involved in the resistance of neoplastic cells to 6-thiopurines. *J. Med. Chem.* **1974**, *17*, 934–938.
(49) McElhinney, R. S. Derivatives of thiocarbamic acid. I. Preparation of 4-substituted thiosemicarbazides. *J. Chem. Soc.* **1966**, *10*, 950–955.
(50) Castineiras, A.; Garcia, I.; Bermejo, E.; West, D. X. Structural and spectral studies of 2-pyridineformamide thiosemicarbazone and its complexes prepared with zinc halides. *Z. Naturforsch., B: Chem. Sci.* **2000**, *55*, 511–518.
(51) Barette, W. C., Jr.; Johnson, H. W., Jr.; Sawyer, D. T. Voltammetric evaluation of the effective acidities (pKa′) for Broensted acids in aprotic solvents. *Anal. Chem.* **1984**, *56*, 1890–1898.
(52) Sheldrick, G. M. *SHELXS-97, Program for Crystal Structure Solution*; University Gottingen: Gottingen, Germany, 1997.
(53) Sheldrick, G. M. *SHELXL-97, Program for Crystal Structure Refinement*; University Gottingen: Gottingen, Germany, 1997.
(54) Johnson, G. K. Report ORNL-5138; Oak Ridge National Laboratory; Oak Ridge, TN, 1976.
(55) *International Tables for X-ray Crystallography*; Kluwer Academic Press: Dodrecht, The Netherlands, 1992; Vol. C, Tables 4.2.6.8 and 6.1.1.4.
(56) Heffeter, P.; Jakupec, M. A.; Korner, W.; Wild, S.; von Keyserlingk, N. G.; Elbling, L.; Zorbas, H.; Korynevska, A.; Knasmuller, S.; Sutterluty, H.; Micksche, M.; Keppler, B. K.; Berger, W. Anticancer activity of the lanthanum compound [tris(1,10-phenanthroline)lanthanum(III)]trithiocyanate (KP772; FFC24). *Biochem. Pharmacol.* **2006**, *71*, 426–440.
(57) Szekeres, T.; Gharehbaghi, K.; Fritzer, M.; Woody, M.; Srivastava, A.; van't Riet, B.; Jayaram, H. N.; Elford, H. L. Biochemical and antitumor activity of trimidox, a new inhibitor of ribonucleotide reductase. *Cancer Chemother. Pharmacol.* **1994**, *34*, 63–66.

2.4 Fluorescence properties and cellular distribution of the investigational anticancer drug triapine (3-aminopyridine-2-carboxaldehyde thiosemicarbazone) and its zinc(II) complex.

Christian R Kowol, Robert Trondl, Vladimir B Arion, Michael A Jakupec, Irene Lichtscheidl, Bernhard K Keppler

Dalton Transactions **2010** 39:3.704-706

Fluorescence properties and cellular distribution of the investigational anticancer drug Triapine (3-aminopyridine-2-carboxaldehyde thiosemicarbazone) and its zinc(II) complex†

Christian R. Kowol,[a] Robert Trondl,[a] Vladimir B. Arion,*[a] Michael A. Jakupec,[a] Irene Lichtscheidl[b] and Bernhard K. Keppler*[a]

Received 14th September 2009, Accepted 9th October 2009
First published as an Advance Article on the web 22nd October 2009
DOI: 10.1039/b919119b

Triapine (3-aminopyridine-2-carboxaldehyde thiosemicarbazone), which entered several phase I and II clinical trials as an antitumor chemotherapeutic agent, was found to possess intrinsic fluorescence properties ($\lambda_{ex} = 360$ nm), which enabled us to monitor the uptake and intracellular distribution in living human cancer cells by fluorescence microscopy.

The antineoplastic activity of α-*N*-heterocyclic thiosemicarbazones was discovered several decades ago.[1] Currently the most promising drug candidate of this class of compounds is Triapine (3-aminopyridine-2-carboxaldehyde thiosemicarbazone, 3-AP), which entered several phase I and II clinical trials as an antitumor chemotherapeutic agent.[2] Triapine is a potent inhibitor of the enzyme ribonucleotide reductase, which catalyzes the reduction of ribonucleotides to deoxyribonucleotides and is essential for cell proliferation.[3] The enzyme consists of two homodimeric subunits R1 and R2. The latter contains a diiron center and a tyrosyl radical.[4] Although the mechanism of action of Triapine is not fully understood, at least at the molecular level, the active species of Triapine is presumed to be an iron complex which is able to generate reactive oxygen species (ROS) and subsequently destroy the tyrosyl radical in the R2 subunit of ribonucleotide reductase.[5] It should also be noted that nothing is known about the cellular distribution of this investigational anticancer drug.

We discovered that Triapine possesses intrinsic fluorescence when light-irradiated at around $\lambda = 360$ nm. This enabled us to monitor for the first time the uptake and intracellular distribution of an α-*N*-heterocyclic thiosemicarbazone in living human cancer cells by fluorescence microscopy. The results of this study are reported herein.

In addition we synthesized the first zinc(II) complex of Triapine (Scheme 1), considering that coordination of α-*N*-heterocyclic thiosemicarbazones to zinc can increase the antineoplastic activity both *in vitro*[6] and *in vivo*,[7] and compared its properties with those of the metal-free Triapine.

The yellow complex [Zn(Triapine)Cl_2]·HCl (**1**)‡ was prepared by reaction of $ZnCl_2$ with Triapine in a 1 : 1 molar ratio in methanol in the presence of 2 equiv of 12 M HCl. In the absence of hydrochloric acid in ethanol, [Zn(Triapine)Cl_2] precipitated with a small amount (<5%) of unidentified by-product. The mother liquor generated single crystals of [Zn(Triapine)Cl_2]·EtOH. The results of an X-ray crystallographic study of the latter are shown in Fig. 1, along with selected bond lengths and angles.§ The geometry around the five-coordinate zinc(II) bound to the neutral tridentate Triapine with *NNS* donor atoms and two chlorido ligands is intermediate between square-pyramidal and trigonal-bipyramidal ($\tau = 0.34$).[8]

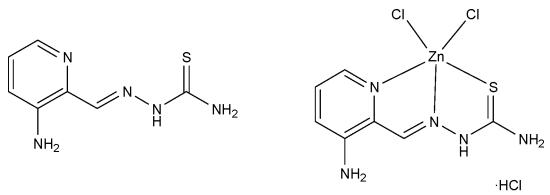

Triapine [Zn(Triapine)Cl_2]·HCl (**1**)

Scheme 1

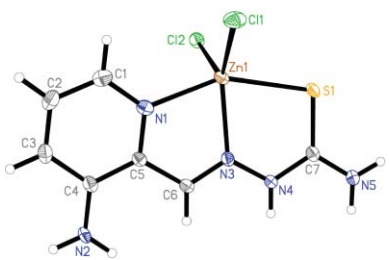

Fig. 1 ORTEP plot of the complex [Zn(Triapine)Cl_2] with thermal ellipsoids at 50% probability level. Selected bond distances (Å) and angles (deg): Zn–Cl1, 2.2657(5); Zn–Cl2, 2.3038(5); Zn–S, 2.5016(5); Zn–N1, 2.1486(16); Zn–N3, 2.1378(15); N1–Zn–S, 151.46(4); N3–Zn–Cl1, 131.02(4); N3–Zn–Cl2, 113.60(4).

The UV/vis spectrum of Triapine in H_2O exhibits an absorption band of the lowest energy at 359 nm, which is 6 nm bathochromically shifted in the spectrum of the zinc(II) complex **1** (Fig. 2). Both compounds show very similar emission spectra with a maximum at 457 nm when irradiated at $\lambda_{ex} = 360$ nm (Fig. 2). The quantum yields of Triapine and **1** in H_2O are 0.018 and 0.021 (each value ± 15%), respectively, with quinine sulfate dihydrate in 0.1 M $HClO_4$ as the standard.

In literature, several intrinsically fluorescent monothiosemicarbazones were documented as sensors for metal ion detection.[9] Zinc(II) complexes of bis(thiosemicarbazones) were reported with

[a]*University of Vienna, Institute of Inorganic Chemistry, Währingerstr. 42, A-1090, Vienna, Austria. E-mail: vladimir.arion@univie.ac.at, bernhard.keppler@univie.ac.at; Fax: +43 1 4277 52680; Tel: +43 1 4277 52615*
[b]*University of Vienna, Institution of Cell Imaging and Ultrastructure Research, Althanstr. 14, A-1090, Vienna, Austria*

† Electronic supplementary information (ESI) available: Experimental details and UV/vis kinetic of **1**·HCl in phosphate buffered solution. CCDC reference number 732708. For ESI and crystallographic data in CIF or other electronic format see DOI: 10.1039/b919119b

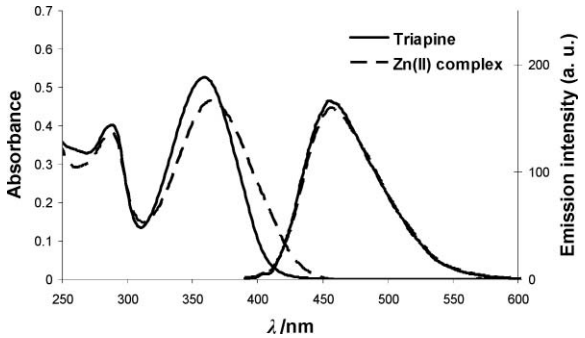

Fig. 2 UV/vis (30 μM) and fluorescence (5 μM, $\lambda_{ex} = 360$ nm) spectra of Triapine and its zinc(II) complex (**1**) in H_2O (maximum content of DMSO = 0.5%).

quantum yields in DMSO in the same range as the compounds studied herein.[10]

UV/vis measurements of **1** in phosphate buffered solution at pH 7.4 containing 0.9% sodium chloride showed only small changes over 15 h suggesting that the chlorido complex is still the major species (see ESI†).

The cellular distribution of both compounds was studied by fluorescence microscopy in living SW480 cells (colon carcinoma, human). Bright-field images of SW480 cells treated with Triapine (0.25 mM in 0.5% DMSO/PBS) or **1** (0.50 mM in PBS) (Fig. 3A, B) were taken prior to fluorescence imaging to ensure that the studied cells were morphologically intact. Fluorescence images (Fig. 3C, D) showed that both compounds are taken up by cells within minutes and that cellular distribution of the compounds can be visualized. Both Triapine and its zinc complex have a striking affinity to the nuclear membrane and to a more diffuse structure in the cytoplasm. Fluorescence images were scaled in pseudocolors to highlight cellular regions with particularly high affinity to the substances (Fig. 3E, F). Remarkably, the zinc complex binds to a substructure within the nucleus, suggestive of nucleoli. Immunostaining of the nucleolar protein fibrillarin and co-staining with **1** unequivocally proved that these substructures are indeed nucleoli (Fig. 3G, H). In contrast, a strong affinity of Triapine to the nucleoli was not discernible. Nevertheless, the distinct differences in the distribution of the two substances suggests that zinc(II) remains coordinated to Triapine within the cell.

The cytotoxic potencies of Triapine and **1** were determined in SW480 (colon carcinoma) and 41M (ovarian carcinoma) cells by means of the colorimetric MTT assay. Comparison of the two compounds did not reveal meaningful differences. The IC_{50} values of Triapine in SW480 and 41M cells are 0.55 ± 0.2 and 0.45 ± 0.03 μM, respectively, whereas **1** shows IC_{50} values of 0.54 ± 0.02 and 0.52 ± 0.02 μM, respectively. Short time incubation in the MTT and trypan blue exclusion assay showed clearly that the compounds have no significant impact on cell viability in the concentrations and exposure times applied for fluorescence microscopy.

In accordance with our findings, other groups suggested considerable uptake of zinc bis(thiosemicarbazone) complexes into the nucleolus.[11] Furthermore, the affinity of nucleoli for exogenous zinc bound to diphenylthiocarbazone was observed in HeLa cells.[12] In literature the presence of physiological zinc in nucleoli of

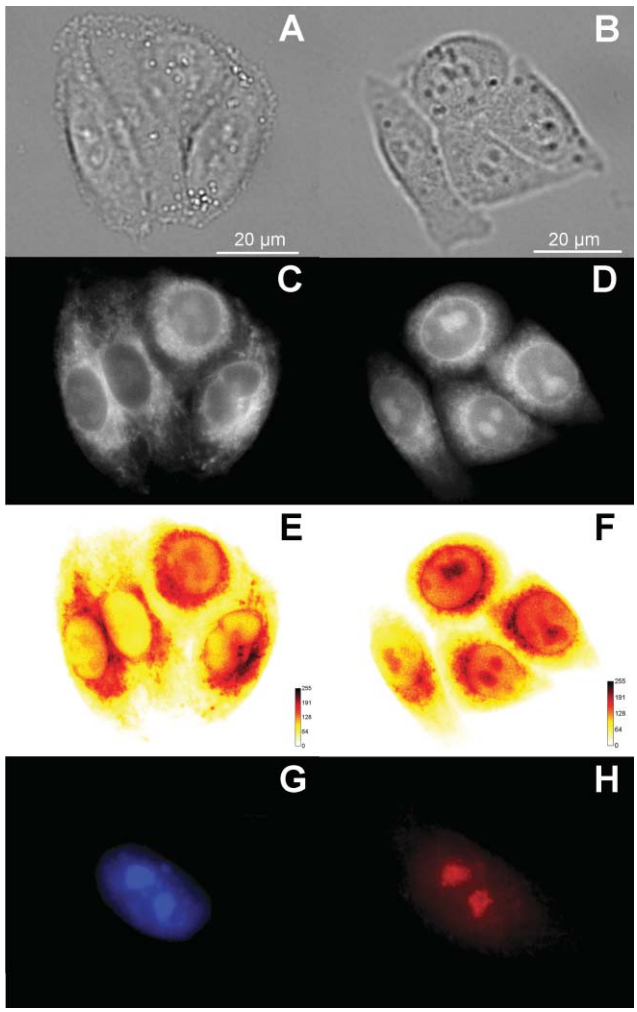

Fig. 3 Live-cell images of SW480 colon carcinoma cells incubated with Triapine (A, C, E) or **1** (B, D, F). (A, B) Bright-field images; (C, D) fluorescence images; (E, F) pseudocolor fluorescence images. Co-staining with **1** (G) and immunofluorescence of the nucleolar protein fibrillarin (H), confirming the localization of the compound in nucleoli.

oocytes of starfish was reported, suggesting that zinc(II) mediates the affinity of the complexes to nucleoli.[13]

Our results demonstrate that Triapine can be visualized with fluorescence microscopy in living cells without any conjugation of fluorophores. Although the cytotoxicities of metal-free Triapine and its zinc(II) complex are very similar *in vitro*, the cellular distributions, especially with regard to the nucleus are distinctly different.

The intrinsic fluorescence properties of Triapine, a feature fairly uncommon among anticancer drugs, may prove useful by providing opportunities to study the influence of cell type and phenotypic changes (*e.g.*, resistance mechanisms) as well as the impact of other drugs on the cellular distribution of this compound without sophisticated labelling techniques.

Acknowledgements

We thank the FFG (Austrian Research Promotion Agency, project no. 811591) and the Austrian Council for Research and Technology Development for financial support, Prof. F. Dickert

for providing the fluorescence spectrometer, Prof. M. Galanski for NMR measurements and Prof. W. Berger for helpful discussions.

Notes and references

‡ **Synthesis of [Zn(Triapine)Cl_2]·HCl (1).** 3-aminopyridine-2-carboxaldehyde thiosemicarbazone (Triapine) (50 mg, 0.26 mmol) dissolved in boiling methanol (10 mL) was slowly added to a mixture of zinc(II) chloride (35 mg, 0.26 mmol) and conc. HCl (43 μL) in methanol (5 mL) at 50 °C. The mixture was stirred for 10 min at 50 °C. The yellow precipitate was filtered off, washed with methanol, diethyl ether, dried *in vacuo* and over P_2O_5. Yield: 62 mg (66%). Anal. Calc. for $C_7H_9Cl_2N_5SZn$·HCl: C, 22.85; H, 2.74; N, 19.03; S, 8.71. Found: C, 23.11; H, 2.71; N, 18.87; S, 8.77%. ESI-MS in MeOH (negative): m/z 292, [Zn(Triapine)Cl_2–2H–Cl]$^-$. IR data, ν_{max}(KBr)/cm^{-1} (selected bands): 3439 m, 3351 s, 3275 m, 3195 m, 1640 s, 1619 s, 1542 s, 1471 s, 1387 m, 1269 s, 1099 m, 947 m, 919 m, 834 m, 782 s, 562 br. m, 482 m. UV–vis, $\lambda_{max}(H_2O)$/nm (ε, M^{-1}cm^{-1}): 216 (17840), 234sh (16500), 288 (12630), 365 (15440). ^{1}H NMR (500.10 MHz, DMSO-d_6): δ 11.91 (s, 1H, NH), 8.54 (s, 1H, NH_2), 8.33 (s, 1H, HC=N), 8.30 (s, 1H, NH_2), 8.04 (d, $^3J_{H,H}$ = 4.4 Hz, 1H, py), 7.68 (d, $^3J_{H,H}$ = 8.5 Hz, 1H, py), 7.56 (m, 1H, py), 7.06 (v. br. s, 2H, NH_2). ^{13}C{^{1}H} NMR (125.81 MHz, DMSO-d_6): δ 178.6 (C=S), 146.0 ($C_{q,\,py}$), 137.0 (HC=N), 131.3 (C_{py}), 130.2 (C_{py}), 127.0 ($C_{q,\,py}$), 126.5 (C_{py}).

§ Crystal data for [Zn(Triapine)Cl_2]·EtOH: $C_9H_{15}Cl_2N_5OSZn$, M_r = 377.61, crystal size 0.20 × 0.10 × 0.03 mm^3, monoclinic, space group $P2_1/c$, a = 11.4639(7), b = 10.2716(5), c = 12.7509(7) Å, β = 99.422(4)°, V = 1481.20(4) Å^3, Z = 4, ρ_c = 1.693 g cm^{-3}, λ(Mo-Kα) = 0.71073 Å, μ(Mo-Kα) = 2.158 mm^{-1}, T = 100 K, 61508 reflections measured, 4342 unique (R_{int} = 0.0692), R_1 = 0.0274 ($I > 2\sigma(I)$), wR_2 = 0.0642 (all data).

1 R. W. Brockman, J. R. Thomson, M. J. Bell and H. E. Skipper, *Cancer Res.*, 1956, **16**, 167.

2 (*a*) Y. Yu, J. Wong, D. B. Lovejoy, D. S. Kalinowski and D. R. Richardson, *Clin. Cancer Res.*, 2006, **12**, 6876; (*b*) B. Ma, B. C. Goh, E. H. Tan, K. C. Lam, R. Soo, S. S. Leong, L. Z. Wang, F. Mo, A. T. C. Chan, B. Zee and T. Mok, *Invest. New Drugs*, 2008, **26**, 169; (*c*) M. J. Mackenzie, D. Saltman, H. Hirte, J. Low, C. Johnson, G. Pond and M. J. Moore, *Invest. New Drugs*, 2007, **25**, 553; (*d*) J. J. Knox, S. J. Hotte, C. Kollmannsberger, E. Winquist, B. Fisher and E. A. Eisenhauer, *Invest. New Drugs*, 2007, **25**, 471; (*e*) J. E. Karp, F. J. Giles, I. Gojo, L. Morris, J. Greer, B. Johnson, M. Thein, M. Sznol and J. Low, *Leuk. Res.*, 2008, **32**, 71; (*f*) W. R. Schelman, S. Morgan-Meadows, R. Marnocha, F. Lee, J. Eickhoff, W. Huang, M. Pomplun, Z. Jiang, D. Alberti, J. M. Kolesar, P. Ivy, G. Wilding and A. M. Traynor, *Cancer Chemother. Pharmacol.*, 2009, **63**, 1147.

3 R. A. Finch, M.-C. Liu, A. H. Cory, J. G. Cory and A. C. Sartorelli, *Adv. Enzyme Regul.*, 1999, **39**, 3.

4 M. Kolberg, K. R. Strand, P. Graff and K. K. Andersson, *Biochim. Biophys. Acta*, 2004, **1699**, 1.

5 J. Shao, B. Zhou, A. J. Di Bilio, L. Zhu, T. Wang, C. Qi, J. Shih and Y. Yen, *Mol. Cancer Ther.*, 2006, **5**, 586.

6 (*a*) D. Kovala-Demertzi, P. N. Yadav, J. Wiecek, S. Skoulika, T. Varadinova and M. A. Demertzis, *J. Inorg. Biochem.*, 2006, **100**, 1558; (*b*) J. M. Perez, A. I. Matesanz, A. Martin-Ambite, P. Navarro, C. Alonso and P. Souza, *J. Inorg. Biochem.*, 1999, **75**, 255.

7 (*a*) G. Atassi, P. Dumont and J. C. E. Harteel, *Eur. J. Cancer*, 1979, **15**, 451; (*b*) D. Kovala-Demertzi, A. Alexandratos, A. Papageorgiou, P. N. Yadav, P. Dalezis and M. A. Demertzis, *Polyhedron*, 2008, **27**, 2731.

8 A. W. Addison, T. N. Rao, J. Reedijk, J. Van Rijn and G. C. Verschoor, *J. Chem. Soc., Dalton Trans.*, 1984, 1349.

9 (*a*) Y. Yu, L.-R. Lin, K.-B. Yang, X. Zhong, R.-B. Huang and L.-S. Zheng, *Talanta*, 2006, **69**, 103–106; (*b*) J. Vazquez Ruiz, A. Garcia de Torres and J. M. Cano-Pavon, *Talanta*, 1984, **31**, 29.

10 J. P. Holland, F. I. Aigbirhio, H. M. Betts, P. D. Bonnitcha, P. Burke, M. Christlieb, G. C. Churchill, A. R. Cowley, J. R. Dilworth, P. S. Donnelly, J. C. Green, J. M. Peach, S. R. Vasudevan and J. E. Warren, *Inorg. Chem.*, 2007, **46**, 465.

11 A. R. Cowley, J. Davis, J. R. Dilworth, P. S. Donnelly, R. Dobson, A. Nightingale, J. M. Peach, B. Shore, D. Kerr and L. Seymour, *Chem. Commun.*, 2005, 845.

12 G. P. Studzinski, *J. Histochem. Cytochem.*, 1965, **13**, 365.

13 T. Fujii, *Nature*, 1954, **174**, 1108.

2.5 Mechanisms underlying reductant-induced reactive oxygen species formation by anticancer copper(II) compounds

Christian R Kowol, Petra Heffeter, Walter Miklos, Lars Gille, Robert Trondl, Loredana Cappellacci, Walter Berger, Bernhard K Keppler.

Journal of Biological Inorganic Chemistry **2012** 17:3.409-423

J Biol Inorg Chem
DOI 10.1007/s00775-011-0864-x

ORIGINAL PAPER

Mechanisms underlying reductant-induced reactive oxygen species formation by anticancer copper(II) compounds

Christian R. Kowol · Petra Heffeter · Walter Miklos · Lars Gille · Robert Trondl · Loredana Cappellacci · Walter Berger · Bernhard K. Keppler

Received: 19 August 2011 / Accepted: 26 November 2011

Abstract Intracellular generation of reactive oxygen species (ROS) via thiol-mediated reduction of copper(II) to copper(I) has been assumed as the major mechanism underlying the anticancer activity of copper(II) complexes. The aim of this study was to compare the anticancer potential of copper(II) complexes of Triapine (3-aminopyridine-2-carboxaldehyde thiosemicarbazone; currently in phase II clinical trials) and its terminally dimethylated derivative with that of 2-formylpyridine thiosemicarbazone and that of 2,2′-bipyridyl-6-carbothioamide. Experiments on generation of oxidative stress and the influence of biologically relevant reductants (glutathione, ascorbic acid) on the anticancer activity of the copper complexes revealed that reductant-dependent redox cycling occurred mainly outside the cells, leading to generation and dismutation of superoxide radicals resulting in cytotoxic amounts of H_2O_2. However, without extracellular reductants only weak intracellular ROS generation was observed at IC_{50} levels, suggesting that cellular thiols are not involved in copper-complex-induced oxidative stress. Taken together, thiol-induced intracellular ROS generation might contribute to the anticancer activity of copper thiosemicarbazone complexes but is not the determining factor.

C. R. Kowol and P. Heffeter contributed equally to this study.

Electronic supplementary material The online version of this article (doi:10.1007/s00775-011-0864-x) contains supplementary material, which is available to authorized users.

C. R. Kowol · R. Trondl · B. K. Keppler
Institute of Inorganic Chemistry,
University of Vienna, Waehringer Str. 42,
1090 Vienna, Austria

C. R. Kowol · P. Heffeter · W. Berger · B. K. Keppler
Comprehensive Cancer Center,
Medical University Vienna,
Borschkegasse 8a,
1090 Vienna, Austria

C. R. Kowol · P. Heffeter · W. Berger · B. K. Keppler
Research Platform "Translational Cancer Therapy Research",
University of Vienna and Medical University of Vienna,
Vienna, Austria

P. Heffeter · W. Miklos · W. Berger (✉)
Department of Medicine I,
Institute of Cancer Research,
Medical University of Vienna,
Borschkegasse 8a,
1090 Vienna, Austria
e-mail: walter.berger@meduniwien.ac.at

L. Gille
Molecular Pharmacology and Toxicology Unit,
Department of Biomedical Sciences,
University of Veterinary Medicine Vienna,
Veterinaerplatz 1, 1210 Vienna, Austria

L. Cappellacci
Medicinal Chemistry Unit, School of Pharmacy,
University of Camerino, Via S. Agostino 1,
62032 Camerino, Italy

Published online: 22 December 2011

Keywords Thiosemicarbazone · Copper · Anticancer · Reactive oxygen species · Glutathione

Abbreviations

AA	Ascorbic acid
APTSC	3-Aminopyridine-2-carboxaldehyde ^4N,^4N-dimethylthiosemicarbazone
BPYTA	2,2′-Bipyridyl-6-carbothioamide
CCDC	Cambridge Crystallographic Data Centre
DCF-DA	2′,7′-Dichlorofluorescein diacetate
DMF	Dimethylformamide
DMSO	Dimethyl sulfoxide
ESI-MS	Electrospray ionization mass spectrometry
FTSC	2-Formylpyridine thiosemicarbazone
GSH	Glutathione
MTT	3-(4,5-Dimethylthiazol-2-yl)-2,5-diphenyltetrazolium bromide
NAC	*N*-Acetylcysteine
NBT	Nitroblue tetrazolium
NHE	Normal hydrogen electrode
PBS	Phosphate-buffered saline
PI	Propidium iodide
ROS	Reactive oxygen species
RR	Ribonucleotide reductase
SOD	Superoxide dismutase
TSC	α-N-heterocyclic thiosemicarbazone

Introduction

Cancer cells are known to differ distinctly from healthy tissues in their redox metabolism [1–3]. Besides enhanced levels of intracellular reactive oxygen species (ROS), the specific milieu of the solid tumor is often characterized by high metabolic activity, hypoxia, and, in general, reductive conditions [1, 2]. Consequently, interference with the cellular redox homeostasis of cancer cells seems to be an attractive and promising approach for cancer therapy [4, 5]. Copper complexes are known for their redox-active properties under physiological conditions, which led to the synthesis and biological characterization of a number of copper-containing anticancer drugs and radiopharmaceuticals [6–8]. Current knowledge of anticancer copper compounds is primarily based on investigations using complexes of α-N-heterocyclic thiosemicarbazones (TSC) [9, 10], 2,2′-bipyridyl-6-carbothioamide (BPYTA) [11, 12], and 1,10-phenanthroline [13, 14]. Thiosemicarbazones and BPYTA are well-known tridentate chelators and have been used for the synthesis of a wide range of metal complexes including, besides copper, also iron, cobalt, zinc, nickel, and gallium complexes [12, 15–18]. BPYTA [12, 19] and thiosemicarbazones [17, 20] are known for their ribonucleotide reductase (RR) inhibitory potential. One of these, 3-aminopyridine-2-carboxaldehyde thiosemicarbazone (Triapine), has already reached clinical phase I/II evaluation, where it showed promising activity against advanced leukemia [21–24]. With regard to copper complexes, Cu-BPYTA [11] and Cu-TSC [25] were also shown to inhibit the RR tyrosyl radical. Interestingly, co-incubation of copper(II) with Triapine significantly increased its RR inhibitory potential [26]. However, no copper complex of Triapine has been synthesized so far. In addition to the RR inhibition by Cu-TSC, generation of ROS is assumed to be a major mechanism of anticancer activity of many copper complexes in general [9, 25, 27–33]. Crucial for this redox reactivity is the presence of a reducing agent such as dithiothreitol, mercaptoethanol, or the biologically relevant glutathione (GSH), which leads to the reduction of copper(II) to copper(I) [9, 25, 27–30]. The reoxidation of copper(I) with molecular oxygen results in the formation of superoxide radicals ($O_2^{\cdot -}$), which has been confirmed in cell-free systems by EPR spin-trapping experiments [30]. The observation of plasmid DNA cleavage provides further evidence that reaction of Cu-TSC complexes with reducing agents generates ROS [34, 35]. Consequently, it is currently widely suggested that these complexes exert their biological activity by intracellular ROS formation after reaction with cellular thiols such as GSH. In accordance, depletion of the intracellular thiol content was reported after treatment of Ehrlich ascites cells with a pyridoxal thiosemicarbazone copper complex [9]. The aim of this study was, on the one hand, to compare the electrochemical properties as well as anticancer activity of the first copper(II) complexes of Triapine and its terminally dimethylated derivative (3-aminopyridine-2-carboxaldehyde ^4N,^4N-dimethylthiosemicarbazone, APTSC) with those of the already known complexes of 2-formylpyridine thiosemicarbazone (FTSC) and BPYTA. On the other hand, the study focuses on the similarities/differences in their interaction with biologically relevant antioxidants (GSH and ascorbic acid, AA) as well as the role of ROS formation in their anticancer activity against tumor cells.

Materials and methods

All solvents and reagents were obtained from commercial suppliers and used without further purification. FTSC, Triapine, and APTSC·HCl were synthesized according to the methods described in our previous publication [18]. Elemental analyses were conducted with a Carlo Erba microanalyzer at the Microanalytical Laboratory of the University of Vienna and are within ±0.4%, confirming 95% or greater purity. Electrospray ionization mass spectrometry (ESI–MS) was performed with a Bruker Esquire 3000 instrument (Bruker Daltonic, Bremen, Germany). Expected

and experimental isotope distributions were compared. UV–vis spectra were recorded with a PerkinElmer Lambda 650 UV–vis spectrophotometer using samples dissolved in methanol (900–200 nm). Thermogravimetric analysis and differential thermal analysis measurements were performed simultaneously using a Mettler Toledo TGA/SDTA851e apparatus, with a 3 °C/min heating rate under an air atmosphere. For all cell- and molecular biological experiments, the compounds were dissolved in DMSO and diluted into the culture media (or buffer) at the concentrations indicated (DMSO concentrations were always below 0.1%).

Synthesis of metal complexes

Pyridine-2-carboxaldehydethiosemicarbazonato-N,N,S-dichloridocopper(II), [Cu(FTSC)Cl$_2$]

The compound was synthesized following a slightly modified published procedure [36]. FTSC (300 mg, 1.66 mmol) was slowly added to a mixture of copper(II)chloride dihydrate (284 mg, 1.66 mmol) and concentrated HCl (278 µL) in methanol (20 mL) at 50 °C. Subsequently, the mixture was stirred for 1 h at room temperature. The green precipitate was filtered off, washed with methanol and diethyl ether, and dried in vacuo. Yield: 380 mg (73%). Anal. Calcd. for $C_7H_8Cl_2CuN_4S$ (M_r = 314.68): C, 26.72; H, 2.56; N, 17.80. Found: C, 26.83; H, 2.25; N, 17.43. ESI–MS in methanol (positive): *m/z* 242, $[M–H–2Cl]^+$; 521, $[2M–3Cl–2H]^+$. UV–vis (MeOH), λ_{max}, nm (ε, M^{-1} cm^{-1}): 292 (14,200), 326 (9,519)sh, 406 (8,430), 636 (160). EPR [dimethyl sulfoxide (DMSO)/dimethylformamide (DMF) (1:3 v/v); −196 °C]: $g_\perp$ = 2.029, $g_\parallel$ = 2.170; hyperfine coupling constants $A_{\perp Cu}$ = 26.8 G, $A_{\parallel Cu}$ = 179.7 G; superhyperfine coupling constants $A_{\perp N1}$ = 20.1 G, $A_{\parallel N1}$ = 16.8 G; $A_{\perp N2}$ = 7.0 G, $A_{\parallel N2}$ = 22.8 G.

3-Aminopyridine-2-carboxaldehyde thiosemicarbazonato-N,N,S-dichloridocopper(II) monohydrate, [Cu(Triapine)Cl$_2$]·H$_2$O

Triapine (150 mg, 0.77 mmol) dissolved in hot methanol (40 mL) was slowly added to a mixture of copper(II)chloride dihydrate (132 mg, 0.77 mmol) and concentrated HCl (130 µL) in methanol (15 mL) at 60 °C [37]. Subsequently, the mixture was stirred for 1.5 h at room temperature. The green precipitate was filtered off, washed with methanol and diethyl ether, and dried in vacuo. Yield: 181 mg (68%). Anal. Calcd. for $C_7H_9Cl_2CuN_5S·H_2O$ (M_r = 347.71): C, 24.18; H, 3.19; N, 20.14; S, 9.22. Found: C, 24.46; H, 3.09; N, 19.89; S, 9.22. ESI–MS in methanol (negative): *m/z* 291, $[M–2H–Cl]^-$. UV–vis (MeOH), λ_{max}, nm (ε, M^{-1} cm^{-1}): 291 (13,450), 367 (3,290), 443 (9,650), 616 (180). EPR [DMSO/DMF (1:3 v/v); −196 °C]: $g_\perp$ = 2.032, $g_\parallel$ = 2.180; hyperfine coupling constants $A_{\perp Cu}$ = 22.4 G, $A_{\parallel Cu}$ = 181.7 G; superhyperfine coupling constants $A_{\perp N1}$ = 11.4 G, $A_{\parallel N1}$ = 0.0 G; $A_{\perp N2}$ = 12.0 G, $A_{\parallel N2}$ = 34.6 G. Crystals suitable for X-ray data collection were obtained by slow diffusion of acetone into an aqueous solution of the complex.

3-Aminopyridine-2-carboxaldehyde N,N-dimethylthiosemicarbazonato-N,N,S-dichloridocopper(II), [Cu(APTSC)Cl$_2$]

APTSC·HCl (60 mg, 0.23 mmol) dissolved in hot methanol (12 mL) was slowly added to a mixture of copper(II)chloride dihydrate (40 mg, 0.23 mmol) and concentrated HCl (38 µL) in methanol (5 mL). The mixture was stirred for 1 h at room temperature. The green precipitate was filtered off, washed with methanol and diethyl ether, and dried in vacuo. Yield: 73 mg (87%). Anal. Calcd. for $C_9H_{13}Cl_2CuN_5S$ (M_r = 357.75): C, 30.22; H, 3.66; N, 19.58; S, 8.96. Found: C, 30.30; H, 3.76; N, 19.27; S, 8.95. ESI–MS in methanol (negative): *m/z* 319, $[M–2H–Cl]^-$. UV–vis (MeOH), λ_{max}, nm (ε, M^{-1} cm^{-1}): 300 (15,300), 371 (4,146), 458 (15,790), 626 (190). EPR [DMSO/DMF (1:3 v/v); −196 °C]: $g_\perp$ = 2.028, $g_\parallel$ = 2.168; hyperfine coupling constants $A_{\perp Cu}$ = 23.2 G, $A_{\parallel Cu}$ = 185.4 G; superhyperfine coupling constants $A_{\perp N1}$ = 17.0 G, $A_{\parallel N1}$ = 7.2 G; $A_{\perp N2}$ = 20.7 G, $A_{\parallel N2}$ = 24.8 G.

Acetato(3-aminopyridine-2-carboxaldehyde thiosemicarbazonato-N,N,S)copper(II)

Triapine (100 mg, 0.51 mmol) dissolved in hot methanol (25 mL) was slowly added to copper(II)acetate monohydrate (104 mg, 0.52 mmol) in methanol (10 mL) at 50 °C. Subsequently, the mixture was stirred for 2 h at room temperature. The brown precipitate was filtered off, washed with methanol and diethyl ether, and dried in vacuo. Yield: 125 mg (77%). Anal. Calcd. for $C_9H_{11}CuN_5O_2S$ (M_r = 316.83): C, 34.12; H, 3.50; N, 22.10; S, 10.12. Found: C, 34.27; H, 3.54; N, 21.93; S, 9.83. ESI–MS in methanol (positive): *m/z* 257, $[M–OAc]^+$; 515, $[2M–2OAc–H]^+$, 573, $[2M–OAc]^+$. UV–vis (MeOH), λ_{max}, nm (ε, M^{-1} cm^{-1}): 291 (17,040), 368 (4,130), 443 (12,220), 616 (130). EPR [DMSO/DMF (1:3 v/v); −196 °C]: $g_\perp$ = 2.031, $g_\parallel$ = 2.191; hyperfine coupling constants $A_{\perp Cu}$ = 26.0 G, $A_{\parallel Cu}$ = 183.2 G; superhyperfine coupling constants $A_{\perp N1}$ = 9.0 G, $A_{\parallel N1}$ = 27.2 G; $A_{\perp N2}$ = 14.6 G, $A_{\parallel N2}$ = 16.3 G.

2,2′-Bipyridyl-6-carbothioamido-N,N,S-dichloridocopper(II), [Cu(BPYTA)Cl$_2$]

The compound was synthesized following a published procedure [19]. Anal. Calcd. for $C_{11}H_9Cl_2CuN_3S·0.5H_2O$

($M_r = 358.73$): C, 36.83; H, 2.81; N, 11.71; S, 8.94. Found: C, 36.76; H, 2.74; N, 11.49; S, 8.97. ESI–MS in methanol (negative): m/z 347, $[M–H]^-$; 659, $[2M–Cl–2H]^-$. EPR [DMSO/DMF (1:3 v/v); −196 °C]: $g_\perp = 2.033$, $g_\parallel = 2.189$; hyperfine coupling constants $A_{\perp Cu} = 18.9$ G, $A_{\parallel Cu} = 180.4$ G; superhyperfine coupling constants $A_{\perp N1} = 10.3$ G, $A_{\parallel N1} = 30.6$ G; $A_{\perp N2} = 15.3$ G, $A_{\parallel N2} = 14.6$ G.

Electrochemistry

Cyclic voltammograms were measured in a three-electrode cell using a 2.0-mm-diameter glassy carbon working electrode, a platinum auxiliary electrode, and an Ag|AgCl reference electrode containing 3 M NaCl. Measurements were performed at room temperature using an EG & G PARC 273A potentiostat/galvanostat. Deaeration of solutions was accomplished by passing a stream of argon through the solution for 5 min prior to the measurement and then maintaining a blanket atmosphere of argon over the solution during the measurement. The potentials were measured in DMF/phosphate-buffered saline (PBS) pH 7.4 (2:1 v/v) containing 0.10 M [n-Bu_4N][BF_4], and are quoted relative to the normal hydrogen electrode (NHE).

Crystallographic structure determination

X-ray diffraction measurements were performed with a Bruker X8 APEXII CCD diffractometer. A twin crystal was positioned at 35 mm from the detector, and 1,033 frames were measured, each for 70 s over 1° scan width. The orientation matrices for two components in the crystal were found by using CELL NOW and were verified by RLATT [38]. The two-component integration was performed using SAINT-Plus [39]. The data were processed using TWINABS [40]. Structure solution and initial refinement were performed in the usual way by direct methods using the HKLF 4 format file. Final refinement including twin fractions (BASF) was accomplished using the HKLF 5 format file. Crystal data, data collection parameters, and structure refinement details are given in Table S1. Non-hydrogen atoms were refined with anisotropic displacement parameters. Hydrogen atoms were inserted in calculated positions and refined with a riding model. Structure solution was achieved with SHELXS-97, refinement was achieved with SHELXL-97 [41], and graphics were produced with ORTEP-3 [42]. Crystallographic data have been deposited with the Cambridge Crystallographic Data Centre (CCDC) with number CCDC-810211. Copies of the data can be obtained free of charge from the CCDC (12 Union Road, Cambridge CB2 1EZ, UK; e-mail: deposit@ccdc.com.ac.uk).

EPR spectroscopy

The copper(II) complexes (1 mM) were dissolved in DMSO/DMF (1:3 v/v) and transferred in an EPR quartz tube (outer diameter 4 mm). Oxygen was removed by passing a stream of argon through the solution for 30 min. Subsequently, the samples were frozen in liquid nitrogen and transferred into a quartz finger dewar for EPR analysis at −196 °C. EPR spectra of the complexes were recorded with a Bruker EMX instrument and a TE102 cavity using the following instrument settings: 9.4-GHz microwave frequency, 5-mW microwave power, 3,134-G center field, 1,080-G sweep, 2-G modulation amplitude, 100-kHz modulation frequency, 1×10^5 receiver gain, 96 G/min scan rate, 0.327-s time constant, and three scans.

Spectral simulations of the copper complexes were performed using the program EasySpin [43]. A coupling of two nonequivalent ^{14}N nuclei with the copper metal center (electron spin of ½) was assumed. Simulations were performed using the Esfit module and the Pepper function of EasySpin. Stepwise g factors, coupling constants, and line widths were optimized using genetic/simplex algorithms, and baseline distortions were corrected by the lsq2 parameter.

Cell culture

The following human cell lines were used in this study: the colon carcinoma cell line SW480, the promyelocytic leukemia cell line HL60, the ovarian carcinoma cell line A2780, and its cisplatin-resistant subline A2780cis. SW480 and HL60 were purchased from American Type Culture Collection (Manassas, VA, USA), and the A2780 lines were obtained from Sigma-Aldrich. All cells were grown in RPMI-1640 supplemented with 10% fetal bovine serum, with the exception of SW480 cells, which were cultivated in minimal essential medium with 10% fetal bovine serum. Cultures were regularly checked for *Mycoplasma* contamination.

3-(4,5-Dimethylthiazol-2-yl)-2,5-diphenyltetrazolium bromide assays

To determine cell viability, cells were plated (2×10^3 cells in 100 µl per well) in 96-well plates and allowed to recover for 24 h. Drugs were added in another 100 µl growth medium and cells were exposed for the time periods indicated. For *N*-acetylcysteine (NAC) and AA experiments, cells were preincubated with 50 µl NAC solution (1 and 2 mM in growth medium) for 30 min. Then, drugs were added in another 50 µl. For washout experiments, NAC-containing medium was replaced with fresh (drug-free) culture medium after the preincubation before Cu-TSC

treatment. After 72 h drug treatment, the proportion of viable cells was determined by 3-(4,5-dimethylthiazol-2-yl)-2,5-diphenyltetrazolium bromide (MTT) assay following the manufacturer's recommendations (EZ4U, Biomedica, Vienna, Austria).

Hoechst 33258/propidium iodide staining

To determine early and late apoptosis as well as necrosis, Hoechst 33258 and propidium iodide (PI) (both from Sigma) were added directly to the culture medium of SW480 cells to final concentrations of 5 and 2 mg/mL, respectively, after 24 h drug incubation. After an incubation period of 1 h at 37 °C, the cells were examined with a Zeiss Axiovert 35 fluorescence microscope with 4′,6-diamidino-2-phenylindole filters. Cells were photographed on Kodak Ektachrome P1600 film (Eastman Kodak, Rochester, NY, USA). Viable cells, apoptotic cells, and necrotic cells were counted. The Hoechst dye stains the nuclei of live and dead cells; therefore, nuclear changes associated with apoptosis, such as chromatin condensation and nuclear fragmentation, can be monitored [44]. On the other hand, PI is excluded from viable and early apoptotic cells. Consequently, PI uptake indicates the loss of membrane integrity characteristic of necrotic and late apoptotic cells. In combination with fluorescence microscopy, selective uptake of the two dyes allows to monitor the induction of apoptosis in intact cultures and to distinguish it from nonapoptotic cell death (necrosis). Necrosis is characterized in this system by nuclear PI uptake without chromatin condensation or nuclear fragmentation. Duplicate slides were prepared for each cell type/treatment group and more than 500 cells were counted for each sample.

Measurement of intracellular oxidants

2′,7′-Dichlorofluorescein diacetate (DCF-DA) was used to detect the production of ROS [45]. DCF-DA stock solutions (33.4 mM) in DMSO were stored at −20 °C. HL60 cells (2.5×10^5 cells per sample in phenol-free Hanks balanced salt solution) were incubated with DCF-DA for 30 min. Subsequently, the copper complexes were added in the indicated concentrations. After incubation for another 30 min, the mean fluorescence intensity was measured by flow cytometry using an FACSCalibur instrument (Becton Dickinson, Palo Alto, CA, USA). A concentration of 200 μM H_2O_2 was used as the control. The resulting histograms were quantified using ModeFit (BD). In the case of experiments with NAC and AA, the reducing agents were added to the samples 15 min prior to addition of the copper complexes.

Generation of superoxide radicals

To examine the cell-free production of superoxide radicals, the reduction of nitroblue tetrazolium (NBT) was analyzed. Briefly, 0.6 mM NBT was incubated with 25 μM copper complexes with or without 2 mM NAC or 50 μM AA. The experiments were performed in 0.1 M PBS (pH 7.8). The extent of NBT reduction was determined spectrophotometrically by measuring the absorbance at 560 nm after 10 min of incubation.

Determination of superoxide dismutase activity by xanthine oxidase assay

Superoxide dismutase (SOD) activity of the complexes was investigated by using their ability to inhibit the reduction of NBT by xanthine/xanthine oxidase generated superoxide radicals [46]. The reaction system contained 0.2 mM xanthine, 0.6 mM NBT, increasing concentrations of the copper compounds, and 70 mU/mL xanthine oxidase to start the reaction in 0.1 M PBS at pH 7.8. The extent of NBT reduction was followed spectrophotometrically by measuring the absorbance at 560 nm. Each experiment was performed in duplicate, and the SOD activity was defined as the concentration of the copper complex tested necessary to inhibit 50% of the NBT reduction (IC_{50} value) caused by superoxide.

Quantification of H_2O_2 production

To measure cell-free production of H_2O_2, the PerOXOquant assay (Pierce, Rockford, IL, USA) was used according to the manufacturer's recommendations. The detection of peroxides by this assay is based on oxidation of ferrous to ferric ions in the presence of xylenol orange at acidic pH. The Fe^{3+} ions are coordinated by xylenol orange, yielding a purple product with an absorbance maximum at 560 nm. Peroxide levels in test samples were determined using H_2O_2 standards.

Results and discussion

Synthesis and characterization

Triapine and APTSC were synthesized in a three-step procedure according to methods described in the literature [18]. FTSC was synthesized by condensation of 2-formylpyridine and thiosemicarbazide in boiling EtOH/H_2O.

Owing to the generally low aqueous solubility of 1:2 complexes of the type $[Cu(L)_2]$ (where L is a monodeprotonated TSC) and their tendency to partially dissociate into the corresponding 1:1 complexes [10], all copper(II)

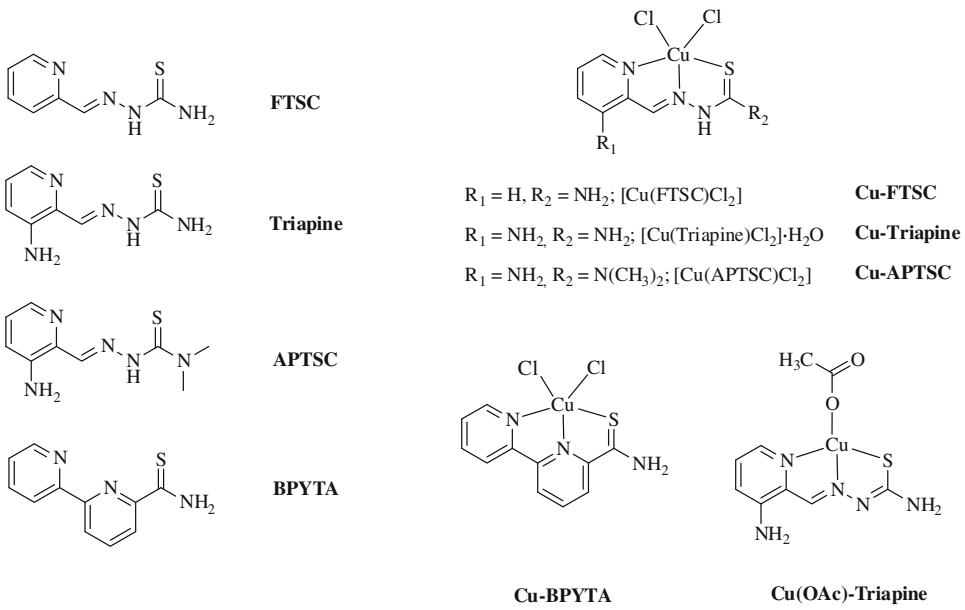

Fig. 1 Overview of compounds investigated

complexes were synthesized in a 1:1 metal-to-ligand ratio (Fig. 1). The reaction of $CuCl_2{\cdot}2H_2O$ with the thiosemicarbazone ligands in methanol in the presence of 2 equiv of concentrated HCl resulted in green complexes of the general formula $[Cu(HL)Cl_2]$ [HL is FTSC (Cu-FTSC), Triapine (Cu-Triapine), APTSC (Cu-APTSC)] in 66–87% yield. In the case of Cu-Triapine, according to the elemental analysis one molecule of water co-crystallized, which was confirmed by thermogravimetric measurements. In addition, reaction of Triapine and $Cu(OAc)_2{\cdot}H_2O$ in methanol resulted in deprotonation of the ligand and isolation of the brown product [Cu(L)OAc] [HL is Triapine; Cu(OAc)-Triapine] in 77% yield. $[Cu(BPYTA)Cl_2]$ (Cu-BPYTA) was synthesized according to a literature procedure [19].

The negative ESI mass spectra of the chlorido complexes Cu-Triapine and Cu-APTSC showed exclusively a strong peak due to $[M–2H–Cl]^-$ ions at *m/z* 291 and 319, respectively. In the case of the acetato complex of Triapine, only the positive ion mode displayed strong peaks due to $[M–OAc]^+$ at *m/z* 257 and additionally two dimeric fragments at *m/z* 515 and 573 attributed to $[2M–2OAc–H]^+$ and $[2M–OAc]^+$, respectively. The UV–vis spectra of the copper(II) thiosemicarbazone complexes in methanol showed the characteristic very weak *d–d* absorption band in the range 616–636 nm. The strong metal-to-ligand charge transfer absorption is redshifted from 406 nm (Cu-FTSC) to 443 nm (Cu-Triapine) and 458 nm (Cu-APTSC) in accordance with the electron-donating properties of the amino and methyl groups.

X-ray crystallography

X-ray diffraction quality single crystals of Cu-Triapine were obtained by slow diffusion of acetone into an aqueous solution of Cu-Triapine. The result of the X-ray diffraction study is shown in Fig. 2. Selected bond distances and angles are quoted in the legend to Fig. 2. The coordination polyhedron around the copper(II) center approaches a square-planar geometry, with a chlorido ligand and the monodeprotonated tridentate Triapine coordinated to the metal ion. In addition, an H_3O^+ molecule and a chlorido counterion are present in the asymmetric unit. The deprotonation in aqueous solution is in agreement with the concentration distribution curves of the Cu^{II}-Triapine system indicating the presence of the $[CuL]^+$ species (HL is Triapine) in a wide pH range [47]. In the solid state the square-planar molecules are linked via

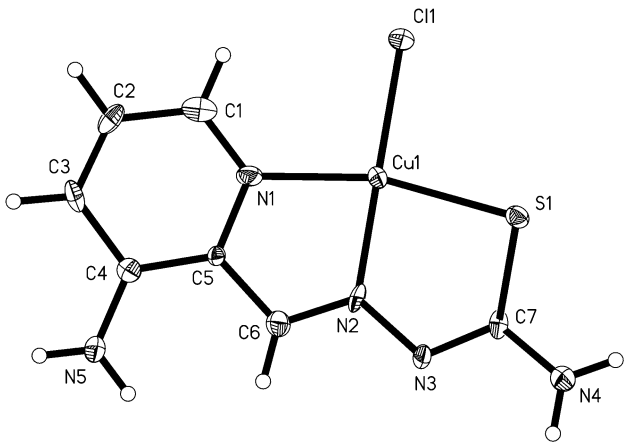

Fig. 2 ORTEP plot of Cu-Triapine with thermal ellipsoids depicted at the 50% probability level (the $H_3O^+Cl^-$ fragment is omitted). Selected bond distances (Å) and angles (°): Cu–Cl, 2.2493(5); Cu–S, 2.281(3); Cu–N2, 1.937(9); Cu–N1, 2.031(8); S1–C7, 1.723(10); C7–N3, 1.311(13); N3–N2, 1.383(11); N2–C6, 1.317(13); N1–Cu–S, 164.5(2); N2–Cu–Cl, 176.9(3); N1–Cu–N2, 81.1(3); N2–Cu–S, 83.6(3)

intermolecular Cu–S bonds [2.986(4) Å], forming a chain structure (see Fig. S1).

EPR spectroscopy

The EPR spectra of the five copper(II) complexes in DMSO/DMF solutions (1:3 v/v) at −196 °C show the typical four hyperfine lines due to the d^9 configuration ($S = ½$) and a nuclear spin $I = 3/2$ of the main isotopes ^{63}Cu and ^{65}Cu as well as a superhyperfine splitting of the high-field lines due to the interaction of copper with the ^{14}N nuclei ($I = 1$) (Fig. 3, S2–S5). All complexes show $g_{\|}$ and $g_{\perp}$ parameters typical of axial symmetry (see "Synthesis of metal complexes"), and $g_{\|} > g_{\perp} > 2.0023$ is consistent with a $d_{x^2-y^2}$ ground state in a square-planar or square-pyramidal geometry [48]. The spectra were simulated using EasySpin [43] assuming the coupling of two nonequivalent ^{14}N nuclei with the copper(II) center and are in good agreement with the experimental data (Fig. 3, S2–S5). Except for the superhyperfine coupling, in the EPR spectra of the copper(II) complexes only small changes could be observed, which is obvious considering the existence of the NNS coordination pattern in all compounds. Comparison of the EPR spectra of Cu-Triapine and Cu(OAc)-Triapine in DMSO/DMF (Fig. S6a) reveals significant differences in the superhyperfine coupling, whereas the same complexes in DMSO/PBS pH 7.4 (1:1 v/v; Fig. S6, plot b) exhibit almost the same spectrum. This further supports the assumption that Cu-Triapine releases 1 equiv of HCl (see above) so that both copper(II) Triapine complexes form a square-planar $[CuL(H_2O)]^+$ species (HL is Triapine) in aqueous solution. The formation of $[CuL(H_2O)]^+$ is also supported by the spectra of the already square-planar complex Cu(OAc)-Triapine, which distinctly differs upon changing the solvent from DMSO/DMF to DMSO/PBS (Fig. S6).

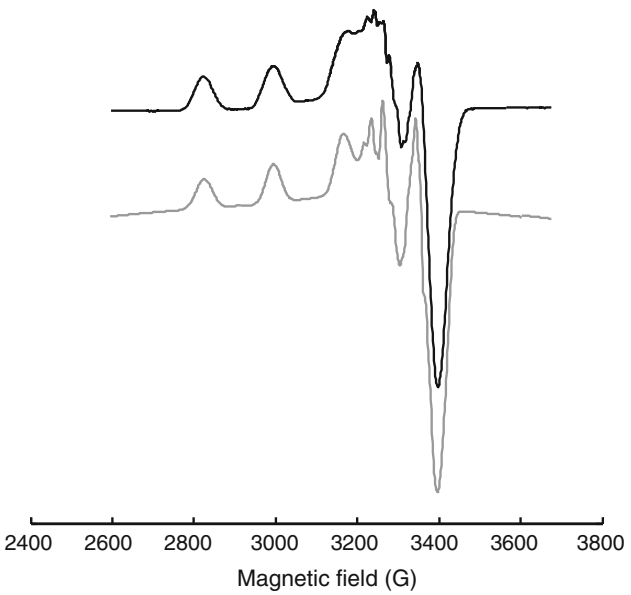

Fig. 3 EPR spectrum of 1 mM Cu-Triapine in dimethyl sulfoxide (DMSO)/dimethyl formamide (DMF) (1:3 v/v) (*black*) and simulated spectrum (*gray*). Experimental conditions: X-band; temperature −196 °C, microwave frequency 9.4 GHz; microwave power 5 mW; modulation amplitude 2 G

Cyclic voltammetry

The electrochemical properties of the five copper(II) complexes were investigated by cyclic voltammetry in DMF/PBS pH 7.4 (2:1 v/v) containing 0.10 M [*n*-Bu_4N][BF_4] as the supporting electrolyte. All complexes display an irreversible copper(II)/copper(I) reduction peak between −0.23 and +0.10 V versus NHE at 200 mV/s scan rate (Table 1). The decrease of the redox potentials in the order Cu-FTSC > Cu-Triapine > Cu-APTSC is in line with the electron donor properties of the NH_2 and CH_3 groups. Owing to the low aqueous solubility of the complexes, the measurements were performed in DMF/PBS mixtures. However, this makes the direct comparison with the literature redox potentials of AA (+0.06 V vs. NHE) [49], NAC (−0.18 V vs. NHE) [50], and GSH (−0.24 V vs. NHE) [51] determined in pure aqueous solutions at pH 7.0 difficult. Nevertheless, the redox potentials of the thiosemicarbazone complexes investigated suggest that AA is not able to reduce them, whereas the redox potentials of NAC and GSH are in the same potential range as the copper(II) to copper(I) reduction.

Anticancer activity and intracellular ROS generation

The antiproliferative activity of the five copper complexes was compared in MTT viability assays using SW480 colon cancer and leukemic HL60 cells. In general, both cell lines displayed widely similar sensitivity to the test compounds, with IC_{50} values in the low micromolar range (Table 2). The most active compound in our test panel was Cu-Triapine, with an IC_{50} value of approximately 1.2 μM,

Table 1 Electrochemical data

	$E_p/Cu^{II/I}$
Cu-FTSC	−0.14
Cu-Triapine	−0.19
Cu(OAc)-Triapine	−0.21
Cu-APTSC	−0.23
Cu-BPYTA	+0.10

See Fig. 1 for an explanation of the compounds. Potentials in volts ± 0.02 versus the normal hydrogen electrode in 2:1 dimethylformamide/0.2 M phosphate-buffered saline pH 7.4 containing 0.10 M [*n*-Bu_4N][BF_4]

Table 2 Cytotoxic/cytostatic activity against two human cancer cell lines after 72 h treatment

	IC_{50} (μM) ± SD	
	SW480	HL60
Cu-FTSC	3.3 ± 1.2	3.4 ± 0.4
Cu-Triapine	1.3 ± 0.3	1.1 ± 0.1
Cu(OAc)-Triapine	2.1 ± 0.2	n.d.
Cu-APTSC	5.5 ± 0.7	3.1 ± 0.6
Cu-BPYTA	8.4 ± 0.4	8.7 ± 0.6
FTSC	10.6 ± 0.1	3.3 ± 0.5
Triapine	0.4 ± 0.05	0.4 ± 0.1
APTSC	0.4 ± 0.01	0.2 ± 0.02
BPYTA	5.8 ± 3.0	7.1 ± 0.5

SD standard deviation

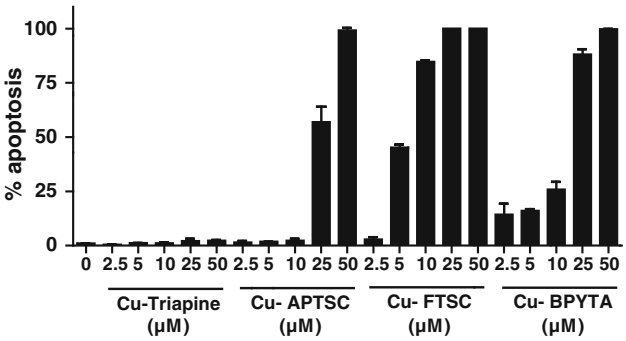

Fig. 4 Cell death induction. The proportion of apoptotic cells (early and late apoptosis) was determined by Hoechst 33258/propidium iodide staining [44] after 24 h treatment with the indicated concentrations of the copper complexes tested. More than 500 cells from at least two samples for each concentration were analyzed and the percentages of early and late apoptotic cells at the indicated concentrations were determined by counting. One representative experiment of two giving comparable results is shown

whereas Cu-BPYTA was least active, with an IC_{50} value of approximately 8.5 μM. On the basis of the rather similar anticancer activity of Cu-Triapine and Cu(OAc)-Triapine and the results obtained by the physicochemical characterization, all further experiments were performed only with Cu-Triapine. The antiproliferative activity of the copper(II) complexes was also compared with that of the corresponding metal-free ligands (Table 2). All copper(II) complexes were found to be slightly less effective than the respective metal-free ligands, with exception of Cu-FTSC, where in SW480 cells an about threefold increased activity compared with metal-free FTSC was observed. However, in HL60 cells these two compounds were comparably active. These results are in accordance with the observations described in previous publications, where complexation of FTSC and copper(II) was reported to result in increasing or decreasing activity depending on the cell type investigated [15, 52, 53].

To investigate whether the reduction in cell viability observed by the MTT assays is based on cytostatic or cytotoxic effects, Hoechst 33258/PI stainings were performed [44]. As shown in Fig. 4, the apoptosis-inducing potential of the copper complexes strongly differed. In the case of Cu-Triapine, virtually no increase in the number of apoptotic cells was observed, indicating that this compound acts solely as a cytostatic agent. In contrast, apoptosis induction by Cu-FTSC correlated with the results obtained in MTT assay (at IC_{50} levels, 45.2% of the cells were apoptotic), identifying this compound as mainly a cytotoxic drug. In the case of Cu-APTSC and Cu-BPYTA, no induction of apoptosis was found at IC_{50} levels. However, at higher drug concentrations a profound increase in the number of apoptotic cells up to 100% was detected. Thus, these drugs have both cytostatic and cytotoxic properties.

The generation of ROS is assumed to be one of the main mechanisms underlying the anticancer activity of copper(II) complexes [31–33]. To evaluate the impact of the copper complexes on the intracellular levels of ROS, the cell-permeable, fluorescent dye DCF–DA was used. An enzymatic hydrolysis by intracellular esterases is necessary to gain the ROS-detecting DCF–H. This assay is frequently applied for the detection of intracellular H_2O_2 and ROS such as $OH^{\cdot}$ and $ROO^{\cdot}$ [45]. Figure 5 shows the induction of ROS after treatment with increasing concentrations of the copper complexes. In accordance with previous reports [9, 25], treatment with Cu-FTSC and Cu-BPYTA led to a significant (in the case of Cu-FTSC dose-dependent) increase of DCF-DA fluorescence (up to approximately fivefold after treatment with 50 μM Cu-FTSC and approximately fourfold after treatment with 25 and 50 μM Cu-BPYTA). In contrast, Cu-Triapine and Cu-APTSC only slightly enhanced intracellular ROS levels (about 1.25-fold). Unexpectedly, treatment with 50 μM Cu-APTSC even strongly decreased the DCF-DA fluorescence by 0.2-fold. None of the metal-free ligands displayed any significant effect on DCF-DA fluorescence (data not shown).

In general, the ROS generation data are in good agreement with the apoptosis-inducing potential of the test compounds, indicating that (in agreement with the literature) the apoptosis induction at higher drug concentrations is mainly based on intracellular ROS. However, it has to be noted that at IC_{50} levels (5 μM) the increase in intracellular ROS levels induced by all the copper complexes is rather low, with Cu-BPYTA displaying the strongest effect (twofold increase). Together with the lack of enhanced anticancer activity of the copper complexes in comparison with their metal-free ligands observed in MTT assay, the data question the relevance of intracellular ROS generation for the anticancer activity of copper thiosemicarbazone complexes in general and especially for Cu-APTSC and

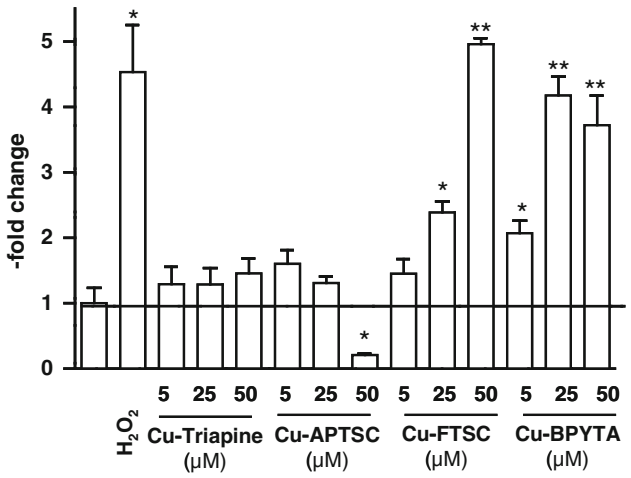

Fig. 5 Intracellular reactive oxygen species (ROS) generation. Intracellular production of ROS in HL60 cells by the indicated concentrations of the copper complexes was determined after 30 min incubation using the ROS indicator 2′,7′-dichlorofluorescein diacetate (DCF-DA). Fluorescence was measured by flow cytometry. One representative experiment of three giving comparable results is shown. Significant differences were calculated by Student's *t* test: *single asterisk* $p < 0.05$, *two asterisks* $p < 0.01$

Cu-Triapine. Notably, preliminary uptake experiments of the copper complexes using inductively coupled plasma mass spectrometry indicate that the lack of intracellular ROS generation is not based on insufficient cellular drug uptake. Even distinctly higher cellular copper levels were detected in the case of Cu-APTSC and Cu-FTSC as compared with equimolar concentrations of $CuSO_4$ (data not shown).

Impact of reductants on the anticancer activity of the copper complexes

It is well established that reduction of copper complexes (e.g., by thiols such as GSH) leads to redox cycling and generation of ROS [9, 25, 27–30]. Thus, the effect of co-incubation with the GSH precursor NAC on the substance panel was investigated. As expected, drastically enhanced anticancer activity of all copper complexes in SW480 cells (Fig. 6, left panel) and HL60 cells (Fig. S7, left panel) was observed in the presence of NAC (1.0 and 2.0 mM). Notably, in the case of Cu-APTSC, addition of NAC had the weakest effect on the activity. In contrast to the NAC experiments, co-incubation with the antioxidant AA (25 and 50 μM) only weakly enhanced the activity of Cu-BPYTA, whereas it had no significant effects on Cu-FTSC and Cu-APTSC (Fig. 6, S7, right panel). In the case of Cu-Triapine, cotreatment with 50 μM AA even slightly decreased the anticancer activity 1.4-fold. These observations are in good agreement with the reduction potential of the copper(II) complexes obtained by cyclic voltammetry (see Table 1), with the highest redox potential for Cu-BPYTA and the lowest for Cu-APTSC.

To evaluate whether these changes in anticancer activity are based on enhanced intracellular ROS levels, DCF–DA stainings were performed after cotreatment with NAC or AA. Figures 7 and S8 show that combination of the copper complexes with 2 mM NAC induced a strong increase of the intracellular ROS levels. In experiments using 25 μM copper complexes (Fig. 7), the strongest effects were observed with Cu-FTSC (eightfold increase) and the weakest effects were observed with Cu-APTSC (fivefold increase). At lower drug concentrations (5 μM), similar effects, however to a lesser extent, were found (Fig. S8). In contrast to the results of the 72-h viability assays (where no or only a minor influence of AA was observed), co-incubation with 50 μM AA significantly enhanced intracellular ROS levels after treatment with the copper complexes, however, in general, to a weaker extent than co-incubation with NAC. The strongest effects of AA on intracellular ROS levels were observed in the case of Cu-FTSC and Cu-BPYTA (fivefold increase).

To test whether cells with increased amounts of GSH are more susceptible to copper compounds, the ovarian cancer cell model A2780 and its cisplatin-resistant subline A2780cis containing higher intracellular GSH levels [54] were used. In general, parental A2780 cells displayed drug sensitivity (Table 3) very similar to the HL60 cells (see Table 2). On the basis of the higher GSH levels in A2780cis cells, enhanced thiol-induced ROS generation leading to increased activity of the copper(II) complexes was expected. In contrast, A2780cis cells were significantly resistant (up to 22-fold in the case of Cu-Triapine) to all the copper complexes tested.

To gain more insight into the impact of the intracellular GSH levels on the anticancer activity and ROS-inducing capability of the copper compounds tested, the intracellular GSH pools of SW480 cells were boosted by preloading with NAC, which is then quickly metabolized to GSH inside the cell. After 30 min preincubation, remaining extracellular NAC was removed and the copper compounds were added to the cells in fresh culture medium. As shown in Fig. 8a, in contrast to the drastic increase in cytotoxic/cytostatic activity caused by NAC co-incubation observed in previous experiments (Fig. 6), enhanced intracellular GSH pools did not increase the activity of the copper complexes tested. Notably, in case of Cu-Triapine, NAC preloading even had protective effects (twofold and fourfold increase in the IC_{50} value caused by preincubation with 1 and 2 mM NAC, respectively). In accordance, no enhanced ROS generation was detected in NAC-preloaded cells (after washout) via DCF–DA stainings (Fig. 8b, right panel). This indicates

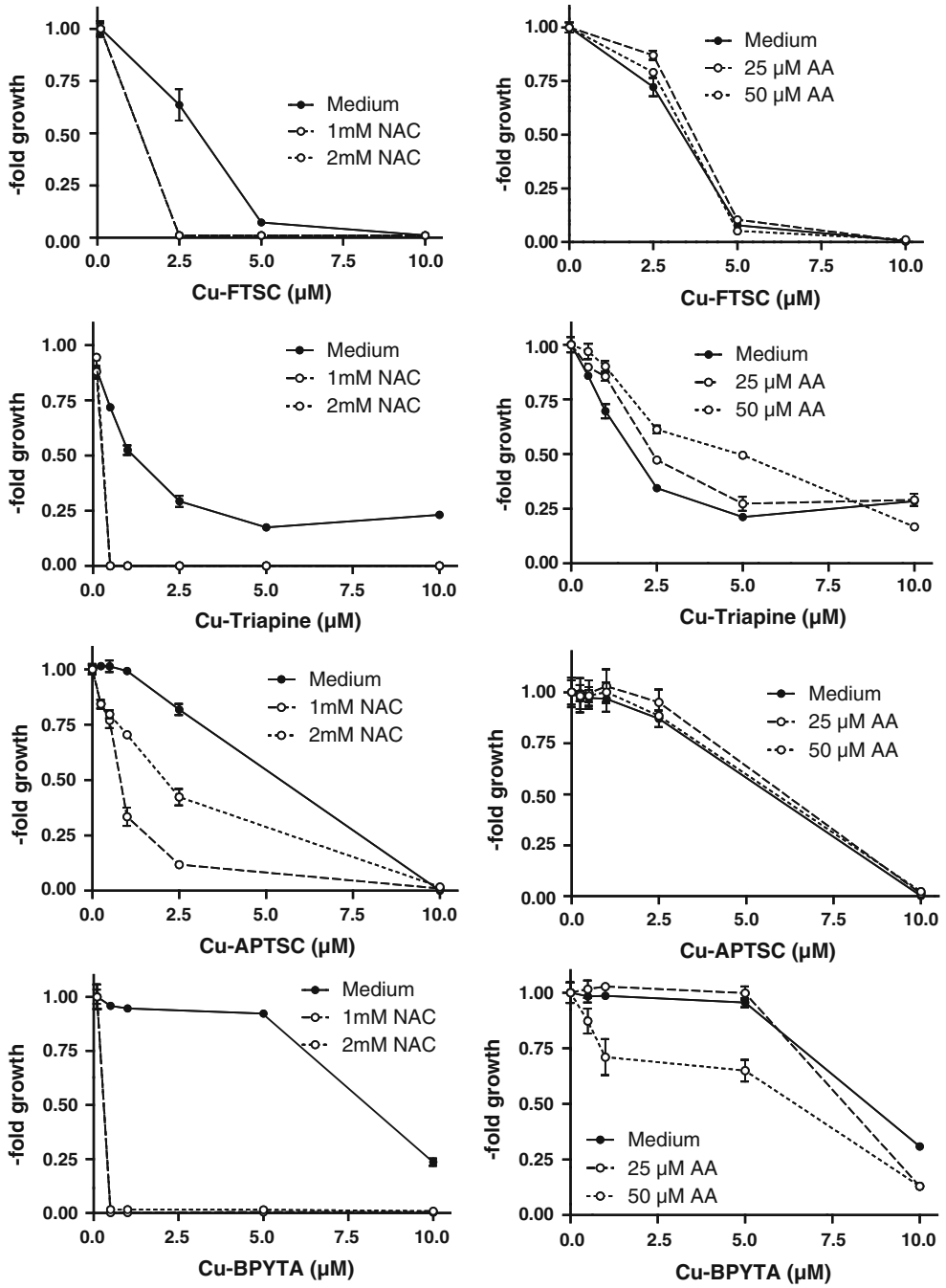

Fig. 6 Impact of reductants on the anticancer activity of the copper complexes. To evaluate the effects of reductants, the glutathione (GSH) precursor *N*-acetylcysteine (*NAC*) and the antioxidant ascorbic acid (*AA*) were used. Briefly, after 30 min preincubation with NAC (1 and 2 mM) or AA (25 and 50 μM), SW480 cells were treated for 72 h with the indicated concentrations of the copper complexes. Viability was determined using 3-(4,5-dimethylthiazol-2-yl)-2,5-diphenyltetrazolium bromide (MTT) assay. The values given are the mean ± the standard deviation of three determinations from three experiments

extracellular generation of ROS, which then react after membrane diffusion with DCF–H inside the cell. As H_2O_2 is the only diffusible ROS species, we suggested that thiol-induced redox cycling of the copper complexes leads to extracellular production of H_2O_2.

Extracellular H_2O_2 and superoxide radical formation by cotreatment with biologically relevant reductants

To test whether coincubation of copper compounds with NAC and AA leads to generation of H_2O_2 under cell-free

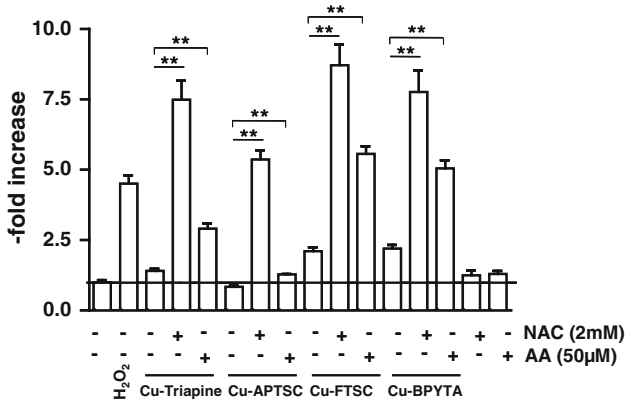

Fig. 7 Reductant-induced ROS generation by the copper complexes. The influence of pretreatment with 2 mM NAC or 50 μM AA on the intracellular ROS levels in HL60 cells after incubation with the copper complexes (25 μM) was determined using the ROS indicator DCF-DA. Fluorescence was measured by flow cytometry. One representative experiment of three giving comparable results is shown. Significant differences were calculated by Student's *t* test: *two asterisks* $p < 0.01$

Table 3 Cytotoxic/cytostatic activity in A2780 and A2780cis cell lines at 72 h treatment

	IC_{50} (μM) ± SD		
	A2780	A2780cis	Resistance
Cu-FTSC	3.0 ± 1.0	8.8 ± 2.2	2.9-fold
Cu-Triapine	1.3 ± 0.1	29 ± 3	22-fold
Cu-APTSC	5.6 ± 0.1	8.3 ± 0.6	1.5-fold
Cu-BPYTA	7.3 ± 1.8	25 ± 70	3.4-fold

conditions, H_2O_2 levels were determined using the xylenol orange-based PerOXOquant assay. Figure 9 shows that without addition of reductants, no H_2O_2 production by the copper complexes was detectable. Co-incubation with 2 mM NAC distinctly induced H_2O_2 formation in the case of all four copper complexes (50 μM). For Cu-APTSC and Cu-BPYTA, 2–3 equiv of H_2O_2 per copper complex molecule was produced, whereas Cu-Triapine and Cu-FTSC were less effective, inducing production of only 1 equiv of H_2O_2. Thus, redox cycling was only observed in the case of Cu-APTSC and Cu-BPYTA. Notably, also after AA cotreatment, minor levels of H_2O_2 were detected. Overall, the results obtained in these cell-free settings are in good agreement with the findings of the intracellular DCF-DA staining experiments (see Fig. 7).

To prove that H_2O_2 is the ROS responsible for the DCF-DA fluorescence reported in Fig. 7, the respective experiments were repeated in the presence of the H_2O_2-metabolizing enzyme catalase (Figs. 10a, S9). In the case of all four copper complexes, addition of extracellular catalase significantly reduced intracellular NAC-induced ROS levels. Application of SOD together with catalase further reduced ROS levels, especially in the case of Cu-FTSC and Cu-APTSC, suggesting that the extracellular H_2O_2 formation is $O_2^{\cdot-}$-dependent (Fig. S9). The protective effects of catalase against the NAC-induced ROS formation were further confirmed for Cu-Triapine using MTT assays (Fig. 10b).

For several copper compounds (including $CuSO_4$), SOD-like activity has been reported [55]. As this ability is probably the underlying mechanism of H_2O_2 formation shown in Fig. 9, the superoxide radical dismutation ability of our complex panel was measured using the xanthine/xanthine oxidase assay (Table 4). In these experiments, the xanthine/xanthine oxidase system was used to generate superoxide radicals, which in turn led to the reduction of NBT, resulting in blue staining. In accordance with already published data [46], the IC_{50} value for the SOD-like activity of $CuSO_4$ was found to be approximately 20 μM. Also Cu-FTSC and Cu-BPYTA had potent activity, with IC_{50} values of 45 and 6 μM, respectively. In the case of Cu-Triapine, only a weak SOD-like activity with an IC_{50} value of 98 μM was detected. Up to 100 μM, Cu-APTSC had no effect on the detected $O_2^{\cdot-}$ levels. These effects are in strong correlation with the redox potential (see Table 1), indicating that the redox potential is important for the SOD-like activity of copper compounds. This is in good agreement with a study on copper 1,10-phenanthroline complexes, which also concluded that there is a direct correlation between the redox potential and SOD-like activity within the phenanthroline compounds studied [56].

With respect to the thiol-induced redox cycling of thiosemicarbazone copper compounds, it has to be kept in mind that the xanthine/xanthine oxidase assay is performed without addition of NAC or AA [46]. Moreover, if the generated H_2O_2 is produced by dismutation of $O_2^{\cdot-}$, the question of the source of $O_2^{\cdot-}$ production arises. To determine whether the copper complexes are able to produce the necessary superoxide radicals upon reduction by NAC (or AA), NBT was used as an $O_2^{\cdot-}$-detecting agent (without xanthine/xanthine oxidase). As shown in Figs. 11 and S10, distinct formation of $O_2^{\cdot-}$ was detected in the samples containing copper complexes with NAC, and this formation was inhibited by cotreatment with natural SOD (Fig. S10). In contrast, without NAC or in the presence of AA, no significant formation of $O_2^{\cdot-}$ was found. Together with the H_2O_2 generation, this indicates that in the presence of NAC, the copper complexes tested generate $O_2^{\cdot-}$, which is then further dismutated to the membrane-permeable H_2O_2, leading to intracellular oxidative stress.

Conclusions

Generation of ROS based on the reduction of copper(II) to copper(I) by intracellular reducing agents has so far been

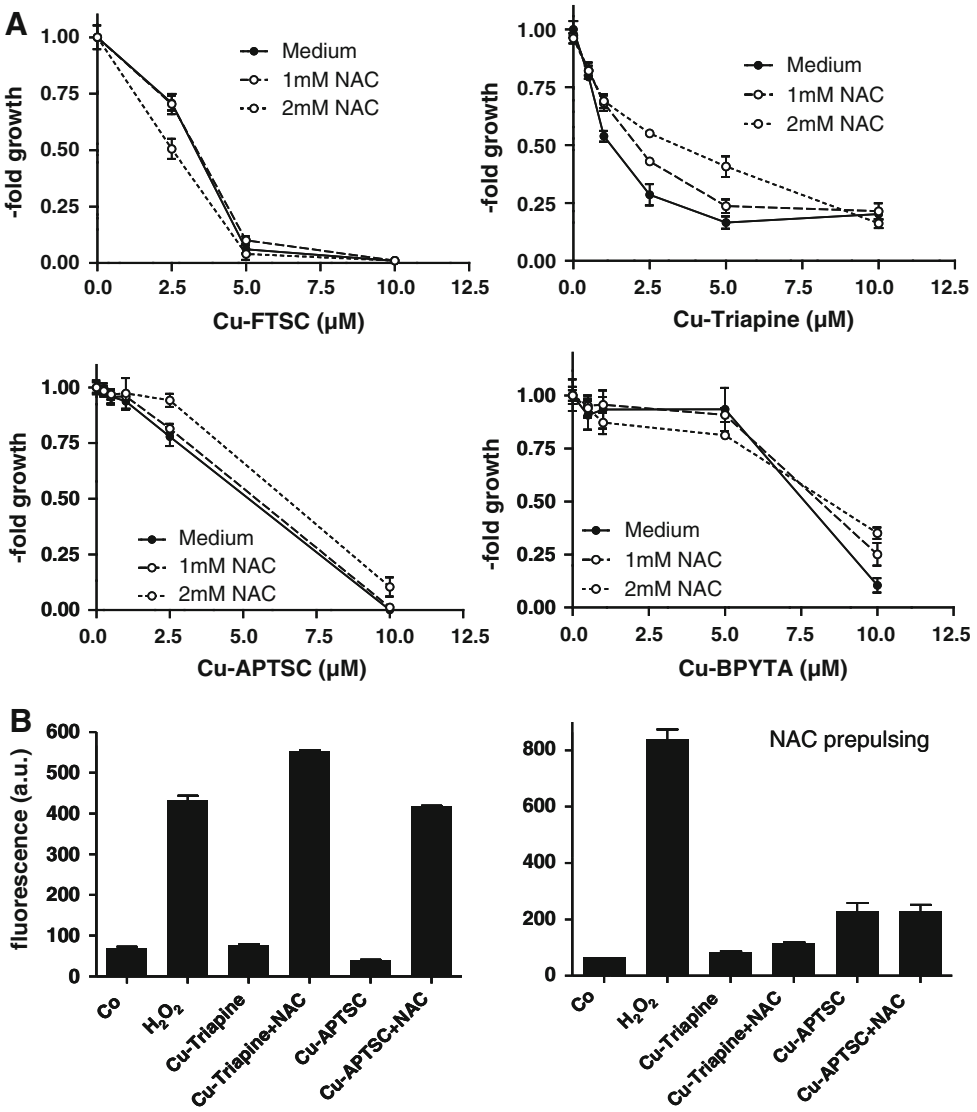

Fig. 8 Impact of enhanced intracellular GSH levels on the anticancer activity of the copper complexes. **a** To evaluate the impact of elevated intracellular GSH levels on the copper complexes tested, SW480 cells were incubated with the GSH precursor NAC. After 30 min pretreatment, NAC-containing medium was replaced by fresh culture medium. Then the copper complexes were added at the indicated concentrations. After 72 h incubation, viability was determined using MTT assay. The values given are the mean ± the standard deviation of three determinations from three experiments. **b** *Left* DCF-DA-loaded HL60 cells were incubated for 15 min with 2 mM NAC, then the test compounds (50 μM) were added in the presence of NAC. After 30 min incubation, fluorescence was measured by flow cytometry. *Right* after preincubation, the NAC-containing buffer was replaced by fresh Hanks balanced salt solution and the test compounds (50 μM) were added. After 30 min incubation, fluorescence was measured by flow cytometry. One representative experiment of three giving comparable results is shown

assumed to be the major mode of action underlying the anticancer activity of copper(II) complexes [9, 25, 27–33]. In accordance, also in our study addition of the GSH precursor NAC drastically increased the anticancer activity of the copper(II) complexes investigated. However, several of our observations indicate that reductant-induced intracellular redox cycling does not dominate the anticancer activity of copper complexes: (1) although potent ROS generation was induced by NAC co-incubation, single treatment with Cu-Triapine, Cu-APTSC, or Cu-FTSC at IC_{50} levels did not induce significant intracellular DCF-DA fluorescence (Fig. 5); (2) cells with significantly enhanced intracellular GSH levels (A2780cis cells) did not show increased sensitivity to treatment with the copper complexes (Table 3); and (3) the presence of extracellular catalase strongly protected cells from reductant-induced copper-complex-mediated oxidative stress and cell death (Fig. 10). Consequently, our data suggest that the frequently reported thiol-induced redox cycling of copper(II) complexes occurs predominantly in the extracellular space. The proposed reaction scheme is

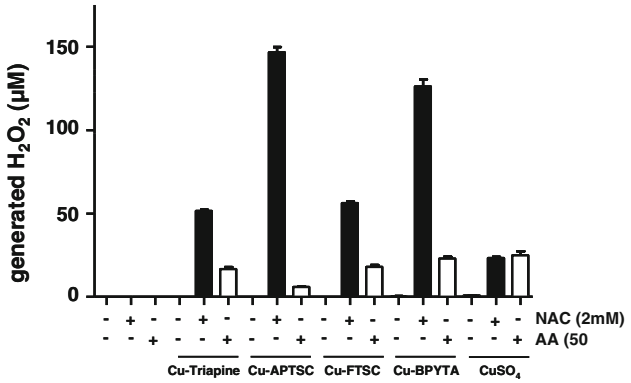

Fig. 9 NAC- and AA-induced H_2O_2 production by the copper complexes. The dependence of the level of copper-complex-generated H_2O_2 on NAC (2 mM) and AA (50 μM) was determined using the xylenol orange-based PerOXOquant assay. The copper complexes were used at concentrations of 50 μM. The values given are the mean ± the standard deviation of three determinations

shown in Fig. 12. Upon copper(II) reduction by NAC, the copper(I) complex formed is able to extracellularly generate H_2O_2 by $O_2^{\cdot-}$ dismutation (accompanied by reoxidation of the copper complex). H_2O_2 is then able to enter the cell by diffusion, where ROS are generated, e.g., by Fenton reactions. Additionally, the copper(I) complexes are able to produce $O_2^{\cdot-}$ in the presence of oxygen. This, on the one hand, leads again to reoxidation of the copper complex and, on the other hand, to generation of $O_2^{\cdot-}$ essential for H_2O_2 production. After reoxidation to copper(II), again reduction by NAC can occur, leading to redox cycling of the copper center. Additionally, the distinct SOD-like activity of

Table 4 Superoxide dismutase (*SOD*)-like activity

	IC_{50} (μM)
Cu-FTSC	45
Cu-Triapine	98
Cu-APTSC	≫100
Cu-BPYTA	6
$CuSO_4$	20
Native Cu/Zn-SOD	0.04[a]

SOD-like activity of the copper complexes was investigated by spectrophotometric determination of their ability to inhibit the reduction of nitroblue tetrazolium by xanthine/xanthine oxidase generated superoxide radicals

[a] Taken from [57]

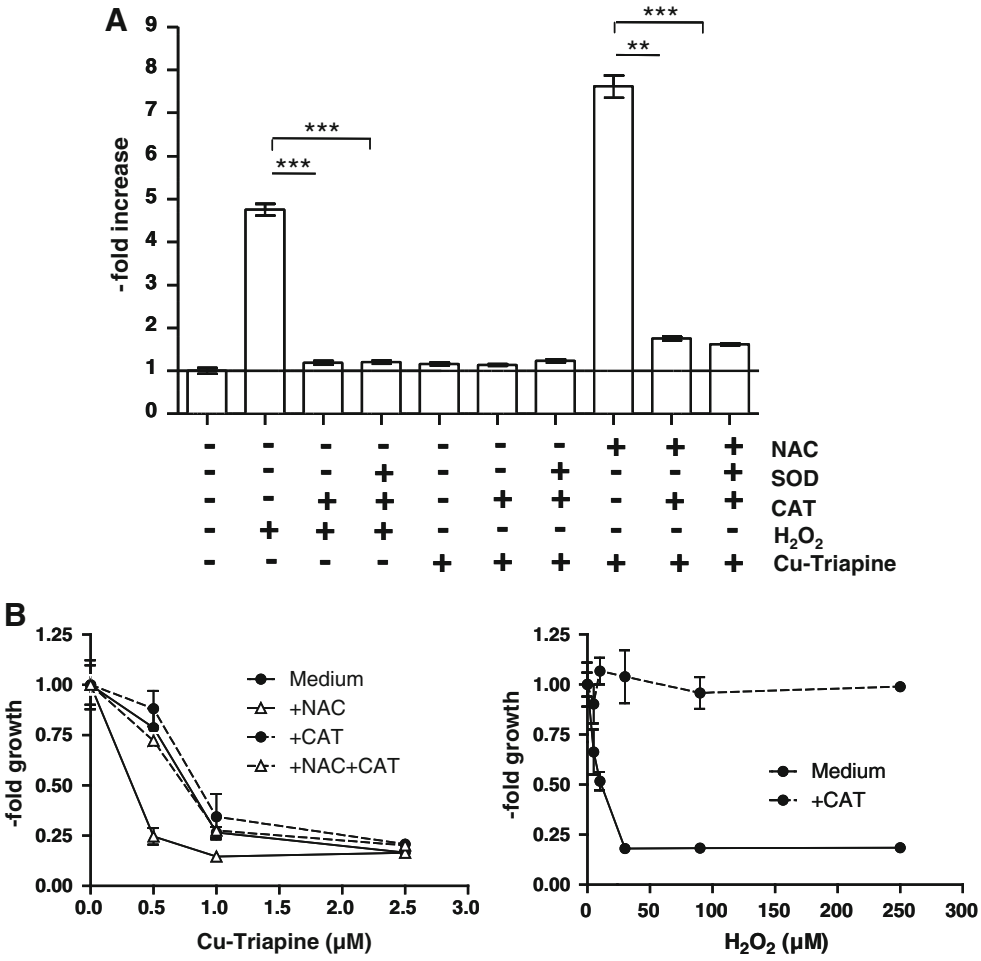

Fig. 10 Effect of extracellular superoxide dismutase (*SOD*) and catalase (*CAT*) on thiol-induced ROS generation. **a** Influence of SOD and CAT cotreatment (100 U/mL) on the NAC-induced (2 mM) ROS formation by Cu-Triapine (25 μM) in HL60 cells was determined using DCF-DA. Fluorescence was measured by flow cytometry. One representative experiment of three giving comparable results is shown. Significant differences were calculated by Student's *t* test: *two asterisks* $p < 0.01$, *three asterisks* $p < 0.001$. **b** *Left* impact of CAT cotreatment (100 U/mL) on the anticancer activity of Cu-Triapine in the presence and absence of NAC. *Right* protective effects of CAT against H_2O_2-induced cell death. Cell viability was determined by MTT assay after 72 h drug treatment

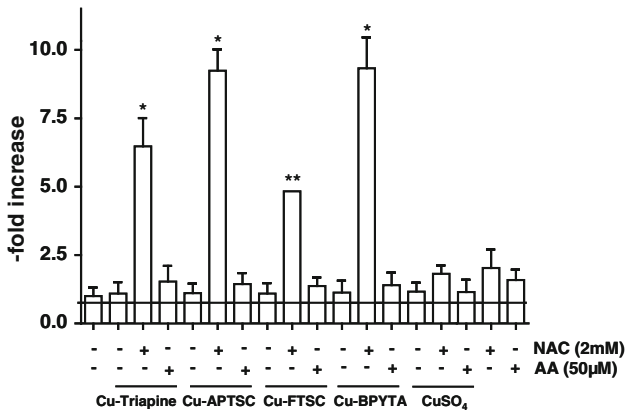

Fig. 11 $O_2^{\cdot-}$ generation ability of the copper complexes in the presence of NAC and AA. The dependence of the level of copper-complex-generated $O_2^{\cdot-}$ on NAC (2 mM) and AA (50 μM) was determined by measuring the reduction of nitroblue tetrazolium spectrophotometrically. The copper complexes were used at concentrations of 25 μM. The values given are the mean ± the standard deviation of three determinations. Significant differences were calculated by Student's *t* test: *single asterisk* $p < 0.05$, *two asterisks* $p < 0.01$

Cu-FTSC and Cu-BPYTA suggests that these compounds are able to be reduced by $O_2^{\cdot-}$, which is in contrast to Cu-Triapine and Cu-APTSC. These differences in the redox activity might be responsible for the observed intracellular ROS generation by high concentrations of Cu-FTSC and Cu-BPYTA in single treatments (see Fig. 5). Owing to the lower redox potential, Cu-Triapine and Cu-APTSC are probably not reduced by $O_2^{\cdot-}$ under physiological conditions and need stronger reductants for H_2O_2 generation. On the basis of our experiments on living cells, we conclude that the intracellular milieu present under cell culture is not sufficient to allow significant redox cycling and ROS generation, especially in the case of Cu-Triapine and Cu-APTSC. Consequently, the assumed mode of action for copper compounds based on thiol-induced intracellular ROS generation urgently needs further investigations and probably reformulation of the proposed mechanisms. Although the similarity in IC_{50} values between the complex and the metal-free ligand indicates that both might share the same mode of action, preliminary data (e.g., in the case in Cu-BPYTA [11]) indicate that not ROS, but other redox-dependent mechanisms underlie the anticancer activity of the copper complexes, which is distinctly different from that of the metal-free ligands. The investigation of this issue is the subject of ongoing studies. In general, on the basis of the strong differences in the cellular redox balance between cancer and nonmalignant cells, the redox activity of copper complexes opens the opportunity for targeting cancer cells. Additionally, this might be further enhanced by targeting strategies (e.g., via albumin binding) to increase the selective accumulation of the compounds in the malignant tissue. Furthermore, the redox activity of the copper complexes can be tuned to selectively target the hypoxic tumor environment, as already shown for copper(II)-containing radiopharmaceuticals.

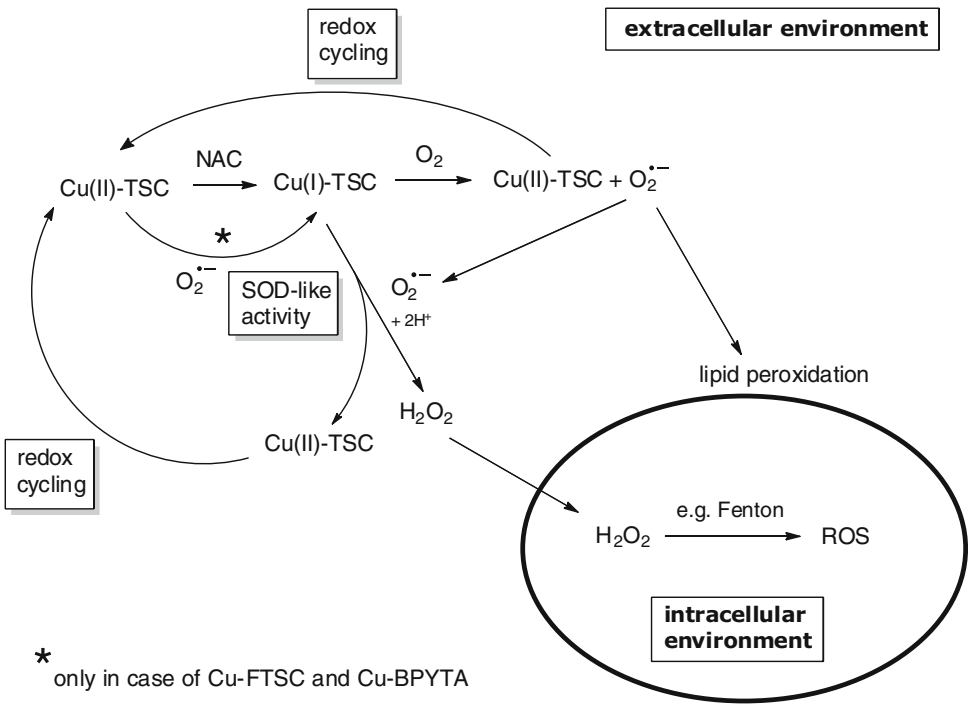

Fig. 12 Proposed extracellular redox reactions underlying the Cu-TSC-induced ROS generation

Acknowledgments We are indebted to Vera Bachinger for the skilful handling of cell cultures, Irene Herbacek for fluorescence-activated cell sorting analysis, and Christian Balcarek for competent technical assistance. We also thank Aliona Luganschi for the measurement of mass spectra, and Alexander Roller as well as Vladimir Arion for the collection/refinement of the X-ray crystal data. This work was supported by Austrian Science Fond (FWF) grants L212-B11 and P22072-B11 (to W.B.).

References

1. Gupte A, Mumper RJ (2009) Cancer Treat Rev 35:32–46
2. Trachootham D, Alexandre J, Huang P (2009) Nat Rev Drug Discov 8:579–591
3. Denny WA (2010) Future Oncol 6:419–428. doi:10.2217/fon.10.1
4. Hartinger CG, Zorbas-Seifried S, Jakupec MA, Kynast B, Zorbas H, Keppler BK (2006) J Inorg Biochem 100:891–904
5. Hall MD, Hambley TW (2002) Coord Chem Rev 232:49–67
6. Wang T, Guo Z (2006) Curr Med Chem 13:525–537
7. Tisato F, Marzano C, Porchia M, Pellei M, Santini C (2010) Med Res Rev 30:708–749. doi:10.1002/med.20174
8. Bonnitcha PD, Vavere AL, Lewis JS, Dilworth JR (2008) J Med Chem 51:2985–2991. doi:10.1021/jm800031x
9. Byrnes RW, Mohan M, Antholine WE, Xu RX, Petering DH (1990) Biochemistry 29:7046–7053
10. Jansson PJ, Sharpe PC, Bernhardt PV, Richardson DR (2010) J Med Chem 53:5759–5769. doi:10.1021/jm100561b
11. Nocentini G, Barzi A (1996) Biochem Pharmacol 52:65–71
12. Nocentini G, Barzi A (1997) Gen Pharmacol 29:701–706
13. Sigman DS, Mazumder A, Perrin DM (1993) Chem Rev 93:2295–2316
14. Jungwirth U, Kowol CR, Keppler BK, Hartinger C, Berger W, Heffeter P (2011) Antioxid Redox Signal 15:1085–1127
15. Saryan LA, Ankel E, Krishnamurti C, Petering DH, Elford H (1979) J Med Chem 22:1218–1221
16. Sammes PG, Yahioglu G (1994) Chem Soc Rev 23:327–334
17. Yu Y, Kalinowski DS, Kovacevic Z, Siafakas AR, Jansson PJ, Stefani C, Lovejoy DB, Sharpe PC, Bernhardt PV, Richardson DR (2009) J Med Chem 52:5271–5294
18. Kowol CR, Trondl R, Heffeter P, Arion VB, Jakupec MA, Roller A, Galanski M, Berger W, Keppler BK (2009) J Med Chem 52:5032–5043
19. Nocentini G, Federici F, Franchetti P, Barzi A (1993) Cancer Res 53:19–26
20. Shao J, Zhou B, Di Bilio AJ, Zhu L, Wang T, Qi C, Shih J, Yen Y (2006) Mol Cancer Ther 5:586–592
21. Giles FJ, Fracasso PM, Kantarjian HM, Cortes JE, Brown RA, Verstovsek S, Alvarado Y, Thomas DA, Faderl S, Garcia-Manero G, Wright LP, Samson T, Cahill A, Lambert P, Plunkett W, Sznol M, DiPersio JF, Gandhi V (2003) Leuk Res 27:1077–1083
22. Karp JE, Giles FJ, Gojo I, Morris L, Greer J, Johnson B, Thein M, Sznol M, Low J (2008) Leuk Res 32:71–77
23. Nutting CM, van Herpen CM, Miah AB, Bhide SA, Machiels JP, Buter J, Kelly C, de Raucourt D, Harrington KJ (2009) Ann Oncol 20:1275–1279. doi:10.1093/annonc/mdn775
24. Kunos CA, Waggoner S, von Gruenigen V, Eldermire E, Pink J, Dowlati A, Kinsella TJ (2010) Clin Cancer Res 16:1298–1306. doi:10.1158/1078-0432.CCR-09-2469
25. Narasimhan J, Antholine WE, Chitambar CR, Petering DH (1991) Arch Biochem Biophys 289:393–398
26. Finch RA, Liu MC, Cory AH, Cory JG, Sartorelli AC (1999) Adv Enzyme Regul 39:3–12
27. Chikira M, Tomizawa Y, Fukita D, Sugizaki T, Sugawara N, Yamazaki T, Sasano A, Shindo H, Palaniandavar M, Antholine WE (2002) J Inorg Biochem 89:163–173
28. Antholine WE, Taketa F (1984) J Inorg Biochem 20:69–78
29. Sigman DS, Graham DR, D'Aurora V, Stern AM (1979) J Biol Chem 254:12269–12272
30. Saryan LA, Mailer K, Krishnamurti C, Antholine W, Petering DH (1981) Biochem Pharmacol 30:1595–1604
31. Byrnes RW, Antholine WE, Petering DH (1992) Free Radic Biol Med 13:469–478
32. McCann M, Geraghty M, Devereux M, O'Shea D, Mason J, O'Sullivan L (2000) Met Based Drugs 7:185–193
33. Tsang SY, Tam SC, Bremner I, Burkitt MJ (1996) Biochem J 317:13–16
34. Ruiz R, Garcia B, Garcia-Tojal J, Busto N, Ibeas S, Leal JM, Martins C, Gaspar J, Borras J, Gil-Garcia R, Gonzalez-Alvarez M (2010) J Biol Inorg Chem 15:515–532. doi:10.1007/s00775-009-0620-7
35. Aguirre MdC, Borras J, Castineiras A, Garcia-Monteagudo JM, Garcia-Santos I, Niclos J, West DX (2006) Eur J Inorg Chem 6:1231–1244
36. Garcia-Tojal J, Garcia-Jaca J, Cortes R, Rojo T, Urtiaga MK, Arriortua MI (1996) Inorg Chim Acta 249:25–32
37. Popović-Bijelić A, Kowol CR, Lind MES, Luo J, Himo F, Enyedy EA, Arion VB, Gräslund A (2011) J Inorg Biochem 105:1422–1431
38. Bruker-Nonius AXS (2008) RLATT. Bruker-Nonius AXS, Madison
39. Bruker-Nonius AXS (2004) SAINT-Plus. Bruker-Nonius AXS, Madison
40. Bruker-Nonius AXS (2008) TWINABS. Bruker-Nonius AXS, Madison
41. Sheldrick GM (2008) Acta Crystallogr Sect A Found Crystallogr 64:112–122
42. Johnson GK (1976) Oak Ridge National Laboratory, Oak Ridge
43. Stoll S, Schweiger A (2006) J Magn Reson 178:42–55. doi:10.1016/j.jmr.2005.08.013
44. Grusch M, Fritzer-Szekeres M, Fuhrmann G, Rosenberger G, Luxbacher C, Elford HL, Smid K, Peters GJ, Szekeres T, Krupitza G (2001) Exp Hematol 29:623–632
45. Gomes A, Fernandes E, Lima JL (2005) J Biochem Biophys Methods 65:45–80. doi: 10.1016/j.jbbm.2005.10.003
46. Ghosh K, Kumar P, Tyagi N, Singh UP, Aggarwal V, Baratto MC (2010) Eur J Med Chem 45:3770–3779. doi:10.1016/j.ejmech.2010.05.026
47. Enyedy EA, Nagy NV, Zsigo E, Kowol CR, Arion VB, Keppler BK, Kiss T (2010) Eur J Inorg Chem 11:1717–1728
48. Hathaway BJ, Billing DE (1970) Coord Chem Rev 5:143–207
49. Fasman GD (1976) CRC handbook of biochemistry and molecular biology. CRC Press, Cleveland
50. Noszal B, Visky D, Kraszni M (2000) J Med Chem 43:2176–2182
51. Schafer FQ, Buettner GR (2001) Free Radic Biol Med 30:1191–1212
52. Ainscough EW, Brodie AM, Denny WA, Finlay GJ, Ranford JD (1998) J Inorg Biochem 70:175–185
53. Garcia-Tojal J, Garcia-Orad A, Diaz AA, Serra JL, Urtiaga MK, Arriortua MI, Rojo T (2001) J Inorg Biochem 84:271–278
54. Jansen BA, Brouwer J, Reedijk J (2002) J Inorg Biochem 89:197–202
55. Diaz AM, Villalonga R, Cao R (2009) J Coord Chem 62:100–107
56. Bijloo GJ, van der Goot H, Bast A, Timmerman H (1990) J Inorg Biochem 40:237–244
57. Pierre J-L, Chautemps P, Refaif S, Beguin C, El Marzouki A, Serratrice G, Saint-Aman E, Rey P (1995) J Am Chem Soc 117:1965–1973

2.6 L- and D-proline thiosemicarbazone conjugates: coordination behavior in solution, and the effect of copper(II) coordination on their antiproliferative activity

Miljan NM Milunovic, Éva A Enyedy, Nóra V Nagy, Tamás Kiss, Robert Trondl, Michael A. Jakupec, Bernhard K. Keppler, Regina Krachler, Ghenadie Novitchi, Vladimir B. Arion

Inorganic Chemistry **2012** submitted May 2012

L- and D-proline thiosemicarbazone conjugates: coordination behavior in solution, and the effect of copper(II) coordination on their antiproliferative activity

Miljan N. M. Milunovic,[a] Éva A. Enyedy,[b] Nóra V. Nagy,[c] Tamás Kiss,[b,d] Robert Trondl,[a] Michael A. Jakupec,[a] Bernhard K. Keppler,[a] Regina Krachler,[a] Ghenadie Novitchi,[e] Vladimir B. Arion*[a]*

[a]*University of Vienna, Institute of Inorganic Chemistry, Währinger Strasse 42, A-1090 Vienna, Austria,* [b]*Department of Inorganic and Analytical Chemistry, University of Szeged, Dóm tér 7. H-6720 Szeged, Hungary,* [c]*Institute of Molecular Pharmacology, Research Centre for Natural Sciences, Hungarian Academy of Sciences, Pusztaszeri út 59-67, H-1025, Budapest, Hungary,* [d]*Bioinorganic Chemistry Research Group of the Hungarian Academy of Sciences, University of Szeged, Dóm tér 7. H-6720 Szeged, Hungary,* [e]*Laboratoire National des Champs Magnétiques Intenses, CNRS UPR-3228, 25 rue des Martyrs, 38042 Grenoble cedex 9, France*

Thiosemicarbazones, Copper(II), Solution equilibrium, Stability constants, Antiproliferative activity

*To whom correspondence should be addressed. E-mail: enyedy@chem.u-szeged.hu (E.A.E.); vladimir.arion@univie.ac.at (V.B.A.).

Abstract

Two enantiomerically pure thiosemicarbazone-proline conjugates with enhanced aqueous solubility, namely 2-hydroxy-3-methyl-(*S*)-pyrrolidine-2-carboxylate-5-methylbenzaldehyde thiosemicarbazone [*L*-Pro-STSC or (*S*)-H_2L] and 2-hydroxy-3-methyl-(*R*)-pyrrolidine-2-carboxylate-5-methylbenzaldehyde thiosemicarbazone [*D*-Pro-STSC or (*R*)-H_2L] have been synthesized and characterized by elemental analysis, spectroscopic methods (UV−vis, ^1H and ^{13}C NMR) and ESI mass spectrometry. Metal complexation behavior of *L*-Pro-STSC, stoichiometry and thermodynamic stability of iron(II), iron(III), copper(II) and zinc(II) complexes in 30% (w/w) DMSO/H_2O solvent mixture have been studied by pH-potentiometric, UV−vis spectrophotometric, CD, EPR, ^1H NMR spectroscopic and spectrofluorimetric measurements. By reaction of $CuCl_2 \cdot 2H_2O$ with (*S*)-H_2L and (*R*)-H_2L, respectively, the complexes [Cu(*S*-H_2L)Cl]Cl and [Cu(*R*-H_2L)Cl]Cl have been prepared and comprehensively characterized. X-ray diffraction study of [Cu(*R*-H_2L)Cl]Cl showed the formation of a square-planar copper(II) complex, which forms stacks with interplanar separation of 3.3 Å. The antiproliferative activity of two chiral ligands and their corresponding copper(II) complexes has been tested in two human cancer cell lines, namely SW480 (colon carcinoma) and CH1 (ovarian carcinoma). The thiosemicarbazone-proline conjugates *L*-Pro-STSC and *D*-Pro-STSC show only moderate cytotoxic potency with IC_{50} values of 62 and 75 μM, respectively, in CH1 cells and > 100 μM in SW480 cells. However, the corresponding copper(II) complexes are 13 and 5 times more potent in CH1 cells, based on comparison of IC_{50} values, and in SW480 cells the increase in antiproliferative activity is even higher. In both tested cell lines the *L*-Pro-STSC as well as its copper(II) complex show slightly stronger antiproliferative activity than the compounds with a *D*-Pro moiety, yielding IC_{50} values of 5.5 and 4.6 μM for [Cu(*L*-Pro-STSC)Cl]Cl in CH1 and SW480 cells, respectively.

Introduction

Thiosemicarbazones (TSCs) are strong chelating ligands for transition metals with a broad spectrum of biological activity.[1,2] α(N)-Heterocyclic TSCs are known as potential antitumour drugs.[3,4] Triapine (3-aminopyridine-2-carboxaldehyde thiosemicarbazone) is the most prominent

example of this family of compounds which is in phase I and II clinical trials, showing, in particular, promising activity in hematological tumours.[5–7] Triapine and other related TSCs, as well as their metal complexes, are known as strong inhibitors of ribonucleotide reductase (RNR), an important enzyme promoting the production of deoxyribonucleotides required for DNA synthesis and cell proliferation,[8–13] while some copper(II) thiosemicarbazonates inhibit DNA topoisomerase II, an enzyme responsible for regulation of DNA topology.[14–16] The formation of an iron(II) complex with Triapine, its reaction with molecular oxygen an subsequent formation of reactive oxygen species (ROS) which destroy the tyrosyl radical of RNR are considered the main steps in their mode of action.[17,18] A potential specific binding pocket for Triapine on the surface of the mouse R2 RNR protein has been proposed quite recently.[19] The ability of TSCs to act as chelators of transition metal ions is well documented in the literature by isolation and characterization of the resulting complexes in the solid state,[20] and, by solution equilibrium studies, which provide valuable information about the chemical species present in aqueous solution at physiological pH and their thermodynamic stability.[21] Studies in solution are of utmost importance for understanding the mechanism of action of biologically active compounds and design of even stronger chelators. However, such investigations are very often hampered by the low aqueous solubility of TSCs.

2-Hydroxybenzaldehyde (or salicylaldehyde) TSC (STSC) was also reported to form complexes with transition metals.[22] However, this organic compound shows only a moderate cytotoxic activity in tumor cells,[23,24] in comparison with α(N)-heterocyclic TSCs exhibiting IC_{50} values in the low micromolar or even high nanomolar range,[25,20f] and the reasons for this dramatic drop in activity are still unknown. The antiproliferative activity of STSC can be enhanced to some extent by attachment of polar, electron-donating substituents, e.g. dimethylamino and/or methoxy group(s) to the 2-hydroxybenzaldehyde moiety[24] or by coordination to metal ions.[23]

Copper(II) chloride forms a square-planar complex with 2-hydroxy-3-methoxybenzaldehyde TSC (HL) of 1:1 stoichiometry, namely $[Cu(L)Cl]\cdot H_2O$.[26] The methoxy group and the co-crystallized water molecule are involved in formation of one-dimensional planar chains via intermolecular hydrogen-bonding interactions. By reaction of copper(II) sulfate with salicylaldehyde-β-D-glycoside TSC followed by re-crystallization of the precipitate from DMSO

the complex $[Cu(L^1)(H_2O)]_2SO_4 \cdot 2DMSO$, where HL^1 = 2-hydroxybenzaldehyde TSC, was isolated and characterized. The crystal structure consists of centrosymmetric dinuclear cations stabilized by $\pi-\pi^*$ interaction between four-coordinate square-planar monocations. The X-ray diffraction structures of both copper(II) complexes imply that both species are potential DNA intercalators. Moreover, it has been reported recently, that square-planar coordination geometry of some copper(II) TSCs is likely the biologically active configuration in Topo-IIα inhbition via an ATP binding site-based mechanism.[15,16]

Reports on thermodynamic stability of the metal complexes of STSC and its derivatives are scarce in the literature,[27] because of their generally low aqueous solubility hampering solution equilibrium studies. Quite recently some of us studied in detail the stoichiometry and thermodynamic stability of the iron(II), iron(III), copper(II), zinc(II) and gallium(III) complexes with STSC in water/dimethyl sulfoxide (DMSO) mixture by pH-potentiometric, UV−vis spectrophotometric, EPR, ^{1}H NMR spectroscopic and spectrofluorimetric measurements and compared these data with those for α(N)-heterocyclic TSCs.[11,20f] Herein we report on the synthesis and spectroscopic characterization of two enantiomerically pure Pro-STSC conjugates with enhanced aqueous solubility, namely, 2-hydroxy-3-methyl-(S)-pyrrolidine-2-carboxylate-5-methylbenzaldehyde thiosemicarbazone [*L*-Pro-STSC or (*S*)-H_2L] and 2-hydroxy-3-methyl-(R)-pyrrolidine-2-carboxylate-5-methylbenzaldehyde thiosemicarbazone [*D*-Pro-STSC or (*R*)-H_2L] (Scheme 1). Metal complexation behaviour of *L*-Pro-STSC, stoichiometry and thermodynamic stability of iron(II) and iron(III), copper(II) and zinc(II) complexes in 30% (w/w) DMSO/H_2O solvent mixture has been studied by pH-potentiometric, UV/Vis spectrophotometric, EPR, ^{1}H NMR, CD spectroscopic and spectrofluorimetric measurements. In addition, the isolation and characterization of square-planar copper(II) complexes with enantiomerically pure Pro-STSC conjugates in the solid state are reported. The effect of copper(II) coordination, as well as chirality of the Pro moiety on the antiproliferative activity of conjugates in two human cancer cell lines has been studied as well.

Results and Discussion

Synthesis and characterization of chiral thiosemicarbazones. The chiral thiosemicarbazone-proline conjugates have been prepared in three steps as shown in Scheme 1. First 3-chloromethyl-2-hydroxy-5-methylbenzaldehyde[28] was allowed to react with *L*- or *D*-proline methyl ester with formation of compounds (*S*)-**1** and (*R*)-**1**, respectively. Condensation reactions of these latter compounds with thiosemicarbazide followed by hydrolysis of the methyl ester groups afforded the corresponding TSCs with coupled via a methylene group Pro moiety [(*S*)-H_2L and (*R*)-H_2L]. The formation of desired species has been confirmed by ^{1}H and ^{13}C NMR measurements, as well as by ESI mass spectra. The number of ^{1}H and ^{13}C resonances in NMR spectra is in accord with the proposed structure of C_1 symmetry. The mass spectra recorded in positive ion mode showed peaks at *m*/*z* 359 and 337 due to $[M+Na]^+$ and $[M+H]^+$ ions. The pH-metric titrations (vide infra) suggest that both compounds are tribasic and adopt zwitterionic structures as shown in Scheme 1.

Scheme 1. Synthesis of chiral thiosemicarbazone-proline derivatives (*S*)-**H_2L**, (*R*)-**H_2L**.[a]

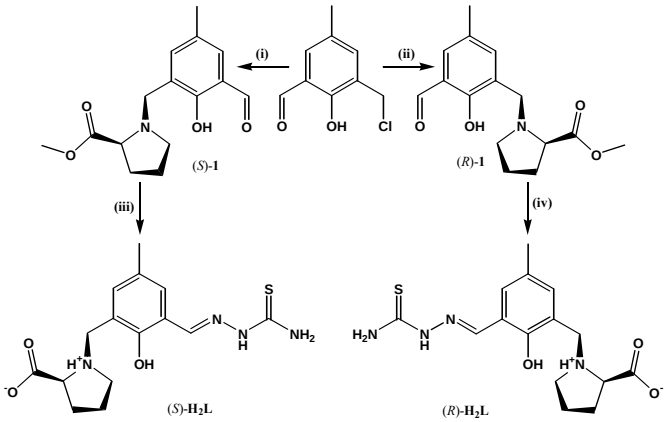

[a]Reagents and conditions: (i) methyl (*S*)-pyrrolidine-2-carboxylate hydrochloride, triethylamine, THF/CH_2Cl_2 1.5:1, rt, purification by column chromatography [(*S*)-**1**, 51%]; (ii) methyl (*R*)-pyrrolidine-2-carboxylate hydrochloride, triethylamine, THF/CH_2Cl_2 1.5:1, rt, purification by column chromatography [(*R*)-**1**, 39%]; (iii) thiosemicarbazide, EtOH/H_2O 1:1, 70–75 °C, 75 h, [(*S*)-**H_2L**, 41%]; (iv) thiosemicarbazide, EtOH/H_2O 1:1, 70–75 °C, 12 h, [(*R*)-**H_2L**, 18%].

Scheme 2. Deprotonation steps of H_3L^+ (relevant for both Pro-STSC enantiomers).

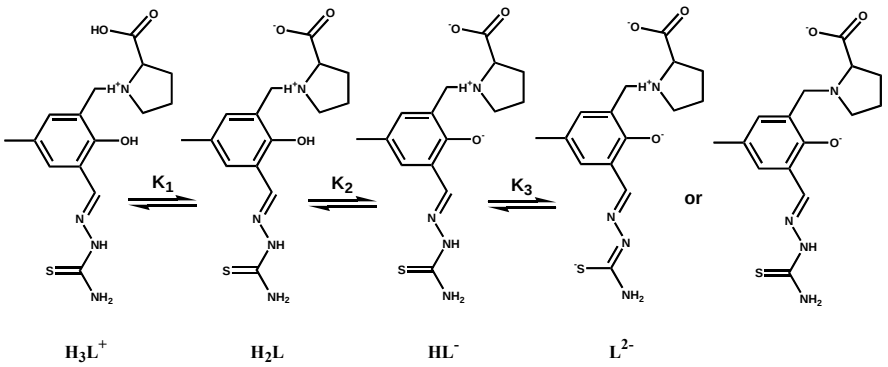

Aqueous solutions of *L*- and *D*-Pro-STSC ligands at neutral pH are indeed optically active and show Cotton effects for both enantiomers (see Figure S1A). As expected they are roughly mirror images over the 240−400 nm region of the circular dichroism (CD) spectra, while their UV–vis spectra are identical.

Proton dissociation processes and lipophilicity. Proton-dissociation processes of (*S*)-H_2L (Scheme 2) were followed by pH-potentiometry, UV–vis spectrophotometry and spectrofluorimetry as well as ^{1}H NMR titrations. Measurements were performed in a 30% (w/w) DMSO/H_2O solvent mixture. Consecutive titrations showed that no ligand decomposition occurred in the pH range studied under the argon atmosphere. Three proton dissociation constants could be determined by different methods (Table 1) and constants obtained are in reasonably good agreement. pK_1 can presumably be attributed to deprotonation of the carboxylic group in (*S*)-H_3L^+, while pK_2 belongs presumably to the phenolic-OH. pK_3 can be related to the proton dissociation of the N^2–H group of the thiosemicarbazide moiety or proton dissociation of the tertiary Pro nitrogen. Based on the methods used we cannot distinguish these most probably overlapping deprotonation processes. It is noteworthy that the magnitudes of pK_1 and pK_3 values, low and high, respectively, hamper their accurate determination by pH-metry as these deprotonation steps take place in the pH ranges where the pH measurements become uncertain.

Table 1. Proton dissociation constants (pK_a) of the ligand *L*-Pro-STSC determined by various methods; [a] λ_{max} and molar absorptivity ($M^{-1}cm^{-1}$) values for ligand species H_2L, HL^-, L^{2-} determined by UV−vis spectrophotometric titrations and calculated chemical shifts (ppm) for H_3L^+, H_2L and HL^- obtained by ^1H NMR titrations. {t = 25.0 °C, I = 0.10 M (KCl) in 30% (w/w) DMSO/H_2O}.

	pH-metry		**UV−vis**		**^{1}H NMR[b]**		
pK_1	2.17(8)		−		2.36(5)		
pK_2	7.90(3)		7.79(8)		7.85(2)		
pK_3	11.88(12)		11.66(10)		−		
	λ_{max} (ε/$M^{-1}cm^{-1}$)						
H_2L	308 nm (19250); 336 nm (15820)						
HL^-	302 nm (16490); 388 nm (11640)						
L^{2-}	308 nm (14700); 362 nm (12200)						
δ/ ppm[b]	CH=N (s)	CH(4)$_{Ar}$ (s)	CH(6)$_{Ar}$ (s)	CH_3 (s)	C-CH_2-N (d)	C-CH_2-N (d)	CH-COOH (m)
H_3L^+	8.243	7.400	7.320	2.294	3.644	4.195	3.311
H_2L	8.239	7.392	7.319	2.292	3.601	3.975	3.231
HL^-	8.420	7.609	7.043	2.184	3.294	3.743	2.916

[a] The numbers in parentheses are standard uncertainties for the species determined in the present work. [b] Determined in 30% (w/w) d_6-DMSO/H_2O

The pH-dependent physico-chemical properties of the *L*-Pro-STSC ligand such as fluorescence emission, absorbance, chemical shifts were monitored by different spectroscopic methods with a

different level of sensitivity to the certain proton dissociation processes. The UV–vis spectra are almost unchanged in the pH range where the deprotonation of the carboxylic group occurs (Figure 1), thus pK_1 could not be determined by this method with acceptable accuracy. Deprotonation of the phenolic OH is accompanied by a considerable shift of the λ_{max} value from 336 to 388 nm and the colorless solution of the ligand turns into yellow. Two well-separated isosbestic points are seen at 355 and 373 nm due to the deprotonation equilibria $H_2L \rightleftharpoons HL^- + H^+$ and $HL^{2-} \rightleftharpoons L^{2-} + H^+$, respectively. Therefore, pK_2, pK_3 values and the spectra of the individual ligand species (H_2L; HL^-; L^{2-}) (Table 1, Figure S2) were calculated on the basis of deconvolution of the UV–vis spectra.

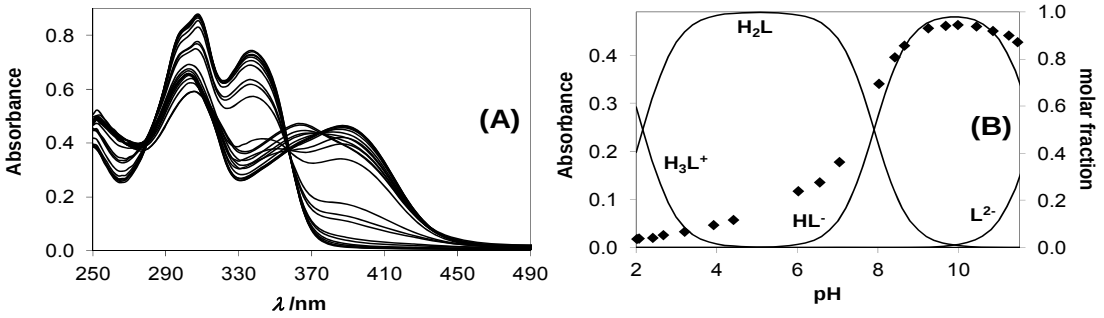

Figure 1. UV−vis absorbance spectra of *L*-Pro-STSC recorded at different pH values (A); Concentration distribution curves for ligand species with the pH-dependence of absorbance values at 384 nm (◆) (B) {c_{ligand} = 4.0 × 10^{-5} M; t = 25.0 °C, I = 0.10 M (KCl) in 30% (w/w) DMSO/H_2O}.

L-Pro-STSC possesses intrinsic fluorescence due to its extended conjugated electronic system as the 3D spectrum shows (see inset of Figure 2), which is a valuable property for e.g. monitoring cellular uptake or intracellular distribution of the ligand or its metal complexes by fluorescence microscopy. The fluorescence emission of *L*-Pro-STSC in its zwitterionic H_3L^+ or H_2L forms is negligible at any excitation wavelength, however, the proton dissociation at the phenolic OH results in a significant increase of the intensity, which is diminished by the third deprotonation step above pH 10.5 (Figure 2).

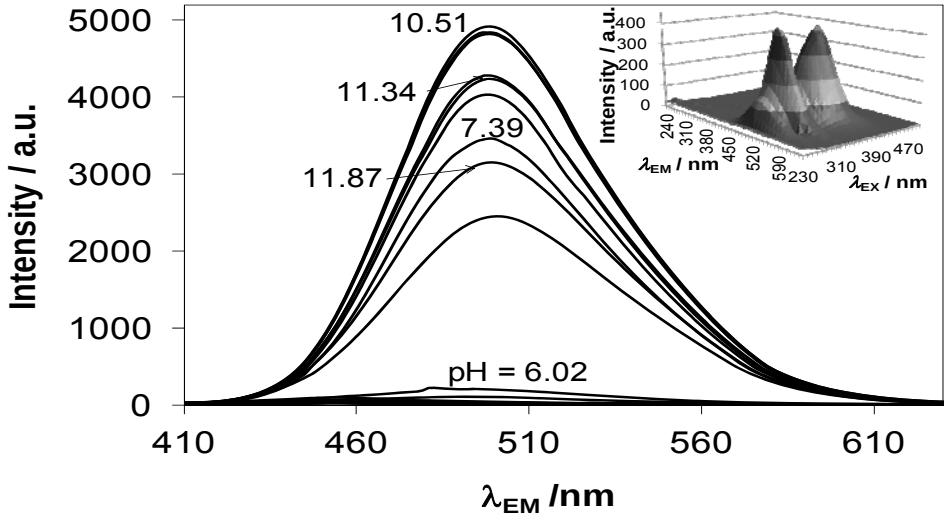

Figure 2. Fluorescence emission spectra of *L*-Pro-STSC recorded at different pH values {c_{ligand} = 5.1 × 10^{-6} M; λ_{EX} = 393 nm; t = 25.0 °C, I = 0.10 M (KCl) in 30% (w/w) DMSO/H_2O; slits: 5 nm/5 nm} *Inset shows the 3D fluorescence spectra at pH 10.0 {slits: 2.5 nm/2.5 nm}.*

The pH-dependent ^{1}H NMR spectra of the ligand (Figure S3) revealed that the protons of the Pro heterocycle, namely C*H*−COOH and CH_2−CH−N are most sensitive to the deprotonation of the COOH group. Therefore pK_1 was calculated based on the changes of the chemical shifts (δ) of these protons (Figure 3). The second proton dissociation step is accompanied by more significant electronic deshielding effects, namely upfield shifts of the C*H*$(6)_{Ar}$, C−CH_2−N, C*H*−COOH and CH_3 protons, while the C*H*=N and C*H*$(4)_{Ar}$ resonances were downfield shifted upon increasing the pH. Further changes were observed at pH > 11 due to the third deprotonation step, but data were not appropriate for calculation of the pK_3 value.

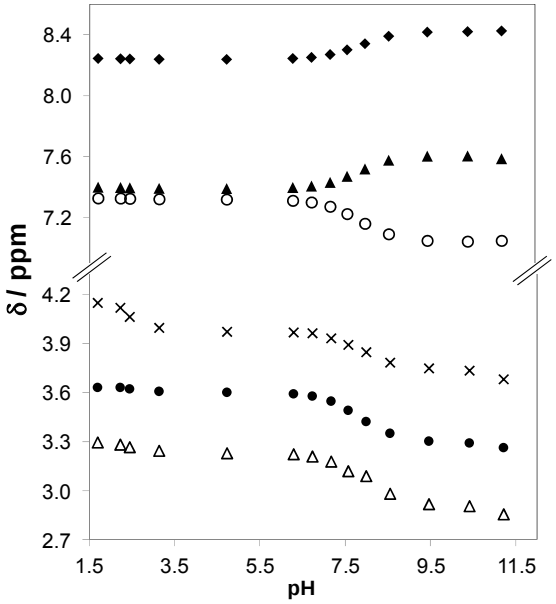

Figure 3. pH-dependence of the chemical shifts (δ) of the various protons of the ligand *L*-Pro-STSC: C*H*=N (♦); C*H*(3)$_{Ar}$ (▲); C*H*(5)$_{Ar}$ (○); C-C*H*$_2$-N (●);C-C*H*$_2$-N (×); C*H*-COOH (Δ) {*t* = 25.0 °C; *I* = 0.10 M (KCl) in 30% (w/w) d_6-DMSO/H_2O}.

It is noteworthy that the phenolic OH of the ligand *L*-Pro-STSC is considerably more acidic compared to those of reference STSC (pK = 8.89[27]).

Partition coefficients (*P*) of *L*- and *D*-Pro-STSC were determined at pH 7.4 via the partitioning between *n*-octanol and water (Figure S4). The Pro-STSC conjugates show a more hydrophilic character ($\log P_{7.4} = -0.56 \pm 0.01$ for the *L*- and -0.60 ± 0.01 for the *D*-enantiomer) compared to that of the reference STSC ($\log P_{7.4} = +1.74$)[27] or Triapine ($\log P_{7.4} = +0.85$).[27] At physiological pH the Pro-STSC ligand is mainly present in the neutral form (75% H_2L, 25% HL^-) and the carboxylic group is fully deprotonated. This relatively low log*P* value results in enhanced aqueous solubility compared to other chemically related TSCs.

Complexation reactions of copper(II), zinc(II), iron(II) and iron(III) with *L*-Pro-STSC. The complex formation processes of the ligand *L*-Pro-STSC with Cu^{2+}, Zn^{2+}, Fe^{2+} and Fe^{3+} were studied primarily by pH-potentiometry in a 30% (w/w) DMSO/H_2O solvent mixture. The

complex formation with Fe^{3+} and Cu^{2+} starts at low pH (pH ~ 2) in the millimolar concentration range (see Figure 4 for Fe^{3+}), while with Zn^{2+} and Fe^{2+} only at pH > 4. Formation of some mixed hydroxido species occurred at basic pH mainly at higher ligand-to-metal ratio, as concluded from the base consumption exceeding the number of dissociable protons in the ligand. The stoichiometries of the metal complexes and the cumulative stability constants furnishing the best fits to the experimental data are listed in Table 2. Stability constant of the species $[Fe(III)\,LH]^{2+}$ was determined by spectrophotometry on individual samples following the changes of the metal-to-ligand charge transfer (CT) and ligand bands in the region of 300 − 470 nm between pH 1 and 2. Then the determined value was kept constant during the pH-metric data evaluation.

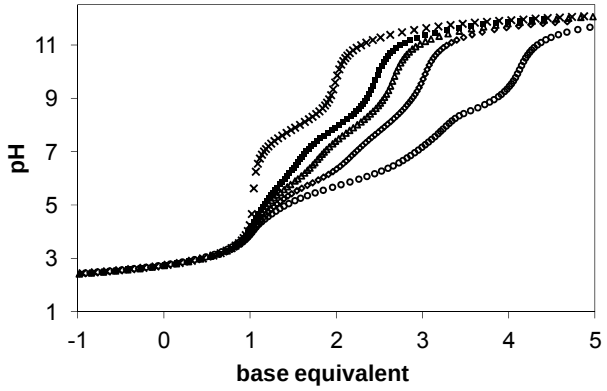

Figure 4. Representative pH-potentiometric titration curves for ligand (×) and for the Fe^{2+} − *L*-Pro-STSC system at 1:1.2 (○), 1:2.3 (◊), 1:3.3 (Δ), 1:4.5 (■) metal-to-ligand ratios {c_{ligand} = 2×10^{-3} M; 30% (w/w) DMSO/H_2O); t = 25 °C; I = 0.10 M (KCl)}.

The data reveal formation of merely mono-ligand complexes of Cu^{2+} and Zn^{2+}, while Fe^{2+} and Fe^{3+} ions, in addition, form bis-ligand complexes. Direct comparison of the overall stability constants undoubtedly shows the significantly higher stability of the Fe^{3+} and Cu^{2+} complexes over that of the Zn^{2+} and Fe^{2+} species. pM values have been computed to provide a basis for comparison of the relative chelating ability of *L*-Pro-STSC at physiological pH (Table 2). (pM stands for the negative logarithm of the equilibrium concentrations of the free metal ion under certain conditions. pM* was also calculated for Fe^{3+} which involves the various hydroxido species $[Fe(III)_pH_r]$, since they belong to the non-bound fraction, in addition to the free Fe^{3+} ion).

Table 2. Stability constants ($\log\beta[M_pL_qH_r]$) for the Cu^{2+}, Zn^{2+}, Fe^{2+} and Fe^{3+} complexes of the *L*-Pro-STSC with some stepwise constants and pM values {t = 25.0 °C, I = 0.10 M (KCl) in 30% (w/w) DMSO/H_2O}[a].

	Cu^{2+}	Zn^{2+}	Fe^{2+}	Fe^{3+}
$\log\beta([MLH])$	21.58(3)	18.12(3)	18.14(4)	22.39(4)[b]
$\log\beta([ML])$	17.54(3)	12.40(3)	12.24(6)	19.48(3)
$\log\beta([MLH_{-1}])$	6.97(4)	2.51(3)	–	–
$\log\beta([ML_2H])$	–	–	28.86(5)	38.24(3)
$\log\beta([ML_2])$	–	–	21.07(6)	33.32(4)
$\log\beta([ML_2H_{-1}])$	–	–	10.99(7)	22.13(8)
fitting parameter (mL)	5.15×10^{-3}	5.52×10^{-3}	8.64×10^{-3}	3.01×10^{-3}
$\log K([ML_2])$	–	–	8.83	13.84
pM[c]	13.4	8.3	8.2	18.9[d]

[a] The numbers in parentheses are standard uncertainties for the complexes determined in the present work. Charges of the complexes are omitted for simplicity (H_2L is charge-neutral). [b] Determined by UV−vis spectrophotometric measurements at pH = 1 − 2. [c] pM (= –log[M]) values at pH = 7.4; $c_M = 1\times10^{-6}$ M; M : L = 1:10. [d] pM* = $-\log(\Sigma[M_pH_r])$ = 10.9 at pH = 7.4; $c_M = 1\times10^{-6}$ M; M : L = 1:10.

According to these pM (pM*) values the ligand effectiveness is varied in the following order at pH 7.4: $Fe^{2+} \sim Zn^{2+} << Fe^{3+} < Cu^{2+}$. It is noteworthy that *L*-Pro-STSC shows the formation of similar type of complexes and quite similar pM values with those of its reference model ligand, STSC. However, a slightly higher efficacy of *L*-Pro-STSC is seen in the case of Fe^{3+} and Zn^{2+}.[27] These findings suggest that both ligands coordinate in a similar fashion to the metal centers and the *L*-Pro moiety does not alter significantly the compositions and stabilities of the metal complexes, but improves their aqueous solubility. In order to elucidate the most probable

coordination modes of the *L*-Pro-STSC in metal complexes and to confirm the speciation obtained by the pH-potentiometry UV−vis, EPR, CD and ^{1}H NMR spectroscopies were applied.

Weak bands in the visible wavelength range belong mainly to the d-d transitions of the Cu^{2+}–*L*-Pro-STSC complexes (ε_{580nm} ~ 100 − 180 $M^{-1}cm^{-1}$), which are partly overlapped by the S–Cu^{2+} ligand-to-metal CT bands and represent characteristic pH-dependent changes (Figure 5A). The λ_{max} of this band is decreased significantly parallel to the formation of species [CuL] from $[CuLH]^{+}$. The formation of $[CuLH_{-1}]^{-}$ is accompanied by a smaller decrease showing an increment in the ligand field and variation of the coordination mode of the ligand in complexes (Figure 5B). As the ligand is optically active due to the presence of chirality at the proline moiety, CD spectra in the wavelength range 460–650 nm were recorded (Figure 5C). The location of the maxima and minima of peaks shows pH-dependence and parallel changes with the transformation processes of the complexes are seen; e.g. the negative peak is shifted from 650 via 615 to 562 nm as species [CuL] and $[CuLH_{-1}]^{-}$ are formed. The CD spectra of both the [CuL] complexes of *L*-Pro-STSC and *D*-Pro-STSC were recorded at pH 7.4 in the UV range in pure aqueous solution (Figure S1B), which clearly show the presence of pure chiral species.

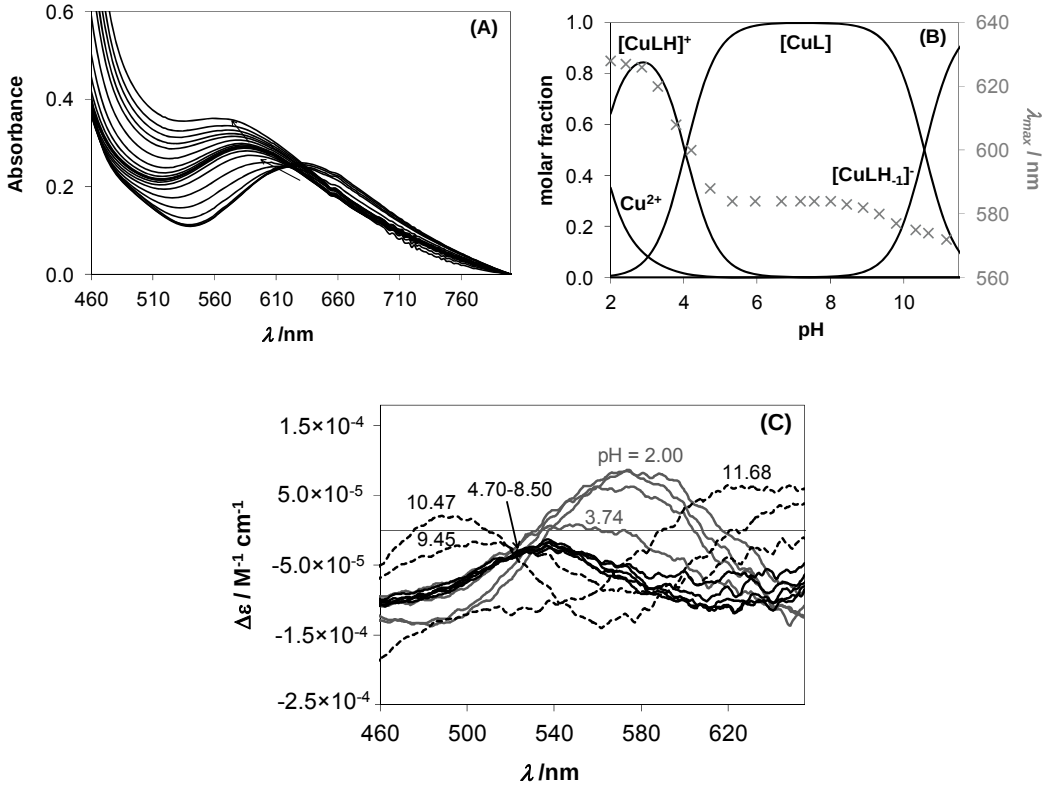

Figure 5. UV–vis absorbance spectra of the Cu^{2+}- *L*-Pro-STSC system recorded at different pH values (A) with the corresponding concentration distribution curves calculated with the stability constants obtained by pH-metry depicted together with the λ_{max} values plotted against pH (B) and the pH-dependent CD spectra of the system (C) {$c_M = 2.0 \times 10^{-3}$ M; M:L = 1:1; t = 25.0 °C, I = 0.10 M (KCl) in 30% (w/w) DMSO/H_2O}.

EPR spectra recorded at various pH values at room temperature (Figure 6) and at 77 K (Figure S5) confirm the speciation obtained by the pH-potentiometry and reveal the coordination modes of the ligand in each Cu^{2+} complex. A two-dimensional simulation of the solution EPR spectra resulted in the individual isotropic EPR parameters of the different Cu^{2+}–*L*-Pro-STSC species (Table 3). The fitted experimental and individual spectra are depicted in Figure 6. The isotropic values calculated by averaging the anisotropic values ($g_{o,calc}$ and $A_{o,calc}$, Table 3) are in good agreement with the corresponding values measured in solution, indicating that the coordination modes adopted by the ligand in solution are preserved upon freezing. The nitrogen splitting, caused by the equatorial coordination of one nitrogen atom, is well resolved in all component

spectra. The deconvolution of the EPR spectra clearly shows that the species $[CuLH]^+$ predominates in solutions already at pH ~ 2.5 – 3 and with increasing pH the species [CuL] is formed in a wide pH range (pH = 6 − 9), then above pH 10 the species $[CuLH_{-1}]^-$ predominates. No dimeric or bis-ligand complexes were found under these conditions. Based on the low g_o and high A_o isotropic values the tridentate coordination of *L*-Pro-STSC and nearly square-planar coordination geometry is suggested for all the complexes. In $[CuLH]^+$ coordination of the ligand via phenolate O^-, N^1 and the thione-S, while the hydrazinic N^2–H moiety is still protonated, is the most likely. (The carboxylic group is supposed to be deprotonated in all species in the partly aqueous solution.) Deprotonation of the hydrazinic N^2–H group of the complex results in lower g_o and higher A_o parameters, thus the (O^-,N^1,S^-) binding mode is feasible in the species [CuL]. Further decrease in g_o and increase in A_o values support the deprotonation of the water molecule coordinating in the fourth equatorial position of the complex $[CuLH_{-1}]^-$. Thus this species is regarded as mixed hydroxido complex, $[CuL(OH)]^-$. Based on EPR data the same coordination modes are realized in the corresponding complexes of *L*-Pro-STSC and STSC,[27] and the carboxylate group of *L*-Pro-STSC is not involved in metal coordination. However, the line width in the component spectra of *L*-Pro-STSC and STSC[27] differs significantly (Figure 6). The broader lines observed for the copper(II) complexes of *L*-Pro-STSC are due to the non-coordinating carboxylate group of the ligand, which leads to a slightly hindered rotation of these complexes in solution. As a consequence, the orientation dependent EPR parameters are not completely averaged out, and the fourth copper line detected in the lower field becomes very broad. Therefore, the simulated spectra, using the equation $\sigma_{MI} = \alpha+\beta M_I+\gamma M_I^2$ for the line width description, showed a systematic deviation from the measured spectra at around 3350 G (Figure 6).

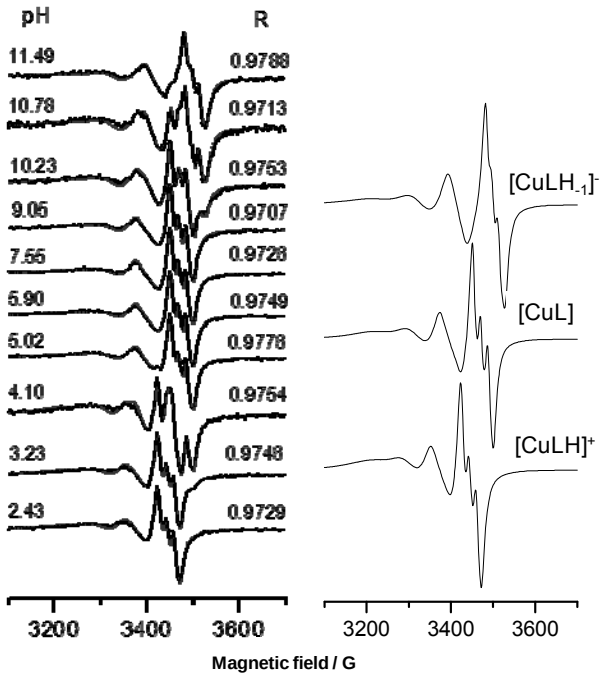

Figure 6. Experimental (black) and simulated (grey) EPR spectra for Cu^{2+} – *L*-Pro-STSC system (left side) and calculated component spectra for complexes [CuLH], $[CuL]^{-}$ and $[CuLH_{-1}]^{2-}$ (right side) {c_{ligand} = 2 mM; M : L = 1:1; room temperature, I = 0.10 (KCl) in 30% (w/w) DMSO/H_2O}.

Table 3. Isotropic EPR parameters of the components obtained for Cu^{2+} – *L*-Pro-STSC system from the two-dimensional simulation of EPR spectra[a,b]

	g_o	A_o /G	a_0^N /G	α / G	β /G	γ /G
Cu^{2+} [c]	2.1970	34.3	−	51.9	−2.2	0.7
$[CuLH]^+$	2.1061(1)	66.1(1)	17.3(1)	35.5(1)	−21.8(1)	3.9(1)
[CuL]	2.0946(1)	76.7(1)	17.5(1)	32.9(1)	−23.0(1)	5.3(1)
$[CuLH_{-1}]^-$	2.0872(2)	84.1(2)	14.9(2)	36.2(1)	−26.5(1)	6.5(1)

[a] The numbers in parentheses are standard uncertainties. [b] Anisotropic EPR parameters for [CuLH]: g_x = 2.0509(1); g_y = 2.0326(1); g_z = 2.2236(1); A_x = 25.4(2) G; A_y = 23.7(2) G; A_z = 170.0(1) G; a_{Nx} = 6.1 G; a_{Ny} = 17.1 G; a_{Nz} = 6.0 G; $g_{0,calc}$ = 2.1024; $A_{0,calc}$ = 75.85 G; for $[CuL]^-$: g_x = 2.0497(1); g_y = 2.0251(1); g_z = 2.2038(1); A_x = 16.3(2) G; A_y = 25.7(2) G; A_z = 176.5(1) G; a_{Nx} = 15.3 G; a_{Ny} = 19.5 G; a_{Nz} = 6.0 G; $g_{0,calc}$ = 2.0929; $A_{0,calc}$ = 75.56 G. [c] Fixed values obtained from separate measurements of Cu^{2+} without ligand.

The tridentate (O^-, N^1, S) coordination of *L*-Pro-STSC in [Cu((*R*)-H_2L)Cl]Cl crystallized from methanol was also confirmed by X-ray diffraction (vide infra).

It should be also noted (based on the stability constants) that the species [CuL] is highly stable even at micromolar concentrations, and practically it does not dissociate at physiological pH.

In the Zn^{2+}–*L*-Pro-STSC system analogous complexes with 1:1 metal-to-ligand ratio were detected, although, with considerably lower stability compared to copper(II) species. The speciation model obtained for the zinc(II) complexes was supported by ^{1}H NMR titrations (Figure 7). In the first instance a slow ligand-exchange process was found with respect to the NMR time scale as the chemical shifts of the protons of the metal-free and the bound ligand can be seen separately. At pH < 5 only the peaks of the metal-free ligand are present. A new set of signals can be found additionally with increasing pH, which most probably belongs to the minor protonated complex $[ZnLH]^+$. These signals with a slightly shifted position become predominant

between pH 7 and 9 where the species [ZnL] is formed. There was no free ligand detected at 1:1 metal-to-ligand ratio at pH > 7. Another species, the mixed hydroxido $[ZnLH_{-1}]^-$ (=$[ZnL(OH)]^-$) starts to be formed at pH > 8.5, its peaks are well-separated from those of [ZnL] due to relatively slow ligand-exchange equilibrium between them (Figure S6). Distribution of the ligand between the bound and non-bound fraction at 1:1 metal-to-ligand ratio was calculated on the basis of the integrated area of the signals of the various ligand protons, and the result is in a good agreement with the concentration distribution curves calculated with the stability constants (Figure 8).

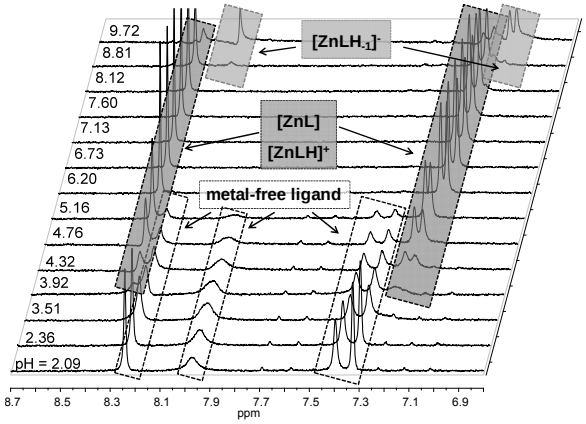

Figure 7. pH-dependent ^{1}H NMR spectra of the Zn^{2+} − *L*-Pro-STSC {c_{ligand} = 2.0 × 10^{-3} M; M : L = 1:1; 30% (w/w) d_6-DMSO/H_2O}

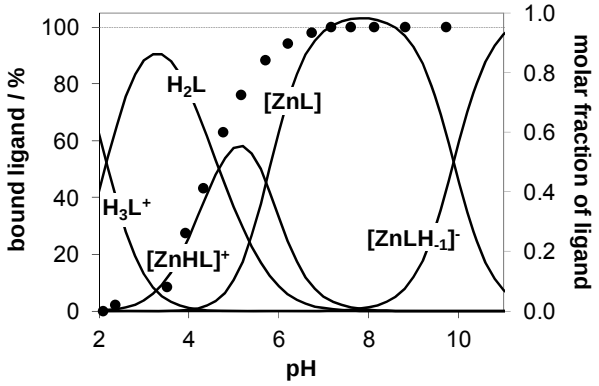

Figure 8. Concentration distribution curves for the Zn^{2+} – *L*-Pro-STSC system (solid lines) calculated on the basis of the stability constants together with the molar fraction of the bound

ligand (●) estimated from the integrated area of the signals of the C*H*=N; C*H*(4)$_{Ar}$; C*H*(6)$_{Ar}$; CH_3; C-CH_2-N; CH_2-CH-N protons {c_{ligand} = 2.0 × 10^{-3} M; M : L = 1:1; 30% (w/w) d_6-DMSO/H_2O}.

Due to the ability of Fe^{2+} and Fe^{3+} ions to form octahedral complexes, bis-ligand iron species could be detected as well (Table 2). In the protonated iron complexes (O^-, N^1, S) coordination mode is supposed when the non-coordinating hydrazinic N^2 atom is protonated, and in the [ML_2] type species the ligand binds via (O^-, N^1, S^-) donor set based on the X-ray diffraction structures of complexes of analogous TSCs.[29–32] Species [ML_2H_{-1}] formed at basic pH are most probably mixed hydroxido species in which a coordinated donor group is displaced by an OH^-. UV−vis spectrophotometric titrations of the Fe^{2+} – *L*-Pro-STSC system under strictly anaerobic conditions show that the formation of the mono-ligand iron(II) species resulted in a shoulder between 430 and 480 nm, whereas formation of the green bis-ligand complexes was accompanied by the development of a wide absorption band with maximum at *ca.* 600 nm (not shown here). The absorbance values at 520 nm are increased mainly due to the formation of the bis-ligand complexes (Figure 9). These Fe^{II} species, however, have intense color, although their molar absorptivities are considerably lower compared to those of the α(N)-pyridyl TSC complexes.[21b,21c] In the case of the Fe^{III} complexes CT bands are found to be strongly overlapped with the ligand bands (Figure S7) and the pH-dependent UV−vis spectra indicate the predominant formation of the $[Fe(III)L_2]^-$ complex (λ_{max} = 374 nm; ε_{374nm}= 18600 $M^{-1}cm^{-1}$) between pH 6.8 and 9.8 even in a diluted solution (c = 2×10^{-5} M), as it is expected on the basis of pH-metry (Figure S7). As a consequence of the high stability of the Fe^{3+} – *L*-Pro-STSC complexes, the bis-ligand species is able to preserve its original integrity almost completely with dilution up to the micromolar concentration range at physiological pH, while the iron(II) complexes with much lower stability can dissociate to the mono-ligand species with decreasing analytical concentrations (Figure 10). Comparing the stability of the iron *L*-Pro-STSC complexes to that of the α(N)-pyridyl TSCs it can be noted that the substitution of the pyridyl nitrogen by the phenolic oxygen results in an increased binding ability for Fe^{3+} and diminished for Fe^{2+} at pH 7.4, as it was found for the STSC complexes previously.[27]

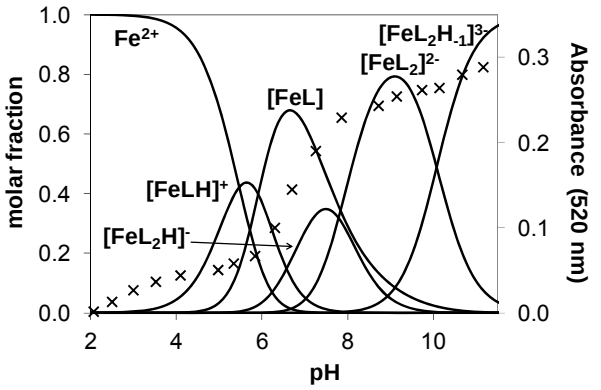

Figure 9. Concentration distribution curves for the Fe^{2+} – *L*-Pro-STSC system (solid lines) calculated on the basis of the stability constants together with the molar fraction of the absorbance values plotted against pH at 520 nm (×){c_{ligand} = 2.0 × 10^{-4} M; M : L = 1:2; *t* = 25.0 °C, *I* = 0.10 M (KCl) in 30% (w/w) DMSO/H_2O}.

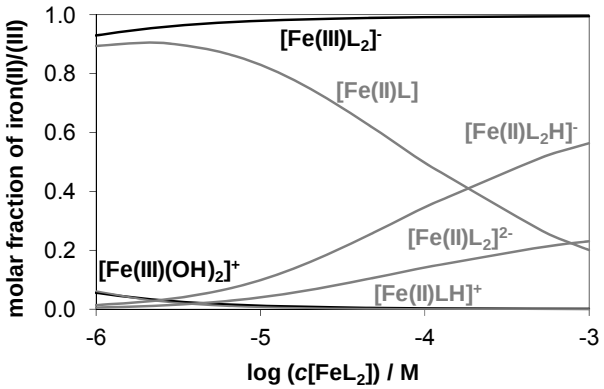

Figure 10. Representative concentration distribution diagram for the Fe^{2+} (grey lines) and Fe^{3+} (black lines) – *L*-Pro-STSC bis-ligand complexes at various total concentrations at pH 7.4 {*t* = 25.0 °C; M:L = 1:2; *I* = 0.10 M (KCl) in 30% (w/w) DMSO/H_2O}.

As ligand *L*-Pro-STSC is strongly fluorescent at physiological pH (see above) the effect of the metal ion binding on the emission was also investigated. The metal coordination can quench the intensity but at different extent in the case of the various metal ions (Figure S8). Fe^{3+} and Cu^{2+} quench almost completely the emission. The fluorescence is still observed in the presence of Zn^{2+}

and Fe^{2+}, and may be satisfactory for monitoring the cellular distribution of these complexes by fluorescence microscopy.

Synthesis and characterization of [Cu(*S*-H_2L)Cl]Cl and [Cu(*R*-H_2L)Cl]Cl. By reaction of methanolic solutions of $CuCl_2 \cdot 2H_2O$ with (*S*)-H_2L and (*R*)-H_2L the complexes [Cu(*S*-H_2L)Cl]Cl and [Cu(*R*-H_2L)Cl]Cl have been isolated in 55 and 84% yield, respectively. The positive ion ESI mass spectra showed the presence of a strong peak at *m*/*z* 398 attributed to $[Cu^{II}(HL)]^+$. In the negative ion mass spectra ions with *m*/*z* 396 and 432 due to $[Cu^{II}(L-H)]^-$ and $[Cu^{II}LCl]^-$, respectively, were observed. The protonation form of the Pro-STSC ligand adopted in the prepared copper(II) complexes could be unequivocally determined by X-ray diffraction study of $[Cu^{II}$(*R*-H_2L)Cl]Cl.

The lipophilicity of both complexes was determined via n-octanol/water partitioning (Figure S9) at physiological pH. As expected similar log$P_{7.4}$ = +0.25 ± 0.01 and +0.24 ± 0.01 values were obtained for the copper(II) complexes with *L*- and *D*-enantiomer, respectively, showing a more lipophilic character compared to the metal-free ligands. (It should be noted that the the partition coefficients were calculated strictly based on the aqueous phase spectra.)

X-ray Crystallography. X-ray diffraction quality crystals were obtained by slow diffusion of diethyl ether into methanolic solution of [Cu(*R*-H_2L)Cl]Cl**.** The result of X-ray diffraction study of [Cu(*R*-H_2L)Cl]Cl is shown in Figure 11. The complex crystallizes in the non-centrosymmetric monoclinic space group $P2_1$ with two crystallographically independent ionic complexes in the asymmetric unit. The copper(II) ion has square-planar coordination geometry. The multidentate tribasic ligand (H_3L^+) uses only in part its donor capacity and acts in the complex as a tridentate one, binding to Cu^{2+} via phenolate oxygen O1a, imine nitrogen N1a and thione sulfur atom S1a. The bond length C8a−S1a of 1.698(6) is equal within 3 σ with that in [Cu(L)Cl]·H_2O, where HL= 2-hydroxy-3-methoxybenzaldehyde thiosemicarbazone. The fourth position in the coordination polyhedron is occupied by a chlorido ligand. In addition, the thiosemicarbazone ligand is protonated at proline nitrogen atom N4a. Protonation is corroborated by difference Fourier map and by the presence of intramolecular bifurcated hydrogen bonding interaction N4a−H···O1a [N4a···O1a 2.695(5) Å, N4a−H···O1a 131.0°] and N4a−H···O2a [N4a···O2a 2.699(5) Å, N4a−H···O2a 113.9°]. The nitrogen atom N2a acts as proton donor in hydrogen bonding

interaction N2a−H···Cl2 [N2a···Cl2 3.067(5) Å, N2a−H···Cl2 148.5°], while O3a in H-bond O3a−H···Cl1a^{i} [O3a···Cl1a^{i} 3.067(5) Å, O3a−H···Cl1a^{i} 148.5°], where *i* denotes symmetry related Cl1a atom generated via symmetry code *x*−1, *y*, *z*. Other hydrogen bonding interactions are shown in unit cell plot in Figure S10. The two crystallographically independent complex cations of the complexes form stacks via π-π* interactions with interplanar separation of about 3.3 Å as shown in Figure S11. This indicates that copper(II) complexes are potential DNA intercalators.

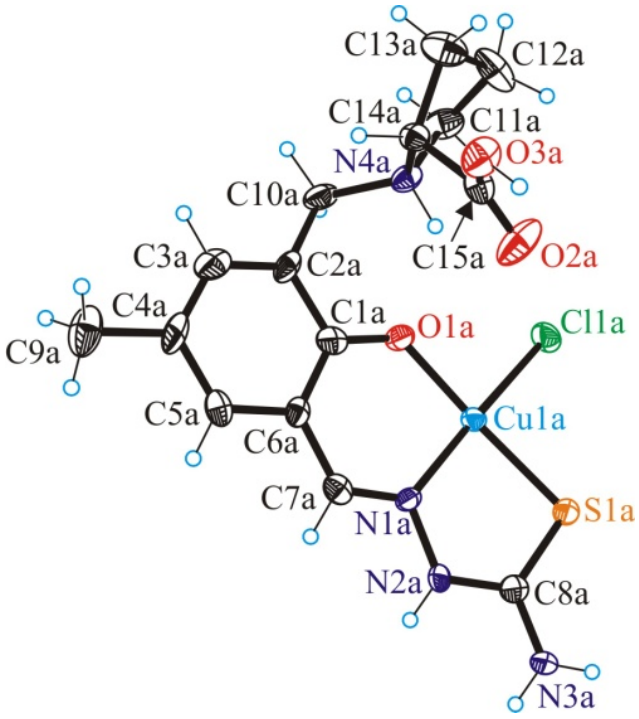

Figure 11. ORTEP view of the first crystalloghraphically independent cation [Cu(H_2L)Cl]$^{+}$ with thermal displacement ellipsoids drawn at 50% probability level. Selected bond distances (Å) and bond angles (deg): Cu1a−Cl1a 2.2677(16), Cu1a−S1a 2.2249(16), Cu1a−O1a 1.888(4), Cu1a−N1a 1.955(5), C1a−O1a 1.318(7), C1a−C6a 1.416(8), C6a−C7a 1.422(8), C7a−N1a 1.294(7), N1a−N2a 1.394(6), N2a−C8a 1.342(7), C8a−S1a 1.698(6), C8a−N3a 1.316(6), C15a−O2a 1.195(6), C15a−O3a 1.328(6); O1a−Cu1a−N1a 92.19(17), N1a−Cu1a−S1a 87.22(13), S1a−Cu1a−Cl1a 90.47(6), O1a−Cu1a−Cl1a 90.48(12).

Cytotoxicity in Cancer Cell Lines. The capacity of inhibiting cancer cell growth *in vitro* of compounds *L*-Pro-STSC and *D*-Pro-STSC and their corresponding copper(II) complexes was determined in human CH1 (ovarian carcinoma) and SW480 (colon carcinoma) cells by means of the colorimetric MTT assay. IC_{50} values are displayed in Table 4. Remarkably, complexation of copper results in a marked increase of antiproliferative activity in both cell lines. The IC_{50} values of Cu^{II} – *L*-Pro-STSC in CH1 and SW480 are 5.5 and 4.6 µM, respectively, whereas Cu^{II} – *D*-Pro-STSC shows IC_{50} values of 14.2 and 11.5 µM, respectively. In contrast, *L*-Pro-STSC and *D*-Pro-STSC showed a low cytotoxic potency with IC_{50} values of 62 and 75 µM in CH1 cells, respectively. In SW480 cells no IC_{50} value could be determined within the chosen range of concentrations up to 100 µM. Comparing IC_{50} values of *L*-Pro-STSC and *D*-Pro-STSC with those of their copper(II) complexes in CH1 cells complexation, of copper hence results in a 13-fold and 5-fold increase in cytotoxicity. In both tested cell lines the ligand as well as the complex with an *L*-proline moiety led to slightly improved antiproliferative activity than the compounds with a D-proline moiety. Assuming that the presence of the proline moiety results in an interference with the cellular amino acid metabolism, this might reflect an influence of stereoselectivity of certain components of this metabolism, which normally deals only with the *L* isomers.

Table 4. Cytotoxicity of *L*-Pro-STSC and *D*-Pro-STSC and their copper(II) complexes in two human cancer cell lines.

	IC_{50} [μM][a]	
	SW480	CH1
L-Pro-STSC	> 100	62 ± 3
[Cu(*L*-Pro-STSC)Cl]Cl	5.5 ± 0.4	4.6 ± 0.6
D-Pro-STSC	> 100	75 ± 8
[Cu(*D*-Pro-STSC)Cl]Cl	12 ± 1	14 ± 2

[a] 50% inhibitory concentrations in SW480 and CH1cells after exposure for 96 h in the MTT assay. Values are the mean ± standard deviation obtained from at least three independent experiments.

Conclusions

Stability and stoichiometry of Cu^{2+}, Zn^{2+}, Fe^{2+} and Fe^{3+} complexes of *L*-Pro-STSC were determined by pH-potentiometry, and the speciation was confirmed and the most feasible coordination modes were determined by various spectroscopic methods (EPR, ^{1}H NMR, CD, UV−Vis). Formation of mono-ligand complexes for Cu^{2+} and Zn^{2+} was found, while Fe^{2+} and Fe^{3+} ions form in addition to mono-ligand complexes bis-ligand species. In the protonated complexes the tridentate coordination mode via the (O^{-},N^{1},S) set with protonated non-coordinating hydrazinic N^{2} atom is the most probable. (O^{-},N^{1},S^{-}) coordination mode is realized in [ML] and [ML_2] complexes, while formation of mixed hydroxido species is found at basic pH values. Complexes $[Fe^{III}L_2]^{-}$ and $[Cu^{II}L]$ possess such high stability that their dissociation at physiological pH hardly takes place at the micromolar, the biologically more relevant concentration range. However, the extent of the complex dissociation in the case of the lower stability Zn^{2+} and Fe^{2+} species is significant. The complexes formed with *L*-Pro-STSC exhibit

fairly similar behavior compared to STSC, the reference model compound, regarding the type, the stability and coordination mode, although, formation of somewhat higher stability Fe^{3+}-complexes is found with *L*-Pro-STSC. The effect of the side chain proline moiety is mainly realized in the increase of the water-solubility of the ligand and its metal complexes.

The thiosemicarbazone-proline conjugates *L*-Pro-STSC and *D*-Pro-STSC show only a moderate cytotoxic potency with IC_{50} values of 62 and 75 μM in CH1 and > 100 μM in SW480 cells. However, the corresponding copper(II) complexes display a 11- and 5-fold increase in antiproliferative activity in CH1 cells, and even a much higher increase in SW480 cells. In both tested cell lines the *L*-Pro-STSC as well as its copper(II) complex show slightly higher antiproliferative activity than the compounds with a *D*-Pro moiety, with IC_{50} values of 5.5 and 4.6 μM for [Cu(*L*-Pro-STSC)Cl]Cl in CH1 and SW480 cells, respectively. Studies on the impact of copper(II) coordination of proline-thiosemicarbazones on topoisomerase IIα and the antiproliferative activity in cancer cells expressing different levels of topoisomerase IIα are underway in our laboratory.

Experimental

Chemicals

2-Hydroxy-5-methylbenzaldehyde, thiosemicarbazide, triethylamine were purchased from Acros Organics, whereas (S)-pyrrolidine-2-carboxylate hydrochloride was from VWR and (R)-pyrrolidine-2-carboxylate hydrochloride from Alfa Aesar. 3-(Chloromethyl)-2-hydroxy-5-methylbenzaldehyde was synthesized according to the slightly modified published procedure.[28]

$CuCl_2$, $ZnCl_2$ and $FeCl_3$ (*puriss*, Reanal) were dissolved in known amount of HCl in order to get the Cu^{2+}, Zn^{2+} and Fe^{3+} stock solutions, respectively. Their concentrations were determined by complexometry via the EDTA complexes. The Fe^{2+} stock solution was obtained from fine Fe powder (*puriss*, Reanal) dissolved in a known amount of HCl solution under a purified, strictly oxygen-free argon atmosphere, then filtered, stored and used under anaerobic conditions. KSCN (Sigma-Aldrich) solution was used to check the absence of Fe^{3+} traces in the Fe^{2+} stock solution. The concentration of the Fe^{2+} solution was determined by permanganometric titrations under

acidic conditions. Accurate strong acid content of the metal stock solutions were determined by pH-potentiometric titrations.

Synthesis of ligands

(*S*)-1-[(3-formyl-2-hydroxy-5-methylbenzyl)methyl]pyrrolidine-2-carboxylate (*S*-1). To a solution of 3-(chloromethyl)-2-hydroxy-5-methylbenzaldehyde (1.34 g, 7.25 mmol) in THF (50 ml) was added under stirring a solution of methyl (*S*)-pyrrolidine-2-carboxylate hydrochloride (1.49 g, 9.00 mmol) in CH_2Cl_2 (50 mL). Afterwards, triethylamine (2.52 mL, 18.00 mmol) in THF (25 ml) was added and stirring continued at room temperature overnight. Next day, the reaction mixture was diluted with THF (300 mL) and the precipitate of triethylammonium chloride was filtered off. The solution was freed from solvent under reduced pressure and the residue was purified by column chromatography by using as eluent ethyl acetate/hexane = 3:7. The product was dried in vacuo. Yield: 1.02 g, 51%. Anal. Calcd for $C_{15}H_{19}O_4N$ (M_r 277.32 g/mol) (%): C, 64.97; H, 6.91; N, 5.05. Found: C, 64.85; H, 6.67; N, 4.98. ^{1}H NMR (DMSO-d_6, δ) 10.29 (s, 1H, HC=O), 7.38 (s, 1H, Ar), 7.26 (s, 1H, Ar), 4.08 (d, 1H, J = 13.98 Hz, CH_2), 3.68 (s, 3H, -OCH_3), 3.6 (d, 1H, J = 13.98 Hz, CH_2), 3.48–3.43 (m, 1H, Pro), 2.92–2.86 (m, 1H, Pro), 2.42–2.36 (m, 1H, Pro), 2.24 (s, 3H, CH_3) 2.22–2.16 (m, 1H, Pro), 1.91–1.70 (m, 3H, Pro). ^{13}C{^{1}H} NMR (DMSO-d_6, δ): 191.49; 174.45; 158.86; 136.73; 128.17; 127.65; 125.50; 122.40; 65.03; 55.27; 53.02; 52.41; 29.52; 23.57; 20.32. ESI-MS in MeOH (negative): *m/z* 276 $[L]^-$.

(*R*)-1-[(3-formyl-2-hydroxy-5-methylbenzyl)methyl]pyrrolidine-2-carboxylate (*R*-1). To a solution of 3-(chloromethyl)-2-hydroxy-5-methylbenzaldehyde (1.95 g, 10.6 mmol) in THF (50 ml) was added under stirring a solution of methyl (*R*)-pyrrolidine-2-carboxylate hydrochloride (2.51 g, 15.1 mmol) in CH_2Cl_2 (50 mL). Afterwards, triethylamine (4.5 mL, 30.0 mmol) in THF (14 mL) was added and stirring continued at room temperature overnight. Next day, the reaction mixture was diluted with THF (300 mL) and the precipitate of triethylammonium chloride was filtered off. The solution was freed from solvent and the residue was purified by column chromatography by using as eluent ethyl acetate/hexane = 3:7. The product was dried in vacuo. Yield: 1.14 g, 39%. Anal. Calcd for $C_{15}H_{19}NO_4$ (M_r 277.32 g/mol) (%): C, 64.97; H, 6.91; N, 5.05. Found: C, 64.85; H, 6.67; N, 4.98. ^{1}H NMR (DMSO-d_6, δ): 10.29 (s, 1H, HC=O), 7.38 (s, 1H, Ar), 7.26 (s, 1H, Ar), 4.08 (d, 1H, J = 13.90 Hz, CH_2), 3.68 (s, 3H, -OCH_3), 3.60 (d, 1H, J =

13.90 Hz, CH_2), 3.48–3.43 (m, 1H, Pro), 2.92–2.86 (m, 1H, Pro), 2.42–2.36 (m, 1H, Pro), 2.24 (s, 3H, CH_3) 2.22–2.16 (m, 1H, Pro), 1.91–1.70 (m, 3H, Pro). $^{13}C\{^1H\}$ NMR (DMSO-d_6, δ): 191.45; 174.43; 158.86; 136.70; 128.15; 127.61; 125.48; 122.39; 65.01; 55.28; 53.00; 52.39; 29.51; 23.56; 20.30. ESI-MS in MeOH (negative): *m/z* 276 $[L]^-$. ESI-MS in MeOH (positive): *m/z* 278 $[HL+H]^+$.

2-Hydroxy-3-methyl-(*S*)-pyrrolidine-2-carboxylate-5-methylbenzaldehyde thiosemicarbazone (*L*-Pro-STSC). To the warm solution of the (*S*)-**1** (1.14 g, 4.10 mmol) in ethanol (30 mL) was added a solution of thiosemicarbazide (0.46 g, 5.00 mmol) in hot water (30 ml). The reaction mixture was heated at 70−75°C with continuous stirring for 75 h. After cooling to room temperature chloroform (100 mL) was added. The aqueous phase was separated and allowed to stand at 5 °C overnight. The white precipitate was filtered off, washed with water, ethanol, chloroform and dried in vacuo. Yield: 0.56 g, 41%. Anal. Calcd for $C_{15}H_{20}N_4O_3S{\cdot}1.5H_2O$ (M_r 363.4 g/mol) (%): C, 49.57; H, 6.38; N, 15.42; S, 8.82. Found: C, 49.62; H, 6.37; N, 15.51; S, 9.07. ^1H NMR (DMSO-d_6, δ): 11.41 (s, 1H, NH); 8.39 (s, 1H, HC=N); 8.11 (s, 1H, NH_2); 7.91 (s, 1H, NH_2); 7.75 (s, 1H, Ar); 6.95 (s, 1H, Ar); 4.14 (d, 1H (*J* = 13.52 Hz), CH_2); 3.49 (d, 1H (*J* = 13.52 Hz), CH_2); 3.39–3.37 (m, 1H, Pro); 2.93–2.84 (m, 1H, Pro); 2.45–2.36 (m, 1H, Pro); 2.27–2.23 (m, 1H, Pro); 2.21 (s, 3H, CH_3); 1.91–1.78 (m, 2H, Pro); 1.77–1.66 (m, 1H, Pro). $^{13}C\{^1H\}$ NMR (DMSO-d_6, δ): 178.11; 174.94; 154.60; 139.61; 131.83; 127.79; 126.11; 123.46; 120.61; 65.59; 56.39; 53.04; 29.46; 23.46; 20.5. ESI-MS in MeOH (positive): *m/z* 359 $[H_2L+Na]^+$; 337 $[H_2L+H]^+$.

2-Hydroxy-3-methyl-(*R*)-pyrrolidine-2-carboxylate-5-methylbenzaldehyde thiosemicarbazone (*D*-Pro-STSC). To the warm solution of (*R*)-**1** (2.05 g; 7.40 mmol) in ethanol (30 mL) was added a solution of thiosemicarbazide (0.78 g, 8.50 mmol) in hot water (30 mL). The reaction mixture was heated at 70−75°C with continuous stirring for 12 h. After cooling to room temperature chloroform (100 mL) was added. The aqueous phase was separated and allowed to stand at 5 °C overnight. The white precipitate was filtered off, washed with water, ethanol, chloroform and dried in vacuo. Yield: 0.45 g, 18%. Anal. Calcd. for $C_{15}H_{20}N_4O_3S{\cdot}H_2O$ (M_r 354.43 g/mol) (%): C, 50.83; H, 6.26; N, 15.81; S, 9.05. Found: C, 51.05; H, 6.21; N, 15.84; S, 9.20. ^1H NMR (DMSO-d6, δ): 11.41 (s, 1H, NH); 8.39 (s, 1H, HC=N); 8.11 (s, 1H, NH_2); 7.91 (s,

1H, NH_2); 7.75 (s, 1H, Ar); 6.95 (s, 1H, Ar); 4.14 (d, 1H (J = 13.52 Hz), CH_2); 3.50 (d, 1H (J = 13.52 Hz), CH_2); 3.39–3.37 (m, 1H, Pro, overlapped water peak); 2.93–2.84 (m, 1H, Pro); 2.45–2.36 (m, 1H, Pro); 2.27–2.23 (m, 4H, Pro, CH_3); 1.91–1.78 (m, 2H, Pro); 1.77–1.66 (m, 1H, Pro). $^{13}C\{^1H\}$ NMR (DMSO-d_6, δ): 178.12; 174.92; 154.60; 139.63; 131.84; 127.8; 126.14; 123.44; 120.61; 65.59; 56.37; 53.04; 29.46; 23.45; 20.5. ESI-MS in MeOH (positive): m/z 359 $[H_2L+Na]^+$; 337 $[H_2L+H]^+$.

Synthesis of copper(II) complexes

[Cu(*S*-H_3L)Cl]Cl. To a solution of *L*-Pro-STSC (0.04 g, 0.12 mmol) in methanol (50 mL) was added a solution of $CuCl_2{\cdot}2H_2O$ (0.04 g, 0.26 mmol) in methanol (3 mL) and the reaction mixture was refluxed for 1 h. After cooling to room temperature the solvent was evaporated under reduced pressure to about 5 mL. The green crystalline product was obtained by slow vapor diffusion of diethylether into the methanolic solution. The product was washed with diethylether/methanol 5:1 (5 mL) and dried in vacuo overnight. Yield: 0.03 g; 55.4%. Anal. Calcd. for $CuC_{15}H_{20}N_4O_3SCl_2{\cdot}0.4CH_3OH$ (M_r 483.68 g/mol) (%): C, 38.24; H, 4.5; N, 11.58; S, 6.63. Found: C, 38.05; H, 4.45; N, 11.23; S, 6.48. ESI-MS in MeOH (positive): m/z 398 $[Cu^{II}(HL)]^+$. ESI-MS in MeOH (negative): m/z 396 $[Cu^{II}(L-H)]^-$; m/z 432 $[Cu^{II}(L)Cl]^-$.

[Cu(*R*-H_3L)Cl]Cl. To a solution of *D*-Pro-STSC (0.04 g, 0.12 mmol) in methanol (50 mL) was added a solution of $CuCl_2{\cdot}2H_2O$ (0.04 g, 0.26 mmol) in methanol (3 mL) and the reaction mixture was refluxed for 1 h. After cooling to room temperature the solvent was evaporated under reduced pressure to about 5 mL. The green crystalline product was obtained by slow vapor diffusion of diethylether into the methanolic solution. The product was washed with diethylether/methanol 5:1 (5 mL) and dried in vacuo overnight. Yield: 0.05 g, 83.9%. Anal. Calcd. for $CuC_{15}H_{20}N_4O_3SCl_2{\cdot}0.3CH_3OH$ (M_r 480.47 g/mol) (%): C, 38.25; H, 4.45; N, 11.66; S, 6.67. Found: C, 37.95; H, 4.35; N, 11.28; S, 6.58. ESI-MS in MeOH (positive): m/z 398 $[Cu^{II}(HL)]^+$. ESI-MS in MeOH (negative): m/z 396 $[Cu^{II}(L-H)]^-$; m/z 432 $[Cu^{II}(L)Cl]^-$.

pH-potentiometric measurements. The purity and aqueous phase stability of the ligand *L*-Pro-STSC was checked and the exact concentrations of the stock solutions prepared were determined by the Gran method.[33]

The pH-metric measurements for determination of the protonation constants of the ligand and the overall stability constants of the metal complexes were carried out at 25.0 ± 0.1 °C in DMSO/water 30:70 (w/w) as solvent and at an ionic strength of 0.10 M (KCl, Sigma-Aldrich) in order to keep the activity coefficients constant. (In the case of STSC and α(N)-pyridyl TSCs 30% (w/w) DMSO/H_2O solvent mixture was used for the studies previously.[21b,21c,27] In order to obtain comparable data the same conditions were applied, however the presence of only 20% (w/w) DMSO is found to be sufficient for dissolution of *L*-Pro-STSC at the concentration levels necessary for pH-potentiometric titrations, i.e. ≥1−2 mM.) The titrations were performed with carbonate-free KOH solution of known concentration (0.10 M). Both the base and the HCl were Sigma-Aldrich products and their concentrations were determined by pH-potentiometric titrations. An Orion 710A pH-meter equipped with a Metrohm combined electrode (type 6.0234.100) and a Metrohm 665 Dosimat burette were used for the pH-metric measurements. The electrode system was calibrated to the pH = log[H^+] scale in the DMSO/water solvent mixture by means of blank titrations (strong acid *vs.* strong base; HCl *vs.* KOH), similarly to the method suggested by Irving *et al.*[34] in pure aqueous solutions. The average water ionization constant, pK_w, is 14.52 ± 0.05 with DMSO/water 30:70 (w/w) as solvent at 25 °C, which corresponds well to the literature data.[21b,21c,35] The reproducibility of the titration points included in the calculations was within 0.005 pH. The pH-metric titrations were performed in the pH range 2.0 – 12.5. The initial volume of the samples was 10.0 mL. The ligand concentration was in the range $2 - 3 \times 10^{-3}$ M and metal ion-to-ligand ratios of 1:1 – 1:4 were used. The accepted fitting of the titration curves was always less than 0.01 mL. Samples were deoxygenated by bubbling purified argon through them for *ca.* 10 min prior to the measurements. In the case of Fe^{2+} samples, argon overpressure was used when Fe^{2+} was added to the samples in tightly closed vessels, which were prior completely deoxygenated by bubbling a stream of purified argon through them for *ca.* 20 min. Argon was also passed over the solutions during the titrations.

The protonation constants of the ligands were determined with the computer program SUPERQUAD;[36] and PSEQUAD[37] was utilized to establish the stoichiometry of the complexes and to calculate the stability constants ($\log\beta(M_pL_qH_r)$) using the literature data for Fe^{III} hydroxido complexes.[38] $\beta(M_pL_qH_r)$ is defined for the general equilibrium $pM + qL + rH \rightleftharpoons M_pL_qH_r$ as $\beta(M_pL_qH_r) = [M_pL_qH_r]/[M]^p[L]^q[H]^r$ where M denotes the metal ion and L the completely

deprotonated ligand (see SI for the details). Using the calibration protocol mentioned above, the protonation and stability constants involving [H^+] were obtained and are considered as K_{mixed} (or practical) constants[39] and are valid only under the given circumstances. The calculations were always made from the experimental titration data measured in the absence of any precipitate in the solution.

UV–vis spectrophotometric, spectrofluorimetric, CD and ^{1}H NMR measurements. A Hewlett Packard 8452A diode array spectrophotometer was used to record the UV–vis spectra in the interval 260 – 820 nm. The path length was 1 cm. Protonation and stability constants and the individual spectra of the species were calculated by the computer program PSEQUAD.[37] The spectrophotometric titrations were performed on samples of the *L*-Pro-STSC alone or with Cu^{2+}, Fe^{3+} or Fe^{2+} ions; the concentration of the ligand was 4×10^{-5} M (for the ligand and Fe^{3+} containing samples), 2×10^{-4} M (for Fe^{2+} containing samples) or 2×10^{-3} M (for Cu^{2+} containing samples) and the metal-to-ligand ratios were 0:1, 1:1 and 1:2 over the pH range between 2 and 12 at an ionic strength of 0.10 M (KCl) in 30% (w/w) DMSO/H_2O at 25.0 ± 0.1 ^oC. For Fe^{2+} samples, spectra were recorded under strictly anaerobic conditions. Measurements for Fe^{3+} − (*S*)-H_3L system at metal-to-ligand ratio 1:1 were also carried out by preparing individual samples in which the 0.1 M KCl was partially or completely replaced by HCl and pH values, varying in the range *ca.* 1.0 – 1.8, were calculated from the HCl content. For the calculation of the stability constants of the protonated mono-ligand Fe^{3+} – *L*-Pro-STSC complex mainly CT bands (which are strongly overlapped with the ligand bands) were used (λ = 300 − 470 nm).

The pH-dependent fluorescence measurements were carried out on a Hitachi-4500 spectrofluorimeter with the excitation at 393 nm. The emission spectra were recorded using 5 nm/5 nm slit widths in 1 cm quartz cell in the pH range between 2 and 12 in 30% (w/w) DMSO/H_2O at 25.0 ± 0.1 ^oC. Samples contained 5×10^{-6} M *L*-Pro-STSC ligand alone or with 5×10^{-6} M Cu^{2+} or Zn^{2+} ions or 2.5×10^{-6} M Fe^{2+} at 0.1 M (KCl) ionic strength. Three-dimensional spectra were recorded at 230 – 500 nm excitations and at 240 – 600 nm emission wavelengths for the 5×10^{-6} M ligand containing samples at pH 5.1; 7.6 and 10.0 using 2.5 nm/2.5 nm slit widths.

^{1}H NMR studies were carried out on a Bruker Ultrashield 500 Plus instrument. *L*-Pro-STSC was dissolved in a 30% (w/w) d_6-DMSO/H_2O mixture in a concentration of 2×10^{-3} M and the Zn^{2+}-to-ligand ratios were 0:1 and 1:1. The direct pH-meter readings were corrected according to method of Irving *et al*.[34]

CD spectra were recorded on a Jasco J-815 spectrometer in an optical cell of 1.0 cm path length. The analytical concentration of *D* or *L*-Pro-STSC ligands or the Cu^{2+}-*D* or *L*-Pro-STSC complexes was 6.5×10^{-5} M at pH 7.4 in pure aqueous solutionand spectra were recorded in the wavelength interval from 215 to 500 nm. 2.0×10^{-3} M ligand concentration was used for the Cu^{2+} − *L*-Pro-STSC system at 1:1 metal-to-ligand ratio in a 30% (w/w) DMSO/H_2O mixture and pH was varied between 2 and 12 and spectra were analyzed in the range of 460 − 700 nm. CD data are given as the differences in molar absorptivities between left and right circularly polarized light, based on the concentration of the ligand ($\Delta\varepsilon = \Delta A / l / c_{\text{ligand or complex}}$).

Determination of the partition coefficient (*P*). *P* values of *D*- and *L*-Pro-STSC and their copper(II) complexes were determined by the traditional shake flask method in *n*-octanol/buffered aqueous solution at pH 7.4 (4-(2-hydroxyethyl)-1-piperazineethanesulfonic acid, HEPES) at 25.0±0.2 ^{o}C as described previously.[27] Two parallel experiments were performed for each sample. The ligands were dissolved at 4×10^{-5} M and the complexes in 6.4×10^{-5} M in the *n*-octanol pre-saturated aqueous solution of the buffer (0.01 M) at constant ionic strength (0.10 M KCl). The aqueous solutions and *n*-octanol with 1:1 phase ratio were gently mixed with 360° vertical rotation for 3 h to avoid the emulsion formation, and the mixtures were centrifuged at 5000 rpm for 3 min by a temperature controlled centrifuge (Sanyo) at 25 ^{o}C. After separation UV–vis spectra of the ligands or complexes in the aqueous phase were compared to those of the original aqueous solutions and $P_{7.4}$ value was calculated as the mean of (Absorbance (original solution) / Absorbance (aqueous phase after separation) – 1) obtained at the region of λ_{max} ± 10 nm values.

EPR measurements and deconvolution of the spectra. All CW-EPR spectra were recorded with a BRUKER EleXsys E500 spectrometer (microwave frequency 9.81 GHz, microwave power 10 mW, modulation amplitude 5 G, modulation frequency 100 kHz). During a titration, the isotropic EPR spectra were recorded at room temperature in a circulating system. Eleven and

ten EPR spectra were recorded for samples with 1:1 and 1:2 Cu^{2+}-to-ligand ratios, respectively at 2.0×10^{-3} M *L*-Pro-STSC concentration between pH 2.4 − 12 in 30% (w/w) DMSO/H_2O at I = 0.10 M (KCl). KOH solution was added to the stock solution to change the pH which was measured with a Radiometer PHM240 pH/ion Meter equipped with a Metrohm 6.0234.100 glass electrode. A Heidolph Pumpdrive 5101 peristaltic pump was used for circulate the solution from the titration pot through a capillary tube into the cavity of the instrument. The titrations were carried out under argon atmosphere. At various pH values, samples of 0.10 mL were taken, and frozen in liquid nitrogen, and the CW-EPR spectra were recorded under the same instrumental conditions as the room-temperature spectra described above.

The series of room-temperature CW-EPR spectra were simulated simultaneously by the „two-dimensional" method using the 2D_EPR program.[40] Each component curve was described by the isotropic EPR parameters g_o, A_o^{Cu} copper hyperfine and A_o^{N} nitrogen hyperfine couplings, and the relaxation parameters α, β, γ which define the line widths in the equation $\sigma_{MI}=\alpha+\beta M_I+\gamma M_I^2$, where M_I denotes the magnetic quantum number of copper nucleus. The concentrations of the complexes were varied by fitting their formation constants $\beta(M_pL_qH_r)$ defined by the general equilibrium found in the pH-potentiometric studies section.

For each spectrum, the noise-corrected regression parameter (R_j for the j^{th} spectrum) is derived from the average square deviation (SQD) between the experimental and the calculated intensities. For the series of spectra, the fit is characterized by the overall regression coefficient R, calculated from the overall average SQD. The details of the statistical analysis were published previously.[41]

The anisotropic spectra were analyzed individually with the EPR program,[41] which gives the anisotropic EPR parameters (g_x, g_y, g_z, A_x^{Cu}, A_y^{Cu}, A_z^{Cu}, A_x^{N}, A_y^{N}, A_z^{N}, and the orientation dependent line width parameters). Since a natural $CuCl_2$ was used for the measurements, the spectra were calculated as the sum of the spectra of ^{63}Cu and ^{65}Cu weighted by their natural abundances. The quality of fit was characterized by the noise-corrected regression parameter R_j as above. The copper and nitrogen coupling constants and the relaxation parameters were obtained in field units (Gauss = 10^{-4} T)

Crystallographic Structure Determination. X-ray diffraction measurement was performed on a Bruker X8 APEXII CCD diffractometer. The single crystal of [Cu(*R*-H_2L)Cl]Cl was positioned at 40 mm from the detector, and 1138 frames were measured, each for 60 s over 1° scan width. The data was processed using SAINT software.[42] Crystal data, data collection parameters, and structure refinement details are given in Table 5. The structure was solved by direct methods and refined by full-matrix least-squares techniques. Non-H atoms were refined with anisotropic displacement parameters. H atoms were inserted in calculated positions and refined with a riding model. The five-membered proline ring in both crystallographically independent complex cations (A and B) of [Cu(*R*-H_2L)Cl]Cl was found to be disordered over two positions with s.o.f. 0.68:0.32 and 0.50:0.50, respectively. In addition, one oxygen atom of the −COOH group in complex cation B is also disordered over two positions, each with 50% occupancy. The disorder was resolved with constrained anisotropic displacement parameters and restrained bond distances using EADP and SADI instructions of SHELX-97, respectively. The following software programs and computer were used: structure solution, *SHELXS-97*; refinement, *SHELXL-97*;[43] molecular diagrams, *ORTEP-3*;[44] computer, Intel CoreDuo.

Table 5. Crystal data and details of data collection for [Cu^{II}(*R*-H_2L)Cl]Cl.

Compound	[Cu^{II}(*R*-H_2L)Cl]Cl
Empirical formula	$C_{15}H_{20}Cl_2CuN_4O_3S$
Fw	470.85
Space group	$P2_1$
a [Å]	7.3130(3)
b [Å]	21.8734(8)
c [Å]	11.7535(5)
β [°]	99.423(2)
V [Å^3]	1854.72(13)
Z	4
λ [Å]	0.71073
ρ_{calcd} [g cm^{-3}]	1.686
Crystal size [mm^3]	0.16 × 0.05 × 0.03
T [K]	120(2)
μ [mm^{-1}]	1.602
R_1[a]	0.0367
wR_2[b]	0.0866
GOF[c]	1.021

[a] $R_1 = \Sigma||F_o| - |F_c||/\Sigma|F_o|$. [b] $wR_2 = \{\Sigma[w(F_o^2 - F_c^2)^2]/\Sigma[w(F_o^2)^2]\}^{1/2}$. [c] GOF = $\{\Sigma[w(F_o^2 - F_c^2)^2]/(n-p)\}^{1/2}$, where n is the number of reflections and p is the total number of parameters refined.

Cell lines and Culture Conditions. Human CH1 (ovarian carcinoma) and SW480 (colon carcinoma) cells were kindly provided by Lloyd R. Kelland (CRC Centre for Cancer Therapeutics, Institute of Cancer Research, Sutton, UK) and Brigitte Marian (Institute of Cancer Research, Department of Medicine I, Medical University of Vienna, Austria), respectively. Cells were grown in 75 cm² culture flasks (CytoOne/Starlabs, Germany) as adherent monolayer cultures in Minimal Essential Medium (MEM) supplemented with 10% heat-inactivated fetal bovine serum, 1 mM sodium pyruvate, 4 mM L-glutamine and 1% non-essential amino acids (from 100× ready-to-use stock) (all purchased from Sigma-Aldrich, Vienna, Austria). Cultures were maintained at 37 °C in a humidified atmosphere containing 5% CO_2.

Cytotoxicity Tests in Cancer Cell Lines. Antiproliferative effects were determined by means of a colorimetric microculture assay (MTT assay, MTT = 3-(4,5-dimethyl-2-thiazolyl)-2,5-diphenyl-2H-tetrazolium bromide). Cells were harvested from culture flasks by trypsinization and seeded in 100 µL aliquots into 96-well microculture plates (CytoOne/Starlabs, Germany) in densities of 2×10^3 cells/well (SW480) and 1×10^3 cells/well (CH1), in order to ensure exponential growth of untreated controls throughout the experiment. After a 24 h pre-incubation, dilutions of the test compounds in 100 µL/well complete culture medium were added. Because of low aqueous solubility, the test compounds were dissolved in DMSO first and then serially diluted in complete culture medium such that the effective DMSO content did not exceed 0.5%. After exposure for 96 h, all media were replaced by 100 µL/well RPMI 1640 medium (supplemented with 10% heat-inactivated fetal bovine serum and 2 mM L-glutamine) plus 20 µL/well MTT solution in phosphate-buffered saline (5 mg/ml). After incubation for 4 h, the medium/MTT mixtures were removed, and the formazan crystals formed by viable cells were dissolved in 150 µL DMSO per well. Optical densities at 550 nm were measured with a microplate reader (Biotek ELx808), using a reference wavelength of 690 nm to correct for unspecific absorption. The quantity of vital cells was expressed in terms of T/C values by comparison to untreated control microcultures, and 50% inhibitory concentrations (IC_{50}) were calculated from concentration-effect curves by interpolation. Evaluation is based on means from at least three independent experiments, each comprising three microcultures per concentration level.

Acknowledgments

This work has been supported by the Hungarian Research Foundation OTKA K77833, K72781; the Hungarian-Austrian Action Foundation and „TÁMOP-4.2.1/B-09/1/KONV-2010-0005. É.A.E. gratefully acknowledges the financial support of Bolyai J. research fellowships. We thank Alexander Roller for collection of X-ray data.

References

(1) (a) West, D. X.; Padhye, S. B.; Sonawane, P. B. Struct. Bond. 1991, 76, 1−50 ; (b) Casas, J. S.; Garcia-Tasende, M. S.; Sordo, J. Coord. Chem. Rev. 2000, 209, 197−261.

(2) Knox, J. J.; Hotte, S. J.; Kollmannsberger, C.; Winquist, E.; Fisher, B.; Eisenhauer, E. A. Invest. New Drugs 2007, 25, 471−477.

(3) Easmon, J.; Heinisch, G.; Holzer, W.; Rosenwirth, B. J. Med. Chem. 1992, 35, 3288−3296.

(4) Klayman, D. L.; Bartosevich, J. F.; Griffin, T. S.; Mason, C. J.; Scovill, J. P. J. Med. Chem. 1979, 22, 855−862.

(5) Ma, B.; Goh, B.C.; Tan, E. H.; Lam, K. C.; Soo, R.; Leong, S. S.; Wang, L. Z.; Mo, F.; Chan, A. T. C.; Zee, B.; Mok, T. Invest. New Drugs 2008, 26, 169−173.

(6) Karp, J. E.; Giles, F. J.; Gojo, I.; Morris, L.; Greer, J.; Johnson, B.; Thein, M.; Sznol, M.; Low, J. Leuk. Res. 2008, 32, 71−77.

(7) Mackenzie, M. J.; Saltman, D.; Hirte, H.; Low, J.; Johnson, C.; Pond, G.; Moore, M. J. Invest. New Drugs 2007, 25, 553−558.

(8) Yu, Y.; Wong, J.; Lovejoy, D. B.; Kalinowski, D. S.; Richardson, D. R. Clin. Cancer Res. 2006, 12, 6876−6883.

(9) Moore, E. M.; Zedeck, M. S.; Agrawal, K. C.; Sartorelli, A. C. Biochemistry 1970, 9, 4492−4498.

(10) Kolberg, M.; Strand, K. R.; Graff, P.; Andersson, K. K. Biochim. Biophys. Acta 2004, 1699, 1−34.

(11) French, F. A.; Blanz Jr., E. J. J. Med. Chem. 1974, 17, 172−181.

(12) Moore, E.; Sartorelli, A. C. Pharmacol. Ther. 1984, 24, 439−447.

(13) Finch, R. A.; Liu, M.; Cory, A. H.; Cory, J. G.; Sartorelli, A. C. Adv. Enzyme Regul. 1999, 39, 3−12.

(14) (a) Easmon, J.; Puerstinger, G.; Heinisch, G.; Roth, T. J. Med. Chem. 2001, 44, 2164−2171; (b) Miller, M. C.; Stineman, N. C.; Vance, R. J.; West, D. X.; Hall, H. I. Anticancer Res. 1998, 18, 4131−4139.

(15) Huang, H.; Chen, W.; Ku, X.; Meng, L.; Lin, L.; Wang, X.; Zhu, C.; Wang, Y.; Chen, Z.; Li, M.; Jiang, H.; Chen, K.; Ding, J.; Liu, H. J. Med. Chem. 2010, 53, 3048−3064.

(16) Zeglis, B. M.; Divilov, V.; Lewis, J. S. J. Med. Chem. 2011, 54, 2391−2398.

(17) Shao, J.; Zhou, B.; Di Bilio, A. J., Zhu, L.; Wang, T.; Qi, C.; Shih, J.; Yen, Y. Mol. Cancer Ther. 2006, 5, 586−592.

(18) Chaston, T. B.; Lovejoy, D. B.; Watts, R. N.; Richardson, D. R. Clin. Cancer Res. 2003, 9, 402−414.

(19) Popović-Bijelić, A.; Kowol, C. R.; Lind, M. E. S.; Luo, J.; Enyedy, E. A.; Arion, V. B.; Gräslund, A. J. Inorg. Biochem. 2011, 105, 1422−1431.

(20) (a) Richardson, D. R.; Sharpe, P. C.; Lovejoy, D. B.; Senaratne, D.; Kalinowski, D. S.; Islam, M.; Bernhardt, P. V. J. Med. Chem. 2006, 49, 6510−6521; (b) Opletalova, V.; Kalinowski, D. S.; Vejsova, M.; Kunes, J.; Pour, M.; Jampilek, J.; Buchta, V.; Richardson, D. R. Chem. Res. Toxicol. 2008, 21, 1878−1889; (c) Jansson, P. J.; Sharpe, P. C.; Bernhardt, P. V.; Richardson, D. R. J. Med. Chem. 2010, 53, 5759−5769; (d) Kalinowski, D. S.; Yu, Y.; Sharpe, P. C.; Bernhardt, P. V.; Richardson, D. R. J. Med. Chem. 2007, 50, 3716−3729; (e) Richardson, D. R.; Kalinowski, D. S.; Richardson, V.; Sharpe, P. C.; Lovejoy, D. B.; Islam, M.; Bernhardt, P. J. J. Med. Chem. 2009, 52, 1459−1470; (f) Kowol, C. R.; Berger, R.; Eichinger, R.; Roller, A.; Jakupec, M. A.; Schmidt, P. P.; Arion, V. B.; Keppler, B. K. J. Med. Chem. 2007, 50, 1254−1265.

(21) (a) Knight, J. M.; Whelan, H.; Petering, D. H. J. Inorg. Biochem. 1979, 11, 327−338; (b) Enyedy, E. A.; Nagy, N. V.; Zsigó, E.; Kowol, C. R.; Arion, V. B.; Keppler, B. K.; Kiss, T. Eur. J. Inorg. Chem. 2010, 1717−1728; (c) Enyedy, E. A.; Primik, M. F.; Kowol, C. R.; Arion, V. B.; Kiss, T.; Keppler, B. K. Dalton Trans. 2011, 40, 5895−5905.

(22) (a) Ryabova, N. A.; Ponomarev, V. I.; Zelentsov, V. V.; Atovmyan, L. O. Kristallografiya 1981, 26, 101−108; (b) Ryabova, N. A.; Ponomarev, V. I.; Zelentsov, V. V.; Atovmyan, L. O. Kristallografiya 1982, 27, 81−91; (c) Schulte, G.; Luo, X.-L.; Crabtree, R. H.; Zimmer, M. Angew. Chem. Int. Ed. 1991, 30, 193−194; (d) Argay, G.; Kalman, A.; Leovac, V. M.; Cesljevic, V. I.; Ribar, B. J. Coord. Chem. 1996, 37, 165−171; (e) Soriano-Garcia, M.; Valdes-Martinez, J.; Toscano, R. A.; Gomez-Lara, J. Acta Crystallogr. 1985, C41, 500−502.

(23) Belicchi Ferrari, M.; Capacchi, S.; Pelosi, G.; Reffo, G.; Tarasconi, P.; Albertini, R.; Pinelli, S.; Lunghi, P. Inorg. Chim. Acta 1999, 286, 134−141.

(24) Dilović, I.; Rubčić, M.; Vrdoljak, V.; Kraljević Pavelić, S.; Kralj, M.; Piantanida, I.; Cindrić, M. Bioorg. Med. Chem. 2008, 16, 5189−5198.

(25) (a) Kowol, C. R.; Eichinger, R.; Jakupec, M. A.; Galanski, M.; Arion, V. B.; Keppler, B. K. J. Inorg. Biochem. 2007, 101, 1946−1957; (b) Arion, V. B.; Jakupec, M. A.; Galanski, M.; Unfried, P.; Keppler, B. K. J. Inorg. Biochem. 2002, 91, 298−305.

(26) Sen, S.; Shit, S.; Mitra, S.; Batten, S. R. Struct. Chem. 2008, 19, 137−142.

(27) Enyedy, E. A.; Zsigo, E.; Nagy, N. V.; Kowol, C. R.; Roller, A.; Keppler, B. K.; Kiss, T. Eur. J. Inorg. Chem. 2012, submitted.

(28) (a) Wang, Q.; Wilson, C.; Blake, J. A.; Collinson, R. S.; Tasker, A. P.; Schröder, M. Tetrahedron Lett. 2006, 47, 8983−8987; (b) Huisman, M.; Koval, I. A.; Gamez, P.; Reedijk, J. Inorg. Chim. Acta 2006, 359, 1786-1794

(29) Wu, W. S.; Feng, Y.-L. Z. Kristallorg. 2003, 218, 529−530.

(30) Ryabova, N. A.; Ponomarev, V. I.; Atovmyan, L. O.; Zelentsov, V. V.; Shipilov, V. I. Coord. Chem. 1978, 37, 119−129.

(31) Ryabova, N. A.; Ponomarev, V. I.; Zelentsov, V. V.; Atovmyan, L. O. Kristallografiya 1982, 27, 279−287.

(32) Floquet, S.; Guillou, N.; Negrier, P.; Riviere, E.; Boillot, M. L. New J. Chem. 2006, 30, 1621−1627.

(33) Gran, G. Acta Chem. Scand. 1950, 4, 559−577.

(34) Irving, H. M.; Miles, M. G.; Pettit, L. D. Anal. Chim. Acta 1967, 38, 475−488.

(35) SCQuery, The IUPAC Stability Constants Database, Academic Software (Version 5.5), Royal Society of Chemistry, 1993–2005.

(36) Sabatini, A.; Vacca, A.; Gans, P. Talanta 1974, 21, 53–77.

(37) Zékány, L.; Nagypál, I. in: Computational Methods for the Determination of Stability Constants (Ed.: D. L. Leggett), Plenum Press, New York, 1985, p. 291–353.

(38) Baes, C.F.; Mesmer, R. E. The Hydrolysis of Cations, Wiley, New York, 1976.

(39) Sigel, H.; Zuberbühler, A. D.; Yamauchi, O. Anal. Chim. Acta 1991, 255, 63–72.

(40) Rockenbauer, A.; Szabó-Plánka, T.; Arkowi, Zs.; Korecz, L. J. Am. Chem. Soc. 2001, 123, 7646−7654.

(41) Rockenbauer, A.; Korecz, L. Appl. Magn. Reson. 1996, 10, 29−43.

(42) SAINT-Plus, version 7.06a and APEX2; Bruker-Nonius AXS Inc.: Madison, WI, 2004.

(43) Sheldrick, G. M. Acta Crystallogr. 2010, A46, 112–122.

(44) Johnson, G. K. Report ORNL-5138; OAK Ridge National Laboratory; Oak Ridge, TN, 1976.

2.7 Targeting the DNA-topoisomerase complex in a double-strike approach with a topoisomerase inhibiting moiety and covalent DNA binder.

Andrea Kurzwernhart, Wolfgang Kandioller, Caroline Bartel, Simone Bachler, Robert Trondl, Gerhard Muhlgassner, Michael A Jakupec, Vladimir Arion, Doris Marko, Bernhard K Keppler, Christian Hartinger

Chemical Communications **2012**, Epub ahead of print

ChemComm

View Online / Journal Homepage
Dynamic Article Links

Cite this: DOI: 10.1039/c2cc31040f

www.rsc.org/chemcomm

COMMUNICATION

Targeting the DNA-topoisomerase complex in a double-strike approach with a topoisomerase inhibiting moiety and covalent DNA binder†

Andrea Kurzwernhart,[ab] Wolfgang Kandioller,[a] Caroline Bartel,[a] Simone Bächler,[c] Robert Trondl,[a] Gerhard Mühlgassner,[a] Michael A. Jakupec,[ab] Vladimir B. Arion,[ab] Doris Marko,[c] Bernhard K. Keppler[ab] and Christian G. Hartinger*[abd]

Received 13th February 2012, Accepted 20th March 2012
DOI: 10.1039/c2cc31040f

Ru^{II}(arene)–flavonoids with high *in vitro* antitumour activity were synthesised. These compounds are capable of inhibiting human topoisomerase IIα and binding covalently to DNA.

Tumourigenic diseases are one of the major burdens of mankind and many patients are still not treatable or do not respond to standard drugs. This is often related to acquired or intrinsic resistance which hampers the success of chemotherapy with organic and inorganic anticancer agents, such as cisplatin. In order to overcome this drawback, several approaches have been used. The concept of multi-targeted anticancer agents (Fig. 1), *i.e.*, components of a molecule impact multiple separate targets,[1] has been shown to offer several advantages over "classic" chemotherapeutics, *e.g.*, altered pharmacological properties, metabolism and resistance development, tuneable antitumour activity, "intramolecular" combination therapy, and also selective targeted properties.[1]

Among the metal complexes developed as anticancer agents, Ru(III) compounds are considered the most promising drug candidates, and KP1019 and NAMI-A are currently undergoing clinical trials. More recently, Ru^{II}(arene) organometallics have attracted considerable interest, and especially the RAPTA family and ethylene-1,2-diamine complexes are at an advanced preclinical development stage.[2]

One way to prepare biologically active molecules with multi-targeted properties is to link metal fragments to bioactive ligand systems. This strategy has already resulted in promising approaches with compounds exhibiting novel modes of action.[3–5] Especially the use of ligand systems derived from natural compounds appears attractive due to the often advantageous toxicity profile.[6] Flavonoids as secondary metabolites of plants are such a compound class with a rich variety of functions.[7] Importantly, flavonoids are known to exhibit properties such as antiradical and antioxidant, anti-inflammatory, estrogenic, antimicrobial and also anticancer activity.[8]

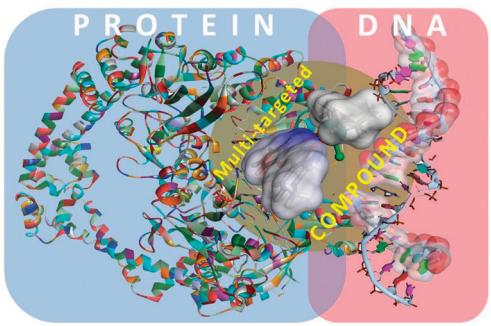

Fig. 1 The concept of a multi-targeted small molecule. We aimed to prepare a compound which is capable of binding *via* its ligand system into the active site of a protein, whereas the metal fragment can form a covalent bond to DNA.

We decided to link flavonoids to Ru^{II}(arene) moieties (Scheme 1), since a few examples of metal–flavonoid complexes are known to exhibit promising biological properties.[9] However, these studies often did not aim to correlate the biological activity with the inhibition of particular targets.[10,11] Flavonoids act primarily through the inhibition of several enzymes, and they have also been shown to interact with human topoisomerases.[7,12]

The flavonol ligands **2a–d** were prepared in two steps by a Claisen–Schmidt condensation and subsequent Algar–Flynn–Oyamada reaction (Scheme 1, ESI†).[13–15] Ligands **2a–d** were converted in good yields into **3a–d** with bis[dichlorido(η^6-*p*-cymene)-ruthenium(II)] under alkaline conditions (Scheme 1).[16] The complexes only show minor signs of hydrolysis in aqueous solution within 6 days.

In addition to characterisation by standard analytical methods (Supporting Information†), single crystals of **3b**·CH_3OH were analysed by X-ray diffraction (Fig. 2).‡ **3b** features a pseudo-octahedral "piano-stool" configuration.[17] The 3-hydroxyflavone upon coordination to Ru acts as a bidentate ligand, forming an envelope-like five-membered cycle, and the two Ru–O bonds

[a] *University of Vienna, Institute of Inorganic Chemistry, Währinger Str. 42, 1090 Vienna, Austria. E-mail: christian.hartinger@univie.ac.at; Fax: 43 1 4277 9526; Tel: 43 1 4277 52609*
[b] *University of Vienna, Research Platform "Translational Cancer Therapy Research", Währinger Str. 42, A-1090 Vienna, Austria*
[c] *University of Vienna, Institute of Food Chemistry and Toxicology, Währinger Str. 38, 1090 Vienna, Austria*
[d] *The University of Auckland, School of Chemical Sciences, Private Bag 92019, Auckland 1142, New Zealand*

† Electronic supplementary information (ESI) available: Materials and methods, synthetic procedures, experimental setup. CCDC 826085. For ESI and crystallographic data in CIF or other electronic format see DOI: 10.1039/c2cc31040f

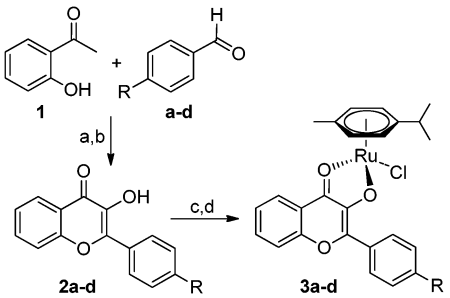

Scheme 1 Synthesis of ligands (**2a–d**) and $Ru^{II}(\eta^6$-*p*-cymene) complexes (**3a–d**): (a) NaOH; (b) H_2O_2; (c) NaOMe; (d) $[Ru(\eta^6$-*p*-cymene$)Cl_2]_2$. **2a/3a**: R = H, **2b/3b**: R = CH_3, **2c/3c**: R = F, **2d/3d**: R = Cl.

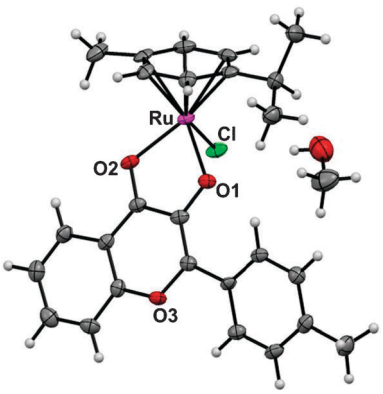

Fig. 2 Molecular structure of the $Ru^{II}(\eta^6$-*p*-cymene) complex **3b**·CH_3OH.

are slightly different with 2.076(2) and 2.099(3) Å, as observed in structurally related compounds.[17] The phenyl substituent of the ligand is twisted with a torsion angle of 15.11°.

The stability of the complexes in aqueous solution has been studied by ^{1}H NMR spectroscopy.

The *in vitro* anticancer activity of ligands **2a–d** and complexes **3a–d** was determined in the human cancer cell lines CH1 (ovarian carcinoma), SW480 (colon carcinoma) and A549 (non-small cell lung carcinoma) by means of the colorimetric MTT assay (Table 1). Notably, the IC_{50} values of **3a–d** were found to be in the low μM range, and only a few examples with similar *in vitro* anticancer activity have been reported.[1,18–20] The substituent in *para* position of the phenyl ring has a significant influence on the *in vitro* activity, with IC_{50} values of the unsubstituted compound **3a** being 2–3 times higher than those of the most active chloro derivative **3d**. Compared to cisplatin, **3a–c** are only 2–3 times less active and **3d** even exhibits the same activity in the SW480 cell line. In the CH1 and A549 cell lines **3a–d** are about one order of magnitude less active than cisplatin (Table 1), but significantly more active than the majority of known tumour-inhibiting organoruthenium compounds.

In order to demonstrate the multi-targeted character of Ru^{II}(flavone) complexes, we studied the inhibition of human topoisomerase IIα activity and the binding ability to DNA models. Topoisomerase IIα is over-expressed in many types of cancer and inhibitors, such as doxorubicin, etoposide and mitoxantrone, are routinely used in the clinic,[21] but only a small number of Ru complexes with topoisomerase inhibitory

Table 1 *In vitro* anticancer activity[a] (IC_{50} values in μM) of **2a–d** and **3a–d** in ovarian (CH1), colon (SW480) and non-small cell lung carcinoma (A549) compared to cisplatin and topoisomerase IIα inhibition of **2a–d** and **3a–d**[b]

	Topoisomerase inhibition[b]	IC_{50}/μM		
		CH1	SW480	A549
2a	+	1.9 ± 0.2	11 ± 3	25 ± 10
3a	++	2.1 ± 0.2	9.6 ± 1.5	20 ± 2
2b	+	1.1 ± 0.1	6.3 ± 1.1	81 ± 9
3b	++	1.8 ± 0.2	7.2 ± 0.5	17 ± 2
2c	+	1.56 ± 0.04	7.0 ± 0.9	37 ± 10
3c	++	1.7 ± 0.4	7.9 ± 2.1	18 ± 1
2d	++	0.60 ± 0.10	3.7 ± 0.4	7.9 ± 1.2
3d	+++	0.86 ± 0.06	3.8 ± 0.5	9.5 ± 0.5
cisplatin[c]	—	0.14 ± 0.03	3.3 ± 0.4	1.3 ± 0.4

[a] 96 h exposure. [b] Estimated 50% inhibitory activity: + >40 μM, ++ ≈ 20–40 μM, +++ <20 μM inhibitor. [c] Taken from ref. 25.

activity have been reported. The major part of them are polypyridyl- and related Ru^{II} complexes with DNA intercalating ligands (for a review see ref. 22) and only a few Ru^{II}(arene) complexes are known which inhibit topoisomerases.[23,24] In this study, human topoisomerase IIα catalytic activity was determined by means of the decatenation assay (Fig. 3; Supporting information†).

Catenated kinetoplast DNA (kDNA) was incubated with topoisomerase IIα in the presence of different concentrations of the flavone complexes **3a–d** and their ligands **2a–d**. Depending on the substituent in *para* position of the phenyl ring, differing potential to inhibit topoisomerase IIα was observed. The chloro compound **3d** is the most potent inhibitor, and in general the extent of inhibition correlates well with the *in vitro* anticancer activity (Table 1). The complexes were generally more active than the ligands, which could however at least be related to a partial release of the ligand. The role of the metal centre in topoisomerase inhibition was recently shown for Cu-thiosemicarbazonato complexes, where the Cu compounds were about an order of magnitude more potent than the respective ligands.[26] However, Ru^{II}(arene) complexes *per se* inhibit the enzyme only to a minor extent, as demonstrated for $[Ru(\eta^6$-benzene$)(DMSO)Cl_2]$.[27] To the best of our knowledge, this is the first example of metal compounds that show topoisomerase inhibitory potency correlating to their antiproliferative activity.

The altered topoisomerase IIα inhibitory activity of the complexes as compared to the ligands may be explained by the multi-targeted character of the complexes. In order to demonstrate the potential of the compounds to interact covalently with DNA as the second target molecule, the reactions of **3a–d**

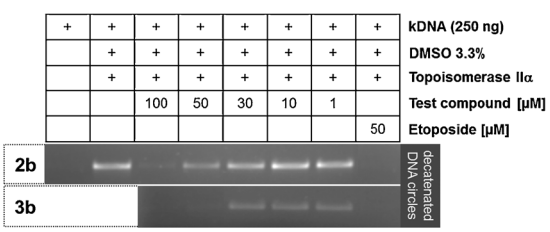

Fig. 3 Effect of complex **3b** and ligand **2b** on the catalytic activity of topoisomerase IIα, as determined by the decatenation assay.

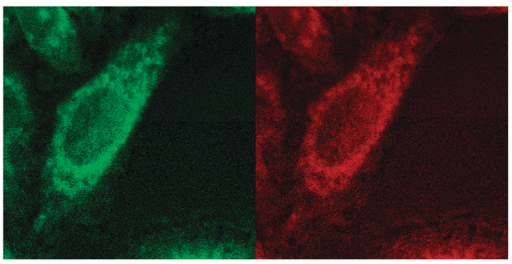

Fig. 4 Live cell imaging with confocal fluorescence microscopy in SW480 cells of **3c** (left) and co-stained with ER-Tracker^{TM} Red (right).

with the DNA model compound 5′-GMP were studied by ^{1}H NMR spectroscopy. Complexes **3a–d** reacted quickly with the *N*7 atom of 5′-GMP (H8 shift from δ = 8.1 to approximately 7.6 ppm). Notably, the flavone ligand remains attached to the Ru centre to interact with topoisomerase IIα. However, the simultaneous interaction of the compounds with DNA and the protein is difficult to prove and will be subject of a separate study.

The flavonoids and their Ru^{II}(η^6-*p*-cymene) complexes are fluorescent, with an emission maximum at *ca.* 520 nm (**3c**; λ_{ex} = 458 nm). This intrinsic property was used to localise **3c** in SW480 cells in co-staining experiments with fluorescence confocal laser scanning microscopy (Fig. 4). **3c** and the endoplasmic reticulum (ER) marker ER-Tracker^{TM} Red (λ_{ex} = 587 nm, λ_{em} = 615 nm) give largely overlapping signals, and therefore we conclude that the ER is the primarily targeted organelle. This observation is common for lipophilic compounds,[28] and the ER might act as a reservoir for the cytotoxic species.

In conclusion, the Ru^{II}(arene)-flavonoid system offers access to multi-targeted anticancer drugs consisting of a DNA binding metal centre and a biologically active ligand system inhibiting topoisomerase IIα. With the accumulation in the endoplasmic reticulum as a reservoir for the anticancer active moiety and the covalent binding to DNA accompanied by increased topoisomerase IIα inhibitory activity as compared to its ligand **2d** and the high *in vitro* antitumour activity, the Ru^{II}(η^6-*p*-cymene) complex **3d** is a promising development candidate for an anticancer drug following a double-strike approach.

We thank the University of Vienna, the Austrian Science Fund (FWF), the Johanna Mahlke geb. Obermann Foundation, and COST D39 for financial support. We gratefully acknowledge Alexander Roller for collecting the X-ray diffraction data.

References

‡ Crystallographic details: **3b**·CH_3OH: $C_{27}H_{29}ClO_4Ru$, M_r = 554.02, 0.12 × 0.05 × 0.01 mm, triclinic, $P\bar{1}$, a = 7.8882(5) Å, b = 11.9690(9) Å, c = 13.5794(11) Å, α = 74.879(5)°, β = 73.366(4)°, γ = 89.101(4)°, V = 1183.49(15) Å^3, Z = 2, ρ_{calcd} = 1.555 mg m^{-3}, μ = 0.807 mm^{-1}, Mo-Kα, λ = 0.71073 Å, T = 100(2)K, $2\theta_{max}$ = 27.50°, 5420 measured independent reflections, R_{int} = 0.0972, R_1 = 0.0466, wR_2 = 0.1020; description of data collection and refinement see supporting information; CCDC 826085 contains the supplementary crystallographic data for this paper (The Cambridge Crystallographic Data Centre, www.ccdc.cam.ac.uk/data_request/cif).

1 G. R. Zimmermann, J. Lehár and C. T. Keith, *Drug Discovery Today*, 2007, **12**, 34.
2 W. H. Ang, A. Casini, G. Sava and P. J. Dyson, *J. Organomet. Chem.*, 2011, **696**, 989.
3 D. Hamels, P. M. Dansette, E. A. Hillard, S. Top, A. Vessieres, P. Herson, G. Jaouen and D. Mansuy, *Angew. Chem., Int. Ed.*, 2009, **48**, 9124.
4 W. H. Ang, L. J. Parker, A. De Luca, L. Juillerat-Jeanneret, C. J. Morton, M. Lo Bello, M. W. Parker and P. J. Dyson, *Angew. Chem., Int. Ed.*, 2009, **48**, 3854.
5 I. Ott, B. Kircher, C. P. Bagowski, D. H. W. Vlecken, E. B. Ott, J. Will, K. Bensdorf, W. S. Sheldrick and R. Gust, *Angew. Chem., Int. Ed.*, 2009, **48**, 1160.
6 J. É. Debreczeni, A. N. Bullock, G. E. Atilla, D. S. Williams, H. Bregman, S. Knapp and E. Meggers, *Angew. Chem., Int. Ed.*, 2006, **45**, 1580.
7 R. J. Nijveldt, E. van Nood, D. E. van Hoorn, P. G. Boelens, K. van Norren and P. A. van Leeuwen, *Am. J. Clin. Nutr.*, 2001, **74**, 418.
8 E. Middleton, Jr., C. Kandaswami and T. C. Theoharides, *Pharmacol. Rev.*, 2000, **52**, 673.
9 M. Grazul and E. Budzisz, *Coord. Chem. Rev.*, 2009, **253**, 2588.
10 X. Chen, L.-J. Tang, Y.-N. Sun, P.-H. Qiu and G. Liang, *J. Inorg. Biochem.*, 2010, **104**, 379.
11 J. Ochocki, M. Kasprzak, L. Checinska, A. Erxleben, E. Zyner, L. Szmigiero, A. Garza-Ortiz and J. Reedijk, *Dalton Trans.*, 2010, **39**, 9711.
12 O. J. Bandele and N. Osheroff, *Biochemistry*, 2007, **46**, 6097.
13 T. A. Geissman and D. K. Fukushima, *J. Am. Chem. Soc.*, 1948, **70**, 1686.
14 M. Bennett, A. J. Burke and W. I. O'Sullivan, *Tetrahedron*, 1996, **52**, 7163.
15 C. X. Qin, X. Chen, R. A. Hughes, S. J. Williams and O. L. Woodman, *J. Med. Chem.*, 2008, **51**, 1874.
16 W. Kandioller, C. G. Hartinger, A. A. Nazarov, J. Kasser, R. John, M. A. Jakupec, V. B. Arion, P. J. Dyson and B. K. Keppler, *J. Organomet. Chem.*, 2009, **694**, 922.
17 W. Kandioller, C. G. Hartinger, A. A. Nazarov, M. L. Kuznetsov, R. O. John, C. Bartel, M. A. Jakupec, V. B. Arion and B. K. Keppler, *Organometallics*, 2009, **28**, 4249.
18 M.G. Mendoza-Ferri, C. G. Hartinger, R. E. Eichinger, N. Stolyarova, K. Severin, M. A. Jakupec, A. A. Nazarov and B. K. Keppler, *Organometallics*, 2008, **27**, 2405.
19 R. E. Aird, J. Cummings, A. A. Ritchie, M. Muir, R. E. Morris, H. Chen, P. J. Sadler and D. I. Jodrell, *Br. J. Cancer*, 2002, **86**, 1652.
20 M. G. Mendoza-Ferri, C. G. Hartinger, A. A. Nazarov, R. E. Eichinger, M. A. Jakupec, K. Severin and B. K. Keppler, *Organometallics*, 2009, **28**, 6260.
21 A. K. Larsen, A. E. Escargueil and A. Skladanowski, *Pharmacol. Ther.*, 2003, **99**, 167.
22 F. Gao, H. Chao and L.-N. Ji, *Chem. Biodiversity*, 2008, **5**, 1962.
23 S. K. Singh, S. Joshi, A. R. Singh, J. K. Saxena and D. S. Pandey, *Inorg. Chem.*, 2007, **46**, 10869.
24 F. Beckford, D. Dourth, M. Shaloski, J. Didion, J. Thessing, J. Woods, V. Crowell, N. Gerasimchuk, A. Gonzalez-Sarrias and N. P. Seeram, *J. Inorg. Biochem.*, 2011, **105**, 1019.
25 Y. Y. Scaffidi-Domianello, A. A. Legin, M. A. Jakupec, V. B. Arion, V. Y. Kukushkin, M. Galanski and B. K. Keppler, *Inorg. Chem.*, 2011, **50**, 10673.
26 B. M. Zeglis, V. Divilov and J. S. Lewis, *J. Med. Chem.*, 2011, **54**, 2391.
27 Y. N. V. Gopal, D. Jayaraju and A. K. Kondapi, *Biochemistry*, 1999, **38**, 4382.
28 D. Marko, K.-H. Merz, C. Kunz, A. Müller, N. Tarasova and G. Eisenbrand, *Biochem. Pharmacol.*, 2002, **63**, 669.

3 Conclusion and Outlook

Since the first synthesis of thiosemicarbazones in the 1950s the proposed mechanism of action did undergo considerable changes. First conceived simply as iron chelators, various studies proved that additional properties of α-heterocyclic thiosemicarbazones contribute to their anticancer effect. The presented research articles in this thesis are focused on metal coordination, structure-activity relationships, cellular accumulation and interaction with novel therapeutic targets for cancer treatment.

In previous studies, iron coordination by Triapine has been assayed by simply adding an iron salt to a solution of Triapine. However, a defined stoichiometric complexation was not guaranteed. This might be the reason for divergent effects of Triapine-iron complexes in cell culture experiments reported in the literature. Stoichiometrically defined iron, gallium, zinc and copper complexes were synthesized and enabled us to study the influence of metal complexation of Triapine and derivates on their biological activity. The isolated iron(III) complex of Triapine was three-times less cytotoxic than the free ligand in the cell lines 41M (ovarian carcinoma) and SK-BR-3 (mammary carcinoma). Unlike conventional iron chelators (e.g. DFO), iron complexation of thiosemicarbazones did not lead to a complete reversal of cytotoxic properties. In good agreement with this finding, complexation to zinc, gallium and copper did not diminish the activity remarkably either. Interestingly, derivatization of Triapine had a more pronounced impact on cytotoxic properties than metal complexation. Dimethylation of the terminal amino group in various derivatives resulted in an up to 725-fold (41M) and 320-fold (SK-BR-3) increase of cytotoxicity.

The intrinsic fluorescence properties of Triapine and its zinc(II) complex facilitated intracellular accumulation studies. Zinc complexation did not lead to enhanced cytotoxic properties but changed the intracellular distribution. Co-staining experiments with immunofluorescence microscopy displayed an accumulation of the Zn-Triapine complex in the nucleoli. Since cellular accumulation and distribution are important factors for therapeutic outcome, metal coordination might serve as an important tool to tune pharmacological properties.

Further fluorescence microscopy studies on terminally dimethylated Triapine in SW480 colon cancer cells revealed a co-localization with the endoplasmic reticulum and mitochondria. Moreover, Triapine and its dimethylated derivative caused ER stress and activated the unfolded protein response. Expression analysis of protein and mRNA levels displayed severe disruption of ER homeostasis. Increased expression of the pro-apoptotic transcription factor CHOP and depolarization of mitochondrial membrane potential was observed after treatment with the dimethylated derivative of Triapine. This suggests that interactions with the protein folding machinery of the ER contribute to the cytotoxic properties of this class of compounds.

Triapine and in general the α-heterocyclic thiosemicarbazones are known as inhibitors of the ribonucleotide reductase, but little attention was given to additional molecular targets. As a potent chelator of biologically relevant metals such as zinc, copper, and iron, additional interactions with metalloproteins are conceivable. The protein machinery of the ER is hypothesized as a potential target for cancer therapy due to a high turnover of newly synthesized proteins.

Given that ER stress induction is enhanced by terminal dimethylation of thiosemicarbazones, further studies will have to characterize the impact on ER homeostasis of dimethylated α-heterocyclic thiosemicarbazones *in vivo*. Furthermore, cellular studies on ER stress-related apoptosis induction will help us to understand the impact of this novel molecular target on the biological activity of thiosemicarbazones.

4 Curriculum Vitae

Personal Data

Name	Robert Trondl
Date of birth	July 14, 1984
Place of birth	Vienna, Austria
Nationality	Austrian
Working Address	Institute of Inorganic Chemistry University of Vienna Althanstraße 14 (UZA II) 1090 Vienna, Austria Phone: +43 1 4277-52610 E-mail: robert.trondl@univie.ac.at

Education

1998-2003	HBLVA Rosensteingasse for Chemistry
2003–2005	University of Applied Sciences Fresenius, Germany: Diplom Studies in Chemical Engineering,
2005	Diploma Project in Biological Chemistry at Austrian Institute of Technology Seibersdorf
2005-2008	Technical University of Vienna: Postgraduate studies in Biochemistry and Genetic Engineering
since 2008	University of Vienna: PhD studies in Chemistry, PhD Project in Bioinorganic Chemistry

Career History

2005	Austrian Institute of Technology Seibersdorf
2006–2008	University of Vienna, Institute of Inorganic Chemistry: Project Employee, Cell culture and molecular biology laboratory
2008–2012	University of Vienna, Institute of Inorganic Chemistry: Pre-Doc, Cell culture and molecular biology laboratory

Participation in Scientific Projects

2009–2013	*Critical Targets of Ruthenium, Platinum and Gold Complexes.* Austrian Science Fund (FWF), Project no. L567 (Principal Investigator: B. K. Keppler): Co-Author, Co-Investigator
2012–	*Functional metal complexes that bind to biomolecules*. European Cooperation in Science and Technology (COST) Action CM1105 MC Substitute Member

Career-related Activities

Memberships in scientific societies	American Association Cancer Research (AACR)

Teaching Experience

2008–2010	University of Vienna: Introductory laboratory courses in Chemistry, advanced laboratory courses in Bioinorganic Chemistry

Publications and Congress Contributions

4 (co-)authored research publications
3 authored poster presentations

Journal Article

T1 Kowol CR, Trondl R, Heffeter P, Arion VB, Jakupec MA, Roller A, Galanski M, Berger W, Keppler BK. **2009**. Impact of metal coordination on cytotoxicity of 3-aminopyridine-2-carboxaldehyde thiosemicarbazone (Triapine) and novel insights into terminal dimethylation. *Journal of Medicinal Chemistry* 52:5032-43

T2 Kowol CR, Trondl R, Arion VB, Jakupec MA, Lichtscheidl I, Keppler BK. **2010**. Fluorescence properties and cellular distribution of the investigational anticancer drug Triapine (3-aminopyridine-2-carboxaldehyde thiosemicarbazone) and its zinc(II) complex. *Dalton Transactions* 39:704-6

T3 Kowol CR, Heffeter P, Miklos W, Gille L, Trondl R, Cappellacci L, Berger W, Keppler BK. **2012**. Mechanisms underlying reductant-induced reactive oxygen species formation by anticancer copper(II) compounds. *Journal of Biological Inorganic Chemistry* 17:409-423

T4 Kurzwernhart A, Kandioller W, Bartel C, Bächler S, Trondl R, Mühlgassner G, Jakupec M, Arion V, Marko D, Keppler BK, Hartinger C. **2012**. Targeting the DNA-topoisomerase complex in a double-strike approach with a topoisomerase inhibiting moiety and covalent DNA binder. *Chemical Communications.* in press

Conference Proceedings

C1 Trondl R, Kowol CR, Arion VB, Jakupec MA, Lichtscheidl I, Keppler BK. **2009**. Subcellular distribution study by means of the inherent fluorescence of the investigational drug Triapine and its zinc(II) complex. In: *AACR-NCI-EORTC International Conference: Molecular Targets and Cancer Therapeutics*, Boston, Massachusetts

C2 Trondl R, Kowol CR, Arion V, Jakupec MA, Keppler BK. **2010**. alpha-N-Heterocyclic thiosemicarbazones induce ER stress-mediated CHOP activation. *In: 16th Scientific Symposium of the Austrian Pharmacological Society (APHAR)*, Vienna, Austria

C3 Trondl R, Jungwirth U, Heffeter P, Kowol CR, Arion VB, Jakupec MA, Keppler BK. **2011**. Terminal dimethyl substitution of Triapine leads to activation of CHOP and induction of apoptosis via ER stress in human colon cancer cells. In: *Proceedings of the 102nd Annual Meeting of the American Association for Cancer Research (AACR)*, Orlando, Florida